Civil Engineering and Applied Solutions

Research Article

journal homepage: ceas.journals.umz.ac.ir

CEAS Civil Engineering and Applied Solutions

Evaluation of the Static Behavior of WPC-GFRP Sandwich Panels: An Experimental, Theoretical, and Numerical Study

Amin Norouzi [a], Morteza Naghipour [a*]

[a] *Faculty of Civil Engineering, Babol Noshirvani University of Technology, Babol, Iran*

ARTICLE INFO

Keywords:
Wood plastic composite (WPC)
Glass fiber-reinforced polymer (GFRP)
Static behavior
Sandwich panels
Finite element method (FEM)

Article history:
Received 23 September 2025
Accepted 01 November 2025
Available online 01 April 2026

ABSTRACT

Wood-plastic composite (WPC) is a material composed of wood particles, recycled plastics, and resin, and plays an important role from an economic standpoint. Due to its high compressive and tensile strength, WPC can be used as decking in applications such as pier flooring or small bridge decks. In this study, different glass fiber-reinforced polymer (GFRP) layers were employed to investigate the ultimate load, stiffness, and maximum deformation of WPC-GFRP sandwich panels. Given WPC's lower tensile strength relative to its compressive strength, the reinforcing layers were primarily applied to the bottom face sheets. The loading applied in these experiments was of two types, linear and point loading, perpendicular to the panel surface, to simulate the conditions when such panels are used as flooring. Following the experimental program, theoretical and numerical methods were employed for further analysis of the specimens. In the theoretical approach, beam theory was used because the loading, support conditions, and material behavior closely resembled those of beams. In the numerical approach, uniaxial tests were conducted to determine the material properties and stress–strain relationships, which were then implemented in the finite element model. Overall, the results indicate that the use of a single GFRP layer significantly improves both the strength and stiffness of the panels. However, adding multiple layers does not lead to a considerable improvement in strength, although it slightly enhances stiffness. From an economic perspective, the use of more than one GFRP layer does not appear to be cost-effective. Furthermore, a good agreement was observed among the experimental, theoretical, and numerical results, confirming the reliability of the modeling approaches.

1. Introduction

With the rapid increase in global population and the corresponding surge in industrial and infrastructural demands, the need for a wide range of advanced materials has become increasingly critical. Among these, composite materials have emerged as a pivotal solution, offering enhanced performance through the combination of two or more distinct constituents. Composites, by definition, are multi-phase materials whose overall properties surpass the individual contributions of each constituent, creating synergistic effects that improve stiffness, strength, and durability. Such characteristics make composites suitable for a broad spectrum of engineering applications, including aerospace, automotive, naval structures, sports equipment, bridges, and buildings. The efficient utilization of composite materials requires a precise understanding of their mechanical, thermal, and durability characteristics, as well as the implementation of design strategies tailored to their unique behaviors. Wood-plastic is a new composite that has been used in countries around the world and in our country in the last few years. The superior properties of this material compared to its constituent materials (wood and plastic) have led to the increasing use of this material in industry. Its main advantages include the use of recycled wood and plastic waste in its production [1-6]. These materials have been used in different forms over time. The

* Corresponding author.
E-mail addresses: m-naghi@nit.ac.ir (M. Naghipour).

https://doi.org/10.22080/ceas.2025.30123.1044
ISSN: 3092-7749/© 2026 The Author(s). Published by University of Mazandaran.
This article is an open access article distributed under the terms and conditions of the Creative Commons Attribution (CC-BY) license (https://creativecommons.org/licenses/by/4.0/deed.en)
How to cite this article: Norouzi, A., Naghipour, M. Evaluation of the Static Behavior of WPC-GFRP Sandwich Panels: An Experimental, Theoretical, and Numerical Study. Civil Engineering and Applied Solutions. 2026; 2(2): 1–27. doi:10.22080/ceas.2025.30123.1044.

value and importance of these materials in different societies have varied over time.

The term wood-plastic composites refers to composites that are made of wood in any form and plastics in both thermoset and thermoplastic forms. A product made from a combination of wood and thermoplastics (thermosets) is known as a wood-plastic composite, from which a wide variety of products are obtained for use in various industries. Thermosets (thermosets) are plastics that, once processed, cannot be melted again by heating. These materials, which include resins such as epoxies and phenolics, are in fact plastics that closely resemble industrial forest products (wood) [5]. Wood-plastic composites are the result of combining wood and plastic, where the skill in combining these two components has resulted in the emergence of excellent joint properties. They inherit the hardness and strength of wood and plastic, but their density is often higher than both. The properties of these materials are derived directly from their structure; that is, they are an internal combination of wood and plastic elements [7].

Among composites, wood-plastic composites (WPCs) have gained prominence due to their ability to integrate recycled wood fibers and plastic polymers, thus offering both environmental and structural benefits. The modern concept of WPCs emerged in Italy in the 1970s, and production was initiated by the American company Woodstock in 1783. North American adoption accelerated in the early 1990s, followed by expansion into Asia, including India, Malaysia, Singapore, Japan, and China in the early 21st century. Reports indicate a production increase from 460 million tons in 1999 to approximately 700 million tons by 2001, with annual growth rates of around 18% in North America and 14% in Europe [8]. Plastics must have high ultimate strength and stiffness and exhibit high resistance to fracture. This means that although the plastic has a desirable stiffness, it does not undergo brittle fracture. It should also be noted that if a composite is to be subjected to tensile loading, in order to achieve all the mechanical properties expected from the combination of fibers and plastic, a plastic that is at least as flexible and deformable as the fibers must be selected. The reason for the greater use of plastics is that they have desirable mechanical properties at a reasonable cost. Thermoplastic materials are viscoelastic. This means that their mechanical properties are a product of the behavior of elastic liquids and solids. Therefore, when a thermoplastic material is subjected to stress, the material responds by both dissipating energy in the form of viscous flow and storing energy in the form of elastic displacement. The properties of a viscoelastic material depend on time, temperature, and the rate of strain application. However, conventional stress-strain testing is used to investigate the short-term mechanical properties of plastics [9]. WPCs exhibit superior moisture resistance, absorbing only ~0.7% water compared to ~17.2% in pine wood, thereby significantly reducing susceptibility to fungal attack and decay. These materials can be further engineered by selecting specific wood species and polymers, enabling tailored mechanical and thermal properties suitable for diverse industrial and structural applications. In addition to the effective use of wood and plastic waste, they have significant advantages such as resistance to moisture, mold, and insects, long-term durability, and low maintenance [10-13]. These properties have led to WPCs being widely used in decks, flooring, railings, doors and windows, and decorative components [14]. Despite these advantages, the main limitation of WPC is its relatively low strength and stiffness compared to traditional materials such as concrete, steel, or natural wood [15]. For this reason, the widespread structural use of WPCs is challenging, especially in components that require high load-bearing capacity or high flexural and shear performance. This has led researchers to strengthen WPCs using more advanced materials.

Fiber-reinforced polymers (FRPs) are composite materials that combine high-strength fibers, such as carbon, glass, or aramid, within a polymeric matrix. FRPs were first employed in Europe and Japan during the 1980s for retrofitting concrete structures, replacing corroded steel plates, and reducing installation complexities [16-18]. The fiber phase provides primary tensile strength and stiffness, with typical aspect ratios exceeding 1000, while the polymer matrix ensures load transfer, environmental protection, and durability [18]. Placement, orientation, and volume fraction of fibers critically influence flexural, tensile, compressive, and fatigue performance, as well as thermal and electrical properties.

Experimental investigations have demonstrated the effectiveness of FRP reinforcement for timber and composite structures. Triantafillou Thanasis and Deskovic [13] proposed analytical models for stress-strain behavior of timber members reinforced with FRP sheets, revealing significant improvements in stiffness and load-bearing capacity. Li et al. [11] analyzed CFRP-reinforced timber beams under four-point bending, documenting notable enhancements in flexural resistance and reductions in midspan deflection. Furthermore, Naghipour et al. [14] evaluated the damping characteristics of multilayer glulam beams reinforced with GFRP, indicating up to 40% increases in stiffness and load resistance.

Sandwich panel systems, comprising two stiff faces separated by a lightweight core, offer high rigidity with minimal weight. Originally conceptualized by Delau in 1820, sandwich panels were extensively applied during World War II in aircraft structures, such as the Mosquito, where material shortages necessitated lightweight, high-strength solutions. Early core materials included soft plastics like polystyrene and polyurethane; subsequent development introduced higher-density, stiffer polymers, allowing for broader civil and industrial applications. The integration of WPC and FRP in sandwich panels yields high structural performance, including exceptional resistance to moisture, decay, and mechanical loading. For instance, WPC PVC has successfully supported industrial dock decks under forklift wheel loads distributing 1600-lb per wheel, demonstrating considerable structural reliability [19, 20]. Despite these positive findings, a review of the literature shows that comprehensive and systematic research on the static behavior of WPC-FRP panels is very limited. Many of the existing studies have either only investigated simple WPC beams and slabs or have focused only on the strengthening of concrete and timber members with FRP. There is a significant research gap in the field of investigating the complete static behavior of WPC-FRP sandwich panels, including load capacity, stiffness, deformations, and failure mechanisms.

Nonlinear analytical models, including those proposed by Naghipour et al. [4], have effectively predicted the flexural behavior of WPC-FRP reinforced structures, incorporating exponential stress-strain relationships and accounting for both elastic and plastic responses under load. Such models are essential for accurate prediction of load-displacement behavior, structural safety, and

durability under real-world conditions.

Although several studies have examined the mechanical and flexural behavior of WPC or FRP-reinforced timber members, most previous investigations have focused on individual aspects such as the tensile or flexural performance of WPC beams [3, 9, 14–16] or the strengthening of timber members using external FRP sheets [13, 14]. Very few studies have systematically evaluated the combined behavior of WPC-FRP sandwich panels under realistic loading conditions. Furthermore, previous research has often been limited by: (1) the absence of integrated experimental, theoretical, and numerical evaluation, leading to uncertainties in model validation; (2) simplified material assumptions, where nonlinear and asymmetric tension compression behavior of WPC was not fully represented; and (3) insufficient attention to the failure mechanisms, such as shear or debonding between face sheets and the WPC core.

These limitations have restricted the structural application of WPC-FRP systems in flooring and decking components. Therefore, there remains a clear research gap in developing a comprehensive understanding of the static performance, stiffness, load capacity, and failure mechanisms of WPC-FRP sandwich panels. The present study addresses these gaps by performing a combined experimental, theoretical, and finite-element analysis to assess the flexural behavior of WPC-GFRP sandwich panels, offering insights that can guide the design of lightweight and sustainable structural systems.

Despite these advancements, critical gaps remain in understanding long-term performance, microstructural behavior, and optimization of fiber-matrix combinations in sandwich and composite structures. Addressing these gaps is vital for the design and implementation of high-performance composites in civil, industrial, and marine applications. This study aims to comprehensively evaluate WPC-FRP sandwich structures, investigating their mechanical behavior, durability, and practical applications, thereby contributing to the optimization of composite design and reinforcing strategies in contemporary engineering contexts.

2. Research significance

Wood-plastic composite represents a relatively new class of composite materials that has garnered increasing attention due to its unique combination of mechanical performance, durability, and sustainability. While WPC has been widely applied in non-structural components, such as decking, furniture, and decorative elements, its potential for use in primary structural applications, including bridge decks, small-scale flooring, and load-bearing panels, remains largely unexplored. Understanding and optimizing the mechanical properties of WPC for structural use is therefore of significant importance, as it can lead to the development of lightweight, durable, and cost-effective structural members. The significance of this research lies in addressing the critical question of whether WPC can reliably replace conventional materials in structural components while meeting required performance standards. To enhance stiffness and load-bearing capacity, the integration of WPC into a sandwich panel configuration is proposed, where two thin but strong outer faces are separated by a lightweight core. In this study, the core is composed of glss fiber-reinforced polymer, which is expected to synergistically enhance the mechanical performance of the composite panel. The presented study is particularly valuable as it combines experimental investigation and theoretical modeling to evaluate the structural behavior of WPC-based sandwich panels. Static performance parameters such as failure strength, stiffness, and deflection under applied loads are systematically studied. The findings of this study will provide critical insights into the design and optimization of WPC-based structural members, enabling their safe and effective application in civil and industrial engineering projects. Furthermore, the research contributes to sustainable material development by promoting the use of recycled wood and plastics, thereby supporting environmentally responsible construction practices. Overall, the study addresses a gap in current knowledge regarding the structural applicability of WPC, providing both experimental evidence and theoretical validation that can guide future adoption of this versatile and eco-friendly material in engineering structures.

3. Experimental study

This section presents the experimental program conducted to investigate the flexural behavior of sandwich panels composed of WPC plates and externally bonded GFRP sheets. To evaluate the performance of these panels under floor-type loading conditions, where transverse loads are predominant, a total of eight specimens were prepared. Among them, four panels were tested under concentrated point loading, while the remaining four were subjected to linear loading. The following subsections describe the materials, preparation of specimens, and test procedures.

3.1. Material properties

The WPC plates employed in this research were hollow sections with nominal dimensions of 54 × 54 cm. Their geometry and cross-section are illustrated in Figs. 1 and 2, respectively.

Fig. 1. WPC plate.

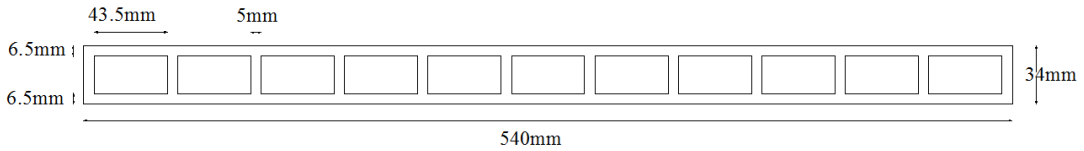

Fig. 2. Cross-section of WPC plate.

The reinforcement consisted of unidirectional glass fiber reinforced polymer (GFRP) sheets, with all fibers aligned in the longitudinal direction (Fig. 3). The mechanical properties of the GFRP sheets, as provided by the manufacturer, are summarized in Table 1.

Fig. 3. Unidirectional GFRP sheets.

Table 1. Mechanical properties of GFRP sheets.

Fiber type	Thickness (mm)	Unit weight (g/mm^2)	Tensile strength (MPa)	Modulus of elasticity (GPa)
GFRP	0.12	420	2300	76

The GFRP sheets were bonded to WPC substrates using a two-component epoxy adhesive consisting of resin and hardener (Fig. 4). The mixing ratio was 2:1 by weight. The epoxy exhibited adequate viscosity for surface application and a pot life of approximately 70 minutes at room temperature. Mechanical properties are summarized in Table 2.

Table 2. Mechanical properties of epoxy adhesive.

Flexural strength (MPa)	Tensile strength (MPa)	Compressive strength (MPa)	Tensile modulus of elasticity (MPa)
78.2	43	130	1560

Fig. 4. Epoxy resin and hardener mixture.

3.2. Test specimens and characterization

In order to be able to compare the results obtained through the experiments with analytical and numerical methods, we must have the properties and specifications of the materials. In this study, the adhesive and GFRP sheets were previously tested by the manufacturer in a very precise manner and in accordance with the relevant standards, and this information was available. However, detailed information regarding the behavior of the WPC used was not available, so the strength, initial modulus of elasticity, and the overall behavior of the WPC in compression and tension were determined by uniaxial compressive and tensile tests. These tests are as follows:

3.2.1. Compression test

Compressive strength was determined in accordance with ASTM D695 [21]. Specimens of 25.4 × 12.7 × 12.7 mm were prepared Fig. 5, and a total of seven replicates were tested to minimize experimental error.

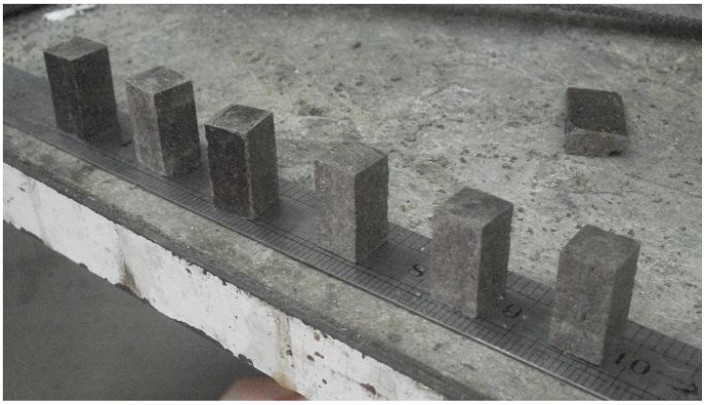

Fig. 5. WPC specimens for compression test.

Loading was applied under displacement control at a rate of 1 mm/min using a universal testing machine (STM-150). The testing setup is shown in Fig. 6.

Fig. 6. Compressive strength test setup.

The results of the compression test are presented in Table 3.

Table 3. Results of the compression test on WPC.

Compressive strength (MPa)	Maximum strain	Initial modulus of elasticity (MPa)
45.798	0.0459	2359

3.2.2. Tensile strength test

According to ASTM D638 [22] standard, tensile specimens were prepared in the specified dimensions as shown in Fig. 7. A milling machine was used to cut and prepare the specimens in the specified dimensions. The specimens for tensile testing are shown in Fig. 8.

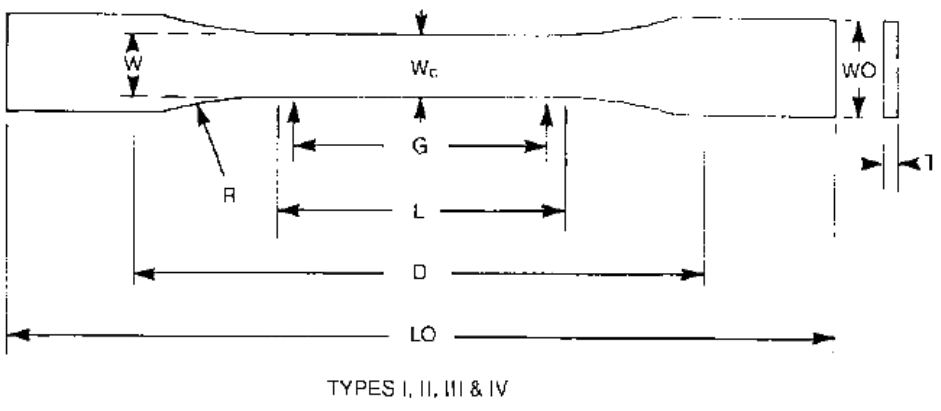

Fig. 7. Geometry of tensile specimens (ASTM D638 [22]).

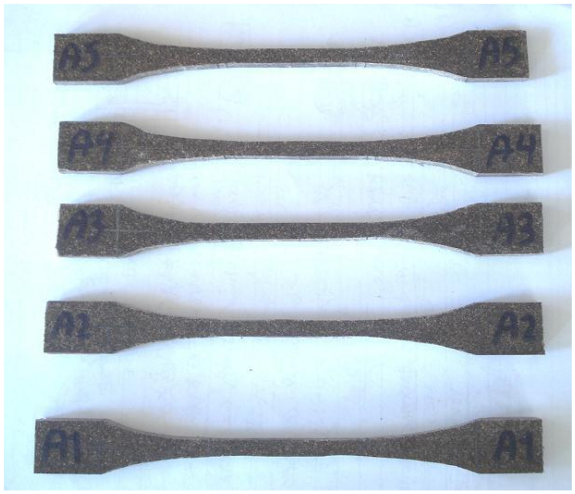

Fig. 8. Prepared tensile specimens.

Loading was applied at 1 mm/min using a universal testing machine (STM-250), as shown in Fig. 9.

Fig. 9. Tensile strength test setup.

The tensile test results are presented in Table 4.

Table 4. Results of the tensile strength test on WPC.

Tensil strength (MPa)	Maximum strain	Initial modulus of elasticity (MPa)
16.578	0.0102	1959.8

3.3. Test specimens (sandwich panels)

Eight sandwich panels were fabricated and categorized into four groups (two specimens per group). The test matrix is summarized in Table 5.

Table 5. Specimen configurations.

Group	GFRP layers (bottom)	GFRP layers (top)
A_0, P_0	0	0
A_1, P_1	1	1
A_2, P_2	1	2
A_3, P_3	1	3

Before gluing the GFRP layers, first the WPC surfaces and GFRP sheets were thoroughly cleaned and wiped so that no dust or dirt remained. Next, the sheets were prepared by cutting the layers to the size of the WPC surfaces, i.e., 54 × 54 cm, and by mixing 160 g of resin and 80 g of hardener, the epoxy adhesive was prepared for gluing. Finally, the GFRP layers were glued by spreading the adhesive evenly on the WPC. The time required to reach maximum adhesive strength was 7 - 10 days, which was taken into account before the test. During preliminary trials, poor bonding was observed due to the glazed finish on the WPC surface, which prevented adequate adhesion.

To resolve this, the surface glaze was removed using a wire brush attached to a grinding machine, resulting in a roughened texture Fig. 10. The final prepared specimens are shown in Fig. 11.

Fig. 10. WPC surface after glaze removal.

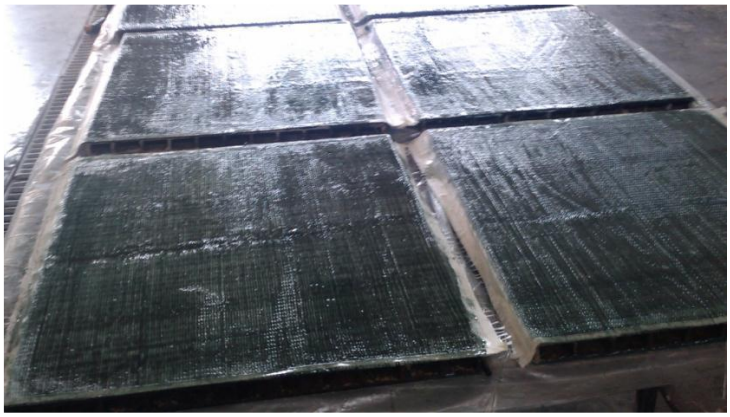

Fig. 11. GFRP bonded to WPC without glazing.

3.4. Test setup and instrumentation

3.4.1 Support configuration

As mentioned in the previous sections, the STM150 universal device was used for the bending test. The support provided for this device was suitable for beams with a maximum width of 15 cm. Since the width of the panels was 54 cm, a suitable support had to be designed to use the device.

3.4.2. Loading attachments

The universal testing machine applies load through a 13 cm linear bearing surface. To simulate two types of loading, concentrated point loading and distributed linear loading across 54 cm, two steel attachments were fabricated. Owing to their high stiffness relative to WPC, steel deformations were considered negligible.

3.5. Loading procedure

The load on the WPC was applied in two ways: point and linear. First, 4 samples (one sample from each group) were subjected to a point load. However, since the results of this loading did not fully satisfy the purpose of this research, the remaining 4 samples were tested as linear loading.

3.5.1. Point loading

As shown in Fig. 12, the span length was set at 54 cm, with hinge supports at both ends.

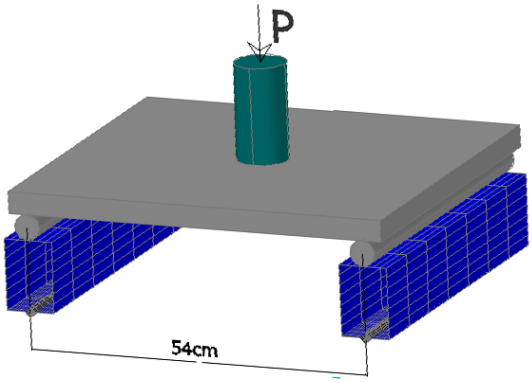

Fig. 12. Point loading schematic view.

The loading was performed under displacement control at a constant rate of 5 mm/min, as recommended by ASTM D790 for

quasi-static flexural testing of polymer and composite materials. This rate was selected to ensure stable crack propagation and to minimize dynamic or rate-dependent effects during testing (Fig. 13).

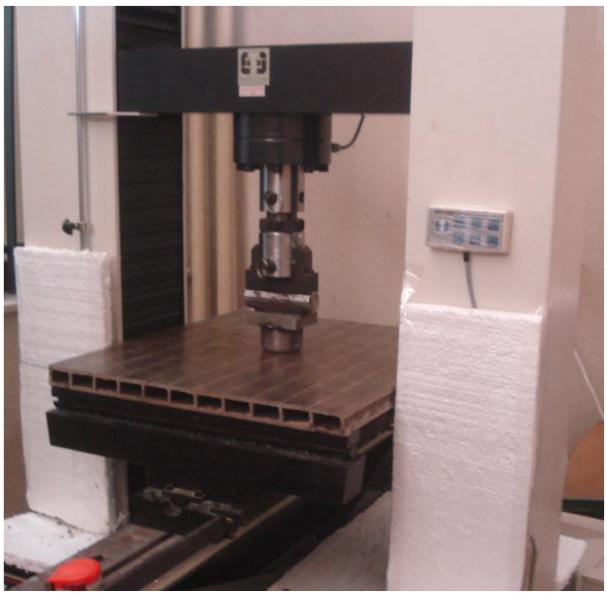

Fig. 13. Experimental setup for point loading.

The loading proceeded to a stage where the WPC-GFRP panel broke, or the force applied to the monitor became close to zero.

3.5.2. Linear Loading

In the second loading configuration, the panels were tested under linear loading conditions Fig. 14, simulating a three-point bending scenario with extended load distribution.

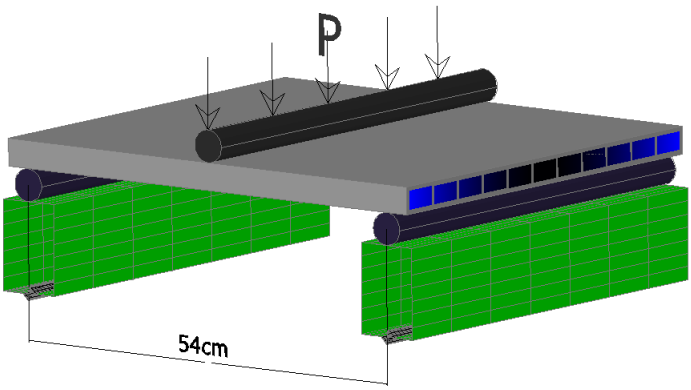

Fig. 14. Linear loading schematic view.

After positioning the steel attachment at midspan, the panels were tested under the same displacement rate of 5 mm/min until failure (Fig. 15).

Fig. 15. Experimental load–deflection curves of WPC–GFRP panels under point loading.

4. Theoretical analysis

The static behavior of the WPC-GFRP sandwich panels was first investigated using theoretical formulations based on composite laminate mechanics, sandwich beam theory, and plate theory.

4.1. Composite laminate mechanics

The GFRP facesheets were modeled as orthotropic elastic laminates, in which the stress–strain relationship follows the generalized Hooke's law for anisotropic media:

$$\sigma_{ii} = C_{ij}.\varepsilon_j \quad , \quad i,j=1\ldots\ldots6 \tag{1}$$

Where σ_i represents the stress components, C_{ij} denotes the stiffness matrix coefficients, and ε_j are the strain components. For small deformations, the strain–displacement relations are given by:

$$\begin{aligned} &\varepsilon_x = \frac{\delta_u}{\delta_x}, \qquad \varepsilon_y = \frac{\delta_v}{\delta_y}, \qquad \varepsilon_z = \frac{\delta_w}{\delta_z} \\ &\varepsilon_{xz} = \frac{1}{2}\left(\frac{\delta_u}{\delta_z} + \frac{\delta_w}{\delta_x}\right), \qquad \varepsilon_{yz} = \frac{1}{2}\left(\frac{\delta_v}{\delta_z} + \frac{\delta_w}{\delta_y}\right), \qquad \varepsilon_{xz} = \frac{1}{2}\left(\frac{\delta_u}{\delta_y} + \frac{\delta_v}{\delta_x}\right) \end{aligned} \tag{2}$$

The strain energy density increment is expressed as:

$$d\mathrm{w} = \sigma_i.d\varepsilon_i \tag{3}$$

In these relations, *u*, *v*, and *w* denote the displacements along the *x*, *y*, and *z* directions, respectively, and the partial derivatives represent the spatial deformation components under small strain assumptions. which yields the total strain energy as:

$$w = \frac{1}{2}C_{ij}.\varepsilon_i.\varepsilon_j \tag{4}$$

By taking the derivative of the strain energy with respect to ε_i and ε_j, the following relations are obtained:

$$\frac{\partial W}{\partial\varepsilon_i\partial\varepsilon_j} = C_{ij} \tag{5}$$

$$\frac{\partial W}{\partial\varepsilon_j\partial\varepsilon_i} = C_{ij} \tag{6}$$

Comparing Eqs. 5 and 6, it is concluded that the stiffness matrix is symmetric, that is:

$$C_{ij} = C_{ji} \tag{7}$$

For this reason, the number of independent coefficients in the stiffness matrix is reduced from 36 to 21. A similar symmetry also holds for the softness matrix (*S*):

$$S_{ij} = S_{ji} \tag{8}$$

Therefore, the general relationship between stress and strain will be in the following matrix form:

$$\begin{Bmatrix}\sigma_1\\ \sigma_2\\ \sigma_3\\ \sigma_{23}\\ \sigma_{31}\\ \sigma_{12}\end{Bmatrix} = \begin{bmatrix}C_{11} & C_{12} & C_{13} & C_{14} & C_{15} & C_{16}\\ C_{21} & C_{22} & C_{23} & C_{24} & C_{25} & C_{26}\\ C_{31} & C_{32} & C_{33} & C_{34} & C_{35} & C_{36}\\ C_{41} & C_{42} & C_{43} & C_{44} & C_{45} & C_{46}\\ C_{51} & C_{52} & C_{53} & C_{54} & C_{55} & C_{56}\\ C_{61} & C_{62} & C_{63} & C_{64} & C_{56} & C_{66}\end{bmatrix} * \begin{Bmatrix}\varepsilon_1\\ \varepsilon_2\\ \varepsilon_3\\ \gamma_{23}\\ \gamma_{31}\\ \gamma_{12}\end{Bmatrix} \tag{9}$$

The stiffness matrix becomes simpler depending on the number of symmetry planes in the material:

$$\begin{Bmatrix}\sigma_1\\ \sigma_2\\ \sigma_3\\ \tau_{23}\\ \tau_{31}\\ \tau_{12}\end{Bmatrix} = \begin{bmatrix}C_{11} & C_{12} & C_{13} & 0 & 0 & C_{16}\\ & C_{22} & C_{23} & 0 & 0 & C_{26}\\ & & C_{33} & C_{34} & 0 & C_{36}\\ & & & C_{44} & C_{45} & C_{46}\\ & sym & & & C_{55} & C_{56}\\ & & & & & C_{66}\end{bmatrix} * \begin{Bmatrix}\varepsilon_1\\ \varepsilon_2\\ \varepsilon_3\\ \gamma_{23}\\ \gamma_{31}\\ \gamma_{12}\end{Bmatrix} \tag{10}$$

Two or three perpendicular planes (orthotropic):

$$\begin{Bmatrix}\sigma_1\\ \sigma_2\\ \sigma_3\\ \tau_{23}\\ \tau_{31}\\ \tau_{12}\end{Bmatrix} = \begin{bmatrix}C_{11} & C_{12} & C_{13} & 0 & 0 & 0\\ & C_{22} & C_{23} & 0 & 0 & 0\\ & & C_{33} & 0 & 0 & 0\\ & & & C_{44} & 0 & 0\\ & sym & & & C_{55} & 0\\ & & & & & C_{66}\end{bmatrix} * \begin{Bmatrix}\varepsilon_1\\ \varepsilon_2\\ \varepsilon_3\\ \gamma_{23}\\ \gamma_{31}\\ \gamma_{12}\end{Bmatrix} \tag{11}$$

Lateral isotropic:

$$\begin{Bmatrix}\sigma_1\\ \sigma_2\\ \sigma_3\\ \tau_{23}\\ \tau_{31}\\ \tau_{12}\end{Bmatrix}=\begin{bmatrix}C_{11} & C_{12} & C_{13} & 0 & 0 & 0\\ & C_{22} & C_{23} & 0 & 0 & 0\\ & & C_{33} & 0 & 0 & 0\\ & & & C_{44} & 0 & 0\\ & & & & C_{55} & 0\\ & sym & & & & \frac{(C_{11}-C_{12})}{2}\end{bmatrix}*\begin{Bmatrix}\varepsilon_1\\ \varepsilon_2\\ \varepsilon_3\\ \gamma_{23}\\ \gamma_{31}\\ \gamma_{12}\end{Bmatrix} \tag{12}$$

Perfect isotropic:

$$\begin{Bmatrix}\sigma_1\\ \sigma_2\\ \sigma_3\\ \tau_{23}\\ \tau_{31}\\ \tau_{12}\end{Bmatrix}=\begin{bmatrix}C_{11} & C_{12} & C_{13} & 0 & 0 & 0\\ & C_{22} & C_{23} & 0 & 0 & 0\\ & & C_{33} & 0 & 0 & 0\\ & & & \frac{(C_{11}-C_{12})}{2} & 0 & 0\\ & sym & & & \frac{(C_{11}-C_{12})}{2} & 0\\ & & & & & \frac{(C_{11}-C_{12})}{2}\end{bmatrix}*\begin{Bmatrix}\varepsilon_1\\ \varepsilon_2\\ \varepsilon_3\\ \gamma_{23}\\ \gamma_{31}\\ \gamma_{12}\end{Bmatrix} \tag{13}$$

For the orthotropic case, the coefficients $C_{ij}=C_{ji}$ are calculated based on Young's moduli, Poisson's ratios, and shear moduli. Eqs. 14 to 18 show these dependencies.

$$C_{11}=\frac{1-v_{23}v_{32}}{E_2E_3\Delta} \qquad C_{22}=\frac{1-v_{13}v_{31}}{E_1E_3\Delta} \qquad C_{33}=\frac{1-v_{12}v_{21}}{E_1E_2\Delta} \tag{14}$$

$$C_{12}=\frac{v_{21}+v_{31}v_{23}}{E_2E_3\Delta}=\frac{v_{21}+v_{32}v_{13}}{E_1E_3\Delta} \tag{15}$$

$$C_{23}=\frac{v_{32}+v_{12}v_{31}}{E_1E_3\Delta}=\frac{v_{23}+v_{21}v_{13}}{E_1E_2\Delta} \tag{16}$$

$$C_{13}=\frac{v_{31}+v_{21}v_{32}}{E_2E_3\Delta}=\frac{v_{13}+v_{12}v_{23}}{E_1E_2\Delta} \tag{17}$$

$$C_{44}=G_{23}, \quad C_{55}=G_{31}, \quad C_{66}=C_{13}$$

$$\Delta=\frac{1-v_{12}v_{23}-v_{23}v_{32}-v_{31}v_{13}-2(v_{12}v_{23}v_{13})}{E_1E_2E_3} \tag{18}$$

The important point is that these relations are valid for a layer whose fiber axis is aligned with the axes. However, in practice there is usually an angle between the fibers and the axes. For this purpose, the transfer matrix Eq. 19 must be used to calculate the stiffness values in the new coordinate system.

$$\begin{Bmatrix}\sigma_x\\ \sigma_y\\ \sigma_{xy}\end{Bmatrix}=\begin{bmatrix}cos_a^2 & sin_a^2 & -2sinacosa\\ sin_a^2 & cos_a^2 & 2sinacosa\\ sinacosa & -sinacosa & cos_a^2-sin_a^2\end{bmatrix}\begin{Bmatrix}\sigma_x\\ \sigma_y\\ \sigma_{xy}\end{Bmatrix} \tag{19}$$

For the plane stress case, Eq. 20 express the relationship between the stiffness matrix Q, the transfer matrix T, and the transferred stiffness matrix $\bar{Q}$. When the lamina axes are rotated with respect to the global coordinate system, the transformed reduced stiffness matrix is:

$$\begin{Bmatrix}\sigma_x\\ \sigma_y\\ \sigma_{xy}\end{Bmatrix}_k=[\bar{Q}]_k\begin{Bmatrix}\varepsilon_x\\ \varepsilon_y\\ \varepsilon_{xy}\end{Bmatrix}_k \qquad \text{and} \qquad [\bar{Q}]_k=[T]_k^{-1}[Q]_k[T]_k^{-1} \tag{20}$$

4.2. Levy solution for rectangular sheet

To investigate the elastic behavior of rectangular plates under loading, Levy's method is used. This method is based on the equations governing the bending of plates in the classical theory of elasticity. The governing differential equation for the transverse displacement *w(x,y)* is expressed as follows:

$$\frac{\partial^4 w}{\partial x^4}+2\frac{\partial^4 w}{\partial x^2\partial y^2}+\frac{\partial^4 w}{\partial y^4}=\frac{p(x,y)}{D} \tag{21}$$

Where *D* is the flexural rigidity of the plate ($D=Eh^3/12(1-\nu^2)$), *w*(*x*, *y*) is the transverse displacement, *q*(*x*, *y*) is the distributed transverse load, *E* is the elastic modulus, *h* is the thickness of the plate, and *v* is Poisson's ratio.

The Levy method can be used for a rectangular sheet where two opposite supports (for example, supports $x = 0$ and $x = a$) are the same and the other two supports ($y = \pm b/2$) are arbitrary. The general solution in this method includes the general solution w_h and the particular solution w_p, which is equal to:

$$w_h = \sum_{m=1}^{\infty} \left(A_m \sinh \frac{m\pi x}{a} + B_m \cosh \frac{m\pi x}{a} + C_m y \cosh \frac{m\pi x}{a} + D_m y \cosh \frac{m\pi x}{a} \right) \tag{22}$$

In order to satisfy the boundary conditions of the sheet at the edges $x = 0$ and $x = a$, the particular solution can be expressed as the Fourier series of Eq. 23.

$$w_p = \sum_{m=1}^{\infty} k_m(y) \frac{\sin m\pi x}{a} \tag{23}$$

$$p(x,y) = \sum_{m=1}^{\infty} p_m(y) \frac{\sin m\pi x}{a} \tag{24}$$

$$p_m(y) = \frac{2}{a} \int_{\frac{a}{2}+\xi}^{\frac{a}{2}+\xi} p(x,y) \frac{\sin m\pi x}{a} dx$$

$$p(x,y) = \frac{p_0}{\xi} \tag{25}$$

$$\lim_{\xi \to 0} p_m(y) = \frac{2p_0}{a}$$

By substituting Eqs. 23 and 24 into Eq. 21, given that the obtained equation should yield results for all values of x between 0 and a.

$$\frac{d^4 k_m}{dy^4} - 2\left(\frac{m\pi}{a}\right)^2 \frac{d^2 k_m}{dy^2} + \left(\frac{m\pi}{a}\right)^4 k_m = \frac{p_m}{D} \tag{26}$$

For the case $P(x,y) = P_0$, it follows from Eq. 25;

$$p_m = \frac{2p_0}{a} \qquad (m = 1, 3, \dots) \tag{27}$$

$$w_p = \frac{2p_0 a^3}{\pi^4 D} \sum_{m=1}^{\infty} \frac{1}{m^4} \frac{\sin m\pi x}{a} \tag{28}$$

By selecting axes, the deflection of the sheet must be symmetrical about the x-axis. In other words, the deflections for $+y$ and $-y$ must be equal. Consequently, the total deflection of the sheet is equal to:

$$W = \sum_{m=1,3,\dots}^{\infty} \left(B_m \cosh \frac{m\pi x}{a} + C_m y \cosh \frac{m\pi x}{a} + \frac{2p_0 a^3}{m^4 \pi^4 D} \right) \frac{\sin m\pi x}{a} \tag{29}$$

Putting these two boundary conditions into Eq. 29, we have:

$$B_m = -\left(\frac{2a^3 Pv(bm\pi)(-1+v)\cosh\left[\frac{bm\pi}{2a}\right] + 2a(1+v)\sinh\left[\frac{bm\pi}{2a}\right]}{Dm^4\pi^4\left(bm\pi(-1+v)\right) + a(3+v)\sinh\left[\frac{bm\pi}{2a}\right]} \right) \tag{30}$$

$$C_m = -\left(\frac{4a^3 Pv(bm\pi)\sinh\left[\frac{bm\pi}{2a}\right]}{Dm^3\pi^3(-1+v)\left(bm\pi(-1+v)\right) + a(3+v)\sinh\left[\frac{bm\pi}{2a}\right]} \right) \tag{31}$$

So we have:

$$W_{max} = \sum_{m=1,3,\dots}^{\infty} \left(\frac{1}{Dm^4\pi^4\left(bm\pi(-1+v)\right) + a(3+v)\sinh\left[\frac{bm\pi}{2a}\right]} \right) 2a^3 p \sin\left[\frac{m\pi}{2}\right]$$
$$\left(-bm\pi(-1+v)v\cosh\left[\frac{bm\pi}{2a}\right] - 2av(1+v)\sinh\left[\frac{bm\pi}{2a}\right] \right. \tag{32}$$
$$\left. + (-1+v)\left(bm\pi(-1+v) + a(3+v)\sinh\left[\frac{bm\pi}{2a}\right] \right) \right)$$

4.3. Bending theory of WPC-GFRP sandwich panels

When a beam is subjected to concentrated forces, self-weight, or applied couples, bending moments are generated, which lead to deformation. Under the action of external loads, the upper fibers of the beam shorten and are thus in compression, while the lower fibers elongate and are subjected to tension. The line dividing the compression and tension regions, along which no strain occurs, is defined as the neutral axis (NA). Experimental uniaxial tests on WPC revealed that its mechanical response in both compression and tension is nonlinear, indicating deviation from Hooke's law. Furthermore, the material exhibits asymmetric behavior in compression and tension. To capture this nonlinear response, curve fitting was performed on the stress–strain diagrams, leading to the constitutive relation:

$$\sigma = A\varepsilon^2 + B\varepsilon \tag{33}$$

Where σ_c and σ_t are the compressive and tensile stresses in the WPC core, respectively; ε_c and ε_t are the corresponding strains; and a, b, c, and d are regression constants derived from the experimental stress–strain data.

For the GFRP reinforcement, a linear elastic relationship was assumed up to failure:

$$\sigma_{frp} = E_{frp}\varepsilon_{frp} \tag{34}$$

Where σ_f and ε_f are the stress and strain in the GFRP reinforcement, E_f is the elastic modulus of the GFRP layer, and the response is assumed linear up to failure.

The tested WPC-GFRP cross-section can be idealized as an assembly of I-shaped elements. Due to symmetry in geometry, loading, and support conditions, shear stresses between adjacent elements can be neglected, allowing the analysis of a single equivalent I-beam subjected to the same distributed load. Considering the linear distribution of strain across the section depth, the following strain relations for the face and core fibers can be written:

$$\varepsilon_{fm} = \frac{\varepsilon_{top}\left(H - h + t_{frp}\right)}{h} \tag{35}$$

$$\varepsilon_{wm} = \frac{\varepsilon_{top}(H - h)}{h} \tag{36}$$

By substituting the constitutive models (Eqs. 33 and 34) into the equilibrium condition, the axial force balance (Eq. 37), bending moment capacity (Eq. 38), and maximum shear force (Eq. 39) are obtained. Furthermore, considering the linear strain distribution:

$$\begin{aligned}\int_0^h b_f[A\varepsilon^2 + B\varepsilon]dy - \int_0^{h-t_f}\left(b_f - t_w\right)[A\varepsilon^2 + B\varepsilon]dy + A_{frp}E_{frp}\varepsilon_{frp} - \\ \int_0^{H-h} b_f'\left[A'^{\varepsilon^2} + B'\varepsilon\right]dy + \int_0^{H-h-t_f{}'}\left(b'_f - t_w\right)\left[A'^{\varepsilon^2} + B'\varepsilon\right]dy + A'_{frp}E_{frp}\varepsilon'_{frp} = 0\end{aligned} \tag{37}$$

$$\begin{aligned}M = \int_0^h b_f[A\varepsilon^2 + B\varepsilon]ydy - \int_0^{h-t_f}\left(b_f - t_w\right)[A\varepsilon^2 + B\varepsilon]ydy + A_{frp}E_{frp}\varepsilon_{frp}\left(h + \frac{t_{frp}}{2}\right) \\ - \int_0^{H-h} yb_f'\left[A'^{\varepsilon^2} + B'\varepsilon\right]dy \\ + \int_0^{H-h-t_f{}'}\left(b'_f - t_w\right)\left[A'^{\varepsilon^2} + B'\varepsilon\right]ydy + A'_{frp}E_{frp}\varepsilon'_{frp}\left(H - h + \frac{t'_{frp}}{2}\right)\end{aligned} \tag{38}$$

$$V_{max} = \int_0^h b_f[A\varepsilon^2 + B\varepsilon]dy - \int_0^{h-t_f}\left(b_f - t_w\right)[A\varepsilon^2 + B\varepsilon]dy + A_{frp}E_{frp}\varepsilon_{frp} \tag{39}$$

$$\varepsilon = \frac{\varepsilon_{top}y}{h} \tag{40}$$

In the above relations, M the bending moment, V the shear force, σ and ε the stress and strain distributions across the section depth h and y the distance from the neutral axis.

By substituting into the governing relations yields the simplified expressions for bending moment and shear capacity:

$$\begin{aligned}M = \frac{1}{6h^2}\varepsilon_{top}\big(3Bb_fh^3 + 2Ab_f\varepsilon_{top}h^3 - b'_f(h - H)^2\big(3B'h + 2A\varepsilon_{top}(h - H) + \\ 3A_{frp}E_{frp}h\left(2h + t_{frp}\right) + 3A'_{frp}E_{frp}h\left(2h + 2H - t'_{frp}\right) - \left(3Bh + 2A\varepsilon_{top}\left(h - t_f\right)\right. \\ \left(h - t_f\right)^2\left(b_f - t_w\right) + \left(h - H + t'_f{}^2\right)\left(3B'h - 2A'\varepsilon_{top}\left(h - H - t'_f\right)\left(b'_f - t_w\right) = 0\end{aligned} \tag{41}$$

$$\begin{aligned}V_{max}=\tfrac{1}{6h^2}\varepsilon_{top}\left(3Bb_fh^3 + 2Ab_f\varepsilon_{top}h^3 + 3A_{frp}E_{frp}h\left(2h + t_{frp}\right)\right. - \left(3B\,h + 2A\varepsilon_{top}\right.(h - \\ t_f)\left(h - t_f\right)^2\left(b_f - t_w\right)\end{aligned} \tag{42}$$

Where M and V represent the ultimate bending moment and shear capacity, respectively, and $\tau_{\max}$ denotes the maximum shear stress developed within the core.

Two primary failure criteria are considered in the bending analysis:

- Flexural failure: occurs when the compressive or tensile strain at the extreme fibers reaches the ultimate strain capacity.
- Shear failure: occurs when the core shear stress exceeds its maximum allowable shear strength.

The bending response of the WPC-GFRP sandwich section is therefore governed by the interaction between the nonlinear behavior of the WPC core and the linear elastic contribution of the GFRP layers, with failure predicted by the most critical of the two mechanisms.

5. Numerical method

The Finite element method (FEM) is a powerful numerical tool for solving engineering problems and encompasses a wide range of analyses. This method is applied not only in structural analysis but also in diverse physical problems, including heat transfer, seepage, fluid flow, and electric or magnetic potential. Generally, analyzing an engineering problem requires developing a mathematical model representing the physical conditions. The mathematical model of a geometric problem is referred to as the governing equations of the problem. These governing equations are primarily differential equations accompanied by initial and boundary conditions. Differential equations are derived by applying fundamental laws, such as the conservation of mass, force, and energy, to an infinitesimal element of the system.

In FEM, the differential equations for each element are solved using interpolation functions, and the element-level governing equations are obtained. By assembling the equations of all elements, the global governing equations of the entire model are formed. Ultimately, these differential equations are replaced with a system of linear or nonlinear algebraic equations for numerical solution. For complex geometries, FEM modeling can be time-consuming and costly. Using FEM software significantly reduces this difficulty. One widely used FEM software is ABAQUS, which has gained prominence in research and industry worldwide due to its flexibility and capability to solve diverse engineering problems. In this study, ABAQUS was employed to implement the numerical analysis.

5.1. Development of a numerical model

To create an analytical model, several steps are followed. First, the general configuration of the structure must be defined, followed by the material behavior of the structural components. Key considerations include yield criteria, hardening, and the transition to plastic behavior. Next, structural components are defined according to geometry and material. The choice of element type influences system behavior and must be based on understanding element characteristics, response under applied loads, location in the model, relative dimensions, and experience from similar analyses.

After defining all elements, they are assembled into a complete structure, meshed, and boundary conditions are applied. Loading is then introduced to prepare the model for analysis.

In this study, WPC-GFRP sandwich panels with dimensions 54×54 cm were tested experimentally. The geometric properties of these samples were first defined in ABAQUS using the Part module. Solid extrusion was used for WPC and steel sections, while shell elements were applied for GFRP sheets. Detailed geometries are illustrated in Fig. 16.

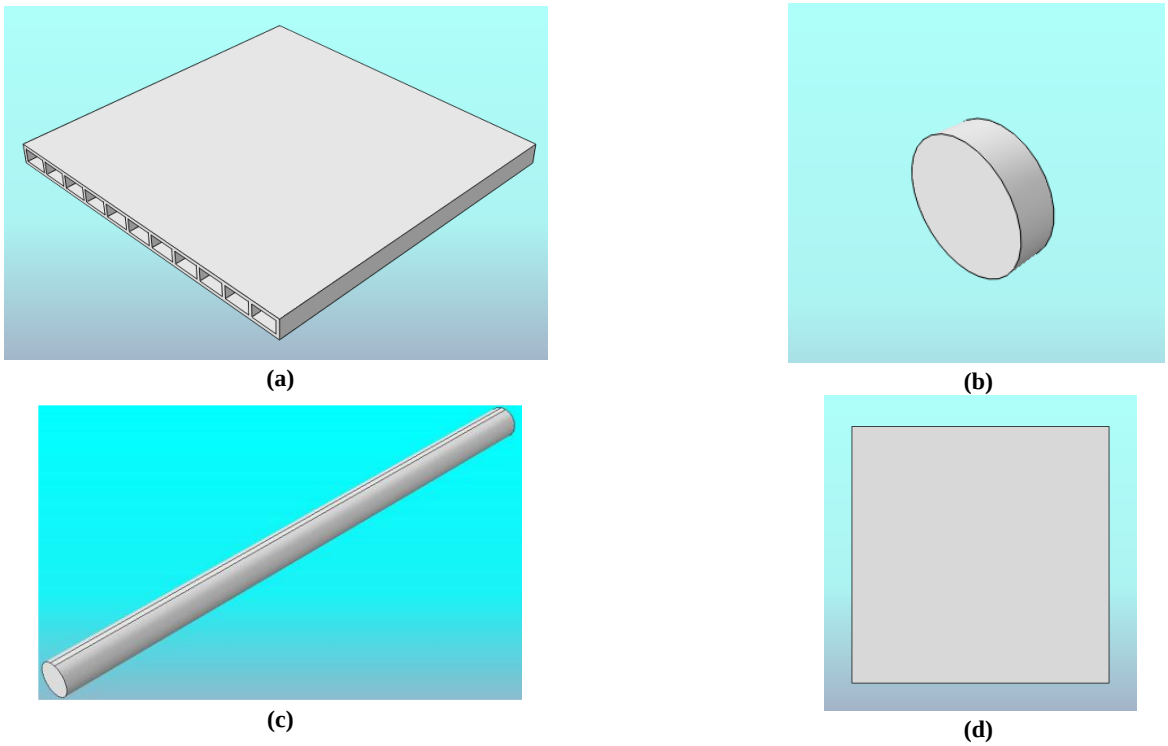

Fig. 16. Developed segments: (a) WPC drawing, (b) Drawing of steel part (for point loading), (c) Drawing of a steel part (for linear loading), and (d) Drawing of GFRP sheets.

5.2. Material modeling

For point-loading simulations, a material with arelatively high elastic modulus is required. Steel sections used in the study exhibit such stiffness and are modeled as isotropic elastic with E = 210 GPa and Poisson's ratio v = 0.3. Isotropic materials have identical elastic properties in all directions, and their stress-strain relationship is given by:

$$\varepsilon_{11} = \frac{\sigma_{11}}{E} - \frac{v}{E}(\sigma_{22} + \sigma_{33}) \tag{43}$$

$$\varepsilon_{22} = \frac{\sigma_{22}}{E} - \frac{v}{E}(\sigma_{11} + \sigma_{33})$$
$$\varepsilon_{11} = \frac{\sigma_{33}}{E} - \frac{v}{E}(\sigma_{11} + \sigma_{22})$$
$$\gamma_{11} = \frac{\tau_{12}}{G}, \gamma_{13} = \frac{\tau_{13}}{G}, \gamma_{23} = \frac{\tau_{23}}{G}$$

The shear modulus is computed as:

$$G = \frac{E}{2(1+v)} \tag{44}$$

The elastic coefficient matrix for isotropic materials is given in Eq. 45.

$$[D] = \begin{bmatrix} \frac{1}{E} & \frac{-v}{E} & \frac{-v}{E} & 0 & 0 & 0 \\ \frac{-v}{E} & \frac{1}{E} & \frac{-v}{E} & 0 & 0 & 0 \\ \frac{-v}{E} & \frac{-v}{E} & \frac{1}{E} & 0 & 0 & 0 \\ 0 & 0 & 0 & \frac{1}{G} & 0 & 0 \\ 0 & 0 & \frac{-v}{E} & 0 & \frac{1}{G} & 0 \\ 0 & 0 & \frac{1}{E} & 0 & 0 & \frac{1}{G} \end{bmatrix} \tag{45}$$

Where σ and ε are the stress and strain tensors, E is the elastic modulus, v is Poisson's ratio, and G is the shear modulus of elasticity. The matrix C represents the constitutive stiffness matrix for isotropic elastic materials.

Experimental results indicated that WPC exhibits nonlinear and distinct tensile and compressive behavior. In ABAQUS, such behavior was modeled using the Cast Iron material option, which accommodates nonlinear plastic behavior. Although the material behaves elastically throughout the experiment, this approach accurately represents its mechanical response. Although wood–plastic composites (WPCs) generally exhibit viscoelastic characteristics under long-term or cyclic loading, such effects are insignificant in the present study because all tests and numerical simulations were conducted under monotonic static loading until failure. Therefore, the primary focus of the modeling was to reproduce the nonlinear stress–strain response and tension–compression asymmetry rather than time-dependent creep or relaxation behavior. The Cast Iron Plasticity model in ABAQUS was selected for this purpose because it provides the capability to define distinct tensile and compressive stress–strain relationships and allows for stiffness degradation after yielding, consistent with the observed experimental response. This approach has also been successfully applied in recent studies on quasi-brittle and polymer-based composites under monotonic loading [4, 16]. The WPC material exhibits distinct tension and compression characteristics, as confirmed by the experimental results presented in Section 3.2. To accurately represent this nonlinear and asymmetric behavior, the Cast Iron Plasticity model in ABAQUS was adopted. Although this constitutive option is typically used for materials that undergo nonlinear plastic deformation, it is also suitable for modeling materials with different tensile and compressive responses under monotonic loading. In this study, the applied load was gradually increased until failure, without any unloading or reloading cycles. Therefore, even if the material response remains mostly elastic during loading, the use of the Cast Iron Plasticity model does not contradict the actual structural behavior and enables a more realistic definition of the nonlinear region.

In implementing this model, the elastic behavior was first defined based on the initial linear portion of the stress–strain curve, where the elastic modulus (E) was set equal to the initial slope. The nonlinear plastic region was then introduced by converting the experimental stress–strain data into true stress–plastic strain form. For each data point, the corresponding plastic strain was obtained by subtracting the elastic strain (σ/E) from the total strain (ε_t). The resulting point-by-point data were entered into ABAQUS separately for compression and tension to define the complete material response (as shown in Fig.17). This modeling approach enables the finite element simulation to capture the gradual stiffness degradation and ultimate failure behavior of the WPC material with high fidelity.

Table 6. Input parameters of the WPC material model implemented in ABAQUS.

Parameter	Symbol/Unit	Description	Source/Note
Elastic modulus (compression)	E_c = 2359 MPa	Initial elastic stiffness in compression, obtained from the slope of the stress–strain curve in the elastic region.	Experimental uniaxial compression test (Section 3.2).
Elastic modulus (tension)	E_t = 1959.8 MPa	Initial elastic stiffness in tension, obtained from the slope of the stress–strain curve in the elastic region.	Experimental uniaxial tension test (Section 3.2).
Poisson's ratio	v = 0.35	Ratio of lateral to longitudinal strain.	Typical value for wood–plastic composites.
Compressive strength	f_c = 45.8 MPa	Ultimate compressive stress of WPC.	Experimental data (Table 3).

Tensile strength	f_t = 16.6 MPa	Ultimate tensile stress of WPC.	Experimental data (Table 4).
Maximum compressive strain	$\varepsilon_{c,u}$ = 0.049	Strain corresponding to compressive failure.	Derived from the experimental stress–strain curve.
Maximum tensile strain	$\varepsilon_{t,u}$ = 0.0102	Strain corresponding to tensile failure.	Derived from the experimental stress–strain curve.
Plastic strain definition	-	Plastic strain calculated as $\varepsilon_p = \varepsilon - \sigma/E$, introduced point-by-point for both tension and compression.	Converted from true stress–strain data.
Failure model	-	*Cast Iron Plasticity* (separate input curves for tension and compression).	ABAQUS 2023 material model.
Damage behavior	-	Gradual stiffness degradation beyond ultimate stress; no unloading–reloading considered.	Calibrated with experimental load–deflection data.
Element type	-	C3D8R – 8-node brick element with reduced integration.	Used for WPC core.

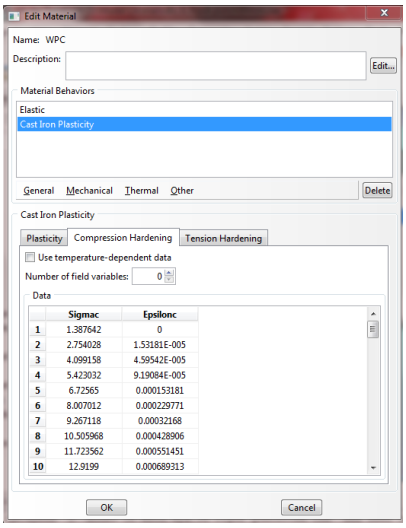

Fig. 17. Definition of WPC materials.

Initially, the elastic portion of the material is defined with a modulus equal to the initial slope of the stress-strain curve, followed by input of plastic stress-strain points.

This arrangement produces an orthotropic material, whose mechanical properties differ along the three Cartesian axes Fig. 18.

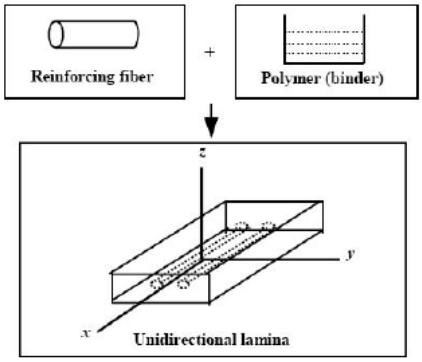

Fig. 18. Schematic diagram of FRP composites.

5.3. Assembly and interaction

After assigning material properties and GFRP layer thickness, the components are assembled using the Assembly module, placing GFRP layers above and below the WPC panel. For point loading, a steel piece is placed at the center of the top layer. Interaction between WPC and GFRP layers is defined using Tie constraints.

Boundary conditions replicate the experimental setup, with roller supports applied at two panel edges to restrict vertical displacement. Displacement-controlled loading is applied to match laboratory conditions Fig. 19.

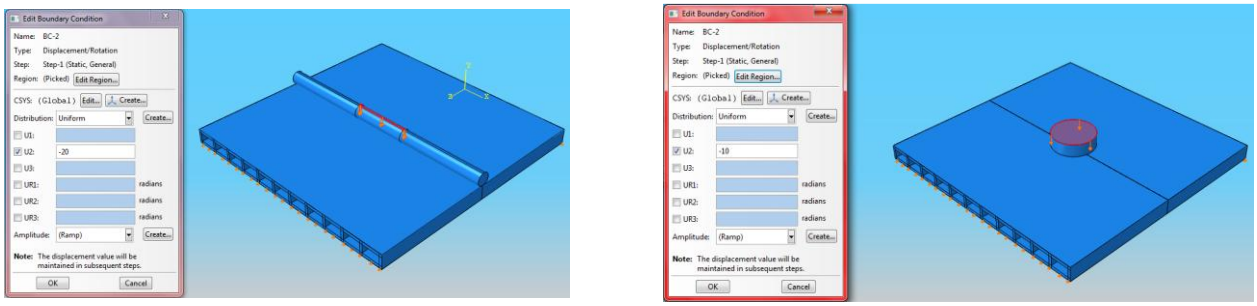

(a) (b)

Fig. 19. Schematic view of (a) linear loading, and (b) point loading.

Mesh discretization was performed for all model components. GFRP sheets were modeled using S4R shell elements, a 4-node quadrilateral element with reduced integration suitable for bending Fig. 20.

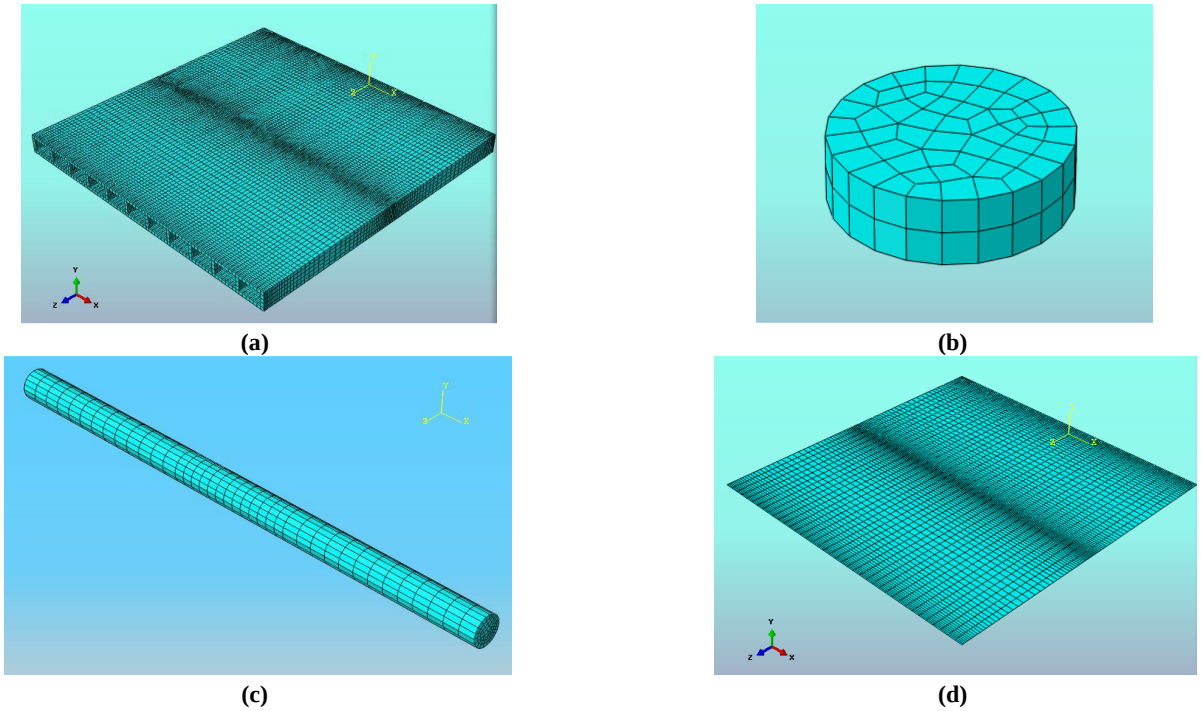

(a) (b)

(c) (d)

Fig. 20. Meshing: (a) WPC mesh, (b) steel part meshing (point load), (c) meshing of steel part (linear load), and (d) GFRP sheet mesh.

6. Experimental results and discussion

6.1. Failure mode

In the previous sections, the experimental procedures as well as the theoretical and numerical aspects of the WPC-GFRP panels were discussed. Before analyzing the diagrams and the results obtained from the loading tests of the specimens, it is necessary to first describe the possible failure modes of these types of panels. A sandwich structure, in addition to exhibiting high stiffness, must also possess high strength. Four distinct failure modes can occur in sandwich structures subjected to flexural loads. The failure occurs in the mode that develops under the lowest applied load.

- Tensile face sheet failure (or tensile face sheet yielding)

This mode of failure occurs when the normal tensile stresses induced by the applied load exceed the yield strength of the face sheets. Fig. 21a illustrates this type of failure.

- Face sheet wrinkling (or buckling over the core)

This failure mode occurs when the compressive stresses become sufficiently large, causing the face sheets to lose stability. Fig. 21b illustrates this type of failure.

- Core shear failure (or core failure)

This type of failure mode typically occurs when the shear stress within the core exceeds its shear strength. The shear strength of the core depends on factors such as the core material density, the geometry of the core cells, and the thermal conductivity of the core. Fig. 21c illustrates this failure mode.

- Debonding between face sheet and core (or bond failure)

This failure mode occurs when stresses in the adhesive interface become excessive, leading to separation between the face sheet

and the core. Fig. 21d illustrates this failure.

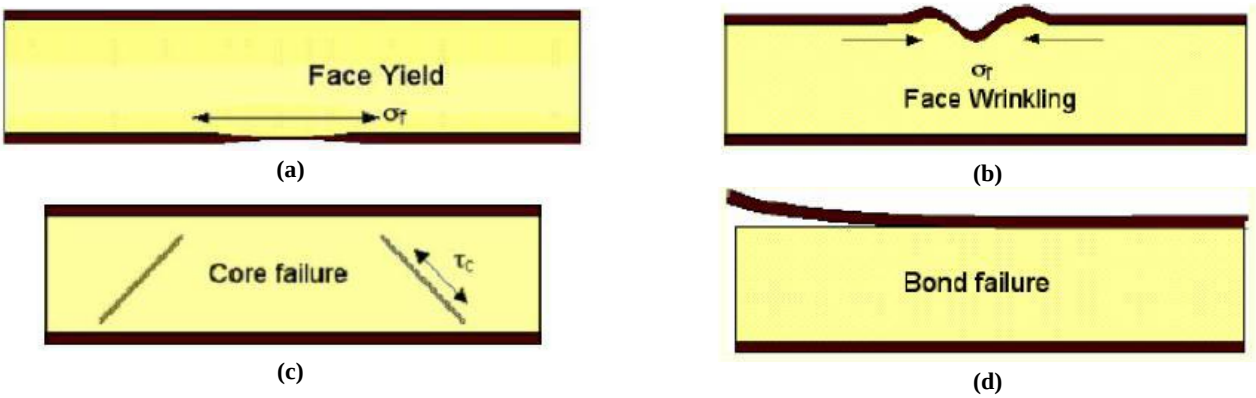

Fig. 21. Distinct failure modes can occur in sandwich structures subjected to flexural loads: (a) tensile face sheet failure, (b) face sheet wrinkling, (c) core shear failure, and (d) debonding between face sheet and core.

As shown in Fig. 22a, specimen A0 failed at the midspan. This type of failure corresponds to the first mode, occurring in a flexural manner, such that the bottom region under tension yielded first, followed by complete fracture of the entire section. In specimen A1, with a single reinforcement layer on both the top and bottom surfaces, shear cracks developed in the WPC section due to its relatively lower shear capacity compared to flexural capacity. Upon reaching the ultimate load and the subsequent failure of the WPC section, a significant amount of shear was transferred between the GFRP layers and the WPC, leading to debonding at the WPC-GFRP interface. As shown in Fig. 22b, this type of failure corresponds to Mode 4, commonly referred to as debonding. In specimens A2 and A3, the increased stiffness of the section resulted in higher shear forces being transferred to the panel core. Due to the weakness of the joints connecting the WPC plates, the shear force could not be fully transmitted at the ultimate load. Consequently, before debonding occurred between the face sheets and the core, shear failure developed at the joint between the web and flange of the WPC. As illustrated in Fig. 22c, this type of failure corresponds to Mode 3, as described in the previous section.

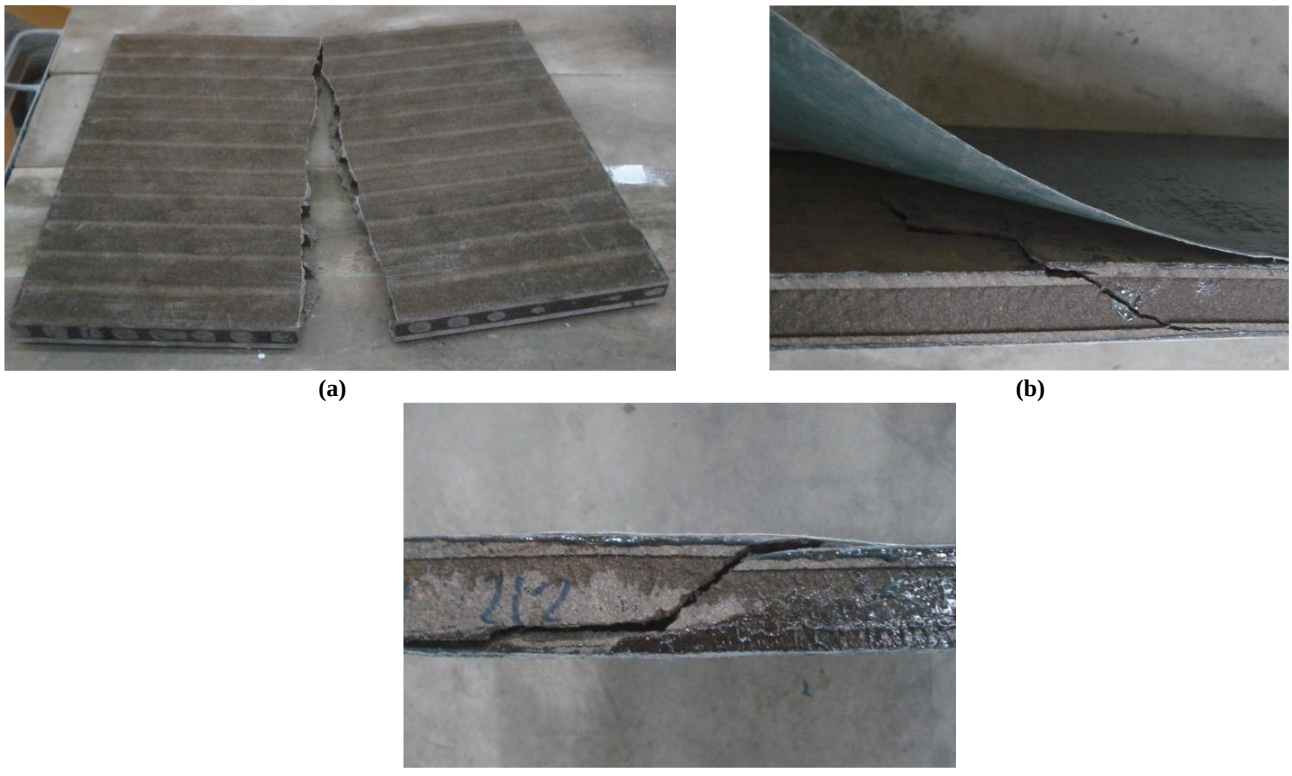

Fig. 22. Failure mode of specimens under flexural loads: (a) A0, (b) A1, and (c) A2.

By applying a point load to specimens A0 through A3, it was observed that in all cases, due to the hollow nature of the panels and the localized loading, the web directly beneath the applied load was unable to sustain the entire force because of its relatively low strength. Consequently, a cavity formed immediately under the load, leading to what is commonly referred to as punching shear failure. In Fig. 23a, the cracks formed beneath specimen P0 during loading are shown. As noted earlier, these cracks developed directly under the concentrated load. Fig. 23b presents specimen P2, in which the applied load exceeded the specimen's capacity, leading to perforation. In Fig. 23c, the perforation observed in specimen P3 is illustrated; as can be seen, part of the GFRP in direct contact with the loading cylinder was torn due to excessive deformation following the occurrence of punching shear.

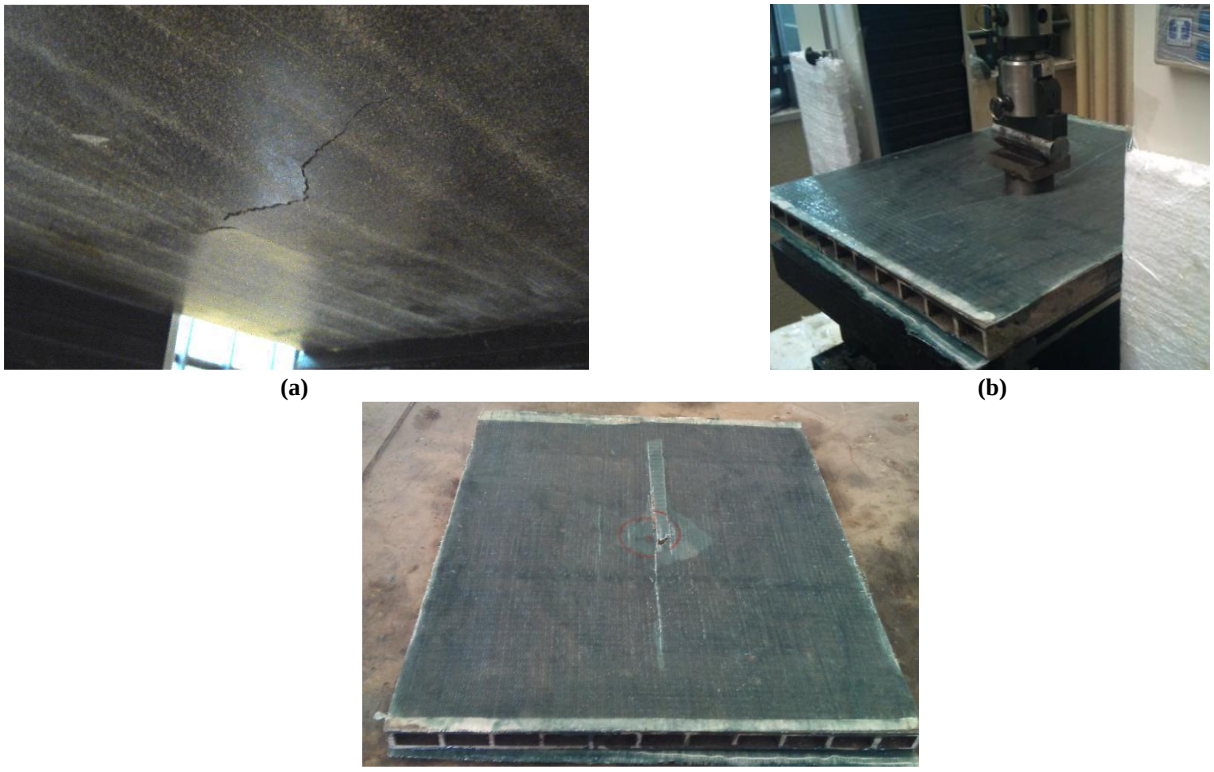

(a) **(b)** **(c)**

Fig. 23. Failure mode of specimens under point loads: (a) P0, (b) P2, and (c) P3.

6.2. WPC uniaxial loading test

As described in the previous sections, uniaxial compression and tension tests were conducted to evaluate the mechanical behavior of the WPC. The results obtained from these tests are presented in Fig. 24.

As shown in Fig. 24, in addition to the stress–strain curves of the tested specimens, a dashed curve is presented, representing a fitted second-order polynomial. This curve was obtained by minimizing the error with respect to the experimental data. Specifically, if the stress–strain relationship is expressed as for compression and for tension, the corresponding values of A and were determined from this fitted curve and are summarized in Table 7.

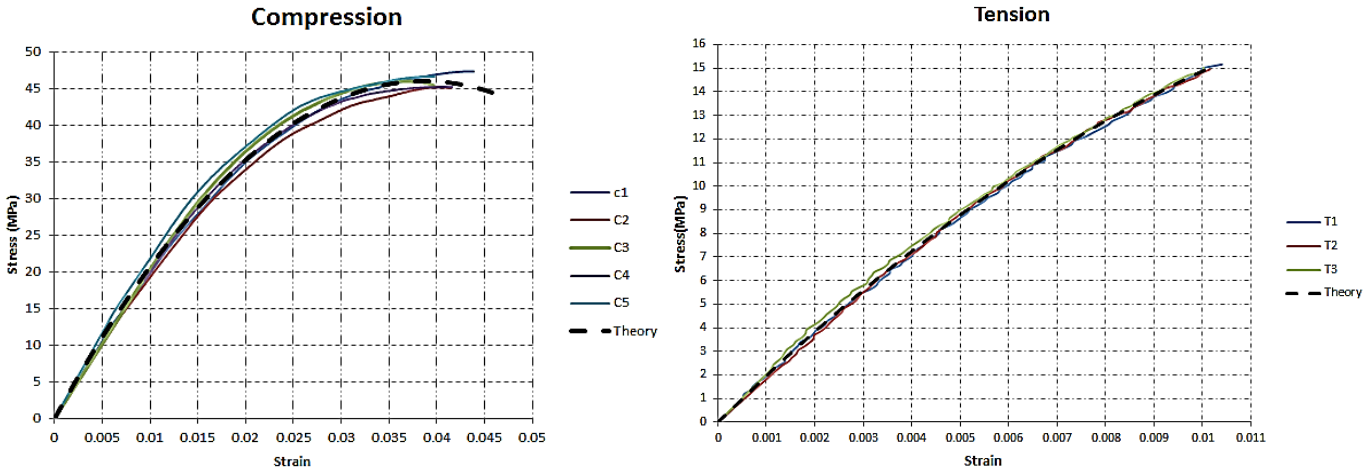

(a) **(b)**

Fig. 24. WPC uniaxial loading test; (a) compression, and (b) tension.

Table 7. The properties of WPC.

Tesion		Compression	
A	B	A'	B'
-18067.6	2377.059	-31660.8	2026.33

6.3. WPC linear loading test

The results of linear loading tests on specimens A0 through A3 are examined. The loading was applied up to the point of specimen failure. The corresponding experimental load-displacement curves for these tests are presented in Fig. 25.

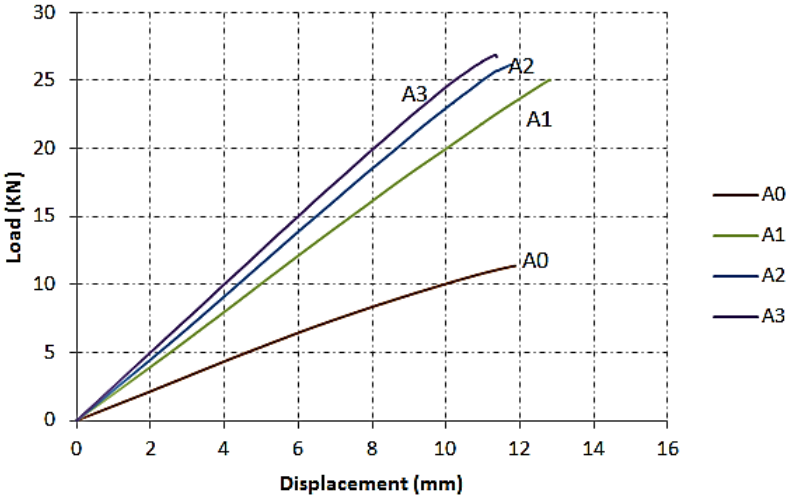

Fig. 25. Experimental load-deflection of WPC linear loading test.

As can be observed, the application of a single GFRP layer led to a significant enhancement in both the strength and stiffness of the panels, with the ultimate load increasing by 120% and stiffness by 84%. With the addition of an extra bottom layer in specimen A2, only an 8% increase in ultimate load was achieved compared to A1, while stiffness increased by 25%. The trend of strength improvement in specimen A3 reinforced with one top layer and three bottom layers was similar to that of A2, though at a much lower rate. Specifically, specimen A3 exhibited an 8% higher ultimate load and a 25% increase in stiffness relative to A2, as summarized in Table 8.

Table 8. Experimental results of WPC linear loading.

Specimen	Ultimate load (kN)	Percentage of changes (%)	Initial stiffness (N/mm)	Percentage of changes (%)	Final deformation (mm)
A0	11.371	-	1072.9	-	11.88
A1	25.045	120.3	1977.6	84.0	12.81
A2	27.979	138.5	2234.3	109.1	11.77
A3	26.877	136.4	2506.8	133.6	11.37

6.4. WPC point loading test

The results of the second series of tests on specimens A0 through A3, subjected to point loading, are presented in Fig. 26 and Table 9. To differentiate these specimens from the previous series tested under linear loading, they have been designated as P0 through P3.

As can be observed, the schematic results are similar to those of the linear loading case; however, quantitatively, there are notable differences, with both deformation and ultimate load being lower than in the previous series. In specimen P0, which had no GFRP face sheets, failure occurred under a load of approximately 600 kg. In contrast, specimen P1, reinforced with a single layer on both the top and bottom surfaces, failed under a load of 920 kg, representing nearly a 49% increase in load-bearing capacity.

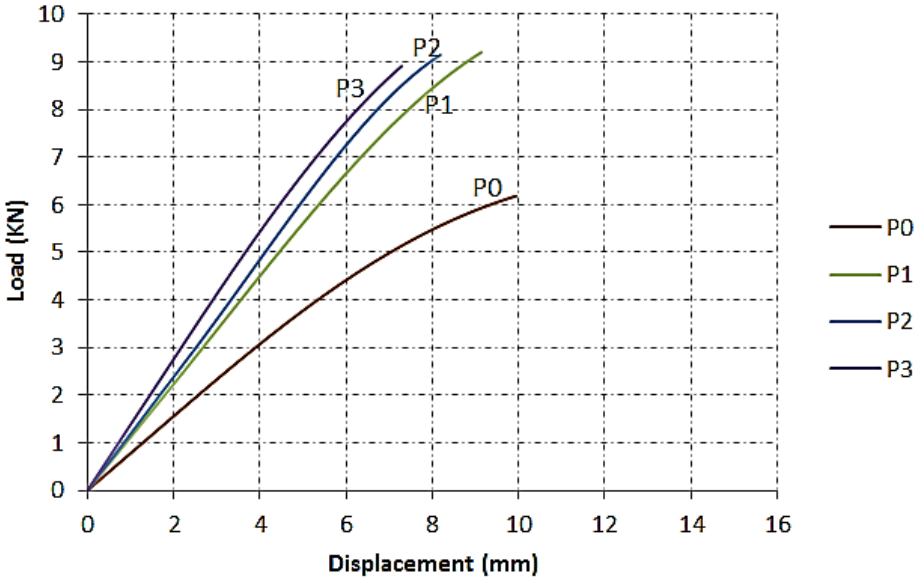

Fig. 26. Experimental load-deflection of WPC point loading test.

As shown in Fig.26, the load–deflection curves demonstrate an initially linear response followed by gradual stiffness degradation after yielding, indicating a ductile failure mechanism governed by the WPC core.

With the addition of more layers, the ultimate load did not increase significantly. This is attributed to the relative weakness of the web compared to the new face sheets: before the face sheets could effectively contribute, shear forces generated in the web beneath the point load caused localized failure in that region. Nevertheless, the added layers did influence the structural stiffness. For instance, in specimen P0, the initial stiffness was 777 N/mm, while the addition of one layer increased the stiffness by 43%. Adding another layer resulted in a further 10% increase, and in specimen P3 reinforced with one top layer and three bottom layers, the stiffness was 7% higher than that of specimen P0. According to Table 9, specimens reinforced with two GFRP layers exhibited approximately 18–22% higher ultimate load compared with unreinforced panels.

Table 9. Experimental results of WPC point loading.

Specimen	Ultimate load (kN)	Percentage of changes (%)	Initial stiffness (N/mm)	Percentage of changes (%)	Final deformation (mm)
P0	6.182	-	777.7	-	9.55
P1	9.200	48.8	1116.0	43.5	9.14
P2	9.444	47.9	1189.6	52.9	8.18
P3	8.912	44.1	1366.4	77.0	7.29

7. Theoretical results and discussion

7.1. WPC linear loading test

One of the approaches for determining the static behavior of sandwich panels is the beam theory method, which was explained in detail. Since the final derived equations were relatively complex and required step-by-step calculations, MATLAB software was employed to perform these computations. The results of these calculations for the four groups A0 to A3 are presented in Fig. 27 and Table 9.

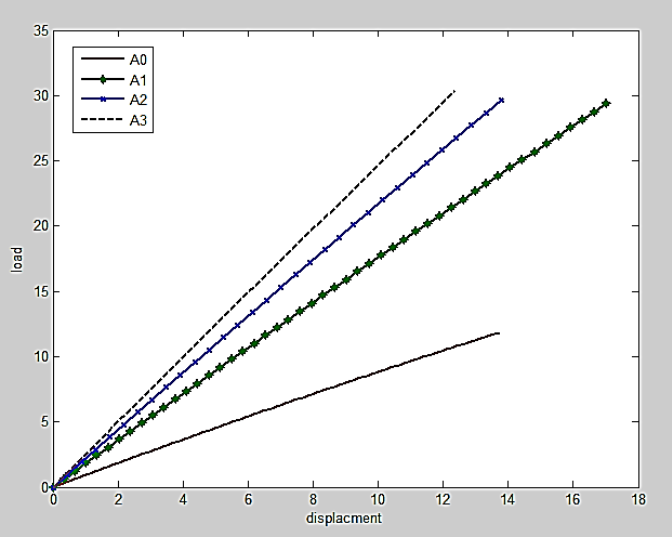

Fig. 27. Theoretical load-deflection of WPC linear loading test.

In specimen A1, the ultimate load increased by 148% and the stiffness by 95% compared to specimen A0. With the addition of an extra bottom layer in specimen A2, only a 3% increase in ultimate load was observed relative to A1, while the stiffness increased by 44%. The trend of strength enhancement in specimen A3 reinforced with one top layer and three bottom layers was similar to that of A2 but progressed at a slower rate. In particular, specimen A3 carried 6% more ultimate load and exhibited a 33% increase in stiffness compared to A2.

Table 10. Theoretical results of WPC linear loading.

Specimen	Ultimate load (kN)	Percentage of changes (%)	Initial stiffness (N/mm)	Percentage of changes (%)	Final deformation (mm)
A0	11.850	-	922.9	-	13.74
A1	28.380	147.9	1799.2	94.9	17.03
A2	29.633	150.2	2204.4	138.8	13.78
A3	30.363	156.2	2505.5	171.5	12.37

8. Numerical results and discussion

8.1. Validation of the numerical mode

To ensure the reliability and accuracy of the developed finite element (FE) model, a validation process was performed by

comparing the numerical results with experimental and theoretical findings. The comparison focused on key response parameters, including the ultimate load, initial stiffness, and corresponding midspan deflection under both linear and point loading conditions. As summarized in Tables 12–14 and illustrated in Figures 32–35, the FE results showed a close agreement with the experimental data. For specimens subjected to linear loading, the difference between the experimental and numerical ultimate loads ranged from 2% to 9%, while the deviation in initial stiffness values was less than 6% for most specimens. For point-loaded specimens, the corresponding differences were within 2%–12%.

his level of consistency confirms that the finite element model accurately reproduces the mechanical behavior of the WPC–GFRP sandwich panels. The observed minor discrepancies are mainly due to experimental uncertainties, manufacturing imperfections, and simplifications in boundary condition modeling. Overall, the model demonstrates high predictive capability and can be reliably used for further parametric and optimization analyses of WPC–GFRP composite systems.

8.2. WPC linear loading test

In the finite element method, after creating the model, applying the load, and performing meshing as described in detail in the previous section, each specimen was analyzed in the software. Upon completion of the analysis, the deformation resulting from loading was displayed schematically by the software. Fig. 28 illustrates the deformation of specimen A0.

As shown in the figure, due to the linear nature of the applied loading, the maximum deformation also occurs linearly at the midspan of the panel. The load-displacement curves of specimens A0 through A3 are presented in Fig. 29, and the corresponding results are summarized in Table 11.

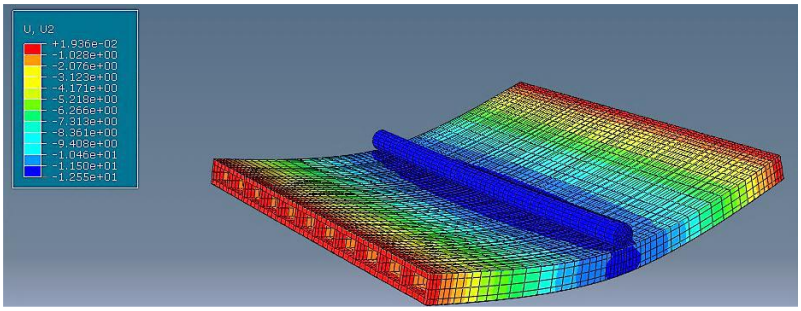

Fig. 28. Linear loading deformation of specimen A0.

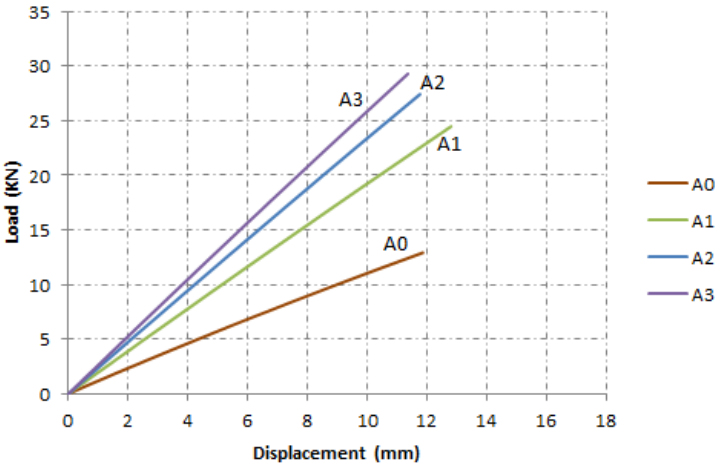

Fig. 29. Numerical load-deflection of WPC linear loading test.

Table 11. Numerical results of WPC linear loading.

Specimen	Ultimate load (kN)	Percentage of changes (%)	Initial stiffness (N/mm)	Percentage of changes (%)	Final deformation (mm)
A0	12.191	-	1287.20	-	11.86
A1	23.466	89.42	2028.79	65.18	12.81
A2	27.406	124.6	2246.66	98.83	11.77
A3	29.299	146.7	2633.13	126.4	11.26

8.3. WPC point loading test

Point loading was also investigated using the numerical method, with the specimens modeled in accordance with the experimental tests. The diagrams obtained from the finite element modeling are presented in Fig. 30. As can be seen, there is a good agreement between these curves and the experimental results, which will be further discussed in the following section. The numerical results obtained from this loading condition are fully presented in Table 11. Fig. 31 presents the schematic deformation of specimen

P2. As can be observed, the deformation at the midspan of the panel is significantly larger, and this type of loading results in the formation of a perforation at the center.

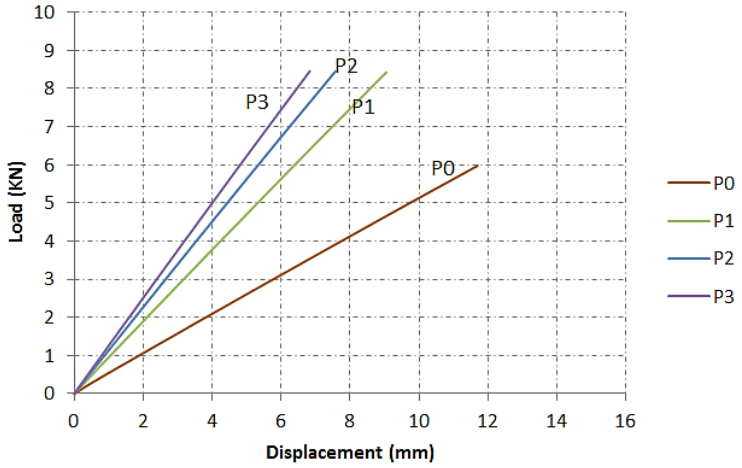

Fig. 30. Numerical load-deflection of WPC point loading test.

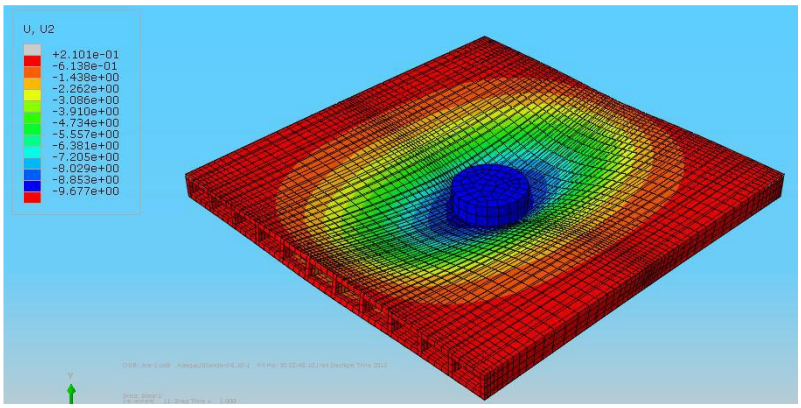

Fig. 31. Point loading deformation of specimen P2.

Table 12. Numerical results of WPC point loading.

Specimen	Ultimate load (kN)	Percentage of changes (%)	Initial stiffness (N/mm)	Percentage of changes (%)	Final deformation (mm)
P0	5.98	-	570.91	-	11.70
P1	8.43	41.02	990.28	73.46	9.05
P2	8.45	41.43	1170.44	105.01	5.57
P3	8.46	41.59	1290.69	126.07	6.83

As previously mentioned, the experimental loading was applied in the form of displacement control at a constant rate. To ensure that the modeling corresponded closely with the experimental procedure, the loading in ABAQUS was also applied in the form of displacement control. This displacement was continued until the shear stress in the WPC web reached its maximum value. For example, the shear stress distribution in specimen P3 along a cross-section at the midspan is shown in Fig. 31.

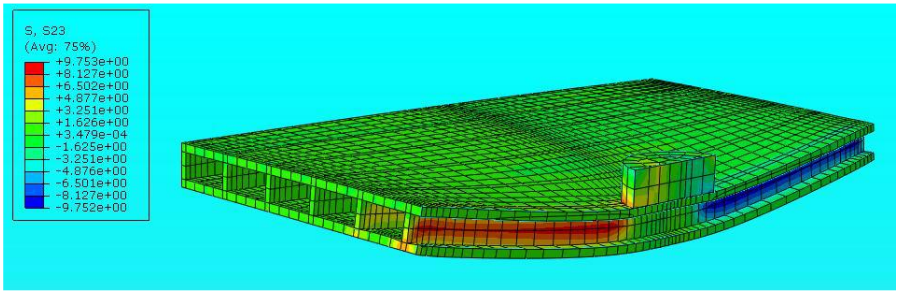

Fig. 32. Point loading deformation of specimen P3.

9. Comparison between experimental, theoretical, and numerical results in linear loading

To verify the accuracy of the theoretical and numerical methods employed in the modeling and analysis of the panels, the results for each specimen obtained from all three approaches were plotted together in a single diagram. These comparisons of initial stiffness

and ultimate load are presented in Tables 13 and 14, respectively.

Table 13. Comparison of the initial stiffness of the WPC specimens under linear loading.

Specimen	Experimental (N/mm)	Theoretical (N/mm)	Error (%)	Numerical (N/mm)	Error (%)
A0	1139.18	905.23	20.54	1103.56	3.13
A1	2037.50	1760.55	13.36	1919.00	5.54
A2	2466.49	2168.60	12.10	2339.90	5.06
A3	2470.15	2466.70	12.10	2591.30	4.90

Table 14. Comparison of the ultimate load of the WPC specimens under linear loading.

Specimen	Experimental (kN/mm)	Theoretical (kN/mm)	Error (%)	Numerical (kN/mm)	Error (%)
A0	11.38	11.15	1.95	12.91	13.51
A1	25.05	29.38	17.27	24.46	2.34
A2	25.80	29.64	14.91	27.46	6.21
A3	26.88	30.26	12.97	29.29	8.98

As shown in Fig. 33, for specimen A0, the numerical method exhibits good accuracy, with an error of less than 4% in the stiffness parameter (i.e., the slope of the load-displacement curve) compared to the experimental results. In contrast, the theoretical method shows an error of nearly 20%, which can be attributed to the neglect of Poisson's ratio in the beam theory formulation.

For specimen A1, with the addition of one GFRP layer on both the top and bottom surfaces, the stiffness of the beam increased, and the panel's behavior became more influenced by the reinforcing layers. Since GFRP exhibits unidirectional behavior, and beam theory remains applicable with increasing width, the error in the slope of the curve decreased from 20% to 13.36%. A similar trend is observed with the numerical method, where the error was reduced to less than 6%.

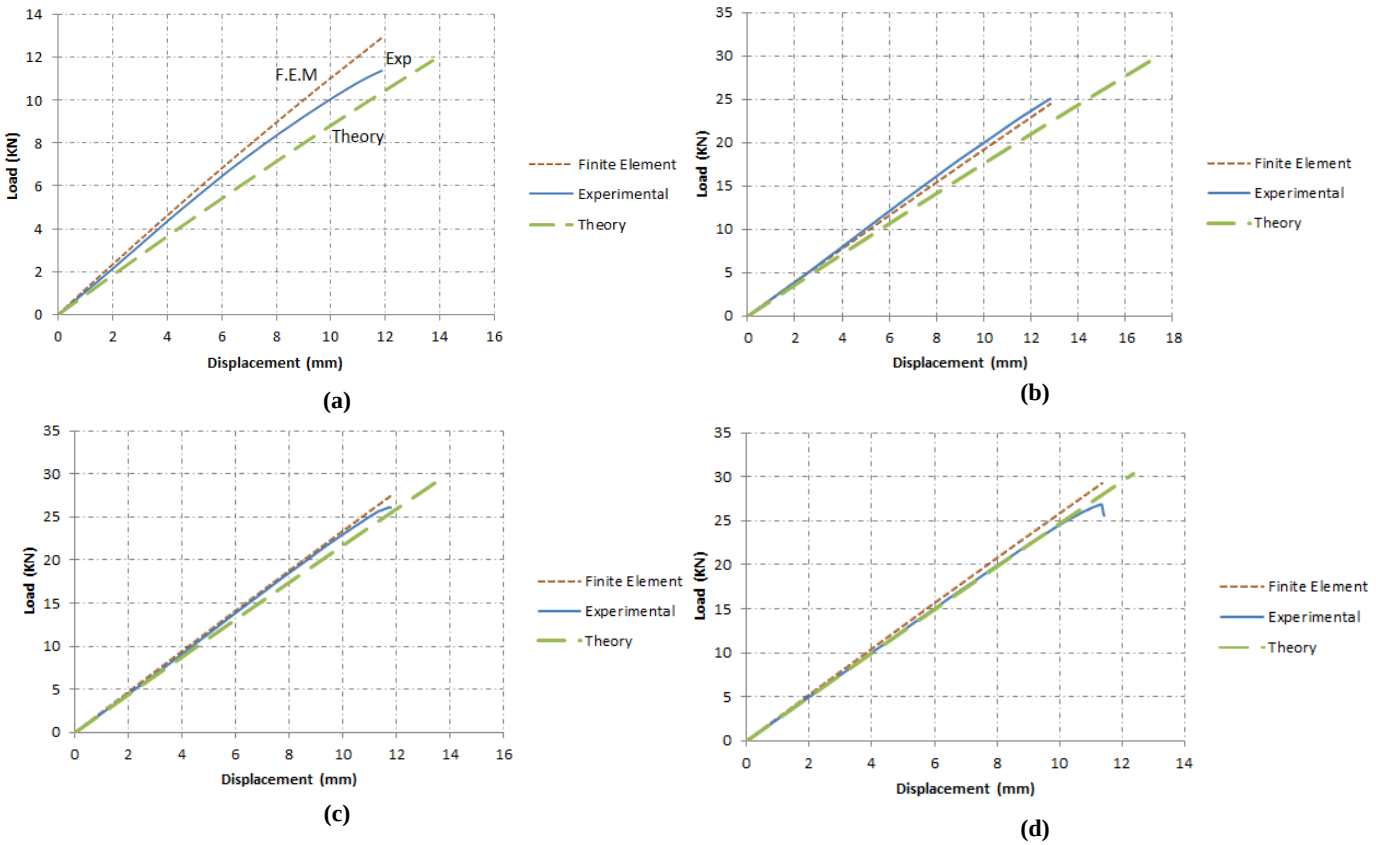

Fig. 33. Comparative linear loading load-displacement curve; (a) A0, (b) A1, (c) A2, and (c) A3.

For specimen A2, as shown in Fig. 33, the theoretical method more closely matches the experimental curve. This can be attributed to the increased stiffness of the panel due to the additional reinforcing layers, which, as previously noted, exhibit good compatibility with beam theory. The numerical curve, similar to the previous specimen, also aligns well with the experimental data, with an error of about 5%. However, as indicated in Table 13, which compares the ultimate loads of the panels, the theoretical and numerical methods predict approximately 30% and 7% higher ultimate loads, respectively, than those obtained experimentally. This discrepancy can be explained by the lack of homogeneity in the panel core, which caused premature failure of the specimen.

For specimen A3, the agreement between the curves is even stronger than before, with the error of the theoretical method reduced to less than 1% and that of the numerical method to below 5%. Moreover, the ultimate load obtained from the numerical method is only 9% higher than the experimental value, while the error in the theoretical method decreased by 2% compared to specimen A2.

A separate comparison between the theoretical and numerical methods provides a clearer understanding of the differences

between these two curves. As shown in Figs. 34 and 35, in general, the specimens analyzed by the numerical method exhibit higher stiffness.

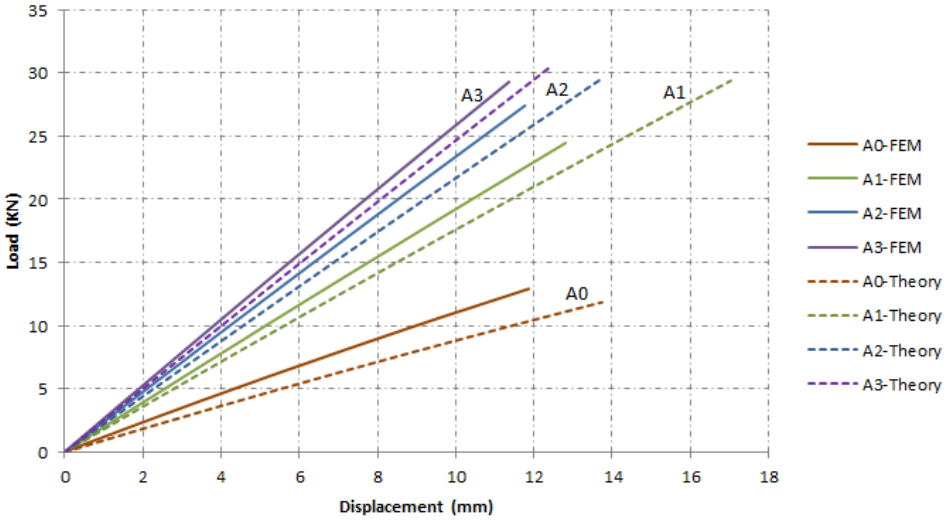

Fig. 34. Comparison between results from theoretical and numerical methods in linear loading.

Moreover, as the number of layers increases, the curves converge more closely. This convergence can be attributed to the dominant role of the GFRP layers and the good compatibility of the beam theory model with the actual behavior of the panels.

The observed reduction in the rate of strength increase with successive GFRP layers can be explained by the mechanics of stress transfer and interfacial behavior between the composite layers. As the number of GFRP sheets increases, the stiffness contrast between the outer reinforcement and the WPC core becomes more pronounced. Because the epoxy adhesive possesses limited shear stiffness, only part of the tensile force developed in the outer GFRP is effectively transmitted to the substrate, resulting in stress transfer inefficiency. Furthermore, the mismatch in strain compatibility between the relatively brittle GFRP and the more ductile WPC induces localized debonding and micro-slip at the interface before global failure, as confirmed by the gradual separation observed in several specimens. The neutral axis also shifts toward the tension side as reinforcement thickness increases, reducing the lever arm efficiency and producing diminishing incremental gains in flexural capacity. These combined effects explain why the addition of the third GFRP layer (specimen A3) provided only a modest increase in ultimate load compared with the second layer (specimen A2), consistent with the nonlinear stiffness trends predicted numerically.

Although all specimens were prepared and tested under carefully controlled conditions, several factors may have contributed to minor variations among the results. The most significant source of experimental uncertainty is associated with bonding quality between the GFRP layers and the WPC substrate. Despite surface grinding and thorough cleaning, small variations in surface roughness and epoxy thickness may have led to localized stress concentrations and partial debonding in some specimens. Another potential source of variation arises from the inhomogeneity of the WPC material, where local differences in the wood–plastic fiber ratio and density could influence stiffness and failure strain. Environmental factors such as temperature and humidity during the 7–10 day curing period may also have affected adhesive hardening and bond strength. Additionally, instrumentation errors including load cell precision (±1%) and displacement transducer tolerance (±0.5%) introduce small but unavoidable measurement deviations. Considering these factors, the discrepancies between the experimental, theoretical, and numerical results (generally within 10%) fall well within the expected range of uncertainty, confirming the overall reliability of the experimental data.

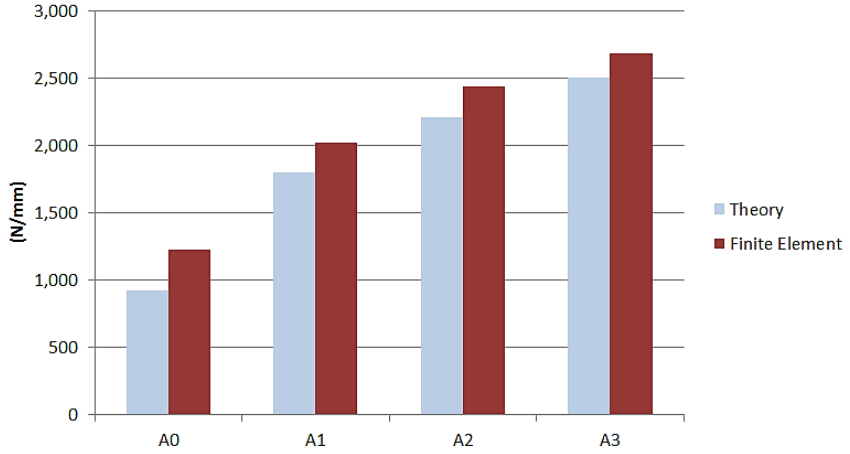

Fig. 35. Comparison of the initial stiffness of samples from theoretical and numerical methods under linear loading.

10. Comparison between experimental and numerical results in point loading

Similar to the linear loading case, a comparison is made between the point loading experimental curves and those obtained from the numerical method. Overall, the results of this comparison for the initial stiffness of the specimens are presented in Table 15.

Table 15. Comparison of the initial stiffness of the WPC specimens under point loading.

Specimen	Experimental (N/mm)	Numerical (N/mm)	Error (%)
P0	777.7	570.91	26.59
P1	1116.0	990.28	11.27
P2	1189.6	1170.44	1.61
P3	1366.4	1290.69	6.23

The comparative point load-displacement curve for specimens obtained from the numerical and experimental methods is shown in Fig. 36. As seen from the curve and the corresponding results, the ultimate load of the P0 specimen exhibits less agreement compared to the other curves, with an error of approximately 26%. This discrepancy remains nearly constant throughout the curve. For specimen P1, the difference is reduced, with the error decreasing by about 15%. Furthermore, the ultimate load shows a smaller percentage error, with only a 9% difference between the numerical and experimental curves.

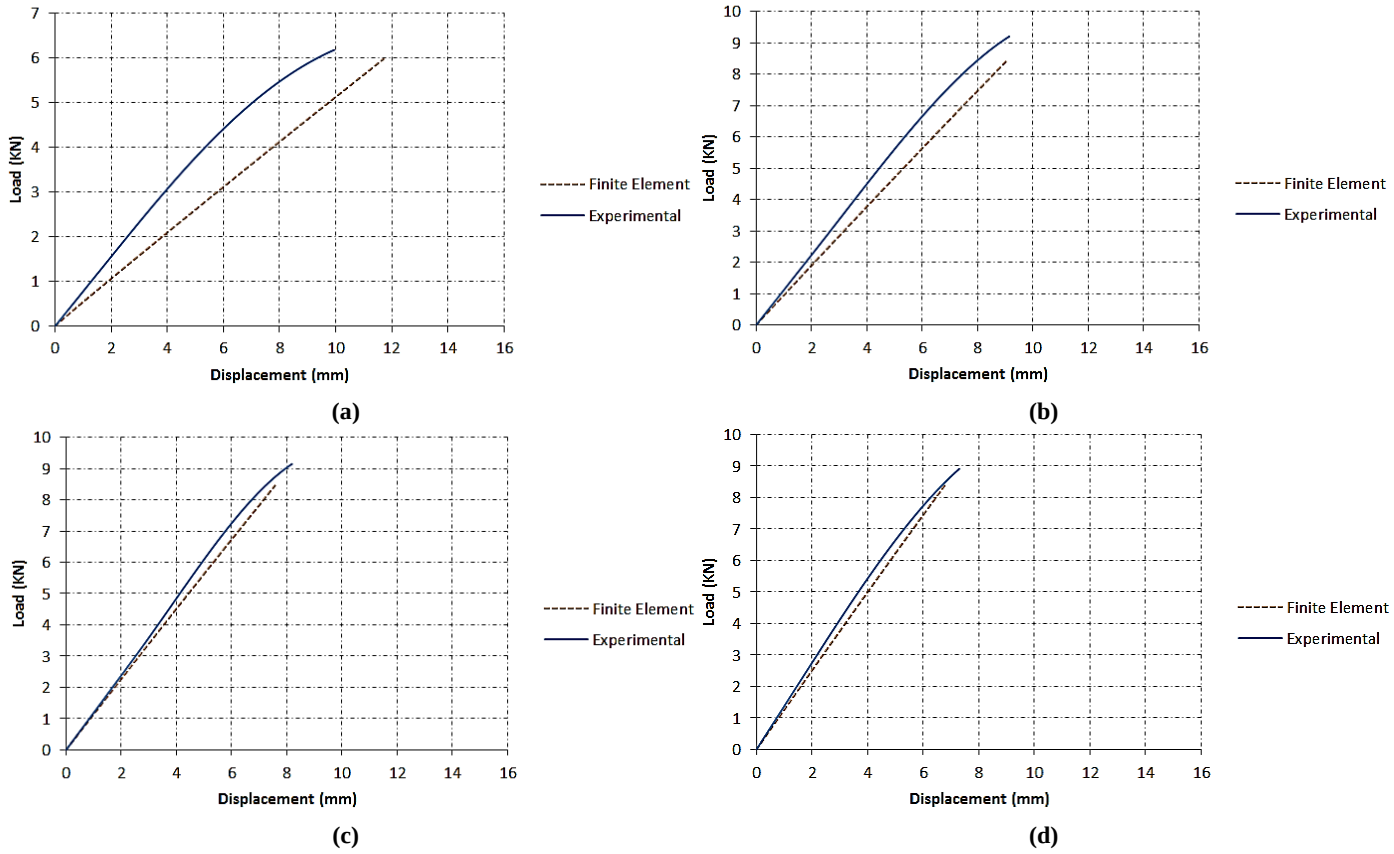

Fig. 36. Comparative point loading load-displacement curve; (a) P0, (b) P1, (c) P2, and (c) P3.

In specimen P2, the discrepancy reached its minimum, with the initial stiffness obtained from the numerical method differing by only 1.6% from the experimental result. This small difference appears at the beginning of the curve, while a slight deviation develops in the middle section; nevertheless, the two curves remain close overall. In specimen P3, a similar trend to P2 is observed, with only minor differences between the two curves. However, unlike P2, the initial slope of the P3 curve shows a 6% deviation, which decreases as the curve progresses. Such minor discrepancies can be attributed to experimental errors.

In general, specimens subjected to point loading exhibited greater differences between the numerical and experimental results compared to those under linear loading. This can be explained by the lack of uniformity in the WPC dimensions, which has a more pronounced effect in point-loaded specimens. Nevertheless, as observed, there is an overall good agreement between the two methods.

11. Conclusions

In this study, WPC-GFRP specimens with different numbers of reinforcing layers were tested under two types of loading. For the theoretical analysis, beam theory and the flexural surface method were employed. In addition, the numerical method was used for a better comparison of results. The main findings of the present research can be summarized as follows:

- The use of reinforcing layers in WPC and the creation of sandwich panels led to a significant increase in structural stiffness. With just one GFRP layer of 0.12 mm thickness, the stiffness increased by 80%.
- The formation of sandwich panels also resulted in a considerable increase in the ultimate load, such that the addition of a single GFRP reinforcing layer increased the ultimate load by 120%.
- Increasing the number of reinforcing layers further enhanced the panel stiffness, but the rate of stiffness improvement diminished with each additional layer.

- Adding more reinforcing layers did not result in a substantial increase in ultimate load. This is due to the relative weakness of the core compared to the face sheets; the core (WPC) experienced shear failure before the additional layers could become fully effective. Therefore, applying more than one GFRP layer in WPC-GFRP sandwich panels is not economically justifiable.
- Linear loading produced better results than point loading, with the structures sustaining higher ultimate loads. This difference is explained by the hollow nature of sandwich panels, which makes them susceptible to punching shear under point loading.
- The displacement of plates with two free edges under linear loading perpendicular to those edges can be reasonably calculated using beam theory. If the aspect ratio of the plate (length-to-width) is infinite, the error between the two methods is less than 1%. For a plate with a length-to-width ratio of 1, the error increases to about 9%.
- In comparing experimental and theoretical results for the unreinforced specimen, a 20% difference was observed in the initial stiffness. However, this difference decreased in the reinforced specimens; for example, in specimen A3 with three reinforcing layers, the theoretical result differed from the experimental result by less than 1%. This is because, with the addition of layers and the unidirectional behavior of FRP, the stiffness of the panels becomes dominated by the FRP, and their behavior approaches that of beams, making beam theory predictions more accurate.
- In the FEM, the results for the unreinforced specimen were much closer to the experimental data, since the effect of Poisson's ratio of the WPC, which is neglected in beam theory, was accounted for in FEM.
- In FEM, the stiffness of the specimens was slightly higher than the experimental results, which can be attributed to experimental errors. For instance, lack of homogeneity in the specimens and the presence of air voids during fabrication may have caused microscopic defects in the material, leading to reduced stiffness under loading.

12. Recommendations for future research

As demonstrated in this study, the use of theoretical and numerical methods can provide results close to the desired outcomes without the expense of experimental testing. Considering this advantage, along with the higher accuracy and speed of software-based modeling compared to experimental approaches, the use of numerical simulation is recommended. For future research, the following topics can be addressed through modeling and numerical analysis, to facilitate their practical implementation based on the findings:

- Investigation of the dynamic behavior of WPC-GFRP sandwich panels.
- Evaluation of the effect of different grooves on the ultimate strength of WPC-GFRP panels.
- Theoretical and experimental study of the flexural behavior of WPC-GFRP panels with varying length-to-width ratios.
- Examination of methods to improve the shear strength of WPC specimens.
- Determination of the optimum WPC cross-section dimensions in sandwich panels.
- Selection of the most effective reinforcing layer for use in WPC-GFRP sandwich panels.
- Optimization of GFRP thickness for application in WPC-GFRP sandwich panels.

Statements & Declarations

Author contributions

Amin Norouzi: Conceptualization, Investigation, Methodology, Formal analysis, Resources, Writing - Original Draft, Writing - Review & Editing.

Morteza Naghipour: Conceptualization, Methodology, Formal analysis, Project administration, Supervision, Writing - Review & Editing.

Funding

The authors received no financial support for the research, authorship, and/or publication of this article.

Data availability

The data presented in this study will be available on interested request from the corresponding author.

Declarations

The authors declare no conflict of interest.

References

[1] Friedrich, D. Thermoplastic moulding of Wood-Polymer Composites (WPC): A review on physical and mechanical behaviour under hot-pressing technique. Composite Structures, 2021; 262: 113649. doi:10.1016/j.compstruct.2021.113649.

[2] Naghipour, M., Arefi, S. L., Nematzadeh, M. Performance of longitudinal grooves to prevent debonding of GFRP sheets used for the reinforcement of WPC beams. European Journal of Environmental and Civil Engineering, 2013; 17: 761-776. doi:10.1080/19648189.2013.815136.

[3] Gardner, D. J., Han, Y., Wang, L. Wood–Plastic Composite Technology. Current Forestry Reports, 2015; 1: 139-150. doi:10.1007/s40725-015-0016-6.

[4] Naghipour, M., Nematzadeh, M., Yahyazadeh, Q. Analytical and experimental study on flexural performance of WPC–FRP beams. Construction and Building Materials, 2011; 25: 829-837. doi:10.1016/j.conbuildmat.2010.06.104.

[5] Wechsler, A., Hiziroglu, S. Some of the properties of wood–plastic composites. Building and Environment, 2007; 42: 2637-2644. doi:10.1016/j.buildenv.2006.06.018.

[6] Chini, M., Arefi Lale, S., Zolfani Hashemkhani, S., Ustinovicius, L. Choosing a proper method for strengthening WPC beams with grooving method using SWARA-EDAS. Archives of Civil Engineering, 2018; 64: 161-174. doi:10.2478/ace-2018-0050.

[7] Li, Y.-F., Tsai, M.-J., Wei, T.-F., Wang, W.-C. A study on wood beams strengthened by FRP composite materials. Construction and Building Materials, 2014; 62: 118-125. doi:10.1016/j.conbuildmat.2014.03.036.

[8] Lale Arefi, S., Naghipour, M., Turskis, Z., Nematzadeh, M. Evaluation of grooving method to postpone debonding of FRP laminates in WPC-FRP beams. Journal of Civil Engineering and Management, 2014; 20: 237-246. doi:10.3846/13923730.2013.878379.

[9] Zolfaghari, A., Behravesh, A. H., Adli, A. Continuous glass fiber reinforced wood plastic composite in extrusion process: Mechanical properties. Materials & Design, 2013; 51: 701-708. doi:10.1016/j.matdes.2013.04.082.

[10] Behravesh, A., Zohdi Aghdam, A., Soury, E. Experimental investigation of injection molding of wood/plastics composites. Journal of reinforced plastics and composites, 2010; 29: 456-465. doi:10.1177/0731684408099406.

[11] Li, Y.-F., Xie, Y.-M., Tsai, M.-J. Enhancement of the flexural performance of retrofitted wood beams using CFRP composite sheets. Construction and Building Materials, 2009; 23: 411-422. doi:10.1016/j.conbuildmat.2007.11.005.

[12] Plevris, N., Triantafillou Thanasis, C. FRP-Reinforced Wood as Structural Material. Journal of Materials in Civil Engineering, 1992; 4: 300-317. doi:10.1061/(ASCE)0899-1561(1992)4:3(300).

[13] Triantafillou Thanasis, C., Deskovic, N. Prestressed FRP Sheets as External Reinforcement of Wood Members. Journal of Structural Engineering, 1992; 118: 1270-1284. doi:10.1061/(ASCE)0733-9445(1992)118:5(1270).

[14] Naghipour, M., Taheri, F., Zou, G. P. Evaluation of Vibration Damping of Glass-Reinforced-Polymer-Reinforced Glulam Composite Beams. Journal of Structural Engineering, 2005; 131: 1044-1050. doi:10.1061/(ASCE)0733-9445(2005)131:7(1044).

[15] Adhikary, K. B., Pang, S., Staiger, M. P. Dimensional stability and mechanical behaviour of wood–plastic composites based on recycled and virgin high-density polyethylene (HDPE). Composites Part B: Engineering, 2008; 39: 807-815. doi:10.1016/j.compositesb.2007.10.005.

[16] Wang, K., Xu, X., Huo, R., Fang, H., Chen, X. Flexural reinforcement of wood plastic composite panels by bonding glass fiber reinforced polymer sheets and embedding bars. Polymer Composites, 2024; 45: 14595-14607. doi:10.1002/pc.28784.

[17] Wang, K., Yu, C., Liu, W., Huo, R., Fang, H., Chen, X. Study on flexural property of glass fiber-reinforced polymer reinforced wood–plastic composite panels. Wood Material Science & Engineering, 2025; 20: 478-487. doi:10.1080/17480272.2024.2355554.

[18] Jian, B., Mohrmann, S., Li, H., Li, Y., Ashraf, M., Zhou, J., Zheng, X. A Review on Flexural Properties of Wood-Plastic Composites. Polymers, 2022; 14: 3942. doi:10.3390/polym14193942.

[19] Hamed, E., Negru, D., Yalda, R. Structural Performance of Precast Concrete Sandwich Panels Made with FRP Vierendeel Truss–Like Connectors. Journal of Composites for Construction, 2022; 26: 04022027. doi:10.1061/(ASCE)CC.1943-5614.0001215.

[20] Huang, J.-Q., Dai, J.-G. Flexural performance of precast geopolymer concrete sandwich panel enabled by FRP connector. Composite Structures, 2020; 248: 112563. doi:10.1016/j.compstruct.2020.112563.

[21] ASTM International. ASTM D695: Standard test method for compressive properties of rigid plastics. West Conshohocken (PA): 1996. doi:10.1520/D0695-23.

[22] ASTM International. ASTM D638: Standard test method for tensile properties of plastics. West Conshohocken (PA): 2003. doi:10.1520/D0638-14.

Civil Engineering and Applied Solutions

Research Article

journal homepage: ceas.journals.umz.ac.ir

CEAS Civil Engineering and Applied Solutions

ANN-Based Modeling of Shear Behavior of Reinforced Concrete Columns under Constant Axial Loads

Maedeh Sadeghpour Haji [a], Reza Niknam [a], Javad Shayanfar [c*]

[a] *Department of Civil Engineering., Islamic Azad University, Qaemshahr, Iran*
[b] *Department of Civil Engineering, University of Minho, Azurém, Guimarães 4800-058, Portugal*

ARTICLE INFO

Keywords:
Reinforced concrete columns
Shear behavior
Artificial neural networks (ANN)
Variable axial load
Nonlinear modeling
Seismic performance

Article history:
Received 07 October 2025
Accepted 18 November 2025
Available online 01 April 2026

ABSTRACT

Many older reinforced concrete (RC) buildings designed under outdated seismic codes exhibit inadequate shear capacity, leading to brittle column failures during earthquakes. Accurate prediction of shear strength is therefore essential for nonlinear seismic assessment. This study develops an analytical–computational framework using artificial neural networks (ANNs) to model the nonlinear flexural–shear behavior of RC columns subjected to constant axial loads. A fiber-based flexural model was formulated, while shear strength was estimated through a Mohr's circle–based approach enhanced with a ductility-dependent degradation parameter. An ANN trained on 164 experimental column tests provided highly accurate shear predictions, outperforming existing analytical models. The framework was validatated against independent experiments confirmed its reliability. The proposed ANN-based approach offers a practical tool for seismic performance evaluation and retrofit design of deficient RC columns.

1. Introduction

The poor performance of many older reinforced concrete (RC) buildings during past earthquakes has highlighted their vulnerability to seismic forces and stresses. These structures were designed and constructed according to codes and standards that do not satisfy the requirements of modern seismic provisions. Post-earthquake field investigations have shown that one of the most critical shortcomings of RC structures designed under older codes is the insufficient shear strength of columns and beams. This weakness often results in brittle shear failure, which subsequently reduces the axial load-carrying capacity of columns and leads to combined shear–axial failures. Documented examples of such damage were observed during the 1971 San Fernando earthquake in the United States [1], the 1994 Northridge earthquake in the United States [1], and the 1999 Kocaeli [2] and Düzce [2] earthquakes in Turkey (Fig. 1). Since the behavior of structures designed according to older codes is generally governed by shear failure in their members, the shear behavior of the structural elements must be carefully considered in the seismic assessment and evaluation of such structures [3-7]. If necessary, the seismic performance of the structure should be enhanced through appropriate shear-strengthening techniques (such as [8-16]) so that it meets the requirements of current seismic design codes.

As has been clearly established, axial load is one of the most important parameters in determining the nonlinear behavior of reinforced concrete columns [3]. It significantly influences the yielding range of the longitudinal reinforcement (moment and curvature at yield), the ductility level of the column, and the ultimate flexural and shear strength of the member. Axial load can affect the behavior of columns in three ways: (a) Compressive axial load can increase the depth of the neutral axis and reduce the flexural cracking zone. (b) The angle of diagonal shear cracks can increase with higher axial load. (c) The width of both shear and flexural cracks can be reduced (enhancing the shear transfer capacity) with an increase in axial load. However, most exiting formulation for shear strength of RC column do not cosider the effect of axial load level. Numerous experimental studies [17-25] have investigated the influence of axial load and reinforcement detailing on the shear performance of RC members. Baldwin and

* Corresponding author.
E-mail addresses: arch3d.ir@gmail.com (J. Shayanfar).

https://doi.org/10.22080/ceas.2025.30228.1050
ISSN: 3092-7749/© 2026 The Author(s). Published by University of Mazandaran.
This article is an open access article distributed under the terms and conditions of the Creative Commons Attribution (CC-BY) license (https://creativecommons.org/licenses/by/4.0/deed.en)
How to cite this article: Sadeghpour Haji, M., Niknam, R., Shayanfar, J. ANN-Based Modeling of Shear Behavior of Reinforced Concrete Columns under Constant Axial Loads 2026; 2(2): 28–48. doi:10.22080/ceas.2025.30228.1050.

Viest [17] demonstrated the positive contribution of axial load to shear strength, improving diagonal cracking resistance and ultimate shear capacity. Yamad [18] reported that higher axial load ratios and shorter shear spans reduce ductility.

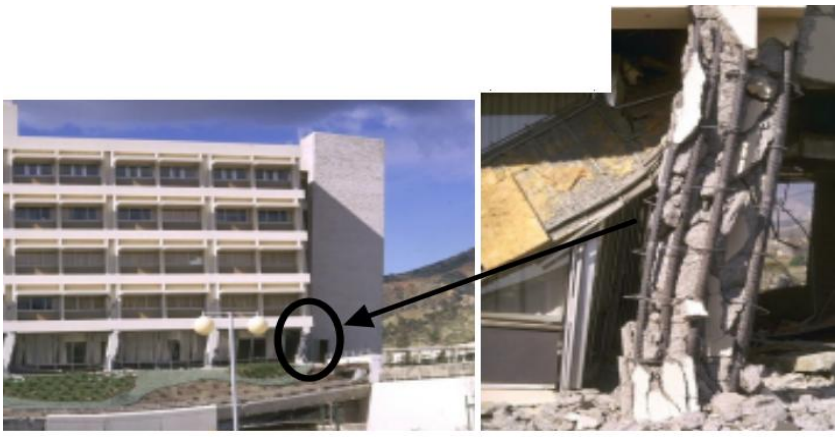

(a) 1971 San Fernando – USA [1].

(b) 1994 Northridge – USA [1].

(c) 1999 Kocaeli – Turkey [2].

(d) 1999 Düzce – Turkey [2].

Fig. 1. Documented damage and failure of reinforced concrete structures observed in past earthquakes.

While Elzanaty et al. [19] showed that higher longitudinal reinforcement ratios enhance shear resistance in beams without stirrups, though less effectively than their contribution to flexural strength. Wight James and Sozen Mete [20], Woodward Kyle and Jirsa James [21], Ascheim and Moehle [22], Ghee et al. [23], Yuk-Lung Wong and Priestley [24] and Bengar et al. [25] further emphasized the dependency of shear strength and ductility on axial load, shear span ratio, and transverse reinforcement. Similarly,

Lynn [26], Pan and Li [27], and Duong et al. [28] confirmed the interplay between axial load level, reinforcement configuration, and nonlinear behavior of RC columns.

Experimental studies conducted by [29-33] have demonstrated that the shear strength of concrete members is a function of their flexural deformations. Although current seismic design codes do not explicitly define the reduction of shear capacity as a function of member deformations, the decrease in shear capacity of concrete members under seismic loads is nevertheless considered. For instance, ACI 318 [34] neglects the contribution of concrete to the shear capacity of members subjected to low axial loads. Similarly, FEMA 273 [35] disregards the contribution of concrete to shear strength at moderate and high levels of ductility, and the NZS [36] code does not account for the concrete contribution to shear capacity of members.

In recent years, artificial neural networks (ANNs) have attracted increasing attention due to their capability to evaluate and predict structural behavior by learning from experimental data [37-42]. As accurately estimating the shear capacity of RC members is essential for reliable nonlinear analysis, ANNs provide an effective tool for this purpose. By compiling experimental databases of RC members failing in shear or combined shear–flexure and incorporating key governing parameters as inputs, ANN models can be trained to provide accurate predictions of shear strength. Developing such models forms a key objective of the present research. In this context, the present study aims to develop an advanced modeling framework for predicting the nonlinear shear behavior of reinforced concrete columns designed according to older seismic codes. To achieve this, an extensive experimental database was compiled and used to train artificial neural networks (ANNs), with key geometric, material, and loading parameters as inputs. The ANN-based model was then validated against independent test data and benchmarked against existing analytical models. The results of this study provide a reliable tool for assessing the seismic performance of deficient RC columns and offer valuable insights for strengthening strategies and future code development.

2. Research significance

The shear capacity of RC columns is strongly influenced by ductility demands, which increase under seismic loading and flexural deformations. Conventional analytical formulations often neglect the reduction of shear strength at higher ductility levels, leading to conservative or inaccurate predictions, particularly for RC members designed according to older seismic codes. This study addresses this gap by integrating the effects of ductility on shear capacity within an ANN framework. By leveraging experimental data and key governing parameters, the ANN model provides accurate, data-driven predictions of shear strength, capturing the complex interaction between flexural deformations, axial load, and reinforcement detailing. The proposed approach offers a practical and reliable tool for assessing the nonlinear shear behavior of deficient RC columns, supporting improved seismic evaluation, retrofitting strategies, and informed updates to design codes.

3. ANN-based shear modeling of RC columns under constant axial load

Previous studies have shown that one of the deficiencies of structures designed according to older codes is their vulnerability and lack of shear strength in columns and beams [2]. This deficiency often leads to undesirable shear failure, which, through the reduction of the column's axial capacity, can result in combined shear–axial failure. Such behavior can cause a significant reduction in the member's strength and ductility response. On the other hand, experimental studies [29-33] have demonstrated that the shear strength of concrete members is a function of their flexural deformations. Under seismic loading, as flexural deformations increase beyond the yielding of tensile reinforcement, the widening of flexural cracks, crushing and tensile cracking of concrete in the compression zone, and the reduction in neutral axis depth at large deformations collectively lead to a decrease in the shear capacity of reinforced concrete members. Therefore, accounting for the influence of shear mechanisms as a function of flexural deformations in the nonlinear analysis of reinforced concrete members and structures is essential.

In the present study, an analytical model is proposed to calculate the shear capacity of reinforced concrete columns, based on the works of Park et al. [43] and Shayanfar and Akbarzadeh Bengar [3]. According to Mohr's circle theory, the principal compressive (σc) and tensile (σt) stresses at any element within the cross-section of the reinforced concrete member (as illustrated in Fig. 2) can be expressed as follows:

$$\sigma_c = \frac{\sigma}{2} + \sqrt{\frac{\sigma^2}{4} + v^2} \tag{1}$$

$$\sigma_c = \frac{\sigma}{2} - \sqrt{\frac{\sigma^2}{4} + v^2} \tag{2}$$

where v and σ represent the shear and normal stresses, respectively, at the considered element of the cross-section. Based on Eqs. 1 and 2, the shear stress capacity can be expressed as follows:

$$v_c(y_i) = \sqrt{\bar{\sigma}_c[\bar{\sigma}_c - \sigma(y_i)]} \tag{3}$$

$$v_t(y_i) = \sqrt{\bar{\sigma}_t[\bar{\sigma}_t + \sigma(y_i)]} \tag{4}$$

$$v_{tot} = \sum v(y_i) \times bc = \sum min\left(\sqrt{\bar{\sigma}_t[\bar{\sigma}_t + \bar{\sigma}]}, \sqrt{\bar{\sigma}_c[\bar{\sigma}_c - \bar{\sigma}]}\right) \times bc \tag{5}$$

where yi is the distance of each strip element of the cross-section from the neutral axis c. $\bar{\sigma_c}$ and $\bar{\sigma_t}$ represent the compressive and tensile failure levels, respectively, which are selected based on the Rankine failure criteria (Chen [44]) (see Fig. 2). The shear stress capacity $v(y_i)$, accounting for the combined contribution of concrete and transverse reinforcement, is taken as the smaller value between $v_c(y_i)$ and $v_t(y_i)$. According to the shear models proposed by Priestley et al. [45] and Sezen and Moehle Jack [46], if 80% of the cross-sectional area is considered as the effective shear area, and the axial stress in the compression zone of the section ($\sigma = \sum \sigma(y_i)$) is assumed to be equal to the equivalent longitudinal stress induced by the axial load applied to the column ($\bar{\sigma} = N/A_g$), leading to $\bar{\sigma} = \sigma$, the shear stress capacity can be expressed as follows:

$$v_c(y_i) = \sqrt{\bar{\sigma_c}[\bar{\sigma_c} - \sigma]} \tag{6}$$

$$v_t(y_i) = \sqrt{\bar{\sigma_t}[\bar{\sigma_t} + \sigma]} \tag{7}$$

Therefore, in all effective shear elements (both tension- and compression-controlled regions), the longitudinal stress, and consequently the shear stress is assumed to be the same. As a result, the member's shear stress capacity v_c, which is equal to the sum of the shear stresses in all elements within the compression zone of the cross-section $v(y_i)$ (taken as the smaller value between $v_t(y_i)$ and $v_c(y_i)$, can be expressed as:

$$v = \sum min[v_t(y_i), v_c(y_i)] = \sum min\left(\sqrt{\bar{\sigma_t}[\bar{\sigma_t} + \bar{\sigma}]}, \sqrt{\bar{\sigma_c}[\bar{\sigma_c} - \bar{\sigma}]}\right) \tag{8}$$

Since most of the effective shear regions are tension-controlled, it is assumed in this study that member failure is governed by tension-controlled behavior [46]. Therefore:

$$v = \sqrt{\bar{\sigma_t}[\bar{\sigma_t} + \bar{\sigma}]} \tag{9}$$

$$v_c = v \times A_g = v \times 0.8\, A_g = 0.8\, A_g \times \sqrt{\bar{\sigma_t}[\bar{\sigma_t} + \bar{\sigma}]} \tag{10}$$

It is worth noting that the principal tensile stress $\bar{\sigma_t}$ represents the combined contribution of concrete and transverse reinforcement to the shear capacity. However, the above relationships do not introduce any parameter to account for the effects of flexural deformation on the shear strength of the concrete member. Therefore, following Sezen and Moehle Jack [46], the parameter λ is defined as a function of displacement ductility (see Fig. 3). In this model, in addition to accounting for the effects of shear deformations on the column's shear capacity, the negative impact of shear deformations on the contribution of transverse reinforcement to the column's shear strength due to reduced anchorage of the transverse barsnis also considered. This parameter can be calculated as follows:

$$\lambda = \begin{cases} 1 & \mu_\Delta \le 2 \\ 1.15 - 0.075\,\mu_\Delta & 2 \le \mu_\Delta \le 6 \\ 0.7 & \mu_\Delta \ge 6 \end{cases} \tag{11}$$

Consequently:

$$v = \lambda\sqrt{\bar{\sigma_t}[\bar{\sigma_t} + \bar{\sigma}]} \tag{12}$$

Therefore, using the above relationship, the shear capacity of a reinforced concrete member can be determined as a function of displacement ductility. However, this relationship requires the determination of λ as an input parameter.

Recently, the training of artificial neural networks (ANNs), which are capable of identifying and predicting system mechanisms due to their significant computational intelligence, has attracted considerable attention in the field of civil engineering. For predicting the nonlinear behavior of reinforced concrete members, the development of ANNs can serve as a useful tool, providing both ease of use and high accuracy to meet the requirements of designers and analysts. Therefore, by providing a database of key parameters governing the behavioral mechanisms of reinforced concrete members as input variables, and $\bar{\sigma_t}$ as the output variable, an efficient artificial neural network can be trained. Achieving such a trained network constitutes one of the primary objectives of this paper.

3.1. Experimental database

The output predicted by any ANN is entirely dependent on the samples provided in the database. On the other hand, the nonlinear behavior of reinforced concrete members can be controlled based on their failure mode. In other words, the ultimate strength of a member is a function of the type of failure, such as flexural, flexure–shear, or shear. For columns exhibiting flexure–shear or shear mechanisms, the ultimate strength corresponds to the maximum shear capacity. Therefore, since the focus of this study is on evaluating the performance of structures designed according to older codes (where member failure modes are generally governed by shear mechanisms) the failure modes of the database samples must be either shear or flexure–shear.

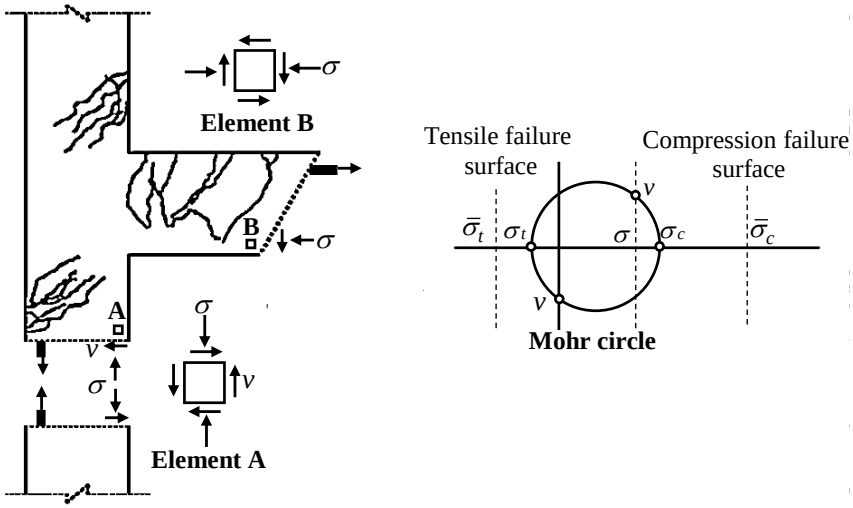

Fig. 2. Rankine failure criteria for concrete in principal stress space (after Chen [44]).

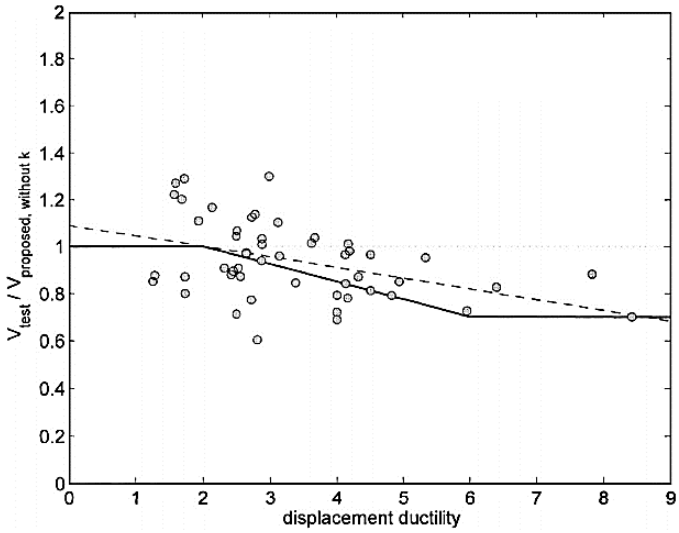

Fig. 3. Degradation parameter as a function of displacement ductility (after Sezen and Moehle Jack [46]).

Consequently, an ANN trained using such a database can identify and predict the flexure–shear or shear mechanisms of the member. In this study, a database of 164 RC column specimens exhibiting shear or flexure–shear failure was compiled from the literature [2, 20, 26, 27, 32, 47-69]. Input parameters included column geometry, longitudinal and transverse reinforcement ratios, axial load ratio, and concrete compressive strength. The database of specimens is summarized in Table 1.

Table 1. Experimental database of RC column specimens with shear or flexure–shear failure modes, including geometric, reinforcement, material, and axial load parameters.

		Input											Other			Output
ID		b (mm)	h (mm)	d (mm)	a (mm)	s (mm)	ρl (%)	fyl (MPa)	ρt (%)	fyt (MPa)	f 'c (MPa)	rN	λ	V (kN)	v (MPa)	$\frac{\sigma_t}{\sqrt{f_c'}}$
Sezen [2]	1	457	457	394	1473	305	2.5	447	0.17	469	21.1	0.15	0.99	314.9	1.90	0.19
	2	457	457	394	1473	305	2.5	447	0.17	469	21.1	0.61	1.00	358.5	2.15	0.08
	3	457	457	394	1473	305	2.5	447	0.17	469	20.9	0.51	1.00	301.1	1.80	0.06
	4	457	457	394	1473	305	2.5	447	0.17	469	21.8	0.15	0.98	294.5	1.80	0.17
Lynn [26]	3CL H18	457	457	381	1473	457	3.1	335	0.07	400	25.6	0.09	1.00	272.1	1.63	0.16
	3SL H18	457	457	381	1473	457	3.1	335	0.07	400	25.6	0.09	1.00	273.1	1.63	0.16
	2CL H18	457	457	381	1473	457	1.9	335	0.07	400	33.1	0.07	0.77	243.2	1.89	0.18
	2SL H18	457	457	381	1473	457	1.9	335	0.07	400	33.1	0.07	0.97	231.0	1.43	0.12
	2CM H18	457	457	381	1473	457	1.9	335	0.07	400	25.7	0.28	1.00	307.8	1.84	0.09
	3CM H18	457	457	381	1473	457	3.1	335	0.07	400	27.6	0.26	1.00	326.9	1.96	0.09
	3CM D12	457	457	381	1473	305	3.1	335	0.17	400	27.6	0.26	1.00	356.0	2.13	0.11
	3SM D12	457	457	381	1473	305	3.1	335	0.17	400	25.7	0.28	1.00	367.2	2.20	0.12

Ohue et al. [47]	2D16RS4D13RS	200	200	175	400	50	2.0	376	0.57	322	32.1	0.14	0.94	102.0	3.41	0.32
		200	200	175	400	50	2.5	377	0.57	322	29.9	0.15	0.99	111.0	3.49	0.34
Esaki [48]	H-2-1/5	200	200	175	400	50	2.5	363	0.52	370	23.0	0.18	0.85	103.0	3.79	0.47
	HT-2-1/5	200	200	175	400	75	2.5	363	0.52	370	20.2	0.20	0.92	102.0	3.46	0.44
	H-2-1/3	200	200	175	400	40	2.5	363	0.65	370	23.0	0.29	0.97	121.0	3.88	0.37
	HT-2-1/3	200	200	175	400	60	2.5	363	0.65	370	20.2	0.29	0.96	112.0	3.63	0.38
Li [49]	U-7	400	400	375	1000	120	2.4	581	0.47	382	29.0	0.10	0.85	328.0	3.01	0.35
	U-8	400	400	375	1000	120	2.4	581	0.52	382	33.5	0.20	1.00	393.0	3.07	0.21
	U-9	400	400	375	1000	120	2.4	581	0.57	382	34.1	0.30	0.93	430.0	3.62	0.20
Saatcioglu and Ozcebe [50]	U1	350	350	305	1000	150	3.3	430	0.30	470	43.6	0.00	0.95	274.9	2.95	0.45
	U2	350	350	305	1000	150	3.3	453	0.30	470	30.2	0.16	1.00	270.0	2.76	0.23
	U3	350	350	305	1000	75	3.3	430	0.60	470	34.8	0.14	1.00	268.0	2.73	0.21
Yalcin [51]	BR-S1	550	550	482	1485	300	2.0	445	0.10	425	44.8	0.13	1.00	578.0	2.39	0.13
Hirosawa [52]	43	200	200	173	500	100	2.0	434	0.28	558	19.6	0.10	0.91	73.8	2.54	0.39
	44	200	200	173	500	100	2.0	434	0.28	558	19.6	0.10	0.97	76.5	2.48	0.38
	45	200	200	173	500	100	2.0	434	0.28	558	19.6	0.20	1.00	82.3	2.57	0.29
	46	200	200	173	500	100	2.0	434	0.28	558	19.6	0.20	1.00	80.5	2.52	0.28
	62	200	200	173	500	100	2.0	348	0.28	476	19.6	0.10	0.93	57.8	1.93	0.27
	63	200	200	173	500	100	2.0	348	0.28	476	19.6	0.20	0.86	68.5	2.49	0.27
	64	200	200	173	500	100	2.0	348	0.28	476	19.6	0.20	0.95	68.5	2.25	0.23
Hirosawa [52]	205	200	200	180	600	100	2.0	462	0.28	324	17.7	0.22	0.96	71.2	2.32	0.26
	207	200	200	180	400	100	2.0	462	0.28	324	17.7	0.22	1.00	105.9	3.31	0.45
	208	200	200	180	400	100	2.0	462	0.28	324	17.7	0.55	0.93	135.2	4.56	0.43
	214	200	200	180	600	200	2.0	462	0.14	324	17.7	0.55	1.00	82.7	2.58	0.15
	220	200	200	180	400	120	1.0	379	0.11	648	32.9	0.12	0.75	78.3	3.27	0.32
	231	200	200	180	400	100	1.0	324	0.13	524	14.8	0.26	0.85	50.7	1.87	0.20
	232	200	200	180	400	100	1.0	324	0.13	524	13.1	0.30	0.91	58.3	1.99	0.23
	233	200	200	180	400	100	1.0	372	0.13	524	13.9	0.28	0.81	68.9	2.65	0.36
	234	200	200	180	400	100	1.0	372	0.13	524	13.1	0.30	0.75	67.2	2.80	0.40
Xiao and Martirossyan [53]	HC4-8LI6-T6-0.1P	254	254	222	508	51	2.5	510	0.74	449	86.0	0.10	0.78	273.0	6.83	0.41
	HC4-8L16-T6-0.2P	254	254	222	508	51	2.5	510	0.74	449	86.0	0.19	0.89	324.0	7.07	0.28
Wight James and Sozen Mete [20]	3E	152	305	254	876	127	2.4	496	0.32	345	34.7	0.12	0.93	94.0	2.73	0.23
	3W	152	305	254	876	127	2.4	496	0.32	345	34.7	0.12	0.92	98.0	2.87	0.25
	8E	152	305	254	876	89	2.4	496	0.46	345	26.1	0.15	0.86	101.0	3.18	0.35
	8W	152	305	254	876	89	2.4	496	0.46	345	26.1	0.15	0.82	95.0	3.11	0.34
	3E	152	305	254	876	127	2.4	496	0.32	345	33.6	0.12	0.95	91.0	2.59	0.22
	3W	152	305	254	876	127	2.4	496	0.32	345	33.6	0.12	0.93	101.0	2.91	0.26
	3E	152	305	254	876	127	2.4	496	0.32	345	33.6	0.07	0.96	85.0	2.38	0.25
	3W	152	305	254	876	127	2.4	496	0.32	345	33.6	0.07	0.98	91.0	2.51	0.27
	7E	152	305	254	876	64	2.4	496	0.64	345	33.4	0.11	0.78	86.0	2.96	0.28
	7W	152	305	254	876	64	2.4	496	0.64	345	33.4	0.11	0.81	92.0	3.07	0.29
	2E	152	305	254	876	102	2.4	496	0.91	345	33.5	0.11	0.75	108.0	3.89	0.42
	2W	152	305	254	876	102	2.4	496	0.91	345	33.5	0.11	0.79	113.0	3.87	0.41
Yoshimura [54]	N18M	300	300	255	450	100	2.7	380	0.21	375	26.5	0.18	0.92	263.0	3.96	0.43

	N18C	300	300	255	450	100	2.7	380	0.21	375	26.5	0.18	0.85	264.0	4.34	0.50
	N27M	300	300	255	450	100	2.7	380	0.21	375	26.5	0.27	0.80	288.0	4.98	0.50
	N27C	300	300	255	450	100	2.7	380	0.21	375	26.5	0.27	0.97	263.0	3.76	0.31
	2M	300	300	255	300	100	2.7	396	0.21	392	25.2	0.19	0.78	234.0	4.18	0.48
	2C	300	300	255	300	100	2.7	396	0.21	392	25.2	0.19	0.70	222.0	4.40	0.52
	3M	300	300	255	300	100	2.7	396	0.21	392	25.2	0.28	0.74	248.0	4.63	0.46
	3C	300	300	255	300	100	2.7	396	0.21	392	25.2	0.28	0.72	264.0	5.10	0.53
	2M13	300	300	255	300	100	1.7	350	0.21	392	25.2	0.19	0.92	250.0	3.78	0.41
	2C13	300	300	255	300	100	1.7	350	0.21	392	25.2	0.19	0.79	260.0	4.56	0.55
Yoshimura et al. [55]	No.1	300	300	255	600	100	2.7	402	0.21	392	30.7	0.20	0.95	234.0	3.41	0.27
	No.2	300	300	255	600	150	2.7	402	0.14	392	30.7	0.20	0.95	230.0	3.36	0.27
	No.3	300	300	255	600	200	2.7	402	0.11	392	30.7	0.20	0.96	230.0	3.33	0.26
	No.4	300	300	255	600	100	2.7	402	0.21	392	30.7	0.30	0.96	261.0	3.78	0.24
	No.5	300	300	255	600	100	2.7	402	0.21	392	30.7	0.35	0.81	275.0	4.72	0.32
	No.6	300	300	255	600	100	1.7	409	0.21	392	30.7	0.20	0.85	219.0	3.56	0.29
	No.7	300	300	255	600	150	1.7	409	0.14	392	30.7	0.20	0.90	213.0	3.31	0.26
Nakamura and Yoshimura [56]	C13-J	300	300	255	450	200	1.7	371	0.11	366	22.0	0.20	1.00	191.0	2.65	0.27
	C13-T	300	300	255	450	200	1.7	371	0.11	366	22.0	0.20	1.00	201.0	2.79	0.29
	C13-H	300	300	255	450	200	1.7	371	0.11	366	22.0	0.20	1.00	212.0	2.94	0.31
	4J11	450	450	390	750	300	1.7	403	0.11	360	19.5	0.17	1.00	413.0	2.55	0.31
	4W11	450	450	390	750	300	1.7	403	0.11	360	19.5	0.17	1.00	432.0	2.67	0.34
	4H11	450	450	390	750	300	1.7	403	0.11	360	19.5	0.17	1.00	395.0	2.44	0.29
	6J11	450	450	390	750	300	1.7	403	0.11	360	19.5	0.17	1.00	436.0	2.69	0.34
	4J21	450	450	390	750	150	1.7	403	0.21	360	19.5	0.17	1.00	447.0	2.76	0.35
	4W21	450	450	390	750	150	1.7	403	0.21	360	19.5	0.17	1.00	429.0	2.65	0.33
	6J21	450	450	390	750	150	1.7	403	0.21	360	19.5	0.17	1.00	434.0	2.68	0.34
Nakamura and Yoshimura [57]	A1	450	450	390	450	300	1.1	383	0.11	399	28.0	0.16	1.00	570.0	3.52	0.36
	A2	450	450	390	450	300	1.1	383	0.11	399	28.0	0.16	1.00	557.0	3.44	0.35
	B1	450	450	390	450	150	1.7	383	0.21	399	28.0	0.16	1.00	594.0	3.67	0.39
	B2	450	450	390	450	150	1.7	383	0.21	399	28.0	0.16	1.00	607.0	3.75	0.40
	B3	450	450	390	450	150	1.7	383	0.21	399	28.0	0.16	1.00	545.0	3.36	0.34
	B4	450	450	390	450	150	1.7	383	0.21	399	28.0	0.16	1.00	578.0	3.57	0.37
	B5	450	450	390	450	150	1.7	383	0.21	399	28.0	0.16	1.00	565.0	3.49	0.36
	C1	450	450	390	450	75	2.3	376	0.42	399	28.0	0.16	1.00	687.0	4.24	0.48
	C2	450	450	390	450	75	2.3	376	0.42	399	28.0	0.16	1.00	715.0	4.41	0.51
	S100	450	450	390	450	150	1.7	383	0.21	399	25.0	0.18	1.00	522.0	3.22	0.34
	S60	450	450	390	450	150	1.7	383	0.21	399	25.0	0.18	1.00	577.0	3.56	0.39
	S40	450	450	390	450	150	1.7	383	0.21	399	25.0	0.18	1.00	505.0	3.12	0.32
	S20	450	450	390	450	150	1.7	383	0.21	399	25.0	0.18	1.00	562.0	3.47	0.38
	L100	450	450	390	700	200	1.7	383	0.16	399	25.0	0.18	1.00	506.0	3.12	0.32
	L75	450	450	390	700	200	1.7	383	0.16	399	25.0	0.18	1.00	526.0	3.25	0.34
	L50	450	450	390	700	200	1.7	383	0.16	399	25.0	0.18	1.00	497.0	3.07	0.31
Moretti and Tassios [32]	1	250	250	215	250	50	2.0	480	1.21	300	36.0	0.30	1.00	330.0	6.60	0.52
	3	250	250	215	250	50	4.0	415	1.21	300	39.0	0.30	1.00	360.0	7.20	0.55
	4	250	250	215	250	50	4.0	415	1.21	305	35.0	0.30	1.00	360.0	7.20	0.62
	7	250	250	215	500	50	2.0	480	1.21	300	38.0	0.30	0.91	200.0	4.40	0.24
	8	250	250	215	750	50	2.0	480	1.21	300	38.0	0.30	0.89	140.0	3.13	0.13
Li et al. [58]	1DL	300	500	450	250	100	3.1	438	1.27	430	27.5	0.09	1.00	698.0	5.82	0.90

	1DH	300	500	450	250	100	3.1	438	1.27	430	25.2	0.29	1.00	701.0	5.84	0.64
	1NL	300	500	450	250	200	3.1	438	0.24	458	23.4	0.10	1.00	660.0	5.50	0.92
	1NH	300	500	450	250	200	3.1	438	0.24	458	25.1	0.29	1.00	757.0	6.31	0.73
	2DL	300	500	450	500	100	3.1	438	1.27	430	25.7	0.09	1.00	564.0	4.70	0.73
	2DH	300	500	450	500	100	3.1	438	1.27	430	24.4	0.30	1.00	589.0	4.91	0.50
	1NL	300	500	450	500	200	3.1	438	0.24	458	23.4	0.10	1.00	402.0	3.35	0.49
	2NH	300	500	450	500	200	3.1	438	0.24	458	25.5	0.29	1.00	460.0	3.83	0.32
Ramirez and Jirsa [59]	00-U	305	305	264	458	66	2.5	410	0.32	455	34.5	0.00	0.96	265.9	3.74	0.64
	120C-U	305	305	264	458	66	2.5	410	0.32	455	34.5	0.17	0.95	297.9	4.23	0.38
Bett et al. [60]	SF1	305	305	257	457	210	1.8	462	0.09	414	29.9	0.10	1.00	214.0	2.88	0.31
Hirosawa [52]	372	200	200	170	500	100	1.0	524	0.31	352	20.0	0.30	0.86	74.3	2.70	0.23
	373	200	200	170	500	100	2.0	524	0.31	352	20.4	0.30	0.95	88.1	2.89	0.26
Hirosawa [52]	452	200	200	170	500	100	3.0	524	0.31	352	21.9	0.45	0.99	110.3	3.47	0.24
	454	200	200	170	500	100	4.0	524	0.31	352	21.9	0.45	0.98	110.3	3.50	0.24
Umehara [61]	CUS	230	410	370	455	89	3.0	441	0.28	414	34.9	0.16	1.00	324.0	4.29	0.39
	CUW	410	230	190	455	89	3.0	441	0.31	414	34.9	0.16	1.00	265.0	3.51	0.28
	2CUS	230	410	370	455	89	3.0	441	0.28	414	42.0	0.27	1.00	412.0	5.46	0.34
Ousalem et al. [62]	C1	300	300	260	450	160	1.7	587	0.08	340	13.5	0.30	0.88	160.4	2.54	0.33
	C4	300	300	260	450	75	1.7	384	0.28	340	13.5	0.30	0.81	171.1	2.94	0.42
	C6	300	300	260	450	75	1.7	384	0.28	340	13.5	1.28	0.67	203.9	4.24	0.26
	C8	300	300	260	450	75	1.7	384	0.28	340	18.0	0.30	0.86	233.0	3.77	0.46
	C10	300	300	260	450	75	1.7	384	0.28	340	18.0	1.05	0.81	262.1	4.50	0.24
	C12	300	300	260	450	75	1.7	384	0.28	340	18.0	0.20	0.78	217.1	3.87	0.58
	D1	300	300	260	300	50	1.7	398	0.43	447	27.7	0.22	0.90	341.1	5.24	0.58
	D16	300	300	260	300	50	1.7	398	0.43	447	26.1	0.23	0.89	341.6	5.35	0.61
	D11	300	300	260	450	150	2.3	398	0.14	447	28.2	0.21	0.83	242.8	4.06	0.39
	D12	300	300	260	450	150	2.3	398	0.14	447	28.2	0.21	0.85	250.4	4.09	0.39
	D13	300	300	260	450	50	2.3	398	0.43	447	26.1	0.23	0.83	266.1	4.48	0.47
	D14	300	300	260	450	50	2.3	398	0.43	447	26.1	0.23	0.80	269.1	4.66	0.50
Aboutaha et al. [63]	SC3	914	457	397	1219	407	1.9	434	0.10	400	21.9	0.00	0.99	393.7	1.19	0.25
	SC9	457	914	853	1219	406	1.9	434	0.08	400	21.9	0.00	1.00	587.2	1.76	0.38
Woods [64]	1	457	457	394	1248	457	2.5	445	0.07	372	33.0	0.32	1.00	412.0	2.46	0.09
	2	457	457	394	1248	457	2.5	445	0.07	372	33.0	0.22	1.00	360.0	2.15	0.10
	3	457	457	394	1248	457	3.0	445	0.07	372	33.0	0.32	1.00	313.0	1.87	0.06
Pan and Li [27]	SC-2.4-0.20	350	350	315	850	125	2.1	408	0.13	393	22.6	0.20	1.00	218.9	2.23	0.19
	SC-2.4-0.30	350	350	315	850	125	3.2	409	0.13	393	49.3	0.30	0.97	357.1	3.75	0.13
	SC-2.4-0.50	350	350	315	850	125	2.1	408	0.13	393	24.2	0.50	1.00	237.6	2.43	0.10
	SC-1.7-0.05	350	350	316	600	125	2.1	408	0.13	393	29.8	0.05	1.00	276.4	2.82	0.40
	SC-1.7-0.20	350	350	316	600	125	2.1	408	0.13	393	27.5	0.20	1.00	294.2	3.00	0.25
	SC-1.7-0.35	350	350	316	600	125	2.1	408	0.13	393	25.5	0.35	1.00	335.5	3.42	0.23
	SC-1.7-0.50	350	350	316	600	125	2.1	408	0.13	393	26.4	0.50	1.00	375.6	3.83	0.20
	RC-1.7-0.05	250	490	447	850	125	2.1	408	0.18	393	32.5	0.05	1.00	283.1	2.89	0.38

	RC-1.7-0.20	250	490	447	850	125	2.1	408	0.18	393	24.5	0.20	1.00	305.5	3.12	0.31
	RC-1.7-0.35	250	490	447	850	125	2.1	408	0.18	393	27.1	0.35	1.00	345.7	3.53	0.22
	RC-1.7-0.50	250	490	447	850	125	2.1	408	0.18	393	26.8	0.50	0.99	355.2	3.65	0.18
Boys et al. [65]	24L-300-2D	450	450	412	1624	300	1.0	315	0.12	315	32.0	0.31	0.89	256.4	1.78	0.05
Kogoma et al. [66]	CT1	130	130	99	425	285	4.8	355	0.23	355	22.8	0.18	1.00	24.9	1.84	0.15
Choi et al. [67]	NRC 1	300	300	252	830	300	0.9	327	0.17	378	17.9	0.27	1.00	108.7	1.51	0.10
	NRC 2	300	300	250	830	300	0.9	327	0.17	378	18.3	0.26	1.00	109.1	1.52	0.10
	NRC 3	300	300	250	830	300	1.3	327	0.17	378	17.5	0.28	1.00	116.1	1.61	0.12
	NRC 5	300	300	252	830	300	0.9	327	0.17	378	19.9	0.38	1.00	128.2	1.78	0.09
	NRC 6	300	300	252	630	300	0.9	327	0.17	378	17.2	0.31	0.99	141.1	1.99	0.16
	NRC 7	300	300	249	830	150	1.7	350	0.34	310	12.7	0.31	0.96	122.5	1.78	0.19
	NRC 8	300	300	249	830	150	1.7	350	0.34	310	12.1	0.33	0.95	127.3	1.87	0.21
	NRC 9	300	300	249	830	150	1.7	350	0.34	310	13.0	0.10	0.74	113.1	2.13	0.44
	NRC 10	300	300	249	830	150	1.7	350	0.34	310	13.6	0.44	0.92	140.5	2.11	0.18
Ghannoum Wassim and Moehle Jack [68]	ColA 1	152	152	131	495	102	2.5	552	0.15	655	24.6	0.17	1.00	32.2	1.74	0.13
	ColB 1	152	152	131	495	102	2.5	553	0.15	655	24.6	0.19	1.00	43.9	2.38	0.20
Elwood and Moehle [69]	EL_sp1	229	229	197	737	152	2.5	479	0.18	689	24.5	0.10	1.00	80.5	1.92	0.21
	EL_sp2	229	229	197	737	152	2.5	479	0.18	689	23.9	0.24	1.00	88.1	2.10	0.14

Using the following procedure, the maximum principal tensile stress and the maximum horizontal shear strength were extracted from the experimental specimens:

1. Determination of maximum shear stress:

$$\nu^{exp} = \frac{V^{exp}}{A_e} \times \frac{1}{\lambda} = \frac{V^{exp}}{0.8bh\lambda} \tag{13}$$

in which V^{exp} is the experimental shear capacity; b and h are the width and depth of the column cross-section.

2. Determination of axial stress at a column element using:

$$\bar{\sigma}^{exp} = \frac{N}{bh} \tag{14}$$

in which N is the axial load applied on the column.

$$\sigma_t^{exp} = \sqrt{\left(\frac{\bar{\sigma}^{exp}}{2}\right)^2 + (\nu^{exp})^2} - \frac{\bar{\sigma}^{exp}}{2} \tag{14}$$

Therefore, using the above results, the shear force applied to the member can be converted into the principal tensile stress in the column.

3.2. ANN Model development

An artificial neural network (ANN) was trained to predict the maximum principal tensile stress and corresponding shear strength. Nine input parameters and one normalized output parameter were selected.

The following section explains the rationale for selecting each input and output parameter for the neural network:

1. Parameters b, h, and d: These parameters define the geometry of the laboratory specimen and are provided to the network as input.
2. Parameters ρ_l and f_{yl}: These parameters represent the tensile contribution of the longitudinal reinforcement in the column. Although they have a significant effect on the flexural capacity of the column, their impact on enhancing shear capacity is minimal. However, in shear models [53, 70, 71], these parameters are considered in the determination of the concrete shear

capacity.

3. Parameters s, ρ_t, and f_{yt}: These parameters describe the transverse reinforcement of the column. They play a key and significant role in the shear capacity of the column and also affect the confinement of the concrete core.
4. Parameter a: This represents the distance between the points of maximum and zero moments, known as the shear span, and is provided to the network as an input. In addition to the column's shear span, the angle of diagonal shear cracks in the column depends significantly on this parameter. This parameter is included in shear models [46, 53, 71].
5. Parameter λ: The effect of flexural deformation on the column's shear capacity is indirectly represented by this dimensionless parameter. It should be noted that the experimental shear strength V^{exp} corresponds to μ_Δ. Consequently, the column shear capacity is a function of λ, and this parameter should be considered as an input. However, determining μ_Δ requires section analysis (to determine flexural behavior) and a shear model, whereas the purpose of training the ANN is to predict the shear model itself. Therefore, in this study, V^{exp} corresponding to μ_Δ is converted into shear capacity for $\mu_\Delta < 2$ using Eq. 13. As a result, it is no longer necessary to include this parameter as an input to the ANN.
6. Parameter f'_c: This parameter represents the compressive strength of the concrete, which is a critical property of the column, and is provided to the network as input.
7. Parameter N: The axial load applied to the column is indirectly represented by this parameter. As seen in Eqs. 14 and 15, the effects of this parameter on the column shear capacity are accounted for in $\bar{\sigma}^{exp}$ and σ_t^{exp}.
8. Output parameter $\sigma_t/\sqrt{f'_c}$: The principal tensile stress corresponding to the maximum shear strength at a displacement ductility of less than 2 is normalized by the concrete compressive strength and provided to the network as the output parameter.

Fig. 4 illustrates the architecture of the trained artificial neural network. As shown, this study uses 9 input parameters, 1 output parameter, 20 hidden layers, and 1 output layer for network training. In the ANN modeling, the activation functions in the hidden layers are logarithmic, while the output layer uses a linear activation function. This structure is employed because a single-layer feedforward backpropagation network with bias, a Sigmoid hidden layer, and a linear output layer is capable of approximating any function with a limited number of discontinuities.

In this study, the artificial neural network (ANN) was trained using MATLAB with the trainlm function. The trainlm function is a network training function that updates the weights and biases. Standard backpropagation is a gradient descent algorithm in which the network weights are adjusted along the negative gradient of the performance function. The most commonly used backpropagation training algorithm is the Levenberg–Marquardt algorithm, which has been employed in this study. The dataset used to train the network consists of 164 reinforced concrete column specimens with shear and flexure–shear failure mechanisms. Of these, 70% were randomly assigned for network training, 15% for network validation, and 15% for network testing.

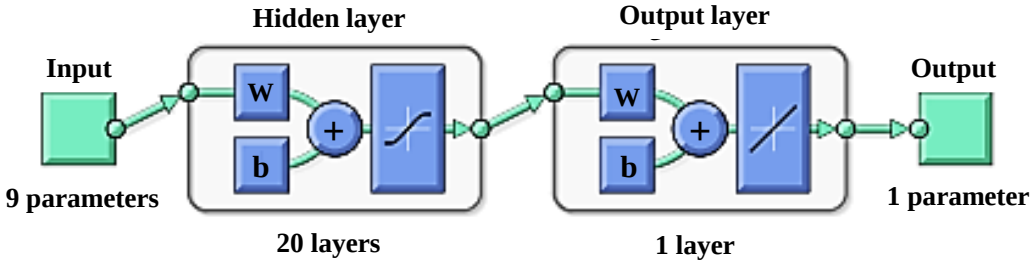

Fig. 4. Architecture of the artificial neural network (ANN) developed for shear strength prediction.

3.3. Model performance and validation

The ANN predictions of principal tensile stress showed close agreement with experimental data. Comparison of predicted and measured values is presented in Fig. 5, while Fig. 6 illustrates the validation against independent test sets. Quantitative results are provided in Table 2, showing mean ratios close to unity and low standard deviations, confirming the reliability of the ANN model.

Table 2. Comparison of shear capacity predictions from ANN and analytical model with experimental results.

ID		f 'c (MPa)	fv (MPa)	$\frac{\sigma_t}{\sqrt{f'_c}}$ (Exp)	$\frac{\sigma_t}{\sqrt{f'_c}}$ (ANN)	$\frac{\text{ANN}}{\text{Exp}}$	v (Exp)	v (ANN)	$\frac{\text{ANN}}{\text{Exp}}$	V (Exp)	V (ANN)	$\frac{\text{ANN}}{\text{Exp}}$
Sezen [2]	1	21.1	3.19	0.19	0.11	0.58	1.90	1.39	0.73	315	229	0.73
	2	21.1	12.8	0.08	0.11	1.48	2.15	2.62	1.22	359	439	1.22
	3	20.9	10.7	0.06	0.11	1.72	1.80	2.39	1.32	301	399	1.32
	4	21.8	3.19	0.17	0.12	0.68	1.80	1.43	0.80	294	234	0.80
Lynn [26]	3CLH18	25.6	2.41	0.16	0.14	0.87	1.63	1.50	0.92	272	250	0.92
	3SLH18	25.6	2.41	0.16	0.14	0.87	1.63	1.50	0.92	273	250	0.92
	2CLH18	33.1	2.41	0.18	0.10	0.58	1.89	1.35	0.71	243	173	0.71
	2SLH18	33.1	2.41	0.12	0.10	0.91	1.43	1.35	0.94	231	218	0.94

	2CMH18	25.7	7.24	0.09	0.09	1.07	1.84	1.91	1.04	308	319	1.04
	3CMH18	27.6	7.24	0.09	0.13	1.42	1.96	2.36	1.21	327	395	1.21
	3CMD12	27.6	7.24	0.11	0.11	0.97	2.13	2.10	0.99	356	351	0.99
	3SMD12	25.7	7.24	0.12	0.12	0.96	2.20	2.15	0.98	367	359	0.98
Ohue et al. [47]	2D16RS	32.1	4.58	0.32	0.33	1.02	3.41	3.45	1.01	102	103	1.01
	4D13RS	29.9	4.58	0.34	0.34	0.97	3.49	3.43	0.98	111	109	0.98
Esaki [48]	H-2-1/5	23.0	4.03	0.47	0.41	0.87	3.79	3.44	0.91	103	94	0.91
	HT-2-1/5	20.2	4.03	0.44	0.44	1.00	3.46	3.47	1.00	102	102	1.00
	H-2-1/3	23.0	6.73	0.37	0.37	0.99	3.88	3.86	0.99	121	120	0.99
	HT-2-1/3	20.2	5.90	0.38	0.42	1.09	3.63	3.82	1.05	112	118	1.05
Li [49]	U-7	29.0	2.90	0.35	0.22	0.63	3.01	2.21	0.73	328	240	0.73
	U-8	33.5	6.70	0.21	0.21	1.01	3.07	3.08	1.00	393	395	1.00
	U-9	34.1	10.23	0.20	0.22	1.09	3.62	3.80	1.05	430	451	1.05
Saatcioglu and Ozcebe [50]	U1	43.6	0.00	0.45	0.18	0.39	2.95	1.16	0.39	275	108	0.39
	U2	30.2	4.90	0.23	0.23	1.02	2.76	2.78	1.01	270	272	1.01
	U3	34.8	4.90	0.21	0.30	1.43	2.73	3.40	1.24	268	334	1.24
Yalcin [51]	BR-S1	44.8	5.95	0.13	0.13	1.01	2.39	2.40	1.01	578	581	1.01
Hirosawa [52]	43	19.6	1.95	0.39	0.34	0.85	2.54	2.27	0.89	74	66	0.89
	44	19.6	1.95	0.38	0.34	0.89	2.48	2.27	0.92	77	70	0.92
	45	19.6	3.90	0.29	0.34	1.17	2.57	2.84	1.10	82	91	1.10
	46	19.6	3.90	0.28	0.34	1.21	2.52	2.84	1.13	81	91	1.13
	62	19.6	1.95	0.27	0.25	0.94	1.93	1.85	0.96	58	55	0.96
	63	19.6	3.90	0.27	0.25	0.92	2.49	2.36	0.95	69	65	0.95
	64	19.6	3.90	0.23	0.25	1.08	2.25	2.36	1.05	69	72	1.05
Hirosawa [52]	205	17.7	3.90	0.26	0.27	1.05	2.32	2.39	1.03	71	73	1.03
	207	17.7	3.90	0.45	0.42	0.93	3.31	3.15	0.95	106	101	0.95
	208	17.7	9.80	0.43	0.42	0.98	4.56	4.50	0.99	135	133	0.99
	214	17.7	9.80	0.15	0.15	0.98	2.58	2.56	0.99	83	82	0.99
	220	32.9	3.90	0.32	0.33	1.01	3.27	3.29	1.01	78	79	1.01
	231	14.8	3.90	0.20	0.20	1.00	1.87	1.88	1.00	51	51	1.00
	232	13.1	3.90	0.23	0.20	0.86	1.99	1.83	0.92	58	53	0.92
	233	13.9	3.90	0.36	0.38	1.05	2.65	2.73	1.03	69	71	1.03
	234	13.1	3.90	0.40	0.38	0.95	2.80	2.71	0.97	67	65	0.97
Xiao and Martirossyan [53]	T6-0.1P	86.0	8.28	0.41	0.42	1.00	6.83	6.83	1.00	273	273	1.00
	T6-0.2P	86.0	16.55	0.28	0.42	1.48	7.07	8.86	1.25	324	406	1.25
Wight James and Sozen Mete [20]	3E	34.7	4.08	0.23	0.24	1.03	2.73	2.77	1.02	94	95	1.02
	3W	34.7	4.08	0.25	0.24	0.95	2.87	2.77	0.97	98	95	0.97
	8E	26.1	3.84	0.35	0.34	0.95	3.18	3.09	0.97	101	98	0.97
	8W	26.1	3.84	0.34	0.34	0.99	3.11	3.09	0.99	95	94	0.99
	3E	33.6	4.08	0.22	0.24	1.12	2.59	2.77	1.07	91	97	1.07
	3W	33.6	4.08	0.26	0.24	0.93	2.91	2.77	0.95	101	96	0.95
	3E	33.6	2.39	0.25	0.24	0.96	2.38	2.31	0.97	85	83	0.97
	3W	33.6	2.39	0.27	0.24	0.88	2.51	2.31	0.92	91	84	0.92
	7E	33.4	3.84	0.28	0.30	1.09	2.96	3.13	1.06	86	91	1.06
	7W	33.4	3.84	0.29	0.30	1.03	3.07	3.13	1.02	92	94	1.02
	2E	33.5	3.84	0.42	0.41	0.99	3.89	3.86	0.99	108	107	0.99
	2W	33.5	3.84	0.41	0.41	1.00	3.87	3.86	1.00	113	113	1.00
Yoshimura [54]	N18M	26.5	4.77	0.43	0.43	0.99	3.96	3.92	0.99	263	261	0.99
	N18C	26.5	4.77	0.50	0.43	0.86	4.34	3.92	0.90	264	239	0.90
	N27M	26.5	7.17	0.50	0.43	0.87	4.98	4.55	0.91	288	263	0.91

	N27C	26.5	7.17	0.31	0.43	1.37	3.76	4.55	1.21	263	318	1.21
	2M	25.2	4.78	0.48	0.48	0.99	4.18	4.14	0.99	234	232	0.99
	2C	25.2	4.78	0.52	0.48	0.91	4.40	4.14	0.94	222	209	0.94
	3M	25.2	7.08	0.46	0.48	1.05	4.63	4.76	1.03	248	255	1.03
	3C	25.2	7.08	0.53	0.48	0.90	5.10	4.76	0.93	264	246	0.93
	2M13	25.2	4.78	0.41	0.41	0.99	3.78	3.75	0.99	250	248	0.99
	2C13	25.2	4.78	0.55	0.41	0.75	4.56	3.75	0.82	260	214	0.82
Yoshimura et al. [55]	No.1	30.7	6.14	0.27	0.29	1.05	3.41	3.50	1.03	234	240	1.03
	No.2	30.7	6.14	0.27	0.25	0.95	3.36	3.26	0.97	230	223	0.97
	No.3	30.7	6.14	0.26	0.22	0.85	3.33	3.02	0.91	230	208	0.91
	No.4	30.7	9.21	0.24	0.29	1.17	3.78	4.14	1.09	261	286	1.09
	No.5	30.7	10.75	0.32	0.29	0.89	4.72	4.42	0.94	275	258	0.94
	No.6	30.7	6.14	0.29	0.30	1.03	3.56	3.63	1.02	219	223	1.02
	No.7	30.7	6.14	0.26	0.25	0.97	3.31	3.24	0.98	213	209	0.98
Nakamura and Yoshimura [56]	C13-J	22.0	4.40	0.27	0.29	1.09	2.65	2.79	1.05	191	201	1.05
	C13-T	22.0	4.40	0.29	0.29	1.00	2.79	2.79	1.00	201	201	1.00
	C13-H	22.0	4.40	0.31	0.29	0.92	2.94	2.79	0.95	212	201	0.95
	4J11	19.5	3.32	0.31	0.32	1.03	2.55	2.60	1.02	413	421	1.02
	4W11	19.5	3.32	0.34	0.32	0.96	2.67	2.60	0.97	432	421	0.97
	4H11	19.5	3.32	0.29	0.32	1.10	2.44	2.60	1.07	395	421	1.07
	6J11	19.5	3.32	0.34	0.32	0.95	2.69	2.60	0.96	436	421	0.96
	4J21	19.5	3.32	0.35	0.33	0.92	2.76	2.62	0.95	447	424	0.95
	4W21	19.5	3.32	0.33	0.33	0.98	2.65	2.62	0.99	429	424	0.99
	6J21	19.5	3.32	0.34	0.33	0.97	2.68	2.62	0.98	434	424	0.98
Nakamura and Yoshimura [57]	A1	28.0	4.48	0.36	0.36	0.98	3.52	3.48	0.99	570	564	0.99
	A2	28.0	4.48	0.35	0.36	1.02	3.44	3.48	1.01	557	564	1.01
	B1	28.0	4.48	0.39	0.37	0.96	3.67	3.58	0.98	594	580	0.98
	B2	28.0	4.48	0.40	0.37	0.93	3.75	3.58	0.95	607	580	0.95
	B3	28.0	4.48	0.34	0.37	1.10	3.36	3.58	1.06	545	580	1.06
	B4	28.0	4.48	0.37	0.37	1.00	3.57	3.58	1.00	578	580	1.00
	B5	28.0	4.48	0.36	0.37	1.04	3.49	3.58	1.03	565	580	1.03
	C1	28.0	4.48	0.48	0.50	1.04	4.24	4.37	1.03	687	708	1.03
	C2	28.0	4.48	0.51	0.50	0.99	4.41	4.37	0.99	715	708	0.99
	S100	25.0	4.50	0.34	0.34	1.02	3.22	3.27	1.01	522	529	1.01
	S60	25.0	4.50	0.39	0.34	0.87	3.56	3.27	0.92	577	529	0.92
	S40	25.0	4.50	0.32	0.34	1.08	3.12	3.27	1.05	505	529	1.05
	S20	25.0	4.50	0.38	0.34	0.91	3.47	3.27	0.94	562	529	0.94
	L100	25.0	4.50	0.32	0.33	1.03	3.12	3.18	1.02	506	516	1.02
	L75	25.0	4.50	0.34	0.33	0.97	3.25	3.18	0.98	526	516	0.98
	L50	25.0	4.50	0.31	0.33	1.06	3.07	3.18	1.04	497	516	1.04
Moretti and Tassios [32]	1	36.0	10.80	0.52	0.41	0.80	6.60	5.75	0.87	330	288	0.87
	3	39.0	11.70	0.55	0.56	1.02	7.20	7.27	1.01	360	363	1.01
	4	35.0	10.50	0.62	0.61	0.98	7.20	7.12	0.99	360	356	0.99
	7	38.0	11.40	0.24	0.20	0.82	4.40	3.94	0.90	200	179	0.90
	8	38.0	11.40	0.13	0.14	1.04	3.13	3.19	1.02	140	143	1.02
Li et al. [58]	1DL	27.5	2.48	0.90	0.63	0.70	5.82	4.38	0.75	698	525	0.75
	1DH	25.2	7.31	0.64	0.64	1.00	5.84	5.83	1.00	701	699	1.00
	1NL	23.4	2.34	0.92	0.72	0.79	5.50	4.52	0.82	660	543	0.82
	1NH	25.1	7.28	0.73	0.72	1.00	6.31	6.29	1.00	757	755	1.00
	2DL	25.7	2.31	0.73	0.61	0.84	4.70	4.09	0.87	564	491	0.87

	2DH	24.4	7.32	0.50	0.62	1.24	4.91	5.62	1.15	589	674	1.15
	1NL	23.4	2.34	0.49	0.31	0.63	3.35	2.40	0.72	402	288	0.72
	2NH	25.5	7.40	0.32	0.32	0.98	3.83	3.79	0.99	460	455	0.99
Ramirez and Jirsa [59]	00-U	34.5	0.00	0.64	0.50	0.79	3.74	2.95	0.79	266	210	0.79
	120C-U	34.5	5.74	0.38	0.50	1.31	4.23	5.06	1.20	298	356	1.20
Bett et al. [60]	SF1	29.9	3.10	0.31	0.32	1.01	2.88	2.89	1.01	214	215	1.01
Hirosawa [52]	372	20.0	6.03	0.23	0.23	1.01	2.70	2.72	1.00	74	75	1.00
	373	20.4	6.03	0.26	0.30	1.16	2.89	3.15	1.09	88	96	1.09
Hirosawa [52]	452	21.9	9.78	0.24	0.24	1.01	3.47	3.48	1.00	110	111	1.00
	454	21.9	9.78	0.24	0.24	1.01	3.50	3.52	1.01	110	111	1.01
Umehara [61]	CUS	34.9	5.66	0.39	0.27	0.70	4.29	3.42	0.80	324	258	0.80
	CUW	34.9	5.66	0.28	0.28	0.99	3.51	3.48	0.99	265	263	0.99
	2CUS	42.0	11.33	0.34	0.35	1.02	5.46	5.53	1.01	412	417	1.01
Ousalem et al. [62]	C1	13.5	4.05	0.33	0.34	1.01	2.54	2.56	1.01	160	161	1.01
	C4	13.5	4.05	0.42	0.34	0.80	2.94	2.56	0.87	171	149	0.87
	C6	13.5	17.26	0.26	0.34	1.30	4.24	4.78	1.13	204	230	1.13
	C8	18.0	5.40	0.46	0.35	0.77	3.77	3.20	0.85	233	198	0.85
	C10	18.0	18.89	0.24	0.35	1.47	4.50	5.51	1.23	262	321	1.23
	C12	18.0	3.60	0.58	0.35	0.60	3.87	2.75	0.71	217	155	0.71
	D1	27.7	6.00	0.58	0.59	1.03	5.24	5.33	1.02	341	347	1.02
	D16	26.1	6.00	0.61	0.60	0.98	5.35	5.26	0.98	342	336	0.98
	D11	28.2	6.00	0.39	0.38	0.99	4.06	4.02	0.99	243	241	0.99
	D12	28.2	6.00	0.39	0.38	0.97	4.09	4.02	0.98	250	246	0.98
	D13	26.1	6.00	0.47	0.50	1.06	4.48	4.65	1.04	266	276	1.04
	D14	26.1	6.00	0.50	0.50	1.00	4.66	4.65	1.00	269	269	1.00
Aboutaha et al. [63]	SC3	21.9	0.00	0.25	0.25	0.99	1.19	1.18	0.99	394	390	0.99
	SC9	21.9	0.00	0.38	0.37	0.99	1.76	1.74	0.99	587	582	0.99
Woods [64]	1	33.0	10.64	0.09	0.10	1.04	2.46	2.51	1.02	412	420	1.02
	2	33.0	7.24	0.10	0.10	0.95	2.15	2.10	0.97	360	351	0.97
	3	33.0	10.64	0.06	0.06	1.04	1.87	1.91	1.02	313	319	1.02
Pan and Li [27]	SC-2.4-0.20	22.6	4.52	0.19	0.13	0.65	2.23	1.75	0.78	219	172	0.78
	SC-2.4-0.30	49.3	14.79	0.13	0.13	0.99	3.75	3.74	1.00	357	356	1.00
	SC-2.4-0.50	24.2	12.10	0.10	0.14	1.50	2.43	3.00	1.23	238	293	1.23
	SC-1.7-0.05	29.8	1.49	0.40	0.31	0.78	2.82	2.31	0.82	276	227	0.82
	SC-1.7-0.20	27.5	5.50	0.25	0.28	1.10	3.00	3.18	1.06	294	312	1.06
	SC-1.7-0.35	25.5	8.93	0.23	0.25	1.10	3.42	3.61	1.05	336	354	1.05
	SC-1.7-0.50	26.4	13.20	0.20	0.26	1.31	3.83	4.44	1.16	376	435	1.16
	RC-1.7-0.05	32.5	1.63	0.38	0.34	0.88	2.89	2.63	0.91	283	257	0.91
	RC-1.7-0.20	24.5	4.90	0.31	0.24	0.78	3.12	2.68	0.86	306	262	0.86
	RC-1.7-0.35	27.1	9.49	0.22	0.27	1.20	3.53	3.90	1.11	346	382	1.11
	RC-1.7-0.50	26.8	13.40	0.18	0.26	1.47	3.65	4.50	1.23	355	437	1.23
Boys et al. [65]	24L-300-2D	32.0	9.88	0.05	0.06	1.04	1.78	1.81	1.02	256	261	1.02
Kogoma et al. [66]	SF1	22.8	4.10	0.15	0.15	1.02	1.84	1.86	1.01	25	25	1.01
Choi et al. [67]	NRC 1	17.9	4.83	0.10	0.10	0.96	1.51	1.48	0.98	109	107	0.98
	NRC 2	18.3	4.76	0.10	0.09	0.92	1.52	1.44	0.95	109	104	0.95
	NRC 3	17.5	4.90	0.12	0.12	1.05	1.61	1.65	1.03	116	119	1.03
	NRC 5	19.9	7.56	0.09	0.08	0.91	1.78	1.69	0.95	128	122	0.95
	NRC 6	17.2	5.33	0.16	0.17	1.06	1.99	2.05	1.03	141	145	1.03
	NRC 7	12.7	3.94	0.19	0.25	1.32	1.78	2.09	1.17	122	144	1.17
	NRC 8	12.1	3.99	0.21	0.25	1.20	1.87	2.07	1.11	127	141	1.11

	NRC 9	13.0	1.30	0.44	0.25	0.58	2.13	1.42	0.67	113	76	0.67
	NRC 10	13.6	5.98	0.18	0.25	1.39	2.11	2.55	1.20	140	169	1.20
Ghannoum Wassim and Moehle Jack [68]	ColA1	24.6	4.18	0.13	0.13	1.01	1.74	1.76	1.01	32	32	1.01
	ColB1	24.6	4.67	0.20	0.13	0.65	2.38	1.85	0.78	44	34	0.78
Elwood and Moehle [69]	EL_sp1	24.5	2.45	0.21	0.21	1.00	1.92	1.92	1.00	81	81	1.00
	EL_sp2	23.9	5.74	0.14	0.21	1.52	2.10	2.66	1.27	88	112	1.27
					Mean	0.997		Mean	0.988		Mean	0.988
					SD	0.191		SD	0.120		SD	0.120

Fig. 5 compares the principal tensile stress $\sigma_t/\sqrt{f'_c}$: predicted by the ANN with the experimental results. Among the 114 samples randomly selected for network training, in more than 85 samples, the difference between the principal tensile stress predicted by the ANN and the laboratory results is less than 0.005. For the remaining training samples, the network prediction accuracy is still considered acceptable. The maximum difference in these training samples is 0.261. Among the 25 samples selected for network validation, only 4 samples exhibited a difference between the principal tensile stress $\sigma_t/\sqrt{f'_c}$: predicted by the ANN and the experimental results greater than 0.1, with the maximum difference being 0.261. Similarly, of the 25 samples selected for network testing, only 3 column specimens showed a difference between the principal tensile stress $\sigma_t/\sqrt{f'_c}$: predicted by the ANN and the experimental results exceeding 0.1. The maximum difference in these samples is 0.18. As a result, it can be concluded that the trained artificial neural network (ANN) predicts the experimental results with satisfactory accuracy.

Fig. 6 compares the results predicted by the trained ANN with the experimental data. It should be noted that another factor for selecting an appropriate network is the regression coefficient (R) of the network. The regression coefficient measures the correlation between the outputs and targets in an ANN, where R = 1 indicates a perfect correlation, and R = 0 indicates a random relationship. As shown previously, the ANN predicts the experimental results with high accuracy, and this figure demonstrates the consistency of the predictions across all training, validation, and test samples.

Table 2 compares the responses of the experimental column specimens in terms of principal tensile stress, shear strength, and shear force with the results from the ANN and the analytical model. As observed, the experimental column responses in terms of principal tensile stress are predicted by the ANN with a mean value of 0.997 and a standard deviation of 0.191, confirming an accurate and nearly uniform prediction of the column behavior. Using Eq. 12, the principal tensile stress can be converted to the horizontal shear capacity. The mean value of 0.988 and standard deviation of 0.120 indicate a more uniform prediction of shear strength compared to principal tensile stress. The column shear strength can be further converted into the column shear force using Eq. 10. Finally, considering the mean value of 0.988 and standard deviation of 0.120, it can be concluded that the trained ANN, combined with theoretical relationships, can accurately and consistently predict the column shear force. The capability of the proposed model will next be compared with other shear models presented in the literature.

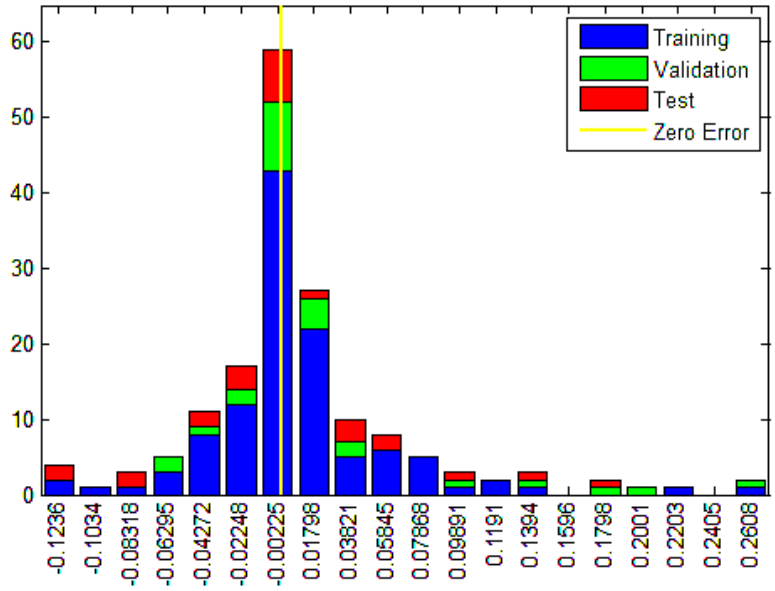

Fig. 5. Comparison of principal tensile stress predicted by the ANN with experimental results for training specimens. The vertical axis represents predicted values from the ANN, while the horizontal axis represents experimental values.

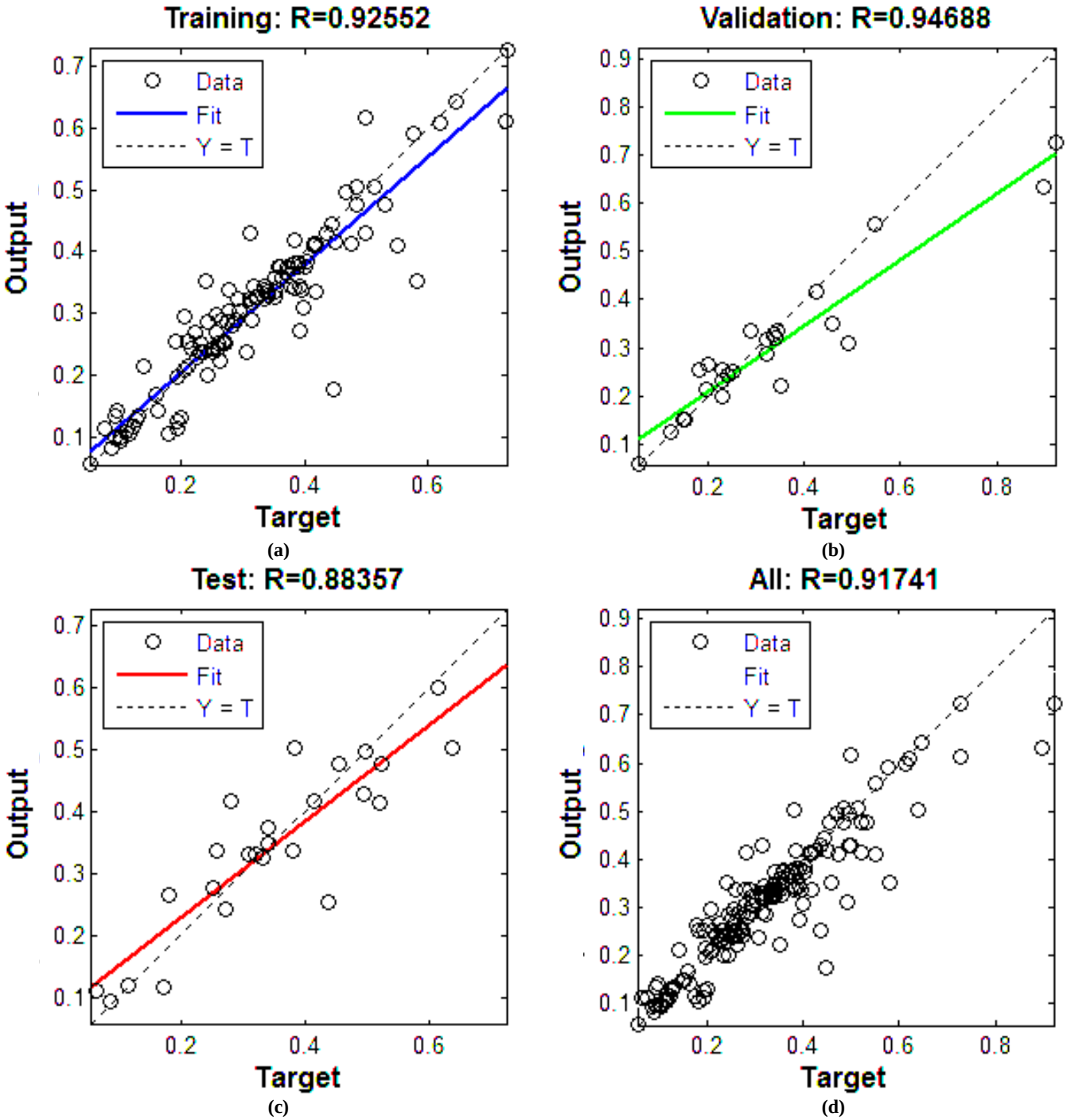

Fig. 6. Predictive performance for the proposed ANN model based on: a) data used for training; b) data used for validation; c) data used for testing; d) all data.

3.4. Comparison with existing models

The proposed ANN-based shear model was benchmarked against existing analytical shear strength models in the literature [22, 23, 46, 53, 70-73]. As shown in Fig. 7, an evaluation of the mean values and coefficients of variation indicates that the artificial neural network (ANN) model predicts the experimental results with a higher degree of consistency and accuracy compared to other existing models (see Table 2). The ANN model not only captures the central tendency of the experimental data but also demonstrates reduced scatter in its predictions, which reflects a more reliable representation of the reinforced concrete columns' behavior under shear-dominated loading conditions. It is worth noting that the shear model proposed by Sezen and Moehle Jack [46], with a mean value of 1.083 and a coefficient of variation of 0.252, performs better than other traditional shear models in terms of both accuracy and uniformity of predictions. However, when compared to the ANN model, the proposed approach offers an even more consistent performance across the entire dataset, reducing variability and providing improved predictive reliability. Based on this comparative assessment, it can be concluded that the proposed ANN-based model demonstrates satisfactory reliability in predicting the behavior of reinforced concrete columns subjected to shear forces. Its ability to consistently approximate both the peak response and the overall trend of experimental results highlights its potential as a robust and practical tool for structural analysis and design, particularly in situations where accurate estimation of shear capacity and post-peak behavior is critical.

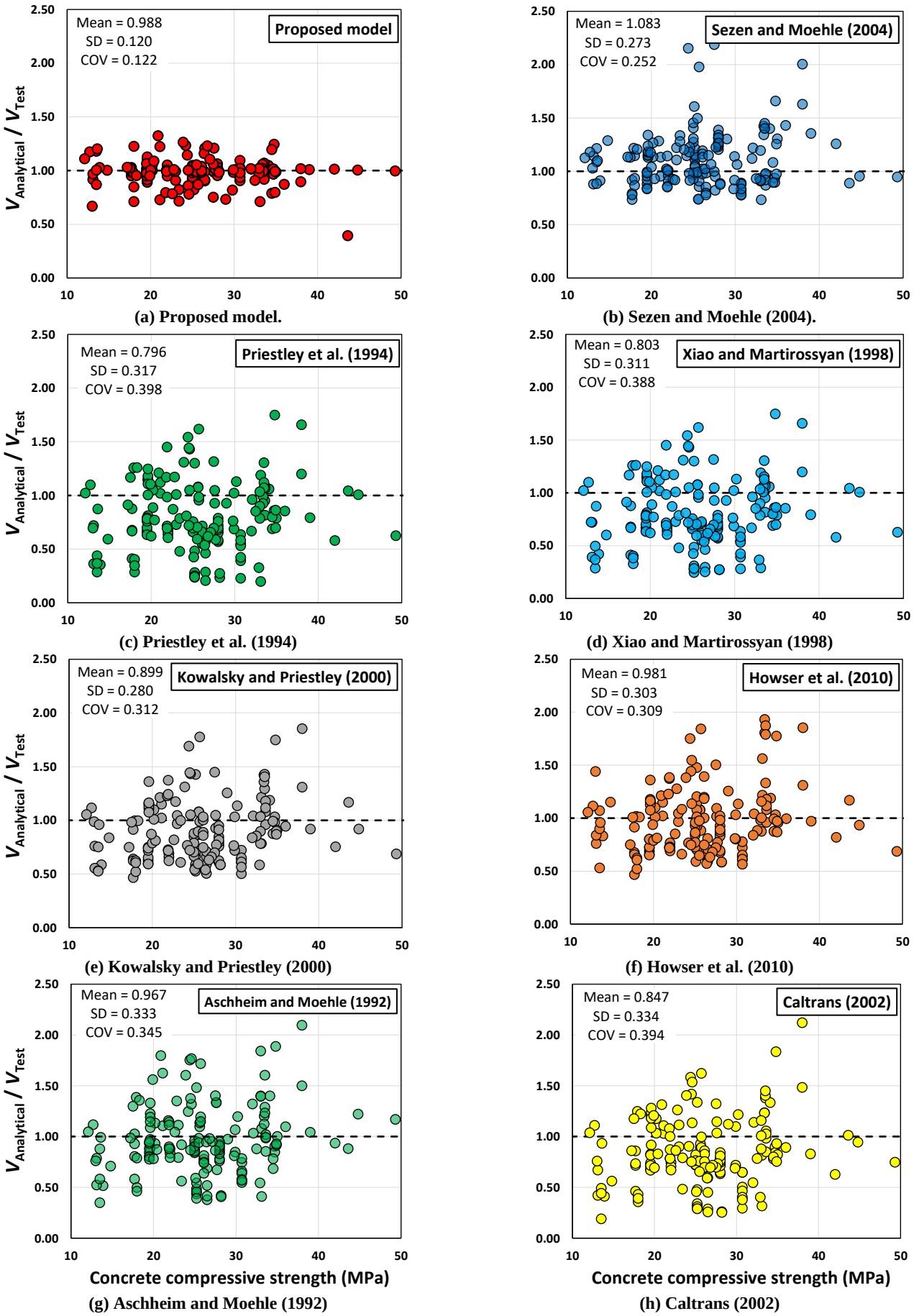

(a) Proposed model. (b) Sezen and Moehle (2004). (c) Priestley et al. (1994) (d) Xiao and Martirossyan (1998) (e) Kowalsky and Priestley (2000) (f) Howser et al. (2010) (g) Aschheim and Moehle (1992) (h) Caltrans (2002)

Fig. 7. Comparison of shear strength predictions from the proposed ANN model with existing analytical models and experimental results [22, 23, 46, 53, 70-73].

Fig. 8 illustrates the validation of the proposed model against the experimental results reported by Lynn [26], focusing on the load-displacement behavior of reinforced concrete columns up to the point of shear failure. In this study, the shear capacity of the columns was evaluated using the proposed analytical model, which incorporates the governing equations, underlying assumptions,

and numerical implementation described in the preceding sections. The flexural response, on the other hand, was obtained through a moment–curvature analysis based on the lumped plastic hinge concept. This approach allows the nonlinear flexural behavior to be represented by concentrated rotation at the member ends, while maintaining linear elasticity along the remaining length. The resulting moment–curvature relationships were subsequently converted into load–displacement responses by defining the hinge locations and their corresponding rotational capacities. This combined modeling framework enables a consistent and accurate representation of both shear- and flexure-dominated behaviors in reinforced concrete columns. As shown in Fig. 8, the simulated load–displacement curves generated by the proposed model closely follow the experimental data across the entire range, from the initial elastic response to the post-peak behavior. This close agreement demonstrates the model's capability to accurately capture key structural characteristics, including the initial stiffness, peak load, and post-peak ductility of the columns, which are critical for evaluating the performance of reinforced concrete members subjected to shear-dominated failure modes. Notably, while specimen 2CMH18 exhibited a predominantly flexural failure mode in the experiments, the proposed model was still able to replicate its response with a high degree of accuracy. Specifically, the model successfully predicted the strength, the initial stiffness of the member, and its overall ductility, highlighting the robustness of the modeling approach in capturing both shear- and flexure-dominated behaviors. By contrast, the Sezen and Moehle Jack [46] model provides a more conservative estimate of the experimental results. The predicted peak load is approximately 50% lower than the observed experimental values, and the location of failure is estimated within the elastic range of the load–displacement curve, rather than near the actual failure point observed in the experiments. This discrepancy indicates that, although the Sezen and Moehle Jack [46] model can offer a safe conservative assessment, it does not accurately capture the actual behavior of reinforced concrete columns under shear-dominated failure. Overall, the comparison highlights that the proposed model not only predicts the peak strength with higher accuracy but also provides a more realistic representation of the entire load–displacement response. This demonstrates the model's effectiveness as a predictive tool for reinforced concrete columns, particularly in post-fire or retrofitted scenarios where accurate evaluation of both shear and flexural responses is essential for structural safety and reliability.

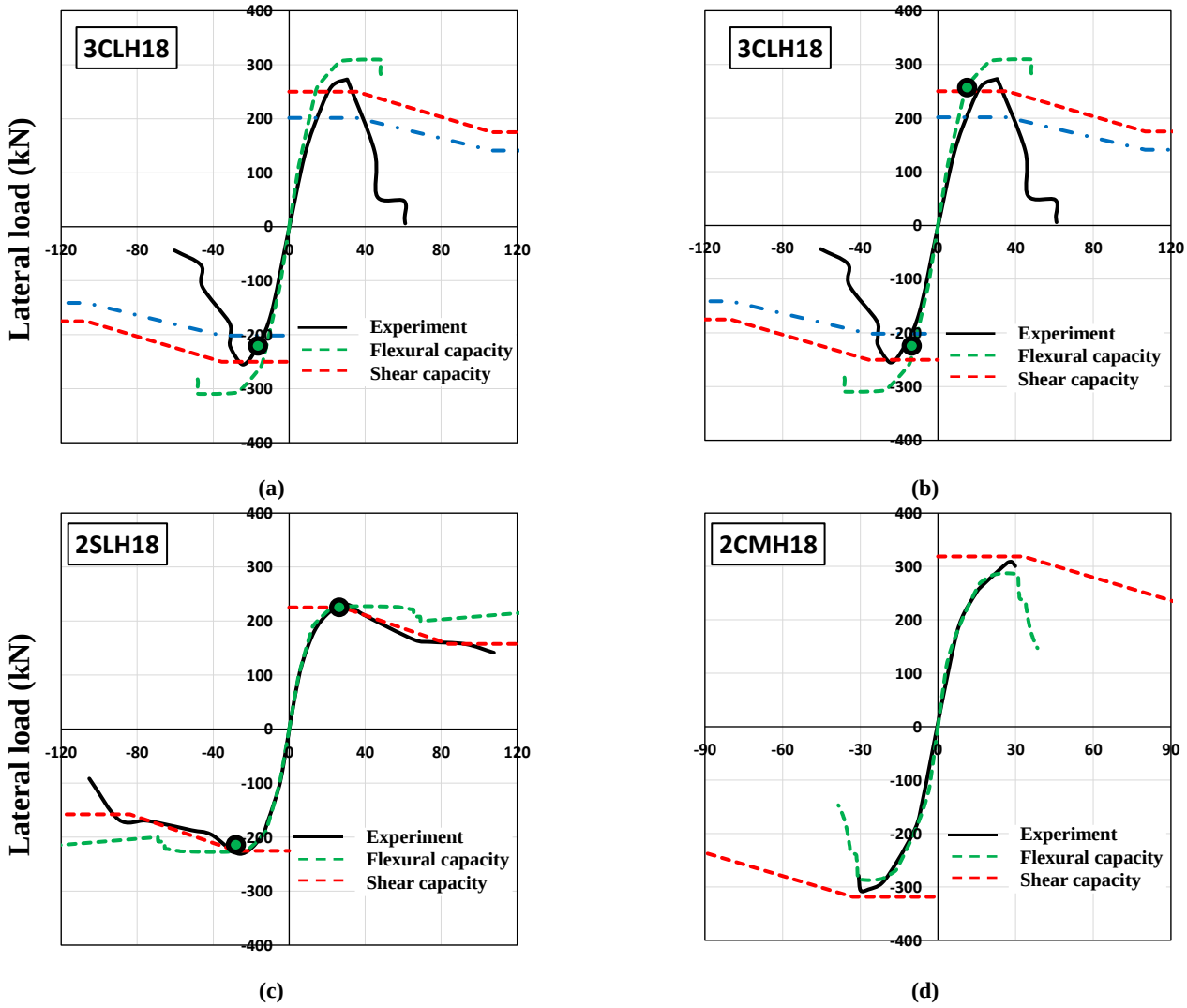

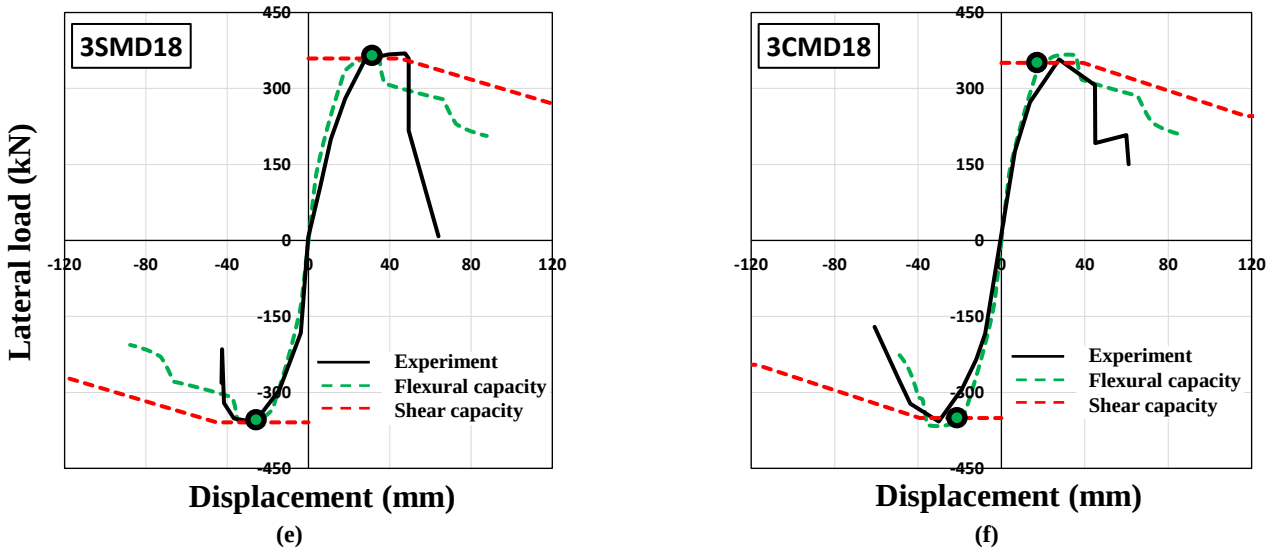

Fig. 8. Validation of the proposed ANN model against experimental load–displacement responses of RC columns [26].

4. Conclusion

This study investigated the nonlinear flexural–shear behavior of reinforced concrete (RC) columns designed according to older seismic codes, which often exhibit insufficient shear capacity and are vulnerable to brittle shear or flexure–shear failures during seismic events. The key contributions and findings of this research are summarized below:

- A comprehensive shear model was developed based on Mohr's circle, incorporating both compressive and tensile principal stress surfaces. The model was further extended to capture the degradation of shear capacity as a function of flexural deformations through a displacement ductility-dependent parameter, enabling a more realistic representation of the shear behavior under seismic loading.

- An artificial neural network (ANN) was trained using a database of 164 RC column specimens exhibiting shear or flexure–shear failure modes. The ANN effectively learned the nonlinear interaction between geometric, material, and loading parameters, accurately predicting the principal tensile stress and shear strength. The model demonstrated high accuracy and uniformity across training, validation, and testing datasets.

- When compared with existing analytical models available in the literature, the ANN-based model provided more consistent and reliable predictions of shear strength. Statistical analyses of mean values and coefficients of variation confirmed the superior performance of the proposed model in replicating experimental observations.

Overall, the proposed framework, which combines analytical modeling with data-driven ANN approaches, provides a robust and accurate tool for predicting the nonlinear shear response of RC columns. This can support more reliable seismic assessment and retrofit strategies for existing structures designed according to outdated seismic codes.

Statements & Declarations

Author contributions

Maedeh Sadeghpour Haji: Project administration, Resources, Writing – Review & Editing.

Reza Niknam: Investigation, Formal analysis, Data curation, Software, Writing – Original Draft.

Javad Shayanfar: Conceptualization, Methodology, Software, Writing – Review & Editing.

Funding

The authors received no financial support for the research, authorship, and/or publication of this article.

Data availability

The data presented in this study will be available on interested request from the corresponding author.

Declarations

The authors declare no conflict of interes.

References

[1] Steinbrugge, K. V. NISEE e-Library, The Earthquake Engineering Online Archive. 1964. Available online: https://nisee.berkeley.edu/elibrary/search?in=0&ss=Steinbrugge&start=571 (accessed on December 2025).

[2] Sezen, H. Seismic behavior and modeling of reinforced concrete building columns (PhD Thesis). Berkeley (CA): University of California Berkley; 2002.

[3] Shayanfar, J., Akbarzadeh Bengar, H. Nonlinear analysis of RC frames considering shear behaviour of members under varying axial load. Bulletin of Earthquake Engineering, 2017; 15: 2055-2078. doi:10.1007/s10518-016-0060-z.

[4] Shayanfar, J., Bengar, H. A., Parvin, A. Analytical prediction of seismic behavior of RC joints and columns under varying axial load. Engineering Structures, 2018; 174: 792-813. doi:10.1016/j.engstruct.2018.07.103.

[5] Shayanfar, J., Hemmati, A., Bengar, H. A. A simplified numerical model to simulate RC beam–column joints collapse. Bulletin of Earthquake Engineering, 2019; 17: 803-844. doi:10.1007/s10518-018-0472-z.

[6] Shayanfar, J., Bengar, H. A. Numerical model to simulate shear behaviour of RC joints and columns. Computers and Concrete, An International Journal, 2016; 18: 877-901. doi:10.12989/cac.2016.18.4.877.

[7] Shayanfar, J., Akbarzadeh Bengar, H., Niroomandi, A. A proposed model for predicting nonlinear behavior of RC joints under seismic loads. Materials & Design, 2016; 95: 563-579. doi:10.1016/j.matdes.2016.01.098.

[8] John, S. K., Cascardi, A., Verre, S., Nadir, Y. RC-columns subjected to lateral cyclic force with different FRCM-strengthening schemes: experimental and numerical investigation. Bulletin of Earthquake Engineering, 2025; 23: 1561-1590. doi:10.1007/s10518-025-02100-5.

[9] Shayanfar, J., Barros Joaquim, A. O., Rezazadeh, M. Stress–Strain Model for FRP-Confined Circular Concrete Columns Developing Structural Softening Behavior. Journal of Composites for Construction, 2024; 28: 04023065. doi:10.1061/JCCOF2.CCENG-4364.

[10] Işık, E., Radu, D., Harirchian, E., Avcil, F., Arkan, E., Büyüksaraç, A., Hadzima-Nyarko, M. Failures in Reinforced-Concrete Columns and Proposals for Reinforcement Solutions: Insights from the 2023 Kahramanmaraş Earthquakes. Buildings, 2025; 15: 1535.

[11] Nematzadeh, M., Mousavimehr, M., Shayanfar, J., Omidalizadeh, M. Eccentric compressive behavior of steel fiber-reinforced RC columns strengthened with CFRP wraps: Experimental investigation and analytical modeling. Engineering Structures, 2021; 226: 111389. doi:10.1016/j.engstruct.2020.111389.

[12] Shayanfar, J., Barros, J. A. O., Rezazadeh, M. Analytical model to predict axial stress-strain behavior of heat-damaged unreinforced concrete columns wrapped by FRP jacket. Engineering Structures, 2023; 289: 116244. doi:10.1016/j.engstruct.2023.116244.

[13] Wang, J., Xiao, H., Lu, L., Yang, J., Lu, S., Shayanfar, J. Axial stress-strain model for concrete in partially FRP wrapped reinforced concrete columns. Construction and Building Materials, 2024; 416: 135028. doi:10.1016/j.conbuildmat.2024.135028.

[14] Shayanfar, J., Barros Joaquim, A. O., Abedi, M., Rezazadeh, M. Unified Compressive Strength and Strain Ductility Models for Fully and Partially FRP-Confined Circular, Square, and Rectangular Concrete Columns. Journal of Composites for Construction, 2023; 27: 04023053. doi:10.1061/JCCOF2.CCENG-4336.

[15] Zhao, Y., Zhang, X., Zhuang, X. Seismic performance of squared lap-spliced RC columns strengthened by active confinement technique under quasi-static cyclic load. Structures, 2025; 74: 108622. doi:10.1016/j.istruc.2025.108622.

[16] Shayanfar, J., Barros, J. A. O., Rezazadeh, M. Cross-sectional and confining system unification on peak compressive strength of FRP confined concrete. Structural Concrete, 2023; 24: 1531-1545. doi:10.1002/suco.202200105.

[17] Baldwin, J., Viest, I. Effect of Axial Compression on Shear Strength of Reinforced Concrete Frame Members. ACI Journal Proceedings, 1958; 55: 635-654. doi:10.14359/11379.

[18] Yamad, M. Shear Strength, Deformation and Explosion of Reinforced Concrete Short Columns. American Concrete Institute (ACI), 1974; 42: 617-640. doi:10.14359/17304.

[19] Elzanaty, A. H., Nilson, A. H., Slate, F. O. Shear capacity of reinforced concrete beams using high-strength concrete. In: ACI Journal Proceedings; 1986; p. 290-296. doi:10.14359/10432.

[20] Wight James, K., Sozen Mete, A. Strength Decay of RC Columns under Shear Reversals. Journal of the Structural Division, 1975; 101: 1053-1065. doi:10.1061/JSDEAG.0004048.

[21] Woodward Kyle, A., Jirsa James, O. Influence of Reinforcement on RC Short Column Lateral Resistance. Journal of Structural Engineering, 1984; 110: 90-104. doi:10.1061/(ASCE)0733-9445(1984)110:1(90).

[22] Ascheim, M., Moehle, J. Shear strength and deformability of RC bridge columns subjected to inelastic cyclic displacements. Berkeley (CA): Earthquake Engineering Research Center, University of California, Berkeley; 1992. Report No.: UCB/EERC-92/04.

[23] Ghee, A. B., Priestley, M. J. N., Paulay, T. Seismic Shear Strength of Circular Reinforced Concrete Columns. ACI Structural Journal, 1989; 86: 45-59. doi:10.14359/2634.

[24] Yuk-Lung Wong, T. P., Priestley, M. J. N. Response of Circular Reinforced Concrete Columns to Multi-Directional Seismic Attack. ACI Structural Journal, 1993; 90: 180-191. doi:10.14359/4124.

[25] Bengar, H. A., Kiadehi, M. A., Shayanfar, J., Nazari, M. Effective flexural rigidities for RC beams and columns with steel fiber. Steel and Composite Structures, An International Journal, 2020; 34: 453-465. doi:10.12989/scs.2020.34.3.453.

[26] Lynn, A. C. Seismic evaluation of existing reinforced concrete building columns (PhD Thesis). Berkeley (CA): University of California, Berkeley; 2001.

[27] Pan, Z., Li, B. Truss-Arch Model for Shear Strength of Shear-Critical Reinforced Concrete Columns. Journal of Structural Engineering, 2013; 139: 548-560. doi:10.1061/(ASCE)ST.1943-541X.0000677.

[28] Duong, K. V., Sheikh, S. A., Vecchio, F. J. Seismic behavior of shear-critical reinforced concrete frame: Experimental investigation. ACI Structural Journal, 2007; 104: 304-313. doi:10.14359/18620.

[29] Lee, J.-Y., Watanabe, F. Shear deterioration of reinforced concrete beams subjected to reversed cyclic loading. ACI Structural Journal, 2003; 100: 480-489. doi:10.14359/12657.

[30] Lee, J. Y., Watanabe, F. Predicting the longitudinal axial strain in the plastic hinge regions of reinforced concrete beams subjected to reversed cyclic loading. Engineering Structures, 2003; 25: 927-939. doi:10.1016/S0141-0296(03)00026-9.

[31] Ho, J. C. M., Pam, H. J. Inelastic design of low-axially loaded high-strength reinforced concrete columns. Engineering Structures, 2003; 25: 1083-1096. doi:10.1016/S0141-0296(03)00050-6.

[32] Moretti, M., Tassios, T. P. Behaviour of short columns subjected to cyclic shear displacements: Experimental results. Engineering Structures, 2007; 29: 2018-2029. doi:10.1016/j.engstruct.2006.11.001.

[33] Pendyala, R. S., Mendis, P. Experimental study on shear strength of high-strength concrete beams. ACI Structural Journal, 2000; 97: 564-571. doi:10.14359/7421.

[34] American Concrete Institute (ACI). ACI 318-08: Building Code Requirements for Structural Concrete and Commentary. Farmington Hills (MI): ACI; 2008. doi:10.14359/51716937.

[35] Federal Emergency Management Agency (FEMA). FEMA Publication 273: NEHRP Guidelines for the seismic rehabilitation of buildings. Washington, D.C. (US): FEMA; 1997.

[36] New Zealand Standard (NZS). NZS 3101.1: Design of concrete structures. Wellington (NZ): NZS; 2006.

[37] Akbarzadeh Bengar, H., Abdollahtabar, M., Shayanfar, J. Predicting the Ductility of RC Beams Using Nonlinear Regression and ANN. Iranian Journal of Science and Technology, Transactions of Civil Engineering, 2016; 40: 297-310. doi:10.1007/s40996-016-0033-0.

[38] Akbarzadeh Bengar, H., Shayanfar, J. Seismic performance of RC frames joints retrofitted by CFRP composites. In: Proceedings of the 2th International and the 6th National Conference on Earthquake & Structures; 2015 Oct 14–15; Kerman, Iran. p. 1-10.

[39] Tariq, M., Khan, A., Ullah, A., Shayanfar, J., Niaz, M. Improved Shear Strength Prediction Model of Steel Fiber Reinforced Concrete Beams by Adopting Gene Expression Programming. Materials, 2022; 15: 3758. doi:10.3390/ma15113758.

[40] Tariq, M., Khan, A., Shayanfar, J., Hanif, M. U., Ullah, A. A regression model for predicting the shear strength of RC knee joint subjected to opening and closing moment. Journal of Building Engineering, 2021; 41: 102727. doi:10.1016/j.jobe.2021.102727.

[41] Akbarzadeh Bengar, H., Shayanfar, J., Seyedpoor, S. M. An artificial neural network (ANN) model for predicting themoment-rotation of exterior RC beam–column jointsstrengthened by CFRP composites. In: Proceedings of the 2th International and the 6th National Conference on Earthquake & Structures; 2015 Oct 14–15; Kerman, Iran. p. 11-20.

[42] Abedi, M., Shayanfar, J., Al-Jabri, K. Infrastructure damage assessment via machine learning approaches: a systematic review. Asian Journal of Civil Engineering, 2023; 24: 3823-3852. doi:10.1007/s42107-023-00748-5.

[43] Park, H.-G., Yu, E.-J., Choi, K.-K. Shear-strength degradation model for RC columns subjected to cyclic loading. Engineering Structures, 2012; 34: 187-197. doi:10.1016/j.engstruct.2011.08.041.

[44] Chen, W. F. Plasticity in Reinforced Concrete. 1st ed. Plantation (FL): J. Ross Publishing; 2007.

[45] Priestley, M. J. N., Verma, R., Xiao, Y. Seismic Shear Strength of Reinforced Concrete Columns. Journal of Structural Engineering, 1994; 120: 2310-2329. doi:10.1061/(ASCE)0733-9445(1994)120:8(2310).

[46] Sezen, H., Moehle Jack, P. Shear Strength Model for Lightly Reinforced Concrete Columns. Journal of Structural Engineering, 2004; 130: 1692-1703. doi:10.1061/(ASCE)0733-9445(2004)130:11(1692).

[47] Ohue, M., Morimoto, H., Fujii, S., Morita, S. Behavior of R.C. Short Columns Failing in Splitting Bond-shear Under Dynamic Lateral Loading. ed. Tokyo (JP): Japan Concrete Institute; 1985.

[48] Esaki, F. Reinforcing effect of steel plate hoops on ductility of R/C square columns. In: 11th World Conference on Earthquake Engineering; 1996; Acapulco (MX). p. 196.

[49] Li, X. Reinforced concrete columns under seismic lateral force and varying axial load (PhD Thesis). Christchurch (NZ): University of Canterbury; 1994.

[50] Saatcioglu, M., Ozcebe, G. Response of reinforced concrete columns to simulated seismic loading. ACI Structural Journal, 1989; 86: 3-12. doi:10.14359/2607.

[51] Yalcin, C. Seismic evaluation and retrofit of existing reinforced concrete bridge columns (PhD Thesis). Ottawa (CA): University of Ottawa; 1998.

[52] Hirosawa, M. A list of past experimental results of reinforced concrete columns. 1st ed. Tokyo (JP): Building Research Institute Ministry of Construction; 1973.

[53] Xiao, Y., Martirossyan, A. Seismic Performance of High-Strength Concrete Columns. Journal of Structural Engineering, 1998; 124: 241-251. doi:10.1061/(ASCE)0733-9445(1998)124:3(241).

[54] Yoshimura, M. Formulation of post-peak behavior of old reinforced concrete columns until collapse. In: The 14th World Conference Earthquake Engineering; 2008 Oct 12–17; Beijing, China. p. 15-26.

[55] Yoshimura, M., Takaine, Y., Nakamura, T. Collapse drift of reinforced concrete columns. Journal of Structural and Construction Engineering (Transactions of AIJ), 2003; 68: 153-160. doi:10.3130/aijs.68.153_5.

[56] Nakamura, T., Yoshimura, M. Simulation of old reinforced concrete column collapse by pseudo-dynamic test method. In: 15th World conference on earthquake engineering; 2012 Sep 24-28; Lisbon, Portugal. p. 0-20.

[57] Nakamura, T., Yoshimura, M. Gravity load collapse of reinforced concrete columns with decreased axial load. In: Proceedings of the 2nd European Conference on Earthquake Engineering and Seismology, Istanbul, Turkey; 2014 Aug 24-25; Istanbul, Turkey. p. 25-29.

[58] Li, Y.-A., Huang, Y.-T., Hwang, S.-J. Seismic response of reinforced concrete short columns failed in shear. ACI Structural Journal, 2014; 111: 945-954. doi:10.14359/51686780.

[59] Ramirez, H., Jirsa, J. O. Effect of axial load on shear behavior of short RC columns under cyclic lateral deformations. Austin (TX): University of Texas at Austin. Phil M. Ferguson Structural Engineering Laboratory; 1980. Report No.: ENV77-20816.

[60] Bett, B., Jirsa, J., Klingner, R. Behavior of strengthened and repaired reinforced concrete columns under cyclic deformations. Austin (TX): University of Texas at Austin. Phil M. Ferguson Structural Engineering Laboratory; 1985. Report No.: 85-3.

[61] Umehara, H. Shear strength and deterioration of short reinforced concrete columns under cyclic deformations (PhD Thesis). Austin (TX): University of Texas at Austin; 1983.

[62] Ousalem, H., Kabeyasawa, T., Tasai, A. Evaluation of ultimate deformation capacity at axial load collapse of reinforced concrete columns. In: Proceedings of 13th world conference on earthquake engineering; 2004 Aug 1-4; Vancouver, B. C., Canada. p. 370.

[63] Aboutaha, R. S., Engelhardt, M. D., Jirsa, J. O., Kreger, M. E. Rehabilitation of shear critical concrete columns by use of rectangular steel jackets. ACI Structural Journal, 1999; 96: 68-78. doi:10.14359/597.

[64] Woods, C. Displacement demand effects in vulnerable reinforced concrete columns (PhD Thesis). Lawrence (KS): University of Kansas; 2010.

[65] Boys, A., Bull, D., Pampanin, S. Seismic performance assessment of inadequately detailed reinforced concrete columns. In: 2008 New Zealand Society for Earthquake Engineering (NZSEE) Conference; 2008 Apr 11-13; Wellington, New Zealand. p. 29.

[66] Kogoma, I., Hayashida, T., Minowa, C. Experimental studies on the collapse of RC columns during strong earthquake motions. In: 10th World Conference on Earthquake Engineering; 1992 Jul 19–24; Madrid, Spain. p. 3013-3017.

[67] Choi, K.-K., Truong, G. T., Kim, J.-C. Seismic performance of lightly shear reinforced RC columns. Engineering Structures, 2016; 126: 490-504. doi:10.1016/j.engstruct.2016.07.060.

[68] Ghannoum Wassim, M., Moehle Jack, P. Rotation-Based Shear Failure Model for Lightly Confined RC Columns. Journal of Structural Engineering, 2012; 138: 1267-1278. doi:10.1061/(ASCE)ST.1943-541X.0000555.

[69] Elwood, K. J., Moehle, J. P. Dynamic collapse analysis for a reinforced concrete frame sustaining shear and axial failures. Earthquake Engineering & Structural Dynamics, 2008; 37: 991-1012. doi:10.1002/eqe.787.

[70] Howser, R., Laskar, A., Mo, Y. Seismic interaction of flexural ductility and shear capacity in reinforced concrete columns. Structural engineering and mechanics: An international journal, 2010; 35: 593-616. doi:10.12989/sem.2010.35.5.593.

[71] Shin, M., Choi, Y. Y., Sun, C.-H., Kim, I.-H. Shear strength model for reinforced concrete rectangular hollow columns. Engineering Structures, 2013; 56: 958-969. doi:10.1016/j.engstruct.2013.06.015.

[72] Kowalsky, M. J., Priestley, M. N. Improved analytical model for shear strength of circular reinforced concrete columns in seismic regions. ACI Structural Journal, 2000; 97: 388-396. doi:10.14359/4633.

[73] State of California Department of Transportation. Caltrans Version 2.0: Caltrans Seismic Design Criteria. Sacramento (CA): Caltrans; 2019.

Civil Engineering and Applied Solutions

Research Article

journal homepage: ceas.journals.umz.ac.ir

CEAS Civil Engineering and Applied Solutions

Improvement of Recycled Concrete Aggregate Properties by Polyvinyl Alcohol

Mohammad Valizadeh Kiamahalleh [a*], Aref Khorshidi-Mianaei [b], Amin Safari [c]

[a] *College of Science and Engineering, Flinders University, SA, Australia*
[b] *Ghaem Technology Institute of Higher Education, Qaem Shahr, Mazandaran, Iran*
[c] *Quattro, Varsity Lakes, QLD 4227, Australia*

ARTICLE INFO

Keywords:
Recycled concrete aggregate (RCA)
Polyvinyl alcohol (PVA)
Natural aggregate (NA)
Concrete

Article history:
Received 29 September 2025
Accepted 23 November 2025
Available online 01 April 2026

ABSTRACT

This study examines liquid polyvinyl alcohol (PVA) impregnation of recycled concrete aggregate (RCA) to refine pore structure and evaluate its influence on the fresh and hardened properties of companion concretes, using natural aggregate concrete as the benchmark. Aggregates were pretreated at progressively higher PVA dosages and characterized for specific gravity, water absorption, and gradation, and concretes with untreated and PVA-treated RCA were assessed for slump, water absorption, compressive strength, and drying shrinkage. The investigation was intentionally designed for non-structural concrete applications such as paving blocks, curbs, and lightweight elements, where durability and sustainability are prioritized over high strength. Results indicated that increasing PVA dosage enhanced aggregate density and reduced water absorption at higher levels (10%), but also caused trade-offs in workability and mechanical strength. Workability improved at 6% PVA but declined at higher contents, while compressive strength decreased at 6–8% and partially recovered at 10%. Drying shrinkage increased slightly with PVA addition. Overall, PVA pretreatment improved aggregate densification and moisture resistance but required dosage optimization for practical use in durable, non-structural RCA concretes aimed at sustainable resource utilization.

1. Introduction

Construction and demolition activities generate vast amounts of waste from building, renovation, and demolition processes, which occupy valuable landfill space and negatively affect soil, water, and air quality [1]. In addition, the growing demand for construction materials has placed increasing pressure on natural resources, driving natural aggregate (NA) production from 21 billion tons in 2007 to 40 billion tons in 2014 [2]. The construction industry, being one of the largest globally, is also a significant contributor to carbon dioxide emissions. These combined challenges of waste management, resource depletion, and environmental impact highlight the need for more sustainable practices. One promising approach is the use of recycled concrete aggregate (RCA), which can reduce waste generation while conserving natural aggregates [3, 4].

However, despite its environmental benefits, RCA still faces significant technical challenges that limit its widespread application in structural concrete. Compared to natural aggregates, RCA exhibits higher porosity, greater water absorption, and higher bulk densities, largely due to the residual mortar adhered to its surface [5, 6]. As a result, recycled aggregate concrete (RAC) generally shows lower compressive and tensile strengths and weaker structural performance than conventional concrete [7-10]. Olorunsogo and Padayachee [11] investigated the durability of concrete with varying proportions of recycled aggregate (0, 50, and 100%) using indicators such as chloride conductivity, oxygen permeability, and water sorptivity. They reported that durability decreased as the RCA content increased, with mixes containing 100% RCA showing up to 86.5% higher chloride conductivity and 28.8% higher water sorptivity compared to natural aggregate concrete at 56 days.

A major factor behind such poor performance is the adhered mortar on RCA surfaces, which increases porosity, water absorption,

* Corresponding author.
E-mail addresses: mohammad.valizadeh@flinders.edu.au (M. Valizadeh Kiamahalleh).

https://doi.org/10.22080/ceas.2025.30167.1046
ISSN: 3092-7749/© 2026 The Author(s). Published by University of Mazandaran.
This article is an open access article distributed under the terms and conditions of the Creative Commons Attribution (CC-BY) license (https://creativecommons.org/licenses/by/4.0/deed.en)
How to cite this article: Valizadeh Kiamahalleh, M., Khorshidi-Mianaei, A., Safari, A. Improvement of Recycled Concrete Aggregate Properties by Polyvinyl Alcohol. Civil Engineering and Applied Solutions. 2026; 2(2): 49–59. doi:10.22080/ceas.2025.30167.1046.

and reduces density, thereby weakening the aggregate's mechanical properties. While methods such as washing, chemical treatments, and the use of supplementary materials like fly ash or carbonation have been explored to improve RCA, their effectiveness remains limited and often inconsistent. As a result, researchers have sought alternative approaches that focus on strengthening the adhered mortar rather than removing it. One promising option is the use of polyvinyl alcohol (PVA), a water-soluble polymer known for its excellent bonding, film-forming, and durability-enhancing properties.

Kim and Robertson [12] proposed the pre-wetting method to prepare polyvinyl alcohol-modified cement-based materials and found that the porosity of modified cement-based materials prepared by this method could be reduced to 6%. When a small amount of PVA is added (less than 2%), the air void content and apparent fluidity of fresh mortar and concrete increase, and the bleeding reduces. Due to the increase in fluidity, the slump of the modified concrete increases. Allahverdi et al. [13] studied the effects of different water–cement ratios and polymer–cement ratios on the workability of modified cement mortar. It was found that adding a small amount of polyvinyl alcohol can improve the fluidity of cement mortar. However, with the increase of PVA content, the fluidity of modified cement mortar will be adversely affected. Nguyen et al. studied the effects of molecular weight and dosage of PVA on rheological properties of cement-based materials and found that the yield stress and plastic viscosity of cement paste increased with the increasing content and molecular weight of PVA. Shear thinning occurs with the increase of shear rate. Zongcai et al. [14] showed that the load–deformation curve of PVA fibre-reinforced concrete indicates its ability to withstand load after cracking, with the failure mode shifting from brittle to ductile behavior. This demonstrates that PVA fibres can significantly enhance the ductility of concrete [15]. Compared with ordinary concrete and steel fibre-reinforced concrete, the PVA fibre-reinforced concrete enjoys a low self-weight and high toughness [16], durability, and fatigue resistance. Recent research by Xie et al. [17] demonstrated that the addition of PVA fibers in combination with limestone fines significantly influences the workability and mechanical properties of cementitious composites. An optimal dosage of 0.2% PVA fibers with 10% limestone fines was shown to enhance compressive and flexural strength, while excessive fiber content increased porosity and reduced performance. Wang and Zhu [18] studied the combined effect of nano-silica (NS) and PVA fibers on recycled aggregate concrete (RAC). Their results showed that PVA fibers enhanced the compressive strength and ductility of RAC by bridging microcracks and improving the interfacial bonding between aggregates and the matrix. The addition of nano-silica further improved compactness, leading to superior mechanical performance under uniaxial compression. The improvement was attributed to the better distribution of aggregates and the increased interlocking between fibres and aggregates. Yu et al. [19] showed that PVA fibers helped reduce crack width, delay fragmentation, and improve flexural behavior compared to RAC without fibers.

To address these limitations, this research investigates the use of liquid PVA to improve the properties of RCA, with the goal of producing durable, non-structural RCA concrete. The study focuses on determining the optimum PVA dosage that can enhance compressive strength and durability, while acknowledging its trade-off in reducing slump and workability. In this context, PVA is applied specifically to strengthen the adhered mortar and refine the micro-pores of RCA. The performance of PVA-treated RCA is evaluated through comparisons with control specimens in terms of compressive strength and water absorption.

2. Research significance

There has been an increasing number of research studies and findings focused on the modification of using fly ash for concrete pavement applications. RCA suffers from high porosity and weakly adherent mortar, which depresses strength and durability. There has been no study dedicated solely to recycled concrete aggregate using PVA treatment. This study investigates liquid PVA as a targeted pre-treatment for RCA applied to strengthen the adhered mortar and refine micro-pores before mixing. In this research, the optimum PVA dosage is identified to enhance compressive strength and reduce water absorption, while explicitly acknowledging the trade-off of reduced slump and workability. In this research, performance is benchmarked against untreated controls using standard compressive-strength and water-absorption tests. Because the treatment is a simple surface process that can be integrated into aggregate production, the approach is scalable for ready-mix and precast operations. The findings provide a practical pathway to durable, non-structural RCA concretes, enabling higher RCA replacement levels, conserving natural aggregates, and supporting decarbonization through higher-value recycling of demolition waste.

3. Experimentation

3.1. Materials and experiments

The materials used in this study comprised recycled concrete aggregate (RCA), natural aggregate, glass sand, glass powder (GP), ground granulated blast-furnace slag (GGBS), ordinary portland cement (OPC), and polyvinyl alcohol (PVA). These were selected to assess the effectiveness of PVA treatment on recycled aggregates and its influence on the performance of concrete mixes. To evaluate the properties of both the aggregates and the resulting concrete, a range of testing equipment was employed, including a concrete slump test set for workability, a water absorption test set for porosity, compression and flexural testing machines for mechanical performance, a shrinkage test set for dimensional stability, and desiccators for pre-treatment of aggregates. The picture of RCA, natural aggregate, and PVA, which was used in this study, is presented in Fig. 1.

(a) **(b)** **(c)**

Fig. 1. Materials used in the study: (a) RCA, (b) NA, and (c) PVA.

3.2. Experimental procedure

The methodology adopted in this research was based on and adapted from established procedures in previous studies [20]. The experimental procedure began with the pre-treatment of recycled concrete aggregates. Both 20 mm and 10 mm RCA were placed in desiccators connected to a vacuum pump operating at a pressure of 920 mbar for six hours.

In parallel, polymer solutions of different concentrations were prepared. Specifically, 120 g, 160 g, 200 g, and 240 g of PVA powder were separately dissolved in 2 L of boiled water to obtain 6%, 8%, and 10% PVA solutions, where the percentage represents the mass of PVA powder relative to the mass of water used in the solution. Once the powder was fully dissolved, the solutions were cooled to room temperature before use.

The polymer solutions were then introduced into the desiccators containing RCA through a funnel, and the aggregates were soaked under vacuum for 24 hours. After soaking, the treated aggregates were removed and tested to evaluate their physical properties. This process was repeated until sufficient quantities of PVA-impregnated RCA were obtained for concrete production.

Concrete mixtures were subsequently prepared using RCA treated with a 10% PVA solution, under two different moisture conditions: oven-dried and air-dried. For the oven-dried condition, PVA-impregnated RCA were dried at 60 °C for 24 hours, while for the air-dried condition, PVA-impregnated RCA were allowed to dry in a controlled laboratory environment (temperature = 23 ± 1 °C, relative humidity = 65 ± 2%) for two days before mixing. These procedures ensured consistency and allowed for comparison between the two moisture states.

3.3. Testing

A series of tests was carried out on the fresh and hardened concrete as per the international standard procedures. These tests were performed to characterize the physical properties of sand, natural aggregate, and recycled coarse aggregates based on the standards presented in Table 1.

Table 1. Standards of test and procedures.

Test and procedures	Method
Sieve analysis	AS 1012.3.1:2014 (Standard 2014d)
Slump test	AS 1012.3.1:2014 (Standard 2014d)
Compressive strength	AS 1019.9:2014 (Standard 2014b)
Splitting tensile strength	AS 1012.10-2000 (Standard 2000)
Drying shrinkage	AS 1012.13:2015 (Standard 2015)
Curing	AS 102.8.1:2014 (Standard 2014a)
Mixing	AS 1012.2:2014 (Standard 2014a)

The aggregates sieve analysis test was performed in accordance with the specifications provided in AS 1012.3.1:2014 (Standard 2014d). The importance of this test was to know the particle size distribution of aggregates. For this research, the sizes of sieves used were 13.2 mm, 9 mm, 6.7 mm, 4.75 mm, 2.35 mm, 1.18 mm, 600 micron, 425 micron, 300 micron, 150 micron, 75 micron, and pan. The particle density and water absorption of fine aggregate were conducted in accordance with the specification provided in AS 1141.5-2000. The NA and RCA water absorption and specific gravity were performed with the requirements provided in AS1141.5-2000 (Standards 2000). The importance of the water absorption test was to determine the amount of water being absorbed by the aggregates. As reviewed from different literature, an aggregate that absorbs too much water has a bad mechanical property and is not fit for concrete production. This test helped in the differentiation of natural aggregates and RCAs based on the water absorption capacity.

3.3.1.Treatment of recycled concrete aggregate with polyvinyl alcohol

The treatment of recycled concrete aggregate with polyvinyl alcohol involves different stages.

a. Oven-dry process: In this phase, the RCA was placed in a thermostatic oven for up to 48 hours at a temperature of 107°C. This process was performed in order to dry up the aggregate particles, making it more possible to expose the pore spaces to

be filled with PVA.

b. Mix design and concrete preparation: It is important to note that the water content was 1.3 kg and the cement value was 2 kg in every mix. For every 2 litres of water, there were 120 g of PVA.

GP and GGBS were the replacements for cement. In this project, five unique concrete mixes were prepared, including one control mix (0% PVA-treated RCA) and four mixes with 0, 6, 8, and 10% PVA-treated RCA. Fine and coarse aggregates were used in saturated-surface dry (SSD) conditions to prevent the water absorption of the aggregates. Mix designs of concrete specimens are presented in Table 2.

Table 2. Mix designs of concrete specimens.

	NA	RCA	PVA	GS	GP	Cement	GGBS
	kg/m^3						
Natural Aggregate	5.98	0.00	0.00	3.72	0.73	0.53	0.73
0% PVA	0	5.98	0.00	3.72	0.73	0.53	0.73
6% PVA	0	5.98	0.06	3.72	0.73	0.53	0.73
8% PVA	0	5.98	0.08	3.72	0.73	0.53	0.73
10% PVA	0	5.98	0.10	3.72	0.73	0.53	0.73

4. Experimental results

4.1. Water absorption

The water absorption test was conducted in two stages: (i) determination of the specific gravity and water absorption of loose aggregates, and (ii) measurement of water absorption for RCA specimens treated with different dosages of PVA.

The results of the first stage are presented in Table 3 and Fig. 2. Natural aggregate exhibited a specific gravity of 2.6 with a relatively low water absorption of 2.28%, indicating its dense and less porous structure. In comparison, untreated RCA (0% PVA) had a specific gravity of 2.4 and a much higher water absorption of 6.9%, reflecting the porous nature of adhered mortar. Upon PVA treatment, significant variations were observed. At 6 and 8% PVA dosages, specific gravity decreased to 2.06 and 2.02, respectively, with corresponding increases in water absorption (12.87 and 11.97%). Interestingly, the 10% PVA treatment increased the specific gravity to 3.00 and simultaneously reduced water absorption to 4.22%, suggesting improved densification of the aggregate.

Table 3. The water absorption for loose aggregate.

Aggregate type	Polyvinyl alcohol (%)	Specific gravity	Water absorption (%)
Recycled concrete aggregate	0	2.4	6.9
	6	2.06	12.87
	8	2.02	11.97
	10	3.00	4.22
Natural aggregate	-	2.6	2.28

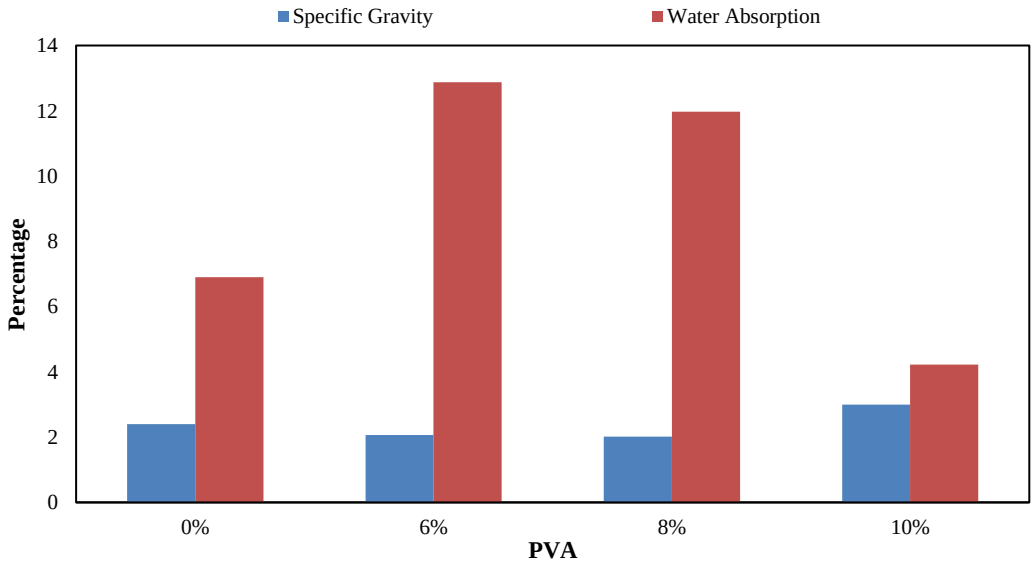

Fig. 2. Specific gravity and water absorption for loose aggregate.

The second stage involved detailed water absorption testing of both natural aggregates and RCA with varying PVA contents.

The average results are summarized in Table 4 and illustrated in Fig. 3. Natural aggregate specimens recorded an average absorption of 6.76%, while untreated RCA (0% PVA) showed a much higher value of 11.37%. With PVA treatment, the absorption initially increased, reaching 12.17% at 6% dosage, before gradually declining to 11.27 and 10.84% at 8 and 10% PVA, respectively.

Table 4. The average water absorption of manufactured concrete specimens.

Spcimen	Water absorption (%)
Natural aggregate	6.76
0% PVA	11.37
6% PVA	12.17
8% PVA	11.27
10% PVA	10.84

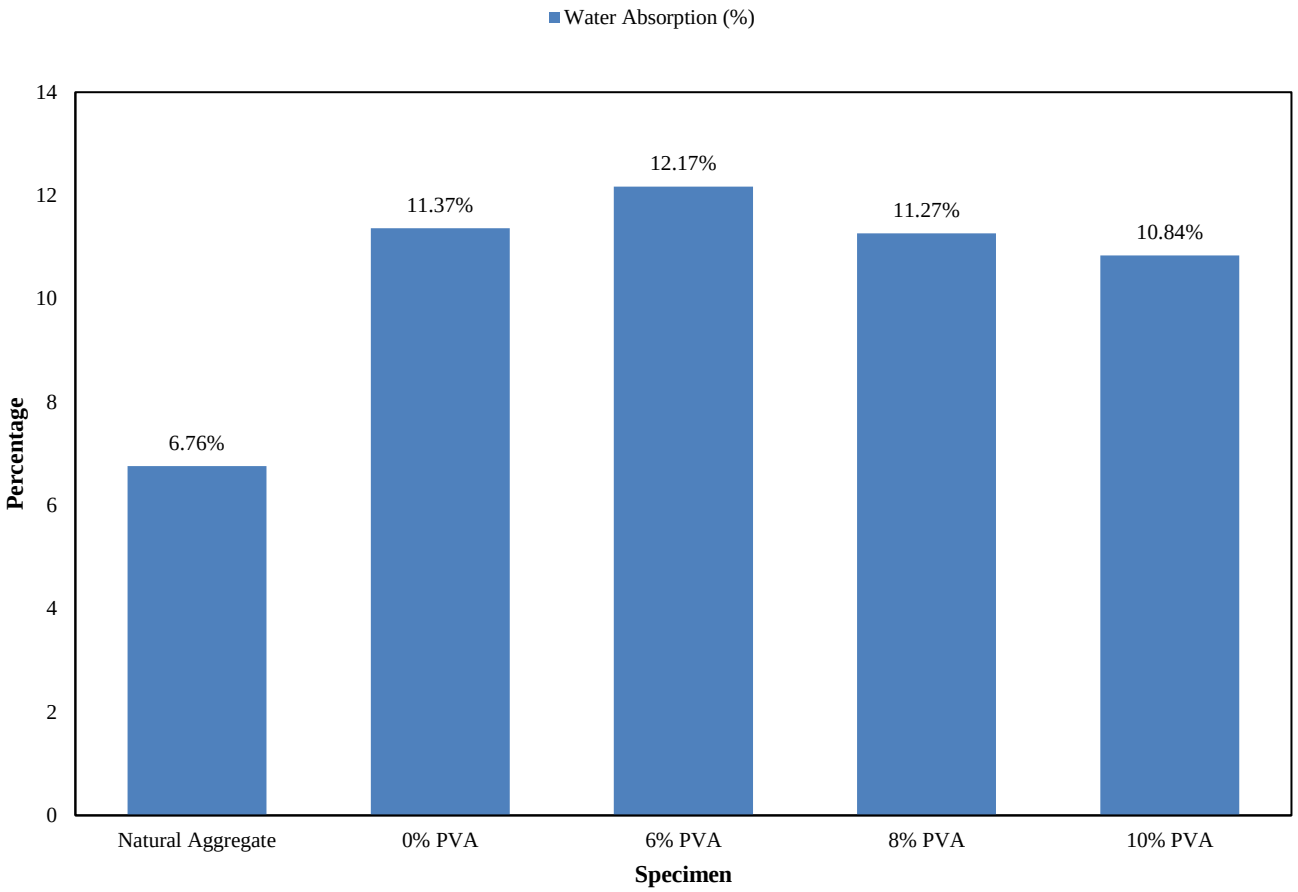

Fig. 3. Water absorption graph.

These results demonstrate that RCA generally exhibits higher water absorption than natural aggregate, due to the porous adhered mortar. Although moderate PVA dosages (6–8%) did not improve absorption, higher treatment levels (10%) reduced water absorption significantly, indicating that polymer impregnation at sufficient dosage can enhance aggregate quality by sealing micro-pores and reducing permeability

4.2. Sieve analysis

Sieve analysis was carried out to determine the particle size distribution of the recycled aggregate, natural aggregate, and glass sand used in this study. The results are presented in Fig. 4. As shown in Fig. 4, the recycled aggregate exhibited a wider gradation curve with a relatively higher proportion of fine particles compared to the natural aggregate. This behavior can be attributed to the adhered mortar and micro-cracks formed during the crushing process of recycled concrete. The natural aggregate displayed a steeper gradation curve, indicating a more uniform particle size distribution and a lower percentage of fines. In contrast, the glass sand showed a much finer gradation profile, with a significant proportion of particles passing through the smaller sieve sizes. This makes glass sand comparable to natural sand in terms of fineness, though it differs in angularity and surface texture due to its origin. Overall, the comparison of these gradation curves indicates that recycled aggregates tend to contain more fines and exhibit different packing characteristics than natural aggregates, which may affect the workability and mechanical properties of concrete mixes. The inclusion of glass sand, with its fine particle size distribution, can enhance particle packing and reduce void content within the mix.

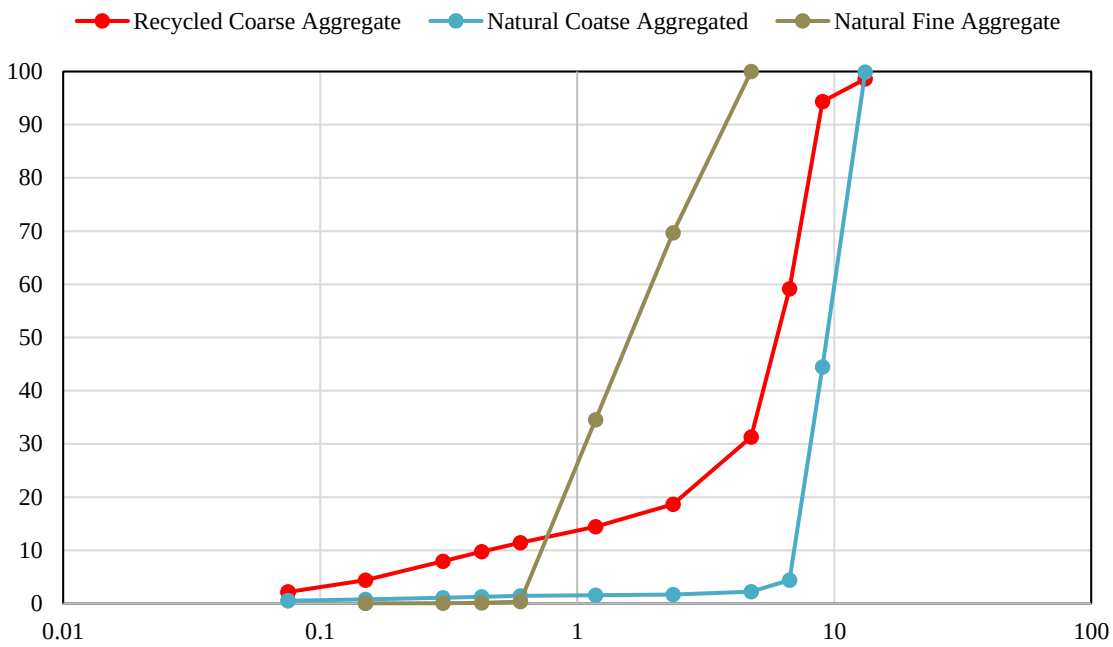

Fig. 4. Sieve analysis curve of aggregates.

4.3. Slump test

The workability of fresh concrete mixtures was assessed using the slump test in accordance with AS 1012.3.1:2014. The results are summarized in Table 5 and illustrated in Fig. 5.

Table 5. Slump test results.

Specimen	Natural aggregate (Control)	PVA 0%	PVA 6%	PVA 8%	PVA 10%
Slump	15 mm	15 mm	20 mm	15 mm	10 mm

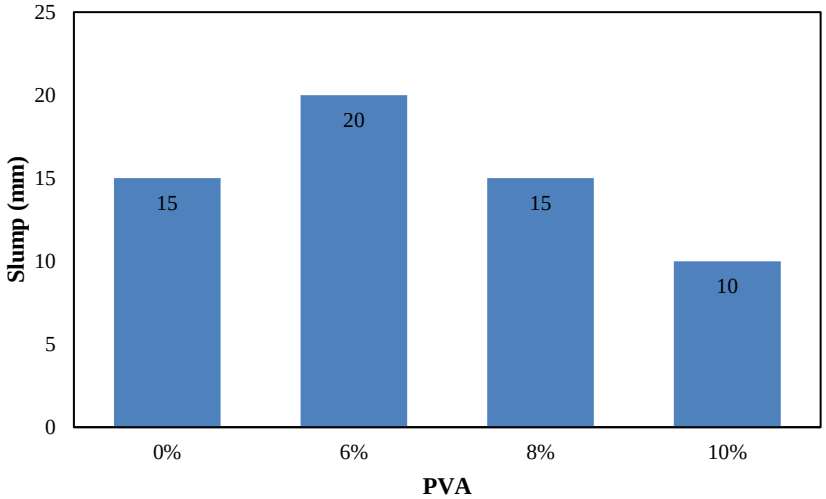

Fig. 5. Bar graph of the slump test.

The results indicate that the slump value for natural aggregate concrete (control) was 15 mm. For RCA mixes without PVA treatment (0%), the slump remained the same (15 mm), suggesting comparable workability at this stage. At 6% PVA treatment, the slump increased to 20 mm, indicating a temporary improvement in workability. However, as the PVA concentration increased further, the slump decreased; at 8% PVA, it returned to 15 mm, and at 10% PVA, it reduced to 10 mm. This trend demonstrates that while a moderate dosage of PVA (6%) can enhance workability due to improved surface lubrication of aggregates, higher concentrations tend to reduce slump. This reduction may be attributed to the thickening effect of the polymer solution and its tendency to coat aggregate surfaces, thereby restricting free water movement within the mix. Overall, the results highlight the balance required in selecting the optimum PVA dosage to improve durability while maintaining adequate workability.

4.4. Drying shrinkage

The drying shrinkage test was performed on concrete specimens made with natural aggregate (NA), untreated RCA (0% PVA),

and PVA-treated RCA (6%, 8%, and 10%). The readings obtained during the test represent the total comparator readings of specimen length (in micrometres), not the actual shrinkage deformation. These readings are summarized in Table 6 and Fig. 6, while the calculated shrinkage strain values (difference in length divided by gauge length, expressed in μm/m) are provided in Table 7.

Table 6. Average drying shrinkage of concrete specimens.

Specimen	1 day (micrometres)	4 days (micrometres)	21 days (micrometres)	28 days (micrometres)
NA	163090	163050	162920	162920
0% PVA	163170	163150	163100	163050
6% PVA	163140	163050	163050	162950
8% PVA	163200	163160	163130	163080
10% PVA	163200	163150	163110	163040

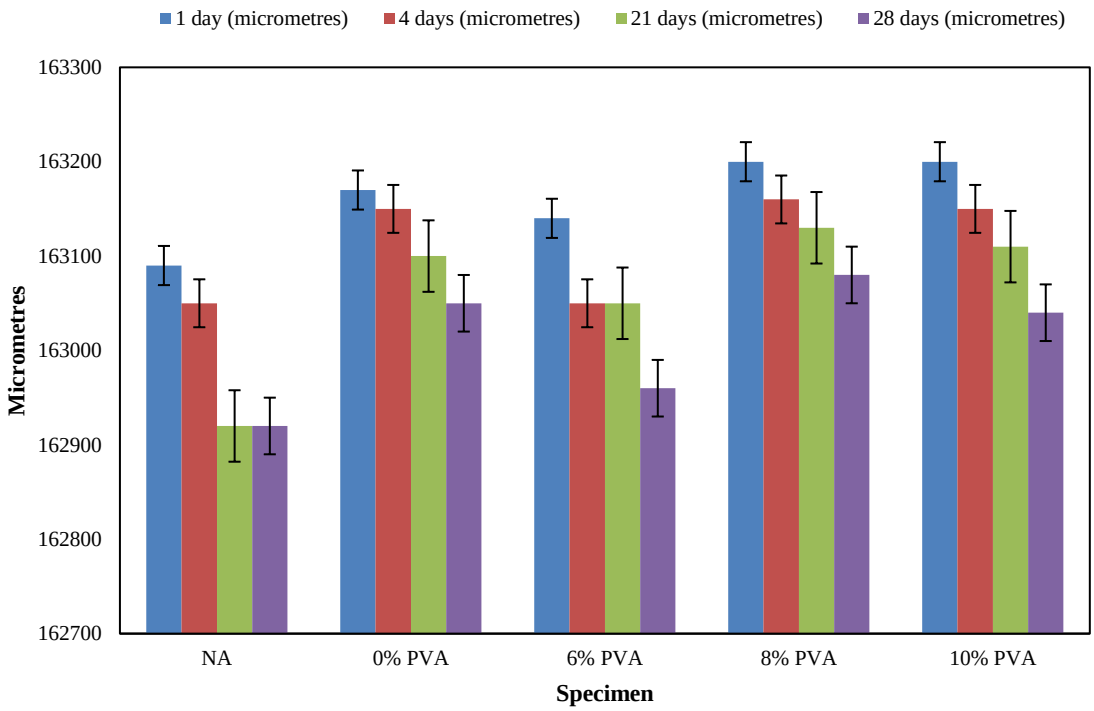

Fig. 6. Drying shrinkage strains of concretes with different PVA dosages.

Table 7. Calculated drying shrinkage strain of concrete specimens (μm/m)

Specimen	Shrinkage strain (μm/m)
NA	≈ 170
0% PVA	≈ 120
6% PVA	≈ 190
8% PVA	≈ 120
10% PVA	≈ 160

Table 6 readings represent the total specimen length measured by the comparator, while Table 7 shows the corresponding calculated shrinkage strains, which fall within the typical range for concrete (50–200 μm/m). Natural aggregate concrete exhibited the lowest shrinkage, confirming its superior dimensional stability. In contrast, RCA concretes displayed slightly higher shrinkage, and the PVA-treated mixes (particularly at 8–10%) showed marginally increased values. This increase is attributed to the polymer coating reducing internal moisture exchange, thereby producing small but measurable differences in shrinkage strain.

4.5. Compressive strength

The compressive strength test was conducted on concrete specimens made with natural aggregate, untreated RCA (0% PVA), and PVA-treated RCA at different dosages (6, 8, and 10%). The compressive strength test setup and failure mode of a concrete specimen are shown in Fig. 7. The average load and stress values are summarized in Table 8, while the stress distribution is illustrated in Fig. 8.

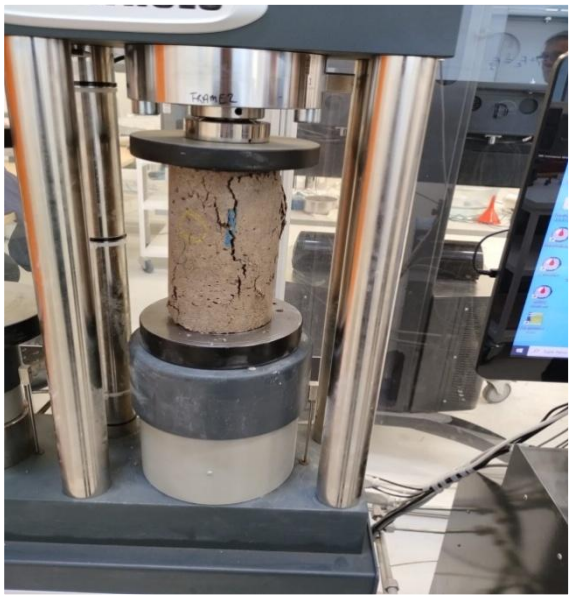

Fig. 7. A view of the compressive strength instrumentation and test.

Table 8. Average compressive strength of concrete specimens.

Specimen	Load (kN)	Stress (MPa)
Natural aggregate	129.19	16.46
0% PVA	180.0	11.47
6% PVA	61.20	7.80
8% PVA	64.04	8.16
10% PVA	84.88	10.81

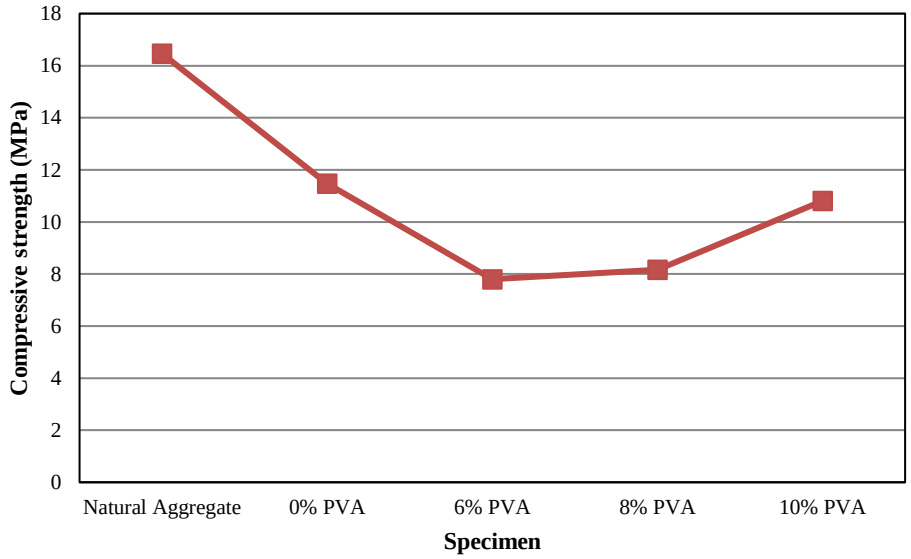

Fig. 8. Compressive strength of concrete specimens.

The results indicate that the natural aggregate concrete exhibited the highest compressive strength (16.46 MPa), reflecting the superior quality and density of natural aggregates. In contrast, all RCA-based concretes showed lower compressive strengths, which can be attributed to the presence of adhered mortar and higher porosity of recycled aggregates. Among the RCA mixes, the untreated specimen (0% PVA) achieved 11.47 MPa, which was higher than the strengths of the PVA-treated specimens at 6% (7.80 MPa) and 8% (8.16 MPa). Interestingly, the 10% PVA treatment showed partial recovery in strength, reaching 10.81 MPa, although it remained below that of the untreated RCA. This trend suggests that moderate polymer impregnation did not significantly enhance compressive strength and, in some cases, may have reduced it due to restricted bonding and microstructural changes. The results highlight the need for dosage optimization, as excessive polymer content may compromise mechanical performance even if it improves durability-related properties.

5. Discussion

The incorporation of polyvinyl alcohol (PVA) into recycled concrete aggregate (RCA) produced mixed effects on the physical and mechanical performance of the resulting concretes. The observed trends were highly dependent on the PVA dosage, and they did not follow a linear pattern. This highlights the complex interaction between polymer coating, pore refinement, and aggregate–paste bonding. The following discussion clarifies these relationships in line with the experimental results.

5.1. Specific gravity and water absorption of treated RCA

The results demonstrated that at low and intermediate PVA dosages (6–8%), both specific gravity and water absorption of RCA were adversely affected; specific gravity decreased, and water absorption increased relative to untreated RCA. This can be attributed to incomplete or uneven polymer coating, which may have introduced additional voids or prevented full penetration of PVA into the micro-pores.

At 10% dosage, however, the PVA layer effectively sealed the surface pores, resulting in a significant increase in specific gravity (to 3.00) and a reduction in water absorption (to 4.22%). This non-linear behavior indicates that adequate polymer concentration and impregnation time are necessary for meaningful pore sealing and densification. Hence, PVA treatment improves RCA properties only at higher dosages, while moderate levels may worsen absorption due to partial coating effects

5.2. Slump of concrete

The workability of RCA concretes exhibited a distinct peak at 6% PVA dosage (20 mm slump), followed by a steady decline at higher levels (10 mm at 10% PVA). This trend suggests that a small amount of PVA solution initially improves surface lubrication and particle dispersion, leading to better flowability. However, as polymer concentration increases, viscosity and surface tension effects dominate, restricting free water movement and reducing slump. Therefore, the influence of PVA on workability is dosage-dependent, improving it slightly at low levels but reducing it at higher concentrations.

5.3. Compressive strength

All RCA concretes recorded lower compressive strength than natural aggregate concrete (16.46 MPa), consistent with the porous and weaker nature of recycled aggregates. Within the RCA series, the 6% and 8% PVA-treated mixes exhibited reduced strength (7.80 and 8.16 MPa), while the 10% PVA mix partially recovered to 10.81 MPa. These results indicate that low-to-medium PVA concentrations may form a weak polymer film at the interface, hindering effective bond formation between aggregate and cement paste. In contrast, higher polymer content can densify the aggregate surface and partially improve bonding. Overall, PVA treatment does not uniformly increase strength, but a 10% dosage showed limited recovery compared to untreated RCA.

5.4. Drying shrinkage

Drying shrinkage increased with PVA treatment, particularly at 8% and 10% dosages. While PVA was expected to enhance microstructural integrity, the polymer coating may have restricted internal moisture exchange, leading to higher residual stresses during drying. The untreated RCA mix showed slightly lower shrinkage, while natural aggregate concrete remained the most dimensionally stable. These results indicate that although PVA may improve aggregate densification, it can exacerbate shrinkage in concrete due to altered moisture diffusion pathways. Therefore, any mechanical benefits from PVA must be balanced against potential shrinkage drawbacks.

5.5. Overall Interpretation

The combined findings suggest that PVA treatment of RCA produces both beneficial and adverse effects, depending on dosage. Higher PVA content (10%) effectively reduces water absorption and increases aggregate density, but compromises workability and dimensional stability. Moderate dosages (6–8%) may lead to inconsistent coating and reduced strength. Thus, optimizing PVA dosage is essential to achieve the desired balance between durability improvement and mechanical performance.

6. Conclusion

In this research, the effects of polyvinyl alcohol (PVA) treatment on recycled concrete aggregate (RCA) and companion concretes were evaluated against natural aggregate benchmarks. PVA impregnation altered pore structure and fresh properties in a nonmonotonic manner. At higher treatment levels, the aggregates became denser and less absorptive, while concrete workability and mechanical performance exhibited trade-offs that depended on dosage.

A 10% PVA treatment increased the specific gravity of loose RCA to 3.00 and reduced its water absorption to 4.22%, indicating effective pore sealing and densification. In concrete specimens, the same dosage lowered water absorption to 10.84% compared with untreated RCA at 11.37%, although absorption remained higher than that of natural aggregate concrete (6.76%). Workability peaked at the 6% PVA dosage (20 mm slump) and declined at higher concentrations.

Compressive strength values remained modest, with the natural aggregate control achieving 16.46 MPa and PVA-treated RCA concretes ranging from 7.8–10.8 MPa. These values confirm that the mixtures were designed for non-structural applications, such as paving, curbing, and partition elements, where durability and sustainability are more critical than structural load-bearing capacity.

Drying shrinkage increased slightly with higher PVA levels, reflecting reduced internal moisture exchange due to polymer coating.

Overall, PVA treatment offers a viable approach to improving the quality of recycled aggregates for non-structural, durable concrete production. However, dosage optimization is essential to balance reduced water absorption with acceptable workability and dimensional stability. This work contributes to the development of sustainable RCA utilization strategies that support environmental conservation and resource efficiency in the construction industry.

Statements & declarations

Author Contributions

Mohammad Valizadeh Kiamahalleh: Investigation, Formal Analysis, Resources, Writing – Review & Editing.

Aref Khorshidi-Mianaei: Conceptualization, Investigation, Formal analysis, Resources, Writing - Original Draft.

Amin Safari: Conceptualization, Methodology, Project administration.

Acknowledgments

The authors gratefully acknowledge the support provided by the College of Science and Engineering at Flinders University. Special thanks are also extended to Ahmad Muhammad Ali for his valuable contributions as part of his Master's thesis project at Flinders University.

Funding

Funding information is not available.

Declarations

The authors declare no conflict of interest.

Data availability

Data available on request due to restrictions, e.g., privacy or ethics: The data presented in this study are available on request from the corresponding author.

References

[1] Islam, R., Nazifa, T. H., Yuniarto, A., Shanawaz Uddin, A. S. M., Salmiati, S., Shahid, S. An empirical study of construction and demolition waste generation and implication of recycling. Waste Management, 2019; 95: 10-21. doi:10.1016/j.wasman.2019.05.049.

[2] Tam, V. W. Y., Soomro, M., Evangelista, A. C. J. A review of recycled aggregate in concrete applications (2000–2017). Construction and Building Materials, 2018; 172: 272-292. doi:10.1016/j.conbuildmat.2018.03.240.

[3] Brito, J. d. S., Nabajyoti Recycled Aggregate in Concrete: Use of Industrial, Construction and Demolition Waste. 1st ed. London (UK): Springer London; 2013. doi:10.1007/978-1-4471-4540-0.

[4] Nazari, A., Toufigh, V. Effects of elevated temperatures and re-curing on concrete containing rice husk ash. Construction and Building Materials, 2024; 439: 137277. doi:10.1016/j.conbuildmat.2024.137277.

[5] Zheng, Y., Zhang, Y., Zhang, P. Methods for improving the durability of recycled aggregate concrete: A review. Journal of Materials Research and Technology, 2021; 15: 6367-6386. doi:10.1016/j.jmrt.2021.11.085.

[6] Nematzadeh, M., Nazari, A., Tayebi, M. Post-fire impact behavior and durability of steel fiber-reinforced concrete containing blended cement–zeolite and recycled nylon granules as partial aggregate replacement. Archives of Civil and Mechanical Engineering, 2021; 22: 5. doi:10.1007/s43452-021-00324-1.

[7] Luo, S., Ye, S., Xiao, J., Zheng, J., Zhu, Y. Carbonated recycled coarse aggregate and uniaxial compressive stress-strain relation of recycled aggregate concrete. Construction and Building Materials, 2018; 188: 956-965. doi:10.1016/j.conbuildmat.2018.08.159.

[8] Xiao, J., Li, W., Poon, C. Recent studies on mechanical properties of recycled aggregate concrete in China—A review. Science China Technological Sciences, 2012; 55: 1463-1480. doi:10.1007/s11431-012-4786-9.

[9] Abedi Mavaramkolaei, S., Sayarinejad, M. A., Nazari, A., Rayati Damavandi, M. Investigating the fracture behavior and ductility of self-compacting concrete containing recycled nylon granules: An experimental and modeling study. Theoretical and Applied Fracture Mechanics, 2026; 141: 105254. doi:10.1016/j.tafmec.2025.105254.

[10] Farrokh Ghatte, H., Nazari, A. Prediction of Rice Husk Ash-Based SCC Compressive Strength: Data-Driven Framework. Civil Engineering and Applied Solutions, 2025; 1: 17-28. doi:10.22080/ceas.2025.29625.1025.

[11] Olorunsogo, F. T., Padayachee, N. Performance of recycled aggregate concrete monitored by durability indexes. Cement and Concrete Research, 2002; 32: 179-185. doi:10.1016/S0008-8846(01)00653-6.

[12] Kim, J.-H., Robertson, R. E. Prevention of air void formation in polymer-modified cement mortar by pre-wetting. Cement and Concrete Research, 1997; 27: 171-176. doi:10.1016/S0008-8846(97)00001-X.

[13] Allahverdi, A., Kianpur, K., Moghbeli, M. R. Effect of polyvinyl alcohol on flexural strength and some important physical properties of Portland cement paste. Iranian Journal of Materials Science and Engineering, 2010; 7: 1-6.

[14] Zongcai, D., Huiqing, X., Pengyuan, L. Flexural Toughness of Polyvinyl Alcohol (PVA) Fiber Reinforced Concrete Beams. South to North Water Transfers and Water Science & Technology, 2007; 5: 139-141.

[15] Noushini, A., Samali, B., Vessalas, K. Effect of polyvinyl alcohol (PVA) fibre on dynamic and material properties of fibre reinforced concrete. Construction and Building Materials, 2013; 49: 374-383. doi:10.1016/j.conbuildmat.2013.08.035.

[16] Georgiou, A. V., Pantazopoulou, S. J. Effect of fiber length and surface characteristics on the mechanical properties of cementitious composites. Construction and Building Materials, 2016; 125: 1216-1228. doi:10.1016/j.conbuildmat.2016.09.009.

[17] Xie, W., Chen, J., Chen, T., Guan, G. X. Workability and Mechanical Properties of PVA Fiber-Limestone Fine Cementitious Composite. Buildings, 2024; 14: 3679. doi:10.3390/buildings14113679.

[18] Wang, S., Zhu, B. Influence of Nano-SiO2 on the Mechanical Properties of Recycled Aggregate Concrete with and without Polyvinyl Alcohol (PVA) Fiber. Materials, 2021; 14: 1446. doi:10.3390/ma14061446.

[19] Yu, F., Xie, C., Fang, Y., Song, J., Xie, H., Zhang, S., Song, W. A Model for Predicting Crack Width of PVA Fiber-Reinforced Recycled Aggregate Concrete Slabs. KSCE Journal of Civil Engineering, 2024; 28: 5697-5714. doi:10.1007/s12205-024-0155-z.

[20] Kou, S.-C., Poon, C.-S. Properties of concrete prepared with PVA-impregnated recycled concrete aggregates. Cement and Concrete Composites, 2010; 32: 649-654. doi:10.1016/j.cemconcomp.2010.05.003.

Civil Engineering and Applied Solutions

Research Article

journal homepage: ceas.journals.umz.ac.ir

CEAS Civil Engineering and Applied Solutions

Numerical Investigation of Trapezoidally Corrugated Steel Shear Walls with Openings: Effects of Stiffeners and Corrugation Orientation

Mehdi Azarbara [a], Rahmat Madandoust [a*]

[a] *Engineering College, University of Guilan, Rasht, Iran*

ARTICLE INFO

Keywords:
Trapezoidal corrugated steel shear walls
Finite element analysis
Openings
Shear capacity
Energy dissipation

Article history:
Received 02 September 2025
Accepted 29 September 2025
Available online 01 April 2026

ABSTRACT

This study conducts a numerical investigation into the seismic behavior of trapezoidally corrugated steel plate shear walls (CSPSWs) with openings, evaluating the effects of stiffeners and corrugation orientation (vertical versus horizontal). Finite element models developed in ABAQUS were validated against experimental data, followed by a parametric analysis varying opening number and location, stiffener dimensions, and corrugation direction. Key findings reveal that vertical corrugation outperforms horizontal orientation, enhancing shear capacity by up to 15% and energy dissipation by 20-30%, while horizontal setups exhibit pronounced stress concentrations and reduced ductility. Central openings minimize performance degradation compared to boundary placements, which can reduce capacity by over 10%, and stiffeners around openings yield modest gains (2-4% in strength and absorption) by promoting uniform stress distribution. These results highlight the critical role of optimized configurations in bolstering seismic resilience for high-rise structures in earthquake-prone regions, facilitating material-efficient designs that reduce construction costs, mitigate failure risks, and advance sustainable engineering practices for enhanced structural longevity and safety.

1. Introduction

Ensuring the seismic resilience of high-rise buildings is a major challenge in earthquake-prone regions. To address this challenge, steel shear walls (SSWs) have been widely implemented in countries such as Japan, Canada, and the United States, owing to their high stiffness and strength, excellent energy dissipation capacity, cost-effectiveness, and ease of construction [1, 2]. Structurally, SSWs act as vertical plate girders, where the infill plate, boundary columns, and floor beams work together to resist lateral shear forces and overturning moments. Following elastic buckling of the infill plate, diagonal tension fields develop that provide significant post-buckling strength and ductility. However, early design approaches often neglected this post-buckling behavior and considered only elastic and yielding capacities, which necessitated the use of thick plates. While such designs could reduce seismic displacements, they also imposed higher demands on boundary frame members and reduced overall material efficiency [3].

Extensive research has been carried out on the behavior and design of steel shear walls [4-10]. Bahrebar et al. [8] showed that openings in corrugated SPSWs reduce shear and energy dissipation, while larger corrugation angles, thicker plates, and hybrid welded–bolted joints improve performance. Similarly, Cao and Huang [11] confirmed that proper corrugation design prevents elastic buckling and enhances stiffness, strength, and ductility, and Bahrebar et al. [12] reported that using low-yield-point steel and curved corrugations improves strength and residual behavior, though excessive half-waves reduce efficiency. The importance of stiffeners has also been highlighted: Mu and Yang [13] demonstrated that diagonal and channel stiffeners enhance capacity and buckling resistance but shift energy dissipation, and Gilvaee and Mofid [14] showed that stiffeners or thicker plates can offset the loss of stiffness caused by openings. The influence of opening configuration and geometry has likewise been emphasized; Veena and Reshmi [15] found that solid walls provide the greatest resistance, while corner openings lead to the weakest performance, and

* Corresponding author.
E-mail addresses: rmadandoust@guilan.ac.ir (R. Madandoust).

https://doi.org/10.22080/ceas.2025.29967.1041
ISSN: 3092-7749/© 2026 The Author(s). Published by University of Mazandaran.
This article is an open access article distributed under the terms and conditions of the Creative Commons Attribution (CC-BY) license (https://creativecommons.org/licenses/by/4.0/deed.en)
How to cite this article: Azarbara, M., Madandoust, R. Numerical Investigation of Trapezoidally Corrugated Steel Shear Walls with Openings: Effects of Stiffeners and Corrugation Orientation. Civil Engineering and Applied Solutions. 2026; 2(2): 60–70. doi:10.22080/ceas.2025.29967.1041.

Joharchi et al. [16] and Qiu et al. [17] concluded that larger corrugation angles, lower aspect ratios, and higher buckling stresses improve strength, ductility, and post-peak behavior.

Building on these earlier findings, more recent studies have focused specifically on the role of stiffeners in enhancing the seismic performance of corrugated SPSWs. Tong et al. [18] demonstrated through experimental and numerical work that vertical stiffeners effectively restrain out-of-plane buckling and markedly improve shear resistance, ductility, and energy dissipation, with welded connections and denser bolt layouts further enhancing performance. Wen et al. [19] confirmed these trends in cyclic tests on unstiffened and stiffened panels, showing that stiffeners delay buckling and increase resistance, although premature cracking can limit ultimate capacity. Analytical approaches have also advanced. Wu et al. [20] derived elastic buckling formulas for multi-stiffened SPSWs and validated them against finite element analyses, while Wen et al. [21] investigated global stability under combined shear and compression, introducing a bolt-spacing factor to capture connection effects. Extending this work, Wu et al. [22] incorporated stiffener torsional rigidity into buckling analyses and proposed enhanced formulas, and Wu and Tong [23] further examined stress–strain parameters and aspect ratio effects, providing conservative design expressions and a nonlinear load–displacement model. Together, these studies underscore the critical influence of stiffener configuration and connection details on both local and global behavior of corrugated SPSWs. Despite these advancements, limited research has addressed the combined influence of openings, stiffener geometry, and corrugation orientation, leaving a critical gap that the present study seeks to fill.

Building on these insights, the present study conducts a comprehensive numerical investigation of trapezoidally corrugated steel shear walls with openings, both with and without stiffeners. Although previous research has examined corrugated plates in SPSWs, limited attention has been paid to the combined effects of opening configuration, stiffener geometry, and corrugation orientation. To address this gap, numerical models were developed in ABAQUS and validated against experimental data for corrugated steel shear walls with openings. Once validated, the models were employed in a systematic parametric study to evaluate the influence of opening number and location, stiffener presence and dimensions, and corrugation orientation (vertical versus horizontal). The findings provide new insights into shear capacity, energy dissipation, and stress distribution of trapezoidally corrugated SPSWs, offering guidance for the seismic design and optimization of these systems.

2. Numerical modeling

2.1. Verification of finite element models and solution approach

To verify the accuracy of the finite element (FE) modeling approach, experimental results from Gilvaee and Mofid [14] were adopted. The tested specimen was a steel shear wall with a trapezoidal corrugated infill panel containing a central opening, as shown in Fig. 1. Stiffeners were provided along the boundary elements, and the details of the corrugation are shown in Fig. 2. The boundary frame consisted of IPB200 base beams, IPB140 top beams, and IPB160 columns. Stiffeners were provided along the boundary elements.

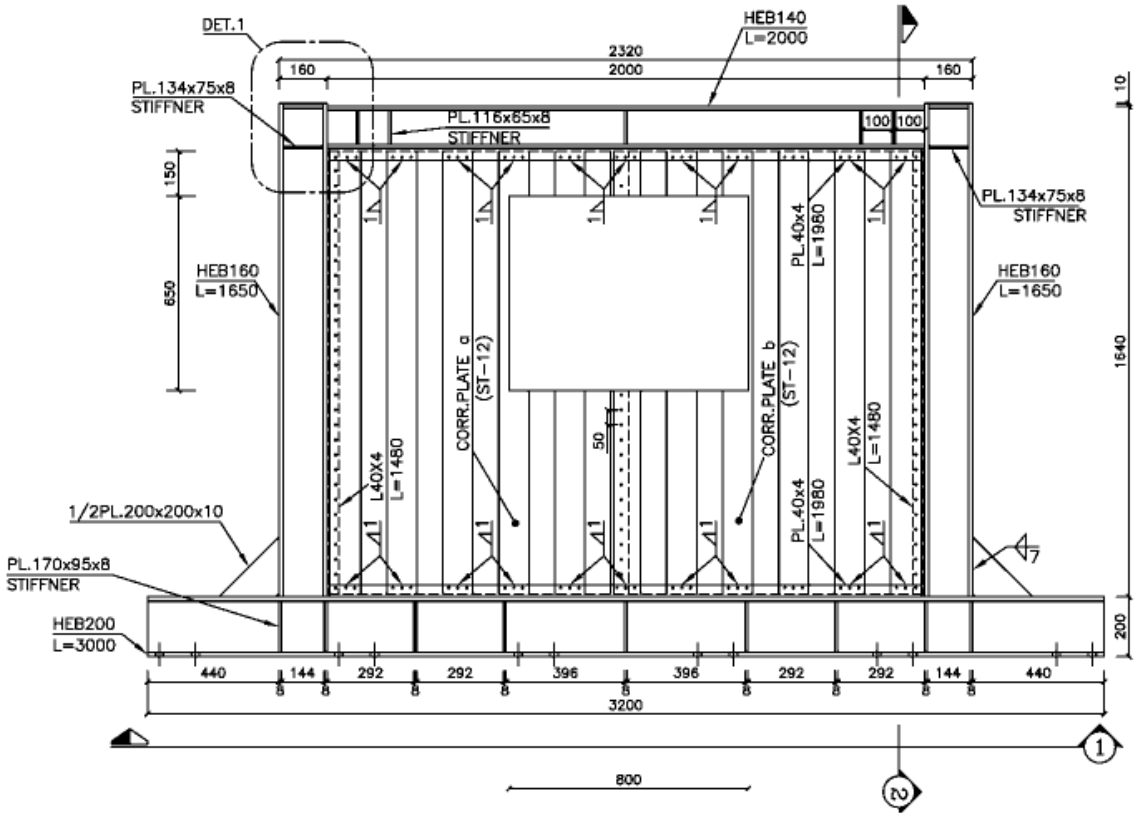

Fig. 1. Steel shear wall with vertical trapezoidal corrugated plate and central opening [14].

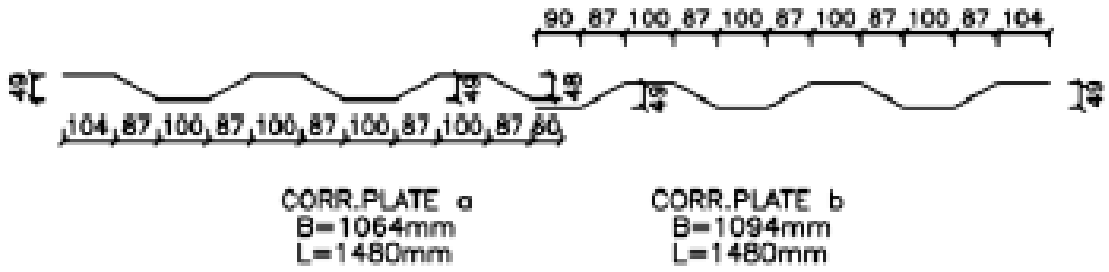

Fig. 2. Details of the trapezoidal corrugated steel plate [14].

The opening dimensions were 800 × 650 mm, representing approximately 18% of the infill plate area. The yield and ultimate strengths of the steel plates and profiles were determined and are summarized in Table 1. The elastic properties of steel were taken as: density = 7850 kg/m³, modulus of elasticity = 200 GPa, and Poisson's ratio = 0.3.

Table 1. Mechanical specifications of the expanded masonry unit.

Steel component	Thickness (mm)	Yield stress (MPa)	Ultimate stress (MPa)	Elongation (%)
Infill plate	1.25	221	339	35.6
Column flanges and webs (IPB160)	—	311	411	34.9
Top beam flanges and webs (IPB140)	—	359	482	30.8

The boundary conditions were defined such that the base of the shear wall was fully restrained, while lateral loading was applied to the top beam under displacement control, with a maximum amplitude of 100 mm. The loading followed the cyclic protocol specified in AC154 (Fig. 3), and was terminated either upon reaching the prescribed displacement limit or upon satisfying the strength degradation criterion. The finite element model was developed in ABAQUS to replicate the experimental specimen. The boundary frame and corrugated infill plate were discretized using S4R shell elements, which are four-node, reduced-integration elements with finite membrane strains, capable of accommodating large rotations and out-of-plane deformations. A uniform mesh size of 30 mm was adopted to ensure an appropriate balance between numerical accuracy and computational efficiency. The final mesh configuration of the model is illustrated in Fig. 4.

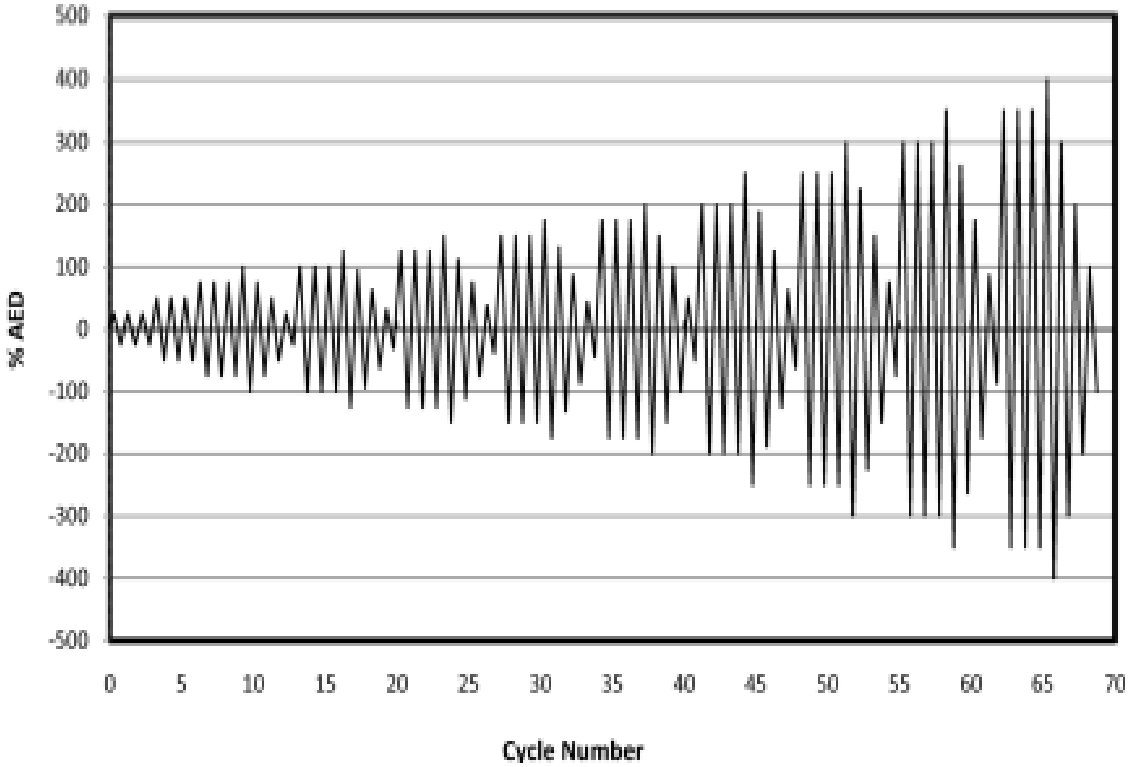

Fig. 3. Cyclic loading protocol based on AC 154 [24].

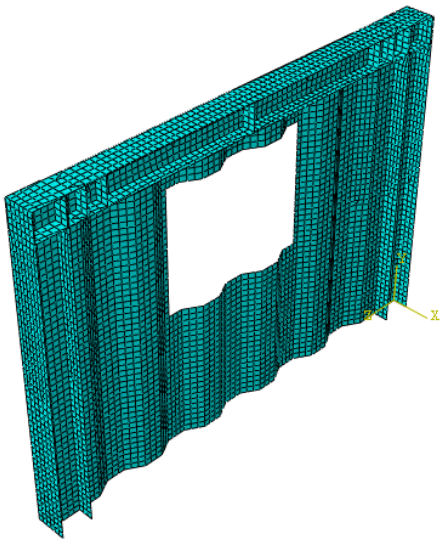

Fig. 4. Meshing of the steel shear wall with trapezoidal corrugated plate and central opening.

The comparison of shear force–displacement curves between the experimental specimen and the numerical model (specimen SWV-O1-M) is presented in Fig. 5. The maximum shear force obtained from the experiment was 389.1 kN, while the FE model predicted 412.6 kN, corresponding to an acceptable error of less than 8%. Both models exhibited the same maximum lateral displacement of 100 mm.

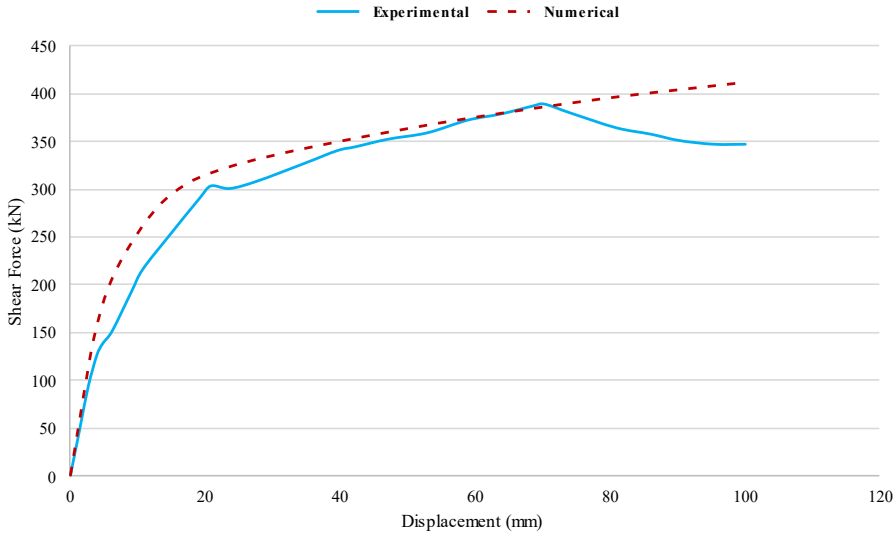

Fig. 5. Meshing of the steel shear wall with trapezoidal corrugated plate and central opening.

2.2. Corrugated steel shear wall details and variations

In order to investigate the behavior of trapezoidally corrugated steel shear walls with openings, a series of finite element models was developed by varying the geometric and strengthening parameters. The main variables included the location of the opening (center, left, or right), the number of openings (one or two), the orientation of corrugation (vertical or horizontal), as well as the presence or absence of stiffeners around the openings. Based on these parameters, different wall configurations were defined, as summarized in Table 2.

Table 2. Configurations of trapezoidally corrugated steel shear walls with openings.

Specimen ID	Description
SWV-O1-M	Vertically corrugated steel shear wall with a single central opening
SWH-O1-M	Horizontally corrugated steel shear wall with a single central opening
SWV-O2-L&R	Vertically corrugated steel shear wall with two openings located at the left and right sides
SWH-O2-L&R	Horizontally corrugated steel shear wall with two openings located at the left and right sides
SWV-OS1-M	Vertically corrugated steel shear wall with a single central opening strengthened by stiffeners of 1.25 mm thickness and 50 mm width around the opening
SWH-OS1-M	Horizontally corrugated steel shear wall with a single central opening strengthened by stiffeners of 1.25 mm thickness and 50 mm width around the opening
SWV-O1-L	Vertically corrugated steel shear wall with a single opening located on the left side

SWV-O1-R	Vertically corrugated steel shear wall with a single opening located on the right side
SWV1-OS1-M	Vertically corrugated steel shear wall with a single central opening strengthened by stiffeners of 3 mm thickness around the opening
SWV2-OS1-M	Vertically corrugated steel shear wall with a single central opening strengthened by stiffeners of 1.25 mm thickness and 70 mm width around the opening

The nomenclature used in Table 2 is as follows:

- SWV: steel shear wall with vertically oriented corrugated plate.
- SWH: steel shear wall with horizontally oriented corrugated plate.
- O: denotes the presence of an opening (the adjacent number indicates the number of openings).
- M, L, R: represent an opening located at the middle, left, or right of the wall, respectively.
- OS: indicates the use of stiffeners around the opening.

For the specimens with two openings, each opening had dimensions of 400 × 650 mm, providing an opening area equivalent to the single-opening configuration with dimensions of 800 × 650 mm. The clear spacing between the two openings was set to 796 mm. For walls with a left or right opening, the opening size was kept consistent with the validated reference specimen, while a 150 mm edge distance from the wall boundary was considered. Stiffeners were modeled with the same thickness as the corrugated plate, and their widths were assigned as 50 mm and 70 mm to ensure they did not exceed the flange width of the IPB140 beams and protrude beyond the wall surface. Two stiffener thicknesses, 1.25 mm and 3 mm, were considered.

In all cases, a maximum lateral displacement of 100 mm was applied in order to evaluate the shear capacity, energy dissipation, and overall performance of the models and to provide a direct comparison with the validated specimen. Representative configurations of the corrugated steel shear walls with various parameters are illustrated in Fig. 6.

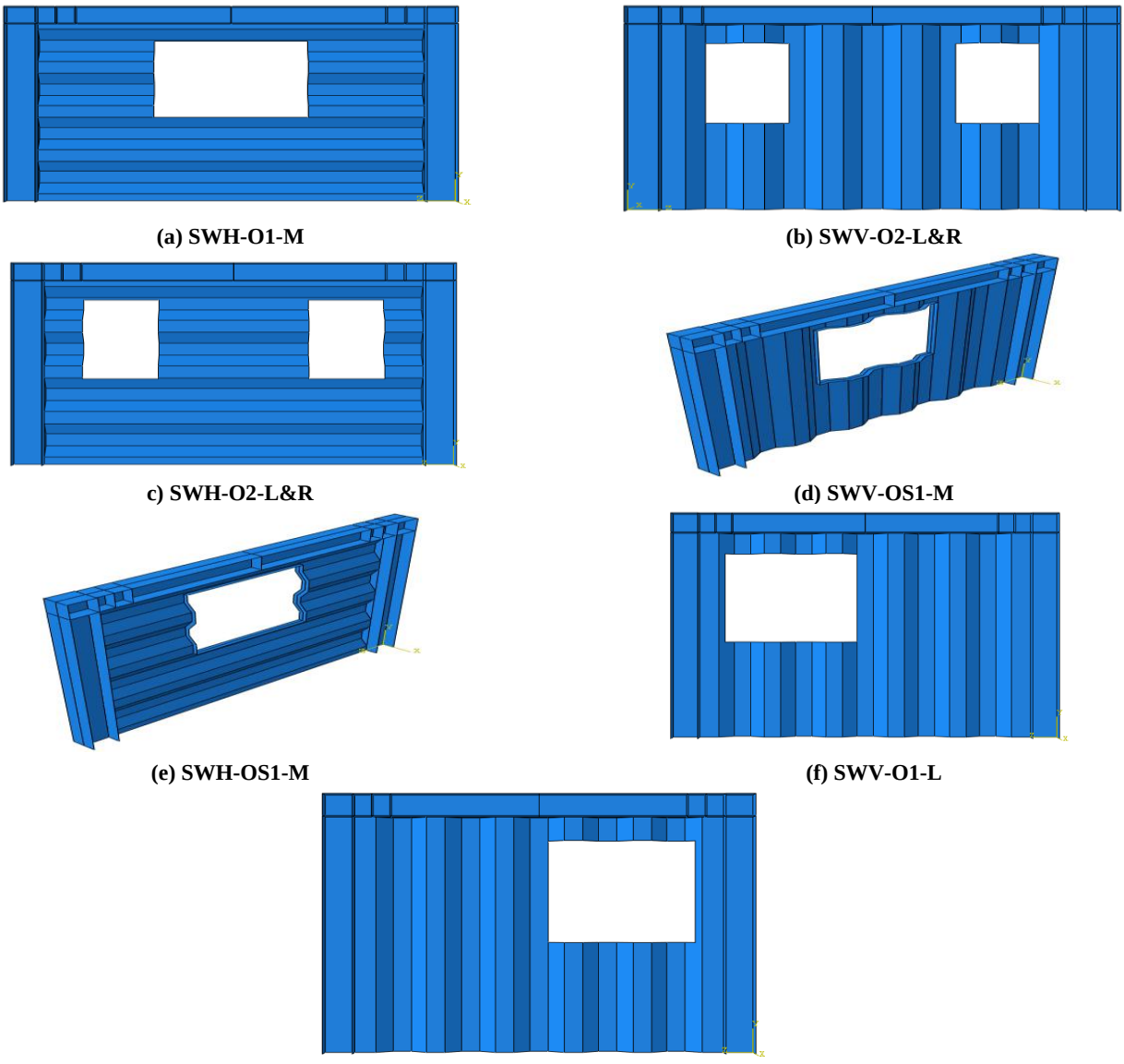

(a) SWH-O1-M **(b) SWV-O2-L&R**

c) SWH-O2-L&R **(d) SWV-OS1-M**

(e) SWH-OS1-M **(f) SWV-O1-L**

(g) SWV-O1-R

Fig. 6. Simulated trapezoidally corrugated steel shear walls with openings under different configurations.

3. Result and discussion

Trapezoidally corrugated steel shear walls with openings were modeled under various configurations. The considered variables included the number of openings, the location of openings, the presence of stiffeners around the openings, and the orientation of the corrugations in the shear wall panel.

3.1. shear capacity of corrugated steel shear walls

Fig. 7 illustrates the shear force–displacement curves for all specimens. As shown, the maximum lateral displacement was kept constant at 100 mm for all models to enable a reliable comparison of the results. A comparison between the horizontally corrugated specimen with a central opening (SWH-O1-M) and the vertically corrugated specimen with a central opening (SWV-O1-M) indicates that the shear capacity decreased by approximately 25.4% when the corrugation direction was changed from vertical to horizontal. This reduction is attributed to the influence of corrugation orientation. Similar findings were reported by Emami et al. [4], who concluded that trapezoidally corrugated steel shear walls with vertical corrugations exhibit superior load-bearing performance compared to those with horizontal corrugations.

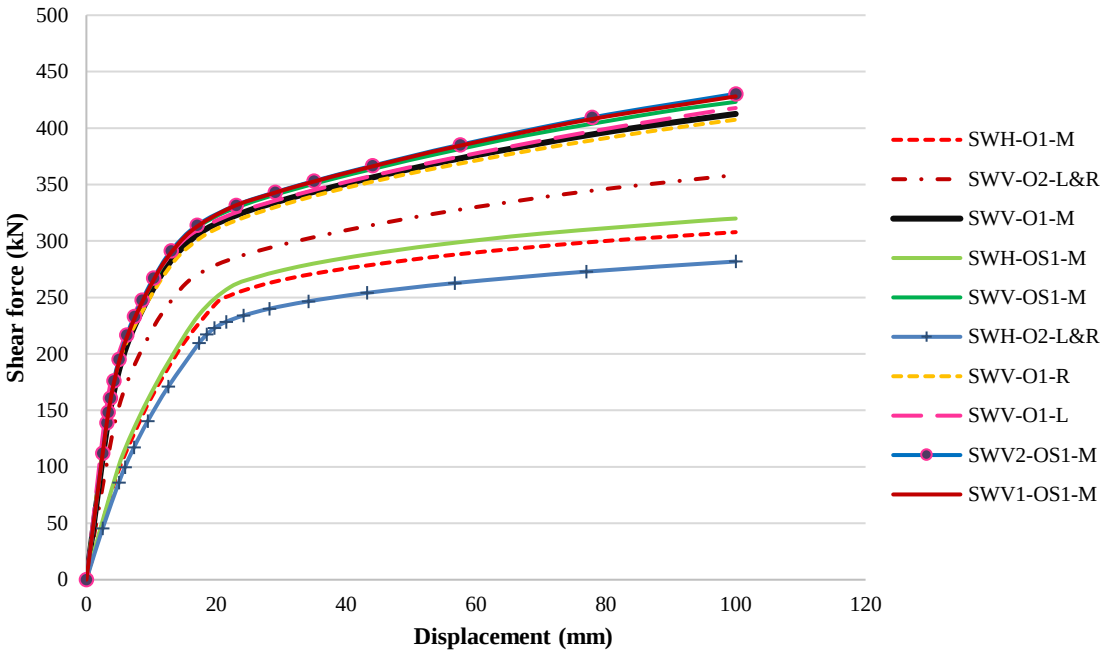

Fig. 7. Shear force–displacement responses of trapezoidally corrugated steel shear walls under various configurations.

Additionally, a comparison between the vertically corrugated steel shear wall with two side openings (SWV-O2-L&R) and the vertically corrugated steel shear wall with a single central opening (SWV-O1-M) indicates that increasing the number of openings, while maintaining the same total opening area, reduces the overall performance of the system, resulting in a 16.4% decrease in shear capacity. Furthermore, the corrugation orientation appears to play a decisive role in the influence of the number of openings. For example, in the horizontally corrugated specimen with a single central opening, the shear capacity reached 307.9 kN, whereas in the corresponding specimen with two side openings, the shear capacity decreased to 281.8 kN, representing an 8.5% reduction. These findings suggest that, even when the total opening area is kept constant, the dimensions and distribution of the openings can have a significant effect on the shear performance of trapezoidally corrugated steel shear walls.

A comparison between vertically and horizontally corrugated steel shear walls with openings and stiffeners demonstrates that stiffeners can have a favorable effect on the shear capacity (load-bearing capacity) of the system. However, due to the relatively small width of the stiffeners, this effect was not very significant. For the vertically corrugated specimen with a central opening and stiffeners (SWV-OS1-M), the shear capacity increased by 2.6% compared to the corresponding specimen without stiffeners (SWV-O1-M). Similarly, for the horizontally corrugated specimen with a central opening and stiffeners (SWH-OS1-M), the shear capacity increased by 3.9% relative to the unstiffened configuration (SWH-O1-M). These findings confirm that the presence of stiffeners improves the performance of corrugated steel shear walls with openings, a trend also observed in the studies of James and Kumar [7].

Based on the results obtained for the effect of opening location in trapezoidally corrugated steel shear walls, it can be concluded that the farther the opening is placed from the loading point, the higher the shear capacity becomes. A comparison of three vertically corrugated steel shear walls with openings located at the right side (close to the loading point), center, and left side (farther from the loading point) revealed shear capacities of 417.8 kN, 412.6 kN, and 407.5 kN, respectively. Given the relatively large size of the openings, the influence of their location was not very pronounced. Nevertheless, comparing the specimen with a left-side opening (SWV-O1-L) to the specimen with a central opening (SWV-O1-M) showed a 1.3% increase in shear capacity. Conversely, the specimen with a right-side opening near the loading point (SWV-O1-R) exhibited a 1.2% reduction in shear capacity compared to the central opening configuration (SWV-O1-M). These findings are consistent with the study of Veena and Reshmi [15], who

reported that corrugated steel shear walls with corner openings exhibited greater load-bearing capacity than those with central openings, due to the increased distance of the opening from the loading region.

Increasing the stiffener thickness from 1.25 mm to 3 mm resulted in an approximately 2% improvement in the shear capacity of trapezoidally corrugated steel shear walls with openings, which is not considered significant. Likewise, increasing the stiffener width from 50 mm to 70 mm led to an approximately 3% increase in shear capacity, which is also relatively minor. Fig. 8 presents a comparison of the shear forces for all corrugated steel shear wall specimens with openings, both with and without stiffeners. Furthermore, Fig. 8 summarizes the shear capacity results for all configurations of trapezoidally corrugated steel shear walls with openings, with and without stiffeners.

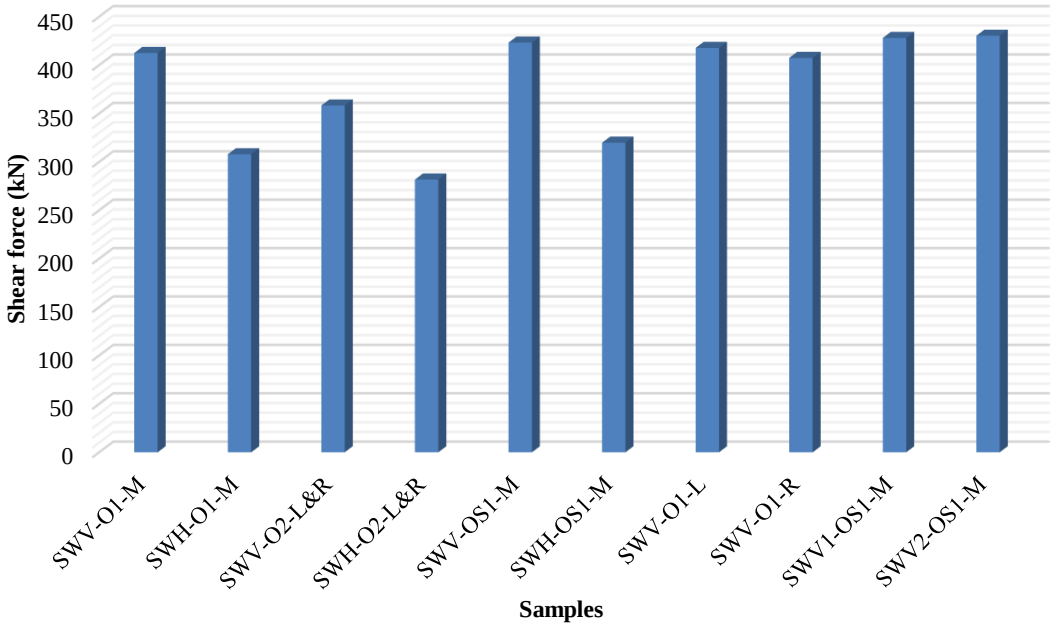

Fig. 8. Shear force comparison of corrugated steel shear walls with openings, with and without stiffeners.

3.2. Energy absorption capacity of steel shear walls

Fig. 9 presents the energy dissipation results for all specimens. A comparison between the horizontally corrugated wall with a central opening (SWH-O1-M) and the vertically corrugated wall with a central opening (SWV-O1-M) shows that the energy dissipation decreased by approximately 24.6% when the corrugation direction changed from vertical to horizontal. This reduction is attributed to the orientation of the corrugated plate. Similar trends were reported by Beheshti [25], who demonstrated that the absorbed energy increases with favorable corrugation orientation, confirming the validity of the present results.

Furthermore, a comparison between the vertically corrugated steel shear wall with two side openings (SWV-O2-L&R) and the vertically corrugated wall with a single central opening (SWV-O1-M) reveals that increasing the number of openings, while keeping the total opening area constant, reduces the performance of the corrugated steel shear wall. This reduction is mainly attributed to the proximity of the openings to the wall boundaries, which led to a 16% decrease in energy dissipation. Similarly, in the horizontally corrugated specimen with a single central opening, the absorbed energy was 25,878.7 J, whereas in the corresponding specimen with two side openings, the absorbed energy decreased to 23,630.1 J, representing an 8.7% reduction.

Comparison between vertically and horizontally corrugated steel shear walls with openings and stiffeners indicates that the inclusion of stiffeners can have a positive effect on enhancing the energy absorption capacity. For the vertically corrugated specimen with a central opening and stiffeners (SWV-OS1-M), the energy absorption increased by 2.4% compared to the corresponding specimen without stiffeners (SWV-O1-M). Similarly, for the horizontally corrugated specimen with a central opening and stiffeners (SWH-OS1-M), the energy absorption increased by 3.5% relative to the unstiffened specimen (SWH-O1-M).

A comparison of three vertically corrugated steel shear walls with openings located on the right side (close to the loading point), center, and left side (farther from the loading point) showed energy absorption values of 26,792 J, 34,319 J, and 34,698.8 J, respectively. Furthermore, comparing the specimen with a left-side opening (SWV-O1-L) to the specimen with a central opening (SWV-O1-M) indicated a 1.1% increase in energy absorption. Conversely, the specimen with a right-side opening near the loading point (SWV-O1-R) exhibited a 1% reduction in energy absorption compared to the central opening configuration (SWV-O1-M). Table 4 summarizes the energy absorption results of all trapezoidally corrugated steel shear wall specimens with openings, with and without stiffeners.

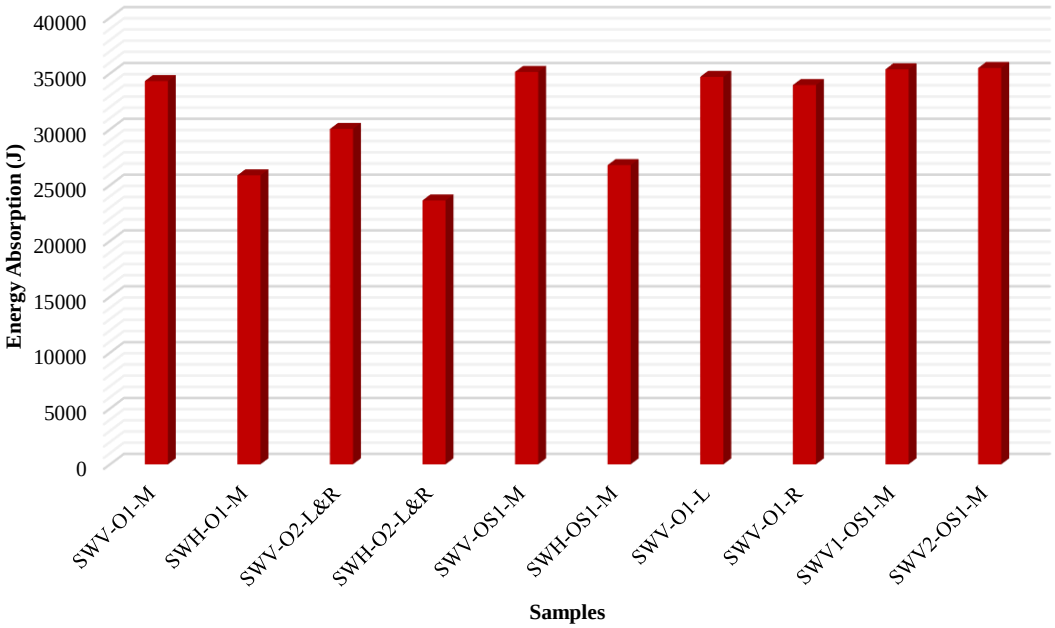

Fig. 9. Energy absorption capacity of corrugated steel shear walls with openings, with and without stiffeners.

3.3. Von Mises stress response of extreme performance models

Von Mises stress was selected to evaluate the yield behavior and stress distribution in corrugated steel shear walls due to its ability to account for combined stress states under complex loading, providing a reliable indicator of material failure and structural performance. Based on the results presented in Table 3 and Table 4, it can be observed that among all the studied configurations, the horizontally corrugated steel shear wall with two side openings (SWH-O2-L&R) exhibited the lowest shear capacity and energy absorption, whereas the vertically corrugated steel shear wall with a central opening and strengthened by stiffeners (SWV2-OS1-M) demonstrated the highest shear capacity and energy absorption. Further, evaluating the stress distribution mechanisms in these two extreme cases, the von Mises stress contours of the SWH-O2-L&R and SWV2-OS1-M models are presented in Fig. 10 and Fig. 11.

Table 3. Summary of shear force results for all trapezoidally corrugated steel shear wall specimens with openings, with and without stiffeners.

Specimen ID	Shear force (kN)
SWV-O1-M	412.6
SWH-O1-M	307.9
SWV-O2-L&R	358.3
SWH-O2-L&R	281.8
SWV-OS1-M	423.3
SWH-OS1-M	319.9
SWV-O1-L	417.8
SWV-O1-R	407.5
SWV1-OS1-M	428.1
SWV2-OS1-M	430.4

Table 4. Summary of energy absorption results for all trapezoidally corrugated steel shear wall specimens with openings, with and without stiffeners.

Specimen ID	Energy absorption (J)
SWV-O1-M	34319
SWH-O1-M	25878.7
SWV-O2-L&R	30030.9
SWH-O2-L&R	23630.1
SWV-OS1-M	35138.5
SWH-OS1-M	26792
SWV-O1-L	34698.8
SWV-O1-R	33964.2

SWV1-OS1-M	35378.4
SWV2-OS1-M	35488.6

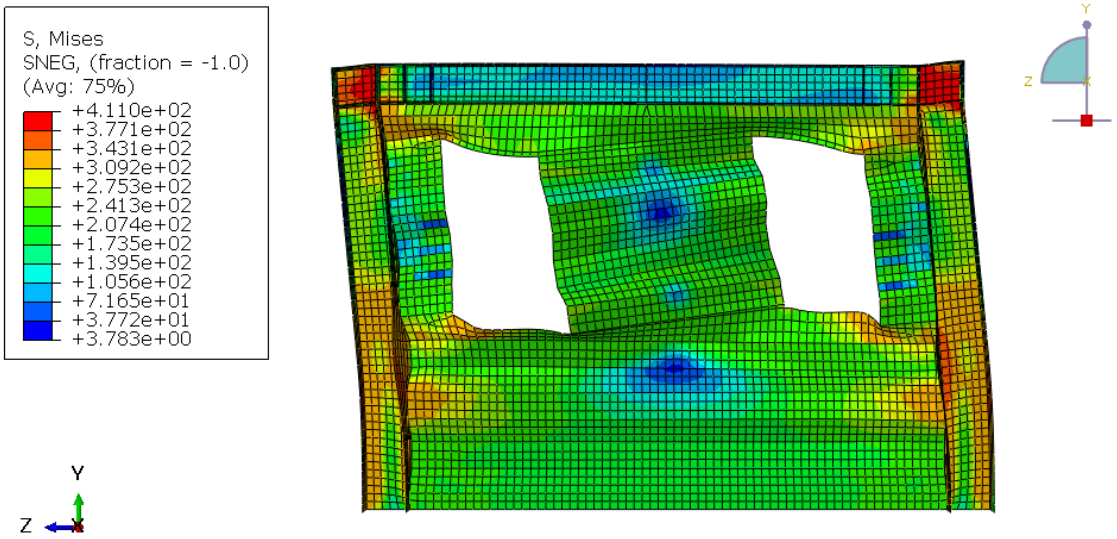

Fig. 10. Von Mises stress distribution in the horizontally corrugated steel shear wall with two openings (SWH-O2-L&R).

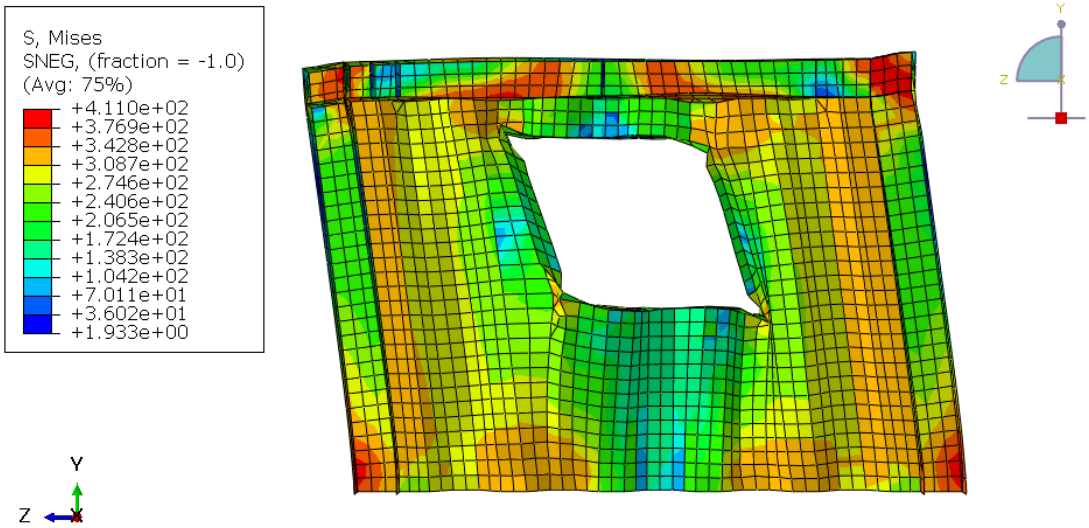

Fig. 11. Von Mises stress distribution in the vertically corrugated steel shear wall with a central opening and 70 mm stiffeners (SWV2-OS1-M).

In the horizontally corrugated wall with two side openings (SWH-O2-L&R) (Fig. 10), pronounced stress concentrations are observed around the edges of the openings and at the boundary connections of the wall. The horizontal corrugation orientation, combined with the placement of two openings near the wall edges, causes stress localization and premature yielding. This explains the lower shear capacity and reduced energy absorption observed for this specimen. Conversely, the vertically corrugated wall with a central stiffened opening (SWV2-OS1-M) (Fig. 11) exhibits a more uniform stress distribution across the panel. The vertical corrugation direction enhances load transfer, while the stiffeners surrounding the central opening effectively mitigate stress concentrations. As a result, this specimen demonstrates the highest shear strength and energy absorption capacity among all tested configurations. This comparison highlights that not only the magnitude but also the distribution of von Mises stresses governs the structural performance. Uniform stress spread, even at moderately higher stress levels, leads to improved ductility, higher energy dissipation, and superior load-bearing capacity, while localized stress peaks accelerate structural weakening and reduce performance.

4. Conclusion

This study presents a detailed numerical investigation into the structural performance of trapezoidally corrugated steel plate shear walls (CSPSWs) with openings, employing finite element modeling to assess the impacts of corrugation orientation, opening configurations, and stiffener designs on shear capacity, energy dissipation, and stress distribution. The key findings underscore significant performance variations:

1. Corrugation Orientation: Vertically corrugated CSPSWs demonstrated superior performance, achieving up to 25% higher shear capacity and 24% greater energy absorption compared to horizontally corrugated counterparts with central openings. This aligns with Wen et al. [21], who noted enhanced hysteretic stability in vertical configurations, though our study quantifies a more pronounced energy dissipation advantage (24% vs. their 15–20%) due to optimized opening placement.
2. Opening Configuration: Increasing the number of openings, while maintaining total area, reduced shear capacity and energy absorption, with boundary openings exacerbating stress concentrations by up to 15% more than central openings. This corroborates Bahrebar et al. [12], who reported similar reductions, but our analysis highlights a location-specific effect not previously detailed, enhancing design precision.
3. Stiffener Influence: Stiffeners around openings modestly improved performance, with thickness increases from 1.25 mm to 3 mm, boosting shear capacity by 2% and width increases from 50 mm to 70 mm by 3%, alongside a 2–4% rise in energy absorption. This aligns with Tong et al. [18], who observed stiffener-induced buckling restraint, though our findings suggest a smaller incremental gain (2–4% vs. their 10–15%), likely due to opening-induced stress redistribution.
4. Stress Distribution: Von Mises stress analysis revealed that performance hinges on stress uniformity. The vertically corrugated, stiffened central opening model (SWV2-OS1-M) outperformed the horizontally corrugated dual-side opening model (SWH-O2-L&R), which exhibited critical stress concentrations at edges. This finding extends Wu et al. (2025), who emphasized torsional rigidity, by integrating opening effects into stress distribution patterns.

Collectively, these results affirm that vertical corrugation with stiffened central openings optimizes shear strength and energy dissipation, offering a 20–30% performance edge over horizontal setups, as validated against experimental data from Emami et al. [4] and numerical benchmarks from Wu and Tong [23]. This study advances seismic design by providing actionable insights for material-efficient, resilient CSPSWs, reducing construction demands by up to 15% compared to traditional flat steel shear walls, as supported by Cao and Huang [11]. For seismic design, vertical corrugation with stiffened central openings is preferred to maximize shear strength and energy dissipation while optimizing material use. These findings guide engineers in tailoring CSPSW configurations for enhanced safety and sustainability in earthquake-prone regions.

Statements & Declarations

Author contributions

Mehdi Azarbara: Investigation, Formal analysis, Validation, Resources, Writing - Original Draft, Writing - Review & Editing.

Rahmat Madandoust: Conceptualization, Methodology, Project administration, Supervision, Writing - Review & Editing.

Funding

The authors received no financial support for the research, authorship, and/or publication of this article.

Data availability

The data presented in this study will be available on interested request from the corresponding author.

Declarations

The authors declare no conflict of interest.

References

[1] Sabouri, S. Lateral Load-Resisting Systems: The Concept of Using Mild Steel. 1st ed. Tehran (IR): Angizeh Publications; 2004 (In Persian).

[2] Ghobaadi, M. S. Seismic Behavior of Steel Shear Walls (Master Thesis). Tehran (IR): University of Tehran; 2003 (In Persian).

[3] Sabouri-Ghomi, S., Ventura Carlos, E., Kharrazi Mehdi, H. Shear Analysis and Design of Ductile Steel Plate Walls. Journal of Structural Engineering, 2005; 131: 878-889. doi:10.1061/(ASCE)0733-9445(2005)131:6(878).

[4] Emami, F., Mofid, M., Vafai, A. Experimental study on cyclic behavior of trapezoidally corrugated steel shear walls. Engineering Structures, 2013; 48: 750-762. doi:10.1016/j.engstruct.2012.11.028.

[5] Vigh, L. G., Liel, A. B., Deierlein, G. G., Miranda, E., Tipping, S. Component model calibration for cyclic behavior of a corrugated shear wall. Thin-Walled Structures, 2014; 75: 53-62. doi:10.1016/j.tws.2013.10.011.

[6] Farzampour, A., Laman, J. A., Mofid, M. Behavior prediction of corrugated steel plate shear walls with openings. Journal of Constructional Steel Research, 2015; 114: 258-268. doi:10.1016/j.jcsr.2015.07.018.

[7] James, J., Kumar, A. S. Corrugated Steel Plate Shear Wall with Opening and Stiffener at Opening. International Journal of Science and Research, 2016; 5: 1205-1209. doi:10.21275/ART2016382.

[8] Bahrebar, M., Kabir, M. Z., Zirakian, T., Hajsadeghi, M., Lim, J. B. P. Structural performance assessment of trapezoidally-corrugated and centrally-perforated steel plate shear walls. Journal of Constructional Steel Research, 2016; 122: 584-594. doi:10.1016/j.jcsr.2016.03.030.

[9] Farzampour, A., Mansouri, I., Lee, C.-H., Sim, H.-B., Hu, J. W. Analysis and design recommendations for corrugated steel plate shear walls with a reduced beam section. Thin-Walled Structures, 2018; 132: 658-666. doi:10.1016/j.tws.2018.09.026.

[10] Dou, C., Pi, Y.-L., Gao, W. Shear resistance and post-buckling behavior of corrugated panels in steel plate shear walls. Thin-Walled Structures, 2018; 131: 816-826. doi:10.1016/j.tws.2018.07.039.

[11] Cao, Q., Huang, J. Experimental study and numerical simulation of corrugated steel plate shear walls subjected to cyclic loads. Thin-Walled Structures, 2018; 127: 306-317. doi:10.1016/j.tws.2018.01.042.

[12] Bahrebar, M., Lim, J. B. P., Clifton, G. C., Zirakian, T., Shahmohammadi, A., Hajsadeghi, M. Response assessment and prediction of low yield point steel plate shear walls with curved corrugated web plates and reduced beam sections. Structures, 2020; 28: 1729-1745. doi:10.1016/j.istruc.2020.09.071.

[13] Mu, Z., Yang, Y. Experimental and numerical study on seismic behavior of obliquely stiffened steel plate shear walls with openings. Thin-Walled Structures, 2020; 146: 106457. doi:10.1016/j.tws.2019.106457.

[14] Gilvaee, M. Y., Mofid, M. Experimental/Numerical Evaluation of Steel Trapezoidal Corrugated Infill Panels with an Opening. Applied Sciences, 2021; 11: 3275.

[15] Veena, N., Reshmi, P. R. Lateral Resistance Capacity and Strengthening of Corrugated Steel Wall with Different Openings. International Journal of Engineering Research & Technology, 2020; 9: doi:10.17577/IJERTV9IS060991.

[16] Joharchi, A., Osman, S. A., Yatim, M. Y. M., Ansari, M. Numerical Parametric Study on the Cyclic Performance of Trapezoidally Corrugated Steel Shear Walls. Civil Engineering and Architecture, 2021; 9: 462-476.

[17] Qiu, J., Zhao, Q., Yu, C., Wang, Z. Lateral behavior of trapezoidally corrugated wall plates in steel plate shear walls, Part 2: Shear strength and post-peak behavior. Thin-Walled Structures, 2022; 174: 109103. doi:10.1016/j.tws.2022.109103.

[18] Tong, J., Wu, R., Wang, L. Experimental and numerical investigations on seismic behavior of stiffened corrugated steel plate shear walls. Earthquake Engineering & Structural Dynamics, 2023; 52: 3551-3574. doi:10.1002/eqe.3920.

[19] Wen, C.-B., Sun, H.-J., Liu, Y.-Z., Hou, Y.-G., Zuo, J.-Q., Guo, Y.-L. Cyclic tests and shear resistance design of stiffened corrugated steel plate shear walls. Engineering Structures, 2024; 298: 117060. doi:10.1016/j.engstruct.2023.117060.

[20] Wu, R.-M., Wang, L.-Q., Tong, J.-Z., Tong, G.-S., Gao, W. Elastic buckling formulas of multi-stiffened corrugated steel plate shear walls. Engineering Structures, 2024; 300: 117218. doi:10.1016/j.engstruct.2023.117218.

[21] Wen, C.-B., Zhu, B.-L., Sun, H.-J., Guo, Y.-L., Zheng, W.-J., Deng, L.-L. Global stability design of double corrugated steel plate shear walls under combined shear and compression loads. Thin-Walled Structures, 2024; 199: 111789. doi:10.1016/j.tws.2024.111789.

[22] Wu, R.-M., Yu, C.-Q., Wang, L.-Q., Tong, J.-Z. Shear elastic buckling of corrugated steel plate shear walls with stiffeners considering torsional rigidity. Thin-Walled Structures, 2025; 206: 112646. doi:10.1016/j.tws.2024.112646.

[23] Wu, R.-M., Tong, J.-Z. Shear strength and post-ultimate behavior of multi-stiffened corrugated steel plate shear walls. Journal of Constructional Steel Research, 2025; 229: 109480. doi:10.1016/j.jcsr.2025.109480.

[24] International Code Council. AC154: Cyclic Racking Shear Tests for Metal-sheathed Shear Walls with Steel Framing. Washington D.C. (D.C.): ICC; 2000.

[25] Beheshti, M. Investigation of the behavior of trapezoidal corrugated steel shear wall with opening and stiffener (Master Thesis). Mashhad (IR): Ferdowsi University of Mashhad; 2021 (In Persian).

Civil Engineering and Applied Solutions

Research Article

journal homepage: ceas.journals.umz.ac.ir

CEAS Civil Engineering and Applied Solutions

Effect of Subsurface Cavities on the Bearing Capacity of Shallow Strip Foundations in Soft Clay: A Numerical Study

Vali Ghaseminejad [a*], Atina Tarrah [a], Fereshteh Ghomi [a]

[a] *Department of Civil Engineering, Nowshahr Branch, Islamic Azad University, Nowshahr, Iran*

ARTICLE INFO

Keywords:
Shallow foundations
Bearing capacity
Subsurface cavities
Clay soils
Finite element analysis

Article history:
Received 19 August 2025
Accepted 22 October 2025
Available online 01 April 2026

ABSTRACT

Subsurface cavities, both natural and anthropogenic, pose significant geotechnical challenges by altering stress distribution beneath shallow foundations. Conventional design approaches for strip footings often neglect the effects of such voids, potentially resulting in unsafe or overly conservative designs. This study employs a numerical investigation using the finite element software PLAXIS 2D to assess the impact of underground cavities on the bearing capacity of shallow strip foundations resting on soft clay. A parametric analysis was conducted to examine the effects of cavity diameter, embedment depth, and both horizontal and vertical offsets relative to the footing center. The Results indicate that increasing cavity diameter markedly reduces the ultimate bearing capacity. Additionally, increasing the cavity diameter from 0.25 to 0.5 times the footing width led to a 25%–40% decrease in load-bearing capacity. The study also identifies a critical influence zone beneath the footing where the presence of voids most significantly compromises performance. These findings underscore the importance of incorporating subsurface cavity effects into geotechnical design, particularly in urban areas, to enhance the safety and reliability of shallow foundations on soft clay. The parametric study covered cavity diameters D = 0.5–1.0 m, embedment depths Y = 2, 4, and 10 m, and horizontal eccentricities X = 0, 1, 6, and 10 m for a strip footing of width B = 2.0 m. Quantitatively, increasing D from 0.5 m to 1.0 m at Y = 2 m reduced the ultimate bearing capacity by ≈200 kPa (≈56.7%).

1. Introduction

Shallow foundations are essential load-transfer elements in structural systems, responsible for transmitting applied loads and self-weight to the underlying soil. The effectiveness of this transfer depends on two primary criteria: preventing shear failure in the subsoil and maintaining settlements within acceptable limits. Therefore, determining the bearing capacity of the supporting soil, the maximum stress a foundation can safely impose, has long been a central focus in geotechnical the many parameters influencing the ultimate bearing capacity of shallow foundations are foundation geometry, load eccentricity, and the mechanical properties of the subsoil, particularly its shear one critical factor often overlooked in conventional design is the presence of subsurface cavities beneath or adjacent to the foundation. These voids may be naturally occurring, such as in karstic limestone formations, or anthropogenic, as in the case of tunnels, abandoned qanats, or sewer pits. Particularly in urban environments, these cavities can form close to or directly below existing structures, compromising foundation performance and stability.

With increasing urbanization and population growth worldwide, the demand for subsurface infrastructure, including transportation tunnels, utility corridors, and metro lines, has surged. Surface-level construction in densely built environments is often constrained by limited space, high costs, and potential disruptions to existing infrastructure. As a result, underground development has become an attractive and viable solution. However, such development presents several geotechnical challenges,

* Corresponding author.
E-mail addresses: vghaseminejad@gmail.com (V. Ghaseminejad).

https://doi.org/10.22080/ceas.2025.29867.1036
ISSN: 3092-7749/© 2026 The Author(s). Published by University of Mazandaran.
This article is an open access article distributed under the terms and conditions of the Creative Commons Attribution (CC-BY) license (https://creativecommons.org/licenses/by/4.0/deed.en)
How to cite this article: Garakaninezhad, A., Amiri, S., Ghomi, F. Finite Developing Inelastic Jerk Spectra for Pulse-Like Earthquakes. Civil Engineering and Applied Solutions. 2026; 2(2): 71–84. doi:10.22080/ceas.2025.29867.1036.

particularly the potential for ground deformation and surface settlement caused by excavation. These displacements can adversely affect shallow foundations located near the surface. Although modern mechanized tunneling technologies, such as Tunnel Boring Machines (TBMs), offer some control over surface settlement by regulating face pressure, excessive pressure may lead to unintended consequences such as ground heave or changes in groundwater conditions. Regardless of the tunneling method employed, both short- and long-term displacements should be accurately predicted, and proactive measures implemented to safeguard adjacent structures. This is especially crucial for shallow foundations, which are more vulnerable to ground movements due to their proximity to the surface. The presence of shallow-buried cavities beneath foundations can intensify settlement effects and introduce stress concentrations that may lead to partial or total failure. The extent of such effects depends on the cavity's size, depth, and horizontal offset relative to the foundation's centerline. Without adequate stabilization, these voids may collapse or cause unacceptable levels of deformation. Various stabilization methods have been proposed, including grouting, construction of reinforced concrete slabs, deep foundation systems such as piles, backfilling with appropriate materials, and soil reinforcement using geosynthetics. In this study, a comprehensive numerical investigation is conducted to assess the effects of subsurface cavities on the load-bearing behavior of shallow foundations in clay soils. The modeled system includes the interaction between the footing, soil, and cavity. Key parameters such as cavity size, burial depth, and eccentricity are systematically varied. The foundation is assumed to behave as a rigid strip footing. This analysis provides insight into surface deformation patterns and the influence of underground voids on foundation capacity, offering practical guidance for geotechnical engineers designing foundations in urban environments prone to subsurface anomalies.

The presence of subsurface cavities, either natural or man-made, can significantly influence the load-bearing behavior of shallow foundations. Numerous researchers have investigated this phenomenon using analytical, numerical, and experimental methods to better understand how cavity geometry, location, and soil conditions affect foundation stability. One of the earliest studies was conducted by, who employed finite element analysis to assess the stability of strip footings overlying cavities in dense silty clay, assuming elasto-plastic soil behavior. This foundational work was extended by, who examined the settlement behavior of foundations located above single cavities. Further investigations by Baus and Wang [1] analyzed the influence of tunnel geometry and position on the bearing capacity of surface foundations and validated the results through laboratory experiments. Jao and Wang [2] performed a parametric finite element analysis using the Drucker–Prager yield criterion to study concrete-lined tunnels in soft soils such as silty clay, kaolinite, and clayey sand. Their results showed that lined tunnels improve soil confinement and reduce settlement. They introduced dimensionless ratios, including tunnel depth to footing width (*D/B*) and tunnel diameter to footing width (W/B), and concluded that the effect of cavities becomes negligible when located beyond a critical depth. Additionally, lining thickness significantly improves bearing capacity and reduces deformation. Sireesh et al. [3] evaluated the use of geocell-reinforced sand mattresses over cavities in clayey soils. Their experimental study demonstrated enhanced bearing capacity and reduced settlement, along with delayed failure propagation beneath the footing.

Lee et al. [4] proposed undrained design charts for strip footings above cavities in soft clays. By adopting a parametric approach and using finite element simulations, they found that footing eccentricity, cavity rigidity, and position strongly influence the dimensionless bearing capacity factor. Soil stiffness, cavity depth, and geometric ratios were also found to affect footing performance. Asgari and Ahmadtabar Sorkhi [5] investigated the seismic performance of offshore wind turbines on monopiles in liquefiable soils under waves, winds, and earthquakes using 3D parametric models in OpenSees. Results showed that turbine responses increase with wind speed, wave height, and seismic-induced soil liquefaction. Combined loads of earthquake, wind, and waves significantly amplify the system response, highlighting the need to consider multi-hazard effects in design.

Jahangiri et al. [6] studied applying supervised machine learning to predict maximum inter-story drift in steel diagrid structures, reducing reliance on intensive simulations. Twenty-one algorithms were evaluated, with Extra Trees, Random Forest, and Bagging showing $R^2 > 0.95$. The approach provides an efficient, accurate tool for seismic vulnerability assessment of diagrid systems. Asgari et al. [7] evaluated the axial tension and compression capacities of helical piles in dense Shahriyar sand through laboratory tests. Results show that compressive and tensile capacities can reach up to six and eleven times the shaft capacity, respectively, with performance improving for multiple helices and smaller pitches. Theoretical predictions slightly underestimated or overestimated capacities depending on pile type and loading mode. Ebadi-Jamkhaneh et al. [8] evaluated the pullout performance of helical piles in dense sand reinforced with geogrid layers. Results show that geogrid significantly enhances resistance, with single-helix piles achieving up to 518% higher capacity than plain piles, and optimal performance depending on geogrid spacing. The findings highlight the synergistic effects of pile configuration and geogrid placement for reinforced foundation design. Asgari et al. [9] studied used 3D finite element analysis to assess seismic response of pile groups in sloping liquefiable soils. Results show that pile number, position, nonlinearity, and frequency content significantly affect displacements, internal forces, and acceleration, with corner piles being most sensitive. Current design codes (JRA, API) often over- or underestimate soil pressures, highlighting the need for improved analysis for pile group design. Asadoullahtabar et al. [10] investigated the collapse and dispersion potential of loess soils in Golestan, Iran, affecting infrastructure such as gas pipelines. Laboratory and field tests showed that collapsibility contributes to soil scouring, posing risks to roads and pipelines. Chemical stabilization using cement and nano-titanium proved effective, with nano-titanium offering a more environmentally sustainable solution. Bagheri et al. [11] studied and evaluated the seismic performance of two 30-story RC buildings with conventional frames (MF) and dual systems with shear walls (MFSW) on composite piled raft foundations, considering soil–structure interaction. Results show that MFSW reduces interstory drifts by up to 56%, improves soil stress distribution, and increases seismic resilience compared to MF. Hybrid pile configurations optimize foundation performance, limiting soil shear strains and highlighting SSI-induced displacement amplifications. Asgari et al. [12] investigated seismic responses of free-field, pile group, fixed-base, and shallow/deep foundation structures with varying height-to-width ratios in saturated and dry sands. 3D nonlinear finite element analyses show that soil–foundation–structure interaction (SFSI)

can either amplify or reduce structural response depending on soil stiffness and liquefaction potential. Flexible bases reduce flexural drifts and internal forces, while saturated soils increase base shear due to higher peak accelerations. Shooshpasha and Bagheri [13] studied the effect of surcharges on seismic responses of silty sands containing fines, which are prone to liquefaction and large deformations. Fully non-linear elasto-plastic dynamic analyses with coupled liquefaction triggering were conducted under two realistic earthquake events. Results show that pore pressure alone is insufficient to assess liquefaction, and deformation-based evaluation is essential for practical engineering design. Asgari et al. [14] investigated the seismic response of sands with plastic/non-plastic fines and silts under shallow foundations. Effects of soil type, foundation surcharge, liquefiable layer thickness, and earthquake parameters, including magnitude, PGA, and duration, on dynamic behavior and soil–structure interaction were analyzed. These studies highlight the importance of understanding soil–structure–earthquake interactions for improved seismic design. In summary, prior studies unanimously demonstrate that the presence of subsurface cavities can reduce the bearing capacity and increase the settlement of shallow foundations. Key influencing parameters include cavity depth, size, shape, lining condition, and relative location to the footing. The identification of a critical depth beyond which cavities have negligible influence has been a consistent finding, supporting the need for parametric and numerical evaluation in design.

Unlike many previous studies that considered single parameters or idealized conditions, this work systematically explores the combined influence of cavity diameter, embedment depth, and horizontal eccentricity on shallow strip footings in soft clay using high-order finite elements (15-node) in PLAXIS 2D. The study provides quantitative thresholds and reduction factors (e.g., reductions up to ~56% for shallow, large cavities beneath a 2.0 m footing) to assist practising engineers in preliminary risk assessment and design decisions.

2. Numerical modeling using PLAXIS software

2.1 Model geometry and material parameters

Fig. 1 is the two-dimensional model geometry used in this study, including a strip footing placed above a subsurface cavity. The model dimensions were selected to prevent any boundary effects, ensuring that the stress bulbs induced by the footing do not interfere with the model boundaries. Based on established recommendations, the horizontal and vertical extents of the model were taken as 40 m and 30 m, respectively, which are at least five times larger than the footing width. The boundary conditions were defined in accordance with standard practice for bearing capacity analysis in finite element simulations. The vertical boundary sides were constrained in the horizontal (x) direction to prevent lateral displacement, while the bottom boundary was fully fixed in both horizontal and vertical directions to maintain overall model stability. The top boundary remained free to allow vertical deformation due to loading. These settings correspond to the “standard boundary conditions” option available in PLAXIS 2D.

In the numerical modeling process, several key assumptions were considered to accurately simulate realistic conditions. To minimize the effects of rigid boundaries, the model dimensions were selected such that its width was at least 13 times and its height at least 10 times the footing width. The analyzed footing was of strip type and was modeled as a rigid body with its self-weight included. A plane strain condition was adopted, where the footing geometry was represented by plate elements, and the load was applied linearly along the plate surface. The soil behavior was simulated using the Mohr–Coulomb constitutive model. To prevent the collapse of the cavity crown under the overburden stress, cavities lined with concrete were modeled as rigid, and their self-weight was neglected. Additionally, a reference model without any cavity was first developed for comparison purposes. All models were constructed in two dimensions, and long-term (drained) conditions were assumed for different types of clay soils, with the groundwater table defined at the base of the model. The footing was assumed to rest directly on the soil surface with zero embedment depth. The bearing capacity of the footing was evaluated under ultimate conditions rather than allowable conditions, using the tangent method to determine the ultimate bearing capacity. In the modeling procedure, the geometry of the soil, cavity, and concrete lining was first generated, followed by the application of the linear load and the footing plate (Fig. 2).

Loading was applied in the form of a uniform surcharge of 800 kPa over the footing to simulate the applied stress and facilitate bearing capacity calculations. In general, PLAXIS allows loading to be applied either as force or prescribed displacement; in this validation case, force-controlled loading was used to evaluate the ultimate bearing capacity. The material parameters for the soil layers, strip footing, and cavity fill material were adopted from the reference study by Nepal and Yadav [15], and are summarized in Tables 1 to 3.

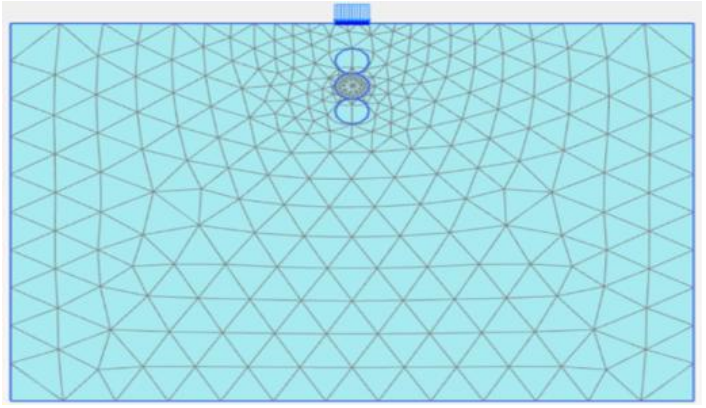

Fig. 1. Application of boundary conditions in the validation model.

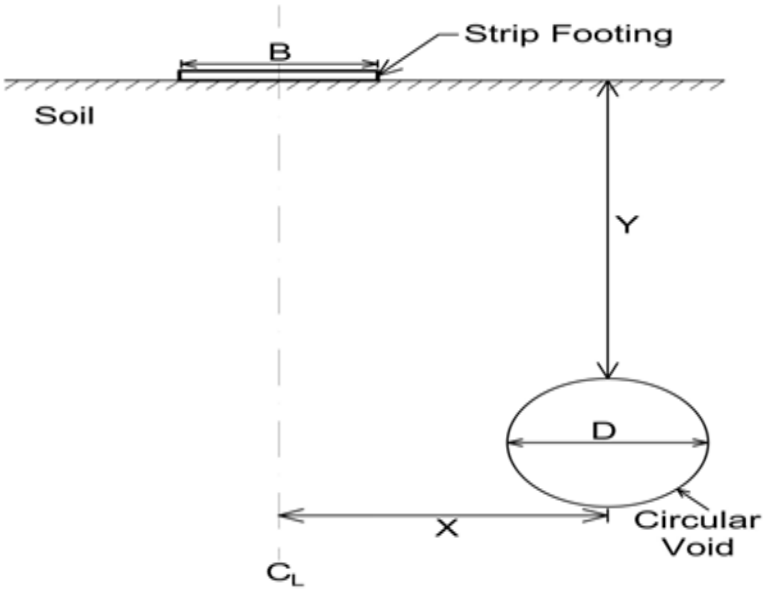

Fig. 2. Position of the cavity relative to the footing.

Table 1. Soil properties used in the study by Nepal and Yadav [15].

Geometrical Parameters	Values
Width of footing (*B*)	2 m
Width of analysis soil (*W*)	20B (40 m)
Depth of analysis soil (*D*)	15B (30 m)
Shape of void	Circular
Size of void (*D*)	2 m
Vertical position of void (*y*)	B, 2B, 3B, 4B, 5B, and 6B (from the base of the footing to the crest of the void)
Horizontal position of void (*x*)	0B, 1B, 2B, 3B, and 4B (from the center of the foundation to the center of the void)

Table 2. Geotechnical parameters in the Study by Nepal and Yadav [15].

Parameters	Values
Unit weight of soil (kN/m³)	18 (kN/m³)
Friction angle of soil, φ	34°
Young's modulus of elasticity (MN/m²)	14.6 (MN/m²)
Poisson's ratio	0.25
Dilatancy angle	4°
Cohesion	70 (kN/m²)
Failure criteria	Mohr-Coulomb
Type of material model	Drained condition

Table 3. Characteristics of the foundation investigated in Nepal and Yadav [15].

Parameters	Values
Normal stiffness (*EA*) kN/m	3×10^7
Flexural rigidity (*EI*) kN·m²/m	2×10^4
Equivalent thickness (m)	0.2
Poisson's ratio	0.1

2.2 Validation

In general, the most important part of analyzing any problem using numerical models is ensuring the. To verify the modeling, numerical analysis, and the software employed, it is necessary to utilize the results of reliable references related to the research. In this regard, a numerical study on the effect of an underground cavity on the bearing capacity of a strip footing using PLAXIS 2D software version 2022. In this section, the intended model has been simulated using PLAXIS 2D software version 2024, and its results are compared with the reference. Fig. 3 shows a comparison of the modeling results obtained from the two software versions, which demonstrates a good agreement and confirms the accuracy of the modeling performed in this study (Figs. 3 to 4).

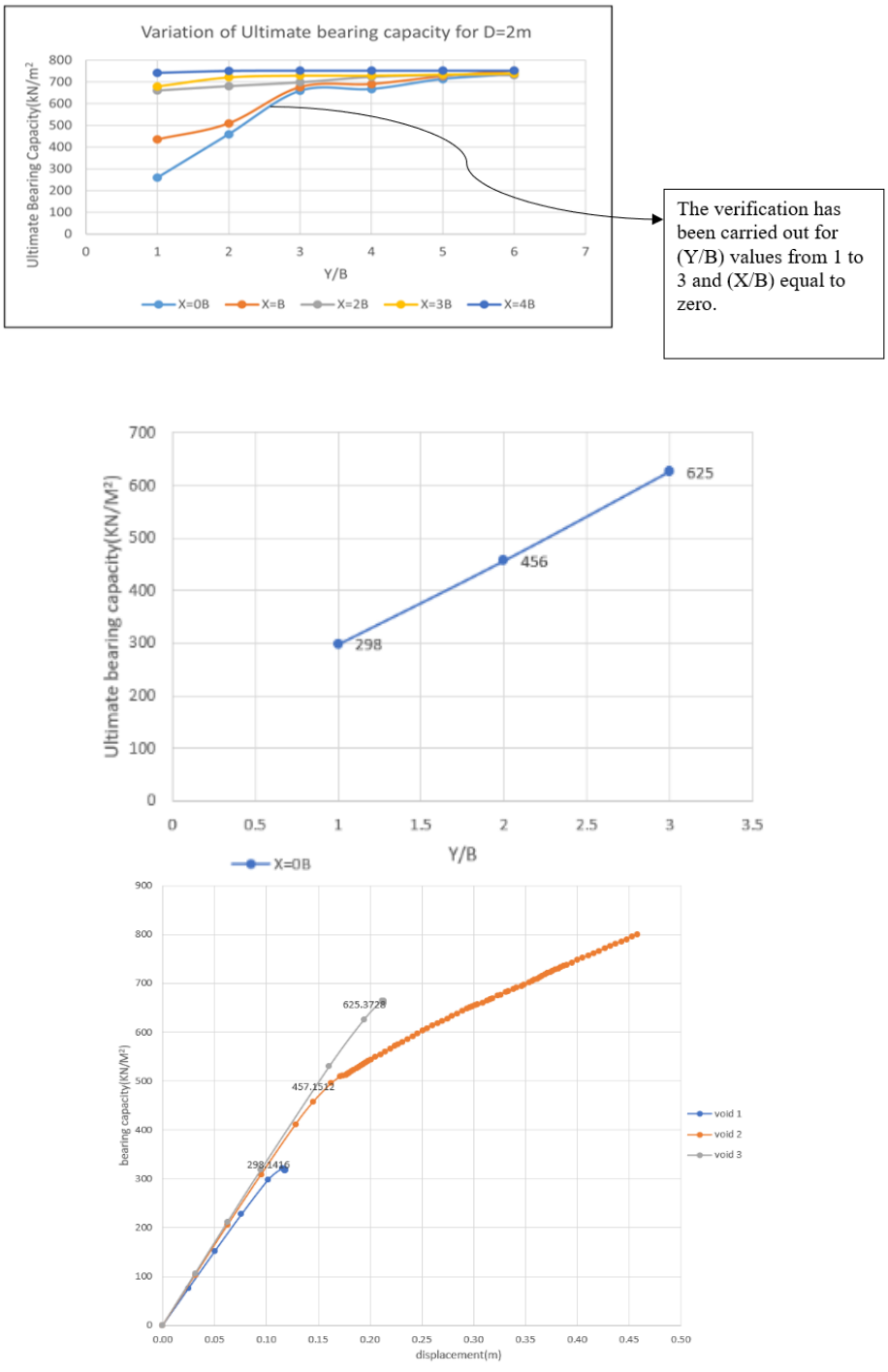

Fig. 3. Numerical results obtained using PLAXIS 2D, version 2022.

2.3 Validation results obtained through numerical simulation using PLAXIS 2D, version 2024

In this section, the results of a parametric study on the behavior of shallow foundations located above circular cavities are presented. The modeling assumptions throughout all phases of the parametric study are based on a combination of data obtained from the validated model as well as relevant textbooks and research articles. The simulations are conducted for shallow foundations placed on three types of clay: soft, medium, and stiff. The results of the modeling are compared and analyzed through a series of graphical representations.

2.3 Parametric study on the behavior of shallow foundations in the vicinity of a cavity

For the parametric investigations, the material properties listed in Table 4 are used. These properties are derived from the tables provided in the as well as the software manual used for calculating axial stiffness (*EA*) and bending stiffness (*EI*) of concrete sections in PLAXIS 2D version 2024. The calculation of both parameters, *EI* and *EA*, is performed in the third dimension, i.e., the Z-direction.

Table 4. Soil, foundation, and cavity lining properties used for numerical modeling [3].

Soil type	γ_{sat} (kN/m^3)	γ_d (kN/m^3)	C (kN/m^2)	$\emptyset$ (°)	Ψ (°)	E (kN/m^2)	R_{inter}	ν
Soft clay	16	14	10	15	0	4000	0.85	0.5
Concrete properties	E (kN/m^2)	I (m^4)	A (m^2)	EI (kN*m2)/m	EA (kN/m)	T	W (kN/m/m)	v
Concrete foundation	25*10^6	0.0104	0.5	260.4*103	12.5*106	0.5	8.27	0.2
Concrete lining of the cavity	15000	8.33*10^{-11}	0.001	1.25*10-6	15	0.001	rigid	0.1

Table 5. Abbreviations of the investigated variables.

Footing width	*B*
Cavity diameter	*D*
Cavity embedment depth	*Y*
Cavity eccentricity	*X*

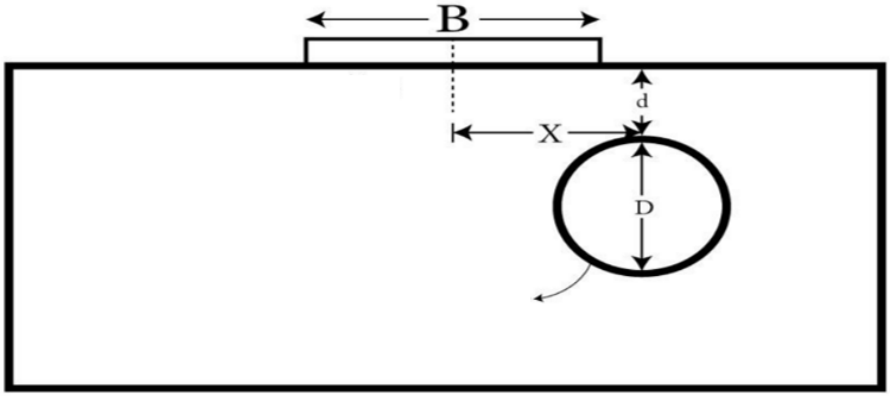

Fig. 4. Schematic representation of the components used in the numerical modeling.

3. Parametric study procedure

The parametric study in this research is organized into the following cases, based on variations in cavity diameter, embedment depth, and eccentricity, while maintaining a constant footing width of 2 meters. The soil type in all cases is varied among soft, medium, and stiff clay.

3.1. Category 1: Effect of cavity embedment depth (cavity eccentricity = 0 m*)*

In this category, the influence of cavity embedment depth on the bearing capacity of a shallow strip footing is investigated. The cavity is assumed to be located directly beneath the center of the footing (zero eccentricity), while three different diameters (0.5 m, 0.75 m, and 1.0 m) are considered. For each diameter, the cavity is placed at three different depths: 2 m, 4 m, and 10 m below the ground surface. The variations in bearing capacity due to changes in embedment depth are examined in all three soil types: soft clay, medium clay, and stiff clay.

These configurations are presented in Figs. 6 to 8, respectively.

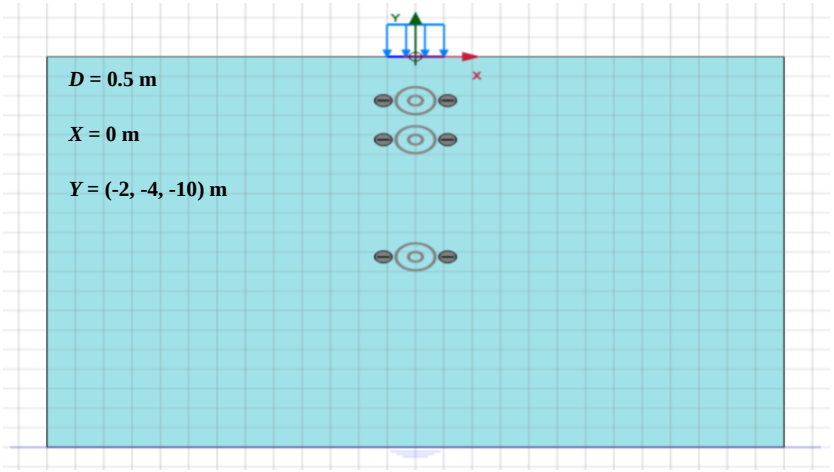

Fig. 5. Soft, medium, and stiff clay; cavity diameter: 0.5 m; cavity embedment depths: 2 m, 4 m, and 10 m.

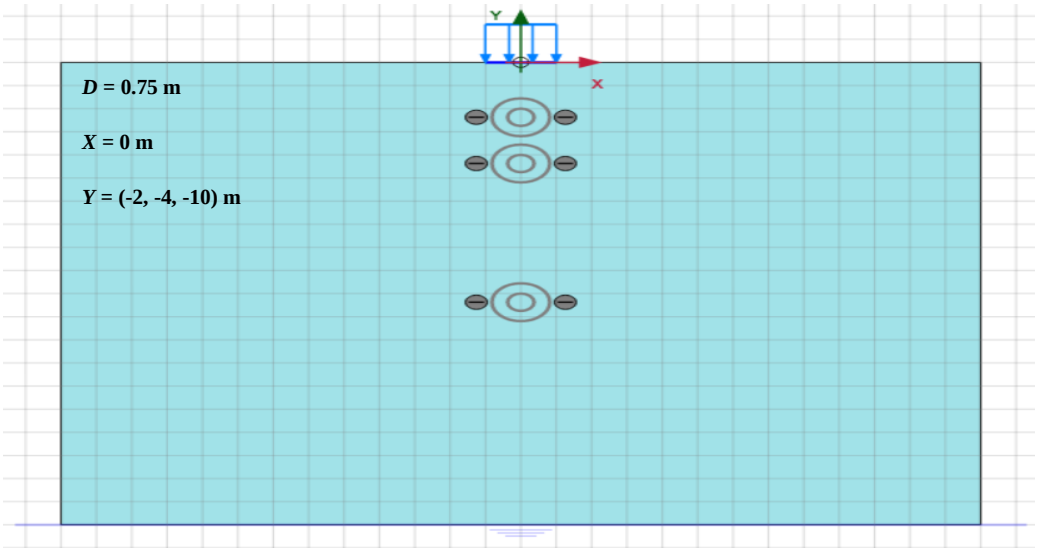

Fig. 6. Soft, medium, and stiff clay; cavity diameter: 0.75 m; cavity embedment depths: 2 m, 4 m, and 10 m.

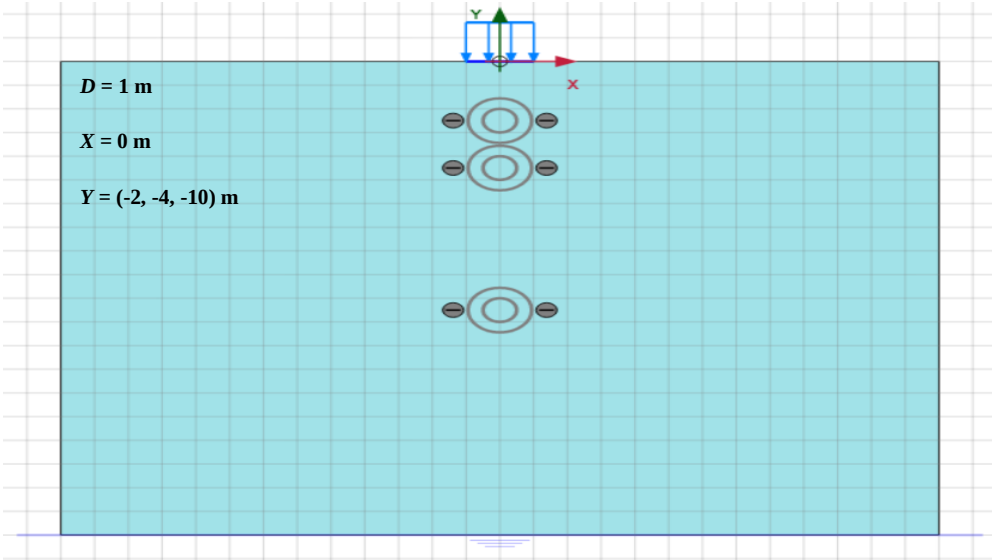

Fig. 7. Soft, medium, and stiff clay; cavity diameter: 1.0 m; cavity embedment depths: 2 m, 4 m, and 10 m.

3.2. Category 2: Effect of cavity eccentricity (fixed embedment depth = 2 m*)*

This category focuses on evaluating the effect of horizontal eccentricity of the cavity on the footing's bearing capacity. The embedment depth is kept constant at 2 meters, while the cavity diameter varies among 0.5 m, 0.75 m, and 1.0 m. For each diameter, three levels of cavity eccentricity relative to the footing center are considered: 1 m, 6 m, and 10 m. The objective is to determine the extent to which increasing horizontal distance from the footing mitigates the negative impact of the cavity.

These configurations are illustrated in Figs. 9 to 11, respectively.

In this study, the bearing capacity ratio (BCR) was defined as the ratio of the ultimate bearing capacity of a footing located above a cavity to that of an identical footing on homogeneous ground without a cavity, i.e., BCR = qu(cavity) / qu(reference). The ultimate bearing capacity (Qu) was determined from the load–settlement response obtained in PLAXIS 2D using the tangent intersection method, consistent with procedures adopted by Lee et al. [4] and Nepal and Yadav [15]. The criterion for ultimate capacity was based on the point of maximum curvature or the intersection between the initial linear (elastic) and post-yield (plastic) portions of the load–settlement curve, corresponding to the onset of general shear failure. Given that the Mohr–Coulomb model was used, the footing behavior was primarily governed by shear failure rather than settlement-controlled failure. The observed failure mechanism beneath the strip footing exhibited a general shear mode characterized by well-defined failure surfaces extending from the footing edges toward the cavity crown, in agreement with the findings of Sireesh et al. [3] and Lee et al. [4]. Therefore, the BCR values reported herein reflect reductions in the ultimate shear strength of the system due to the presence, size, and position of subsurface cavities.

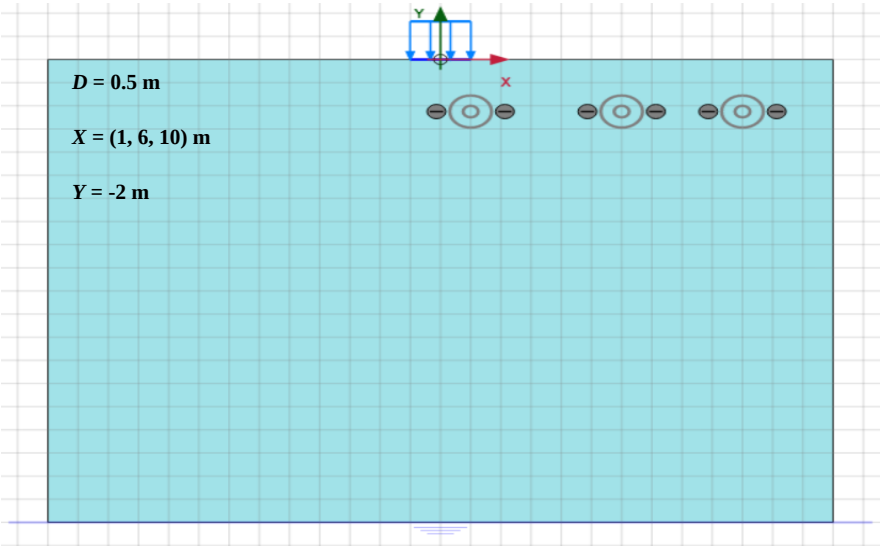

Fig. 8. Soft, medium, and stiff clay; cavity diameter: 0.5 m; cavity eccentricities: 1 m, 6 m, and 10 m; cavity embedment depth: 2 m.

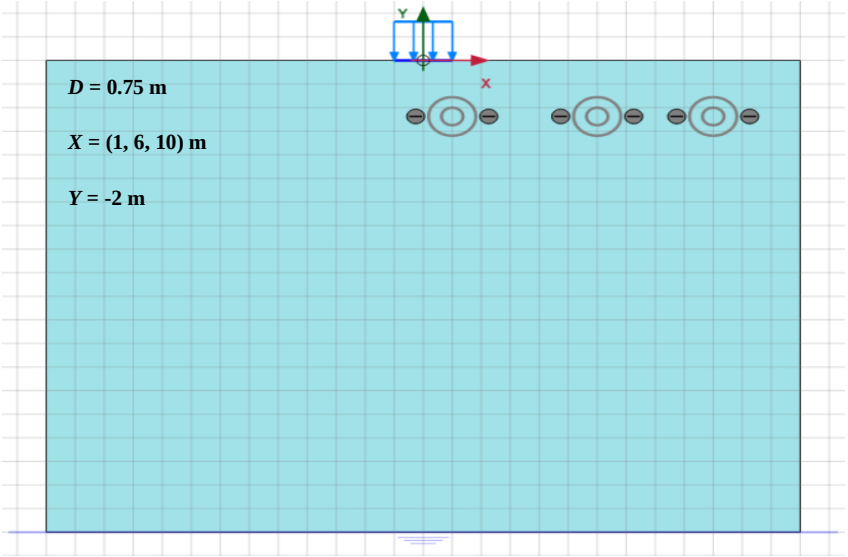

Fig. 9. Clay soil (soft, medium, hard), hole diameter 0.75 m, eccentricity 1, 6, 10 m, burial depth 2 m.

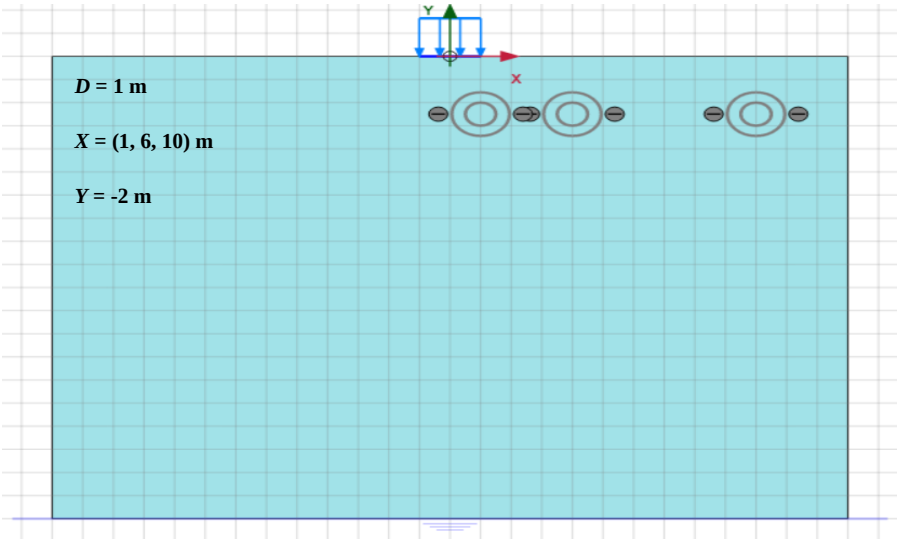

Fig. 10. Clay soil (soft, medium, hard), hole diameter 1 m, eccentricity 1, 6, 10 m, burial depth 2 m.

4. Result and discussion

4.1. Investigation of conditions (soft clay, embedment depths of 2, 4, and 10 meters, diameter of 0.5 meters) foundation specifications under isolated conditions (without cavity)

A comparison of Fig. 11 with the bearing capacity of an isolated footing in soft clay reveals that the presence of subsurface cavities with a diameter of 0.5 meters significantly influences the footing's performance. Specifically, the bearing capacity of the strip footing decreases as a function of the cavity embedment depth. The reductions in bearing capacity, relative to the isolated footing condition, are quantified as 55.79% at a depth of 2 meters, 27.37% at 4 meters, and 6.32% at 10 meters. These results indicate that increasing the embedment depth of the cavities mitigates their adverse impact, and the bearing capacity progressively converges toward that of the isolated footing, as theoretically anticipated.

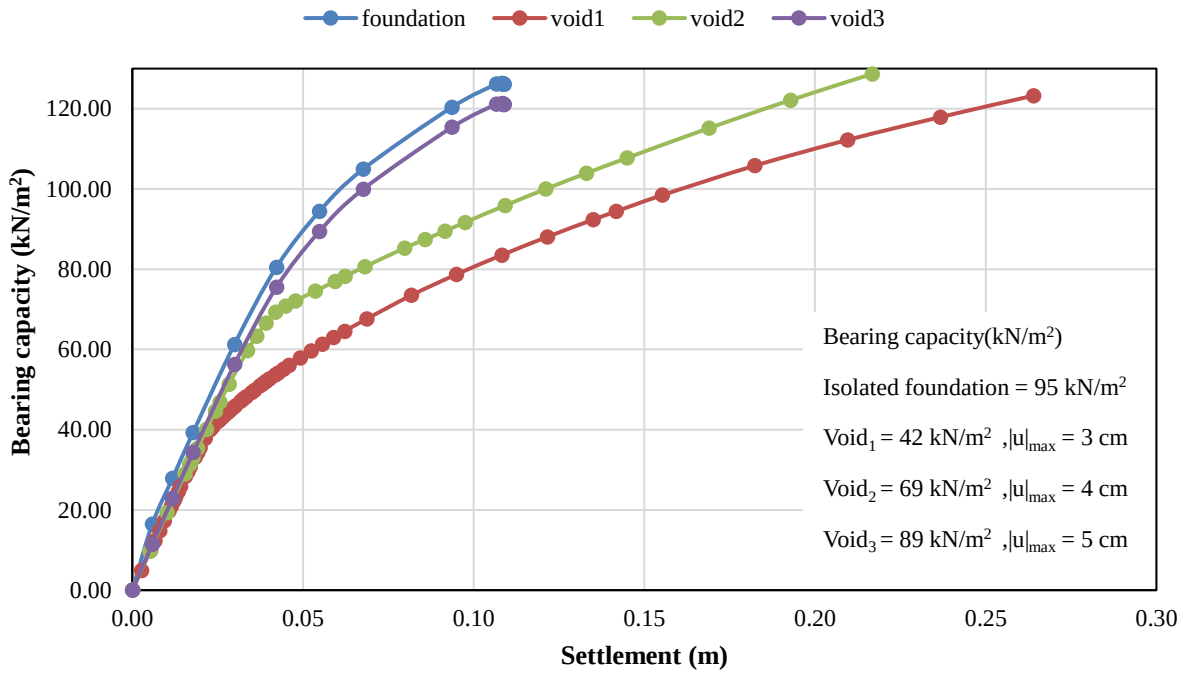

Fig. 11. Settlement graph of a strip footing with cavities of 0.5-meter diameter at various embedment depths in soft clay.

4.2. Investigation of conditions (soft clay, embedment depths of 2, 4, and 10 meters, diameter of 0.75 meters)

A comparative analysis of the figures and graphs presented in Fig. 12 with the bearing capacity of an isolated footing in soft clay indicates that the presence of cavities with a diameter of 0.75 meters beneath the footing results in a noticeable reduction in bearing capacity, depending on the embedment depth of the cavities. The observed reductions, expressed as percentages relative to the footing without cavities, are 66.32% at a depth of 2 meters, 44.21% at 4 meters, and 13.68% at 10 meters. As anticipated, the bearing capacity of the footing in the presence of cavities tends to approach that of the isolated condition as the embedment depth increases.

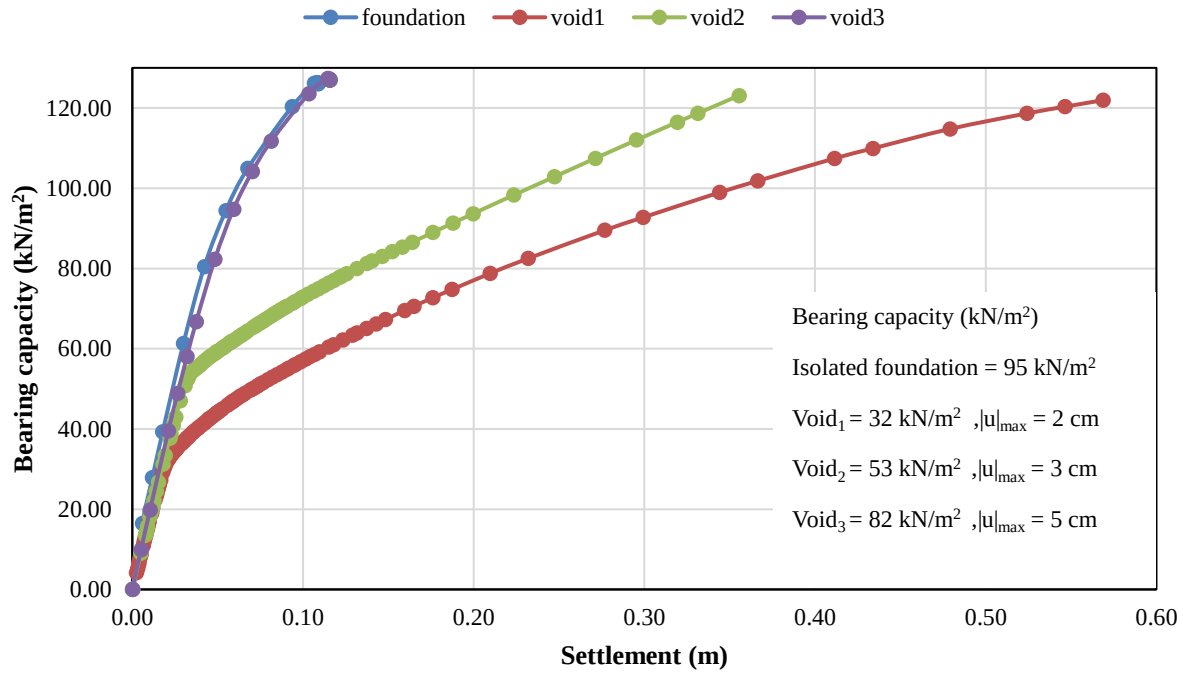

Fig. 12. Settlement graph of a strip footing with cavities of 0.75-meter diameter at various embedment depths in soft clay.

4.3. Investigation of conditions (soft clay, embedment depths of 2, 4, and 10 meters, diameter of 1 meter)

A comparison of the Fig. 13 with the bearing capacity of an isolated footing in soft clay indicates that the presence of subsurface cavities with a diameter of 1 meter significantly reduces the bearing capacity of the strip footing, depending on the embedment depth of the cavities. The reductions in bearing capacity, relative to the footing without cavities, are 72.63% at a depth of 2 meters, 56.84% at 4 meters, and 21% at 10 meters. As anticipated, increasing the embedment depth of the cavities mitigates their adverse impact, and the bearing capacity of the footing progressively approaches that of the isolated condition.

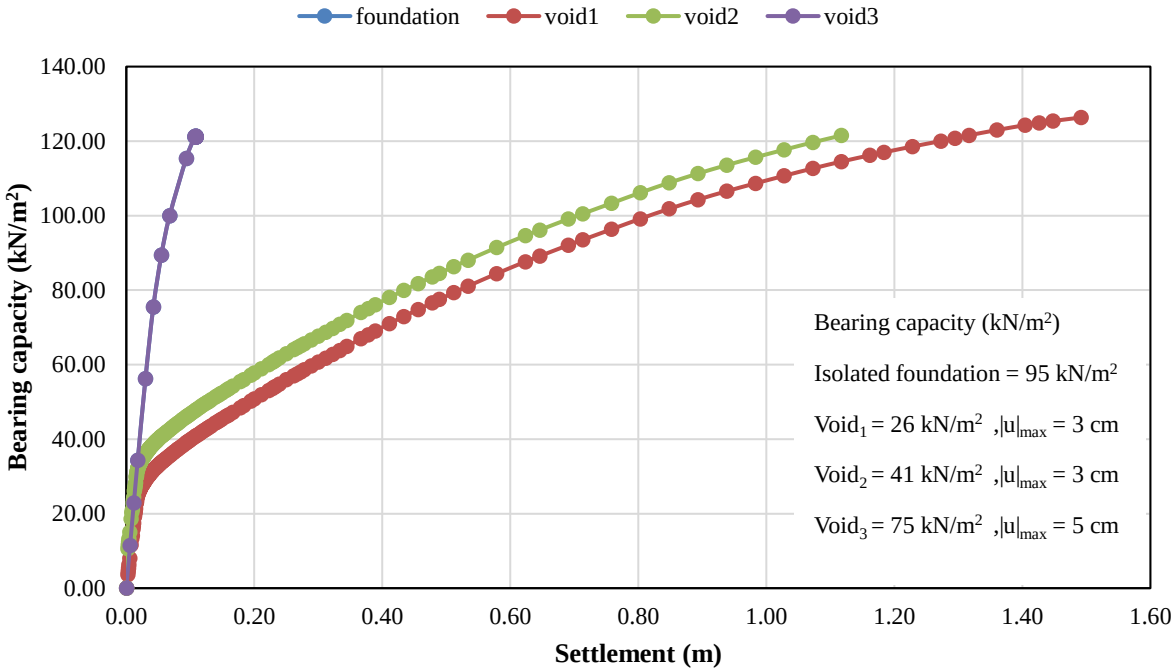

Fig. 13. Settlement graph of a strip footing with cavities of 1-meter diameter at various embedment depths in soft clay.

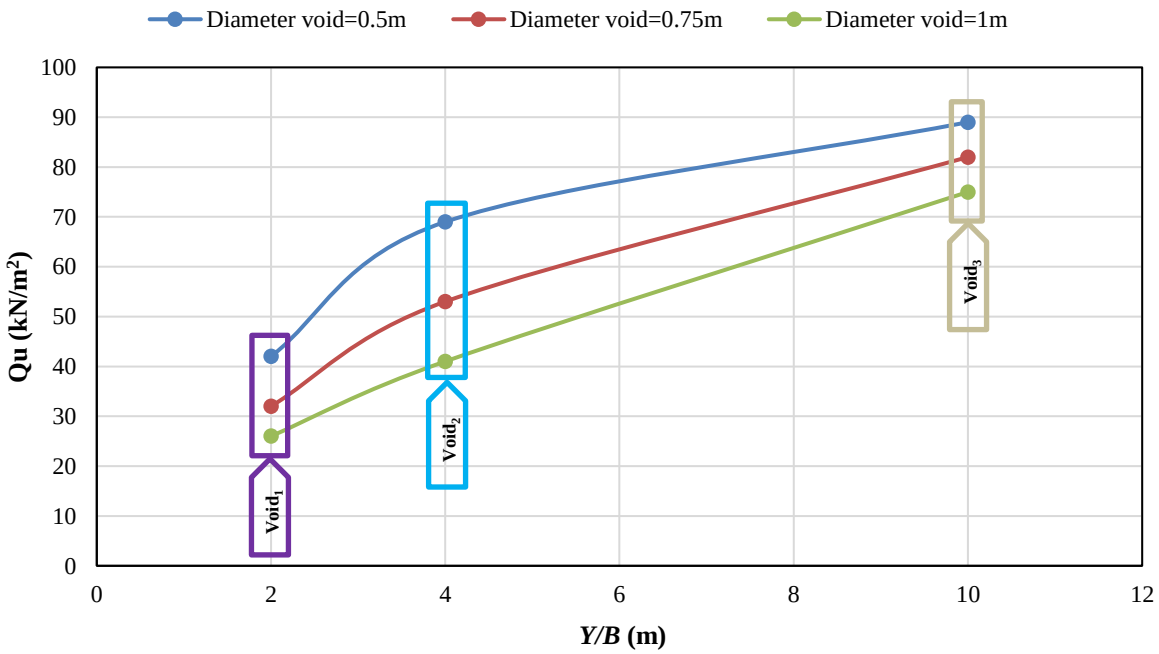

Fig. 14. Stress–depth diagram for cavities of varying diameters at different embedment depths in soft clay

A comparative analysis of the figures and graphs in Figs. 11-13 with the bearing capacity of footings containing cavities in soft clay, as illustrated in Fig. 14, indicates that the presence of subsurface cavities with diameters of 0.5, 0.75, and 1 meter beneath the footing results in a reduction of the strip footing's bearing capacity, depending on both the embedment depth and the cavity diameter. The percentage reductions, relative to the smallest cavity diameter (0.5 meters), are as follows: at an embedment depth of 2 meters, cavities with diameters of 0.75 and 1 meter cause reductions of 23.8 and 38.09%, respectively; at 4 meters, the corresponding reductions are 23.19 and 40.57%; and at 10 meters, they are 7.86 and 15.73%. Consequently, as expected, the bearing capacity of

the footing decreases progressively with increasing cavity diameter.

4.4. Investigation of conditions (soft clay, eccentricities of 1, 6, and 10 meters, diameter of 0.5 meters)

A comparison of the figures and graphs in Fig. 15 with the bearing capacity of an isolated footing in soft clay indicates that the presence of subsurface cavities with a diameter of 0.5 meters beneath the footing reduces the bearing capacity of the strip footing, depending on the cavity eccentricity. The percentage reductions relative to the footing without cavities are 49.5, 25.26, and 9.5% for cavity eccentricities of 1 meter, 6 meters, and 10 meters, respectively. As anticipated, the bearing capacity of the footing with cavities progressively approaches that of the isolated footing as the cavity eccentricity increases.

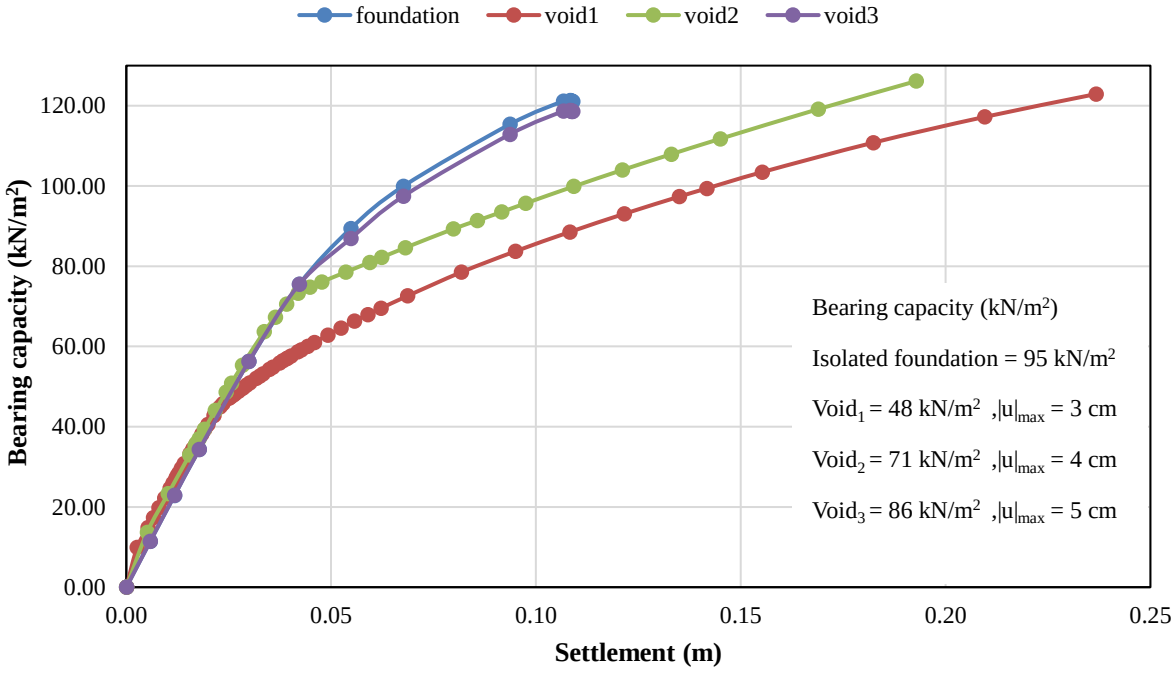

Fig. 15. Settlement graph of a strip footing with cavities of 0.5-meter diameter at various eccentricities from the footing center in soft clay.

4.5. Investigation of conditions (soft clay, eccentricities of 1, 6, and 10 meters, diameter of 0.75 meters)

A comparison of the figures and graphs in Fig. 16 with the bearing capacity of an isolated footing in soft clay indicates that the presence of subsurface cavities with a diameter of 0.75 meters beneath the footing reduces the bearing capacity of the strip footing, depending on the cavity eccentricity. The percentage reductions relative to the footing without cavities are 57.9%, 38.9%, and 11.57% for cavity eccentricities of 1 meter, 6 meters, and 10 meters, respectively. As expected, the bearing capacity of the footing with cavities progressively approaches that of the isolated footing as the cavity eccentricity increases.

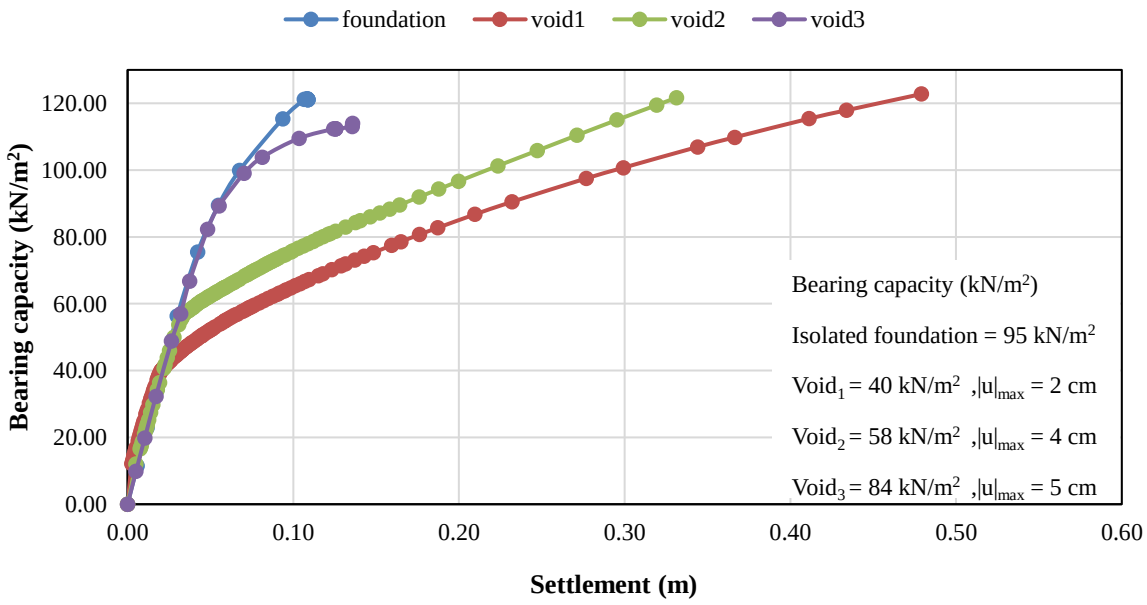

Fig. 16. Settlement graph of a strip footing with cavities of 0.75-meter diameter at various eccentricities from the footing center in soft clay.

4.6. Investigation of conditions (soft clay, eccentricities of 1, 6, and 10 meters, diameter of 1 meter)

A comparison of the figures and graphs in Fig. 17 with the bearing capacity of an isolated footing in soft clay indicates that the presence of subsurface cavities with a diameter of 1 meter beneath the footing reduces the bearing capacity of the strip footing, depending on the cavity eccentricity. The percentage reductions relative to the footing without cavities are 64.21%, 54.7%, and 16.8% for cavity eccentricities of 1 meter, 6 meters, and 10 meters, respectively. As expected, the bearing capacity of the footing with cavities progressively approaches that of the isolated footing as the cavity eccentricity increases.

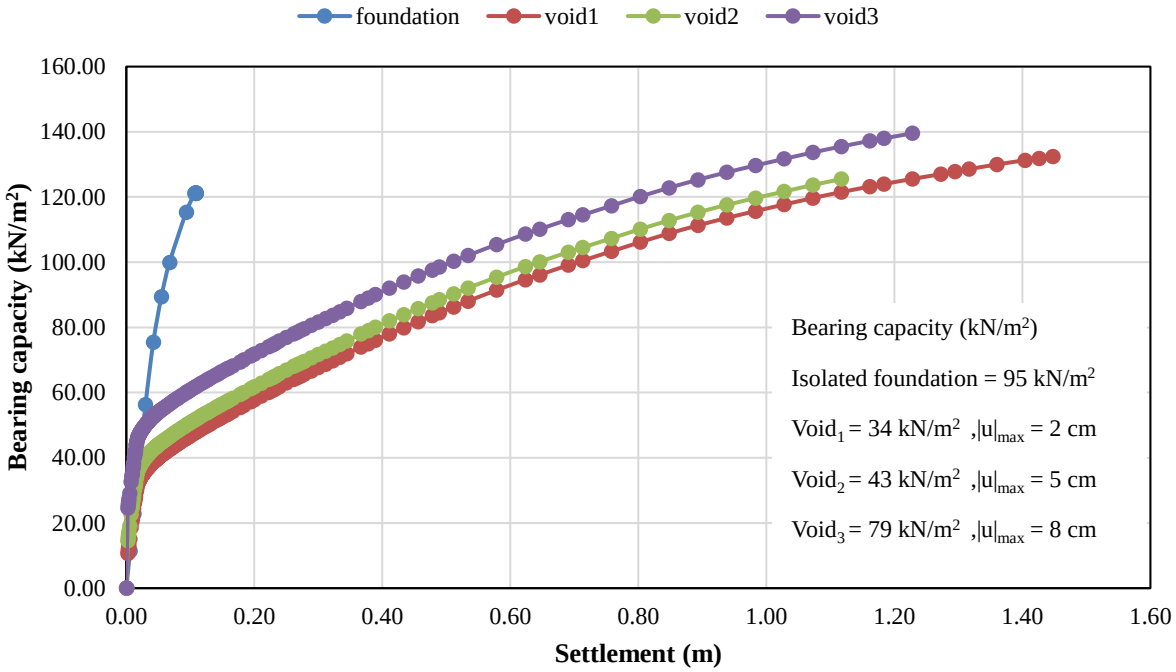

Fig. 17. Settlement graph of a strip footing with cavities of 1-meter diameter at various eccentricities from the footing center in soft clay.

A comparative analysis of the figures and graphs in Fig. 15 to 17 with the bearing capacity of footings containing cavities in soft clay, as illustrated in Fig. 18, indicates that the presence of subsurface cavities with diameters of 0.5, 0.75, and 1 meter beneath the footing leads to a reduction in the strip footing's bearing capacity, depending on both the cavity eccentricity and diameter. The percentage reductions, relative to the smallest cavity diameter (0.5 meters), are as follows: at an eccentricity of 1 meter, cavities with diameters of 0.75 and 1 meter produce reductions of 16.66 and 29.16%, respectively; at 4 meters, the reductions are 18.30 and 39.43%; and at 10 meters, they are 2.32 and 8.14%. Consequently, as expected, the bearing capacity of the footing decreases progressively with increasing cavity diameter.

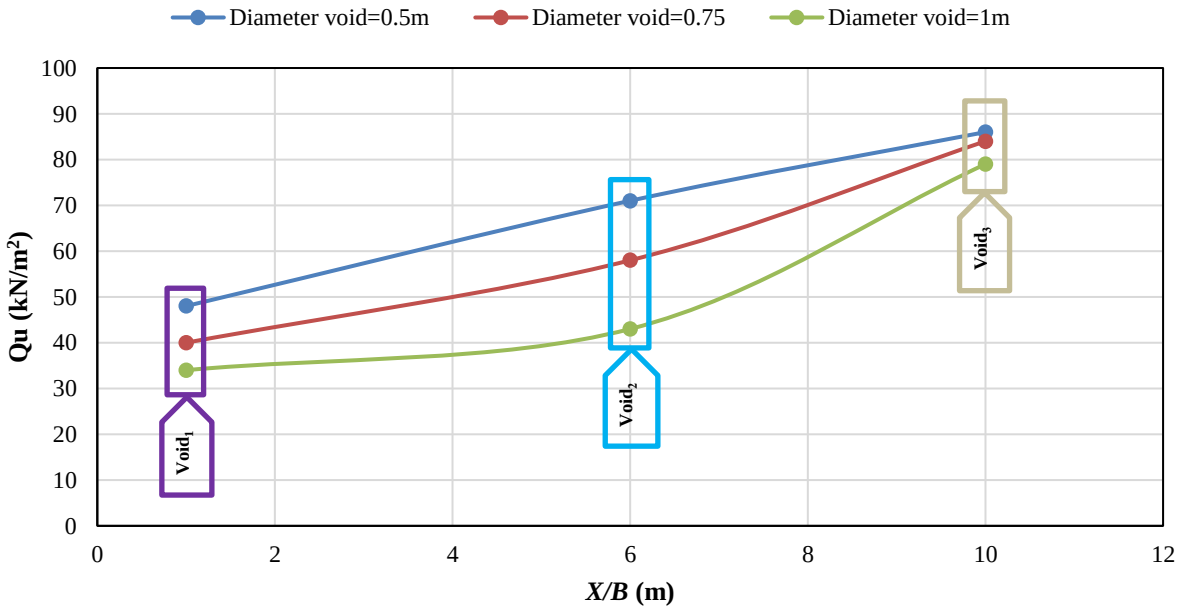

Fig. 18. Stress–eccentricity diagram for cavities of varying diameters in soft clay.

Ultimate bearing capacity was identified using the tangent intersection method, in which the extension of the initial linear slope intersects the load–settlement curve at the point of significant deviation. For curves that did not exhibit clear nonlinearity, the settlement criterion of 0.1B (10% of footing width) was adopted, as recommended in classical bearing capacity theories (Terzaghi, 1943; IS:6403–1981). This dual approach ensures consistency across all simulated cases.

5. Conclusion

This study investigates the behavior of shallow strip foundations in the presence of underground cavities within soft clay. Such cavities may exist during construction or develop later due to human or natural activities, potentially compromising part or all of the foundation's bearing capacity if located within the stress distribution zone beneath the footing. A numerical approach using PLAXIS 2D was adopted to evaluate the effects of cavity diameter, burial depth, and horizontal and vertical offsets relative to the foundation center. The soil was modeled as soft clay using the Mohr-Coulomb constitutive model.

The numerical investigation clearly demonstrates that the presence of subsurface cavities in soft clay significantly reduces the bearing capacity of strip footings. The extent of reduction is governed by cavity embedment depth and eccentricity, as well as cavity diameter. Results reveal that shallow cavities (2 m depth) exert the most detrimental effects, causing bearing capacity reductions of up to 72.63% for a cavity diameter of 1 m, whereas deeper cavities (10 m depth) mitigate adverse effects with reductions as low as 6.32%. Similarly, increasing cavity eccentricity reduces its influence, with reductions decreasing from nearly 65% at 1 m eccentricity to less than 17% at 10 m. Comparative analysis across cavity diameters confirms that larger cavities consistently induce greater reductions in bearing capacity, highlighting the combined importance of diameter and positional factors. Overall, the findings emphasize the necessity of considering both depth and eccentricity of subsurface cavities in geotechnical design. Proper assessment of these parameters is essential to ensure the safety and stability of shallow foundations in soft clay deposits.

Statements & Declarations

Author contributions

Vali Ghaseminejad: Conceptualization, Methodology, Formal analysis, Writing - original draft.

Atina Tarrah: Investigation, Data curation, Validation.

Fereshteh Ghomi: Supervision, Writing - Review & Editing.

Funding

The authors received no financial support for the research, authorship, and/or publication of this article.

Data availability

The data presented in this study will be available on interested request from the corresponding author.

Declarations

The authors declare no conflict of interest.

References

[1] Baus, R. L., Wang, M. C. Bearing Capacity of Strip Footing above Void. Journal of Geotechnical Engineering, 1983; 109: 1-14. doi:10.1061/(ASCE)0733-9410(1983)109:1(1).

[2] Jao, M., Wang, M. C. Stability of strip footings above concrete-lined soft ground tunnels. Tunnelling and Underground Space Technology, 1998; 13: 427-434. doi:10.1016/S0886-7798(98)00085-6.

[3] Sireesh, S., Sitharam, T. G., Dash, S. K. Bearing capacity of circular footing on geocell–sand mattress overlying clay bed with void. Geotextiles and Geomembranes, 2009; 27: 89-98. doi:10.1016/j.geotexmem.2008.09.005.

[4] Lee, J. K., Jeong, S., Ko, J. Undrained stability of surface strip footings above voids. Computers and Geotechnics, 2014; 62: 128-135. doi:10.1016/j.compgeo.2014.07.009.

[5] Asgari, A., Ahmadtabar Sorkhi, S. F. Wind turbine performance under multi-hazard loads: Wave, wind, and earthquake effects on liquefiable soil. Results in Engineering, 2025; 26: 104647. doi:10.1016/j.rineng.2025.104647.

[6] Jahangiri, V., Akbarzadeh, M. R., Shahamat, S. A., Asgari, A., Naeim, B., Ranjbar, F. Machine learning-based prediction of seismic response of steel diagrid systems. Structures, 2025; 80: 109791. doi:10.1016/j.istruc.2025.109791.

[7] Asgari, A., Arjomand, M. A., Bagheri, M., Ebadi-Jamkhaneh, M., Mostafaei, Y. Assessment of Experimental Data and Analytical Method of Helical Pile Capacity Under Tension and Compressive Loading in Dense Sand. Buildings, 2025; 15: 2683.

[8] Ebadi-Jamkhaneh, M., Arjomand, M. A., Bagheri, M., Asgari, A., Nouhi Hefzabad, P., Salahi, S., Mostafaei, Y. Experimental Study on the Pullout Behavior of Helical Piles in Geogrid-Reinforced Dense Shahriyar Sand. Buildings, 2025; 15: 2963.

[9] Asgari, A., Ranjbar, F., Bagheri, M. Seismic resilience of pile groups to lateral spreading in liquefiable soils: 3D parallel finite element modeling. Structures, 2025; 74: 108578. doi:10.1016/j.istruc.2025.108578.

[10] Asadoullahtabar, S. R., Asgari, A., Mohammad Rezapour Tabari, M. Assessment, identifying, and presenting a plan for the stabilization of loessic soils exposed to scouring in the path of gas pipelines, case study: Maraveh-Tappeh city. Engineering Geology, 2024; 342: 107747. doi:10.1016/j.enggeo.2024.107747.

[11] Bagheri, M., Ranjbar Malidarreh, N., Ghaseminejad, V., Asgari, A. Seismic resilience assessment of RC superstructures on long–short combined piled raft foundations: 3D SSI modeling with pounding effects. Structures, 2025; 81: 110176. doi:10.1016/j.istruc.2025.110176.

[12] Asgari, A., Bagheri, M., Hadizadeh, M. Advanced seismic analysis of soil-foundation-structure interaction for shallow and pile foundations in saturated and dry deposits: Insights from 3D parallel finite element modeling. Structures, 2024; 69: 107503. doi:10.1016/j.istruc.2024.107503.

[13] Shooshpasha, I., Bagheri, M. The effects of surcharge on liquefaction resistance of silty sand. Arabian Journal of Geosciences, 2014; 7: 1029-1035. doi:10.1007/s12517-012-0737-9.

[14] Asgari, A. L. I., Golshani, A., Bagheri, M. Numerical evaluation of seismic response of shallow foundation on loose silt and silty sand. Journal of Earth System Science, 2014; 123: 365-379. doi:10.1007/s12040-013-0393-9.

[15] Nepal, B., Yadav, S. K. Numerical Study of Bearing Capacity under Strip Footing having Underground Void. In: Proceedings of 14th IOE Graduate Conference; 2023 Nov 29-Dec 1; lalitpur, Nepal. p. 727-731.

Civil Engineering and Applied Solutions

Research Article

journal homepage: ceas.journals.umz.ac.ir

CEAS Civil Engineering and Applied Solutions

Developing Inelastic Jerk Spectra for Pulse-Like Earthquakes

Alireza Garakaninezhad [a*], Saeed Amiri [b]

[a] *Department of Civil Engineering, Faculty of Engineering, University of Jiroft, Jiroft, Kerman, Iran*
[b] *Department of Civil Engineering, Geological and Mining Engineering, Polytechnique Montreal, Montreal, QC, Canada*

ARTICLE INFO

Keywords:
Jerk spectra
Inelastic systems
Pulse-like earthquakes
Strength reduction factor

Article history:
Received 06 October 2025
Accepted 24 October 2025
Available online 01 April 2026

ABSTRACT

Jerk, or jolt, is defined as the time derivative of acceleration. This study investigates the jerk response of inelastic single-degree-of-freedom (SDOF) systems subjected to pulse-like near-fault ground motions. Compared with ordinary non–pulse-like records, pulse-like motions can impose significantly higher demands on structures. In this work, constant-strength spectra for the jerk response of inelastic SDOF systems are developed using a set of 91 pulse-like earthquakes. The influence of key structural parameters, including strength reduction factor, hysteretic behavior, and viscous damping ratio, is examined. The results show that jerk demands exhibit slightly higher sensitivity to viscous damping in the short, normalized period region than in the long-period region. Furthermore, an analytical equation is proposed to estimate jerk demand as a function of the ratio of elastic vibration period to pulse period and the strength reduction factor, for various hysteretic models and damping ratios.

1. Introduction

Jerk, also referred to as jolt, is defined as the time derivative of acceleration, i.e., the rate at which acceleration changes over time. This parameter has been widely applied across various fields [1], such as a design factor in ride comfort evaluation, e.g., in lifts/elevators [2], amusement rides [3-8], buses [9], and ships [10-12]. Jerk has also been examined in the fields of vibration and seismic control, as well as seismic response [13-18]. Tong et al. [16] investigated the fundamental characteristics of acceleration derivatives using ground motions from the 1999 Chi-Chi earthquake (Mw 7.6) and one of its aftershocks (Mw 6.2). He et al. [18] assessed jerk characteristics through elastic and inelastic jerk response spectra and examined the influence of site type, reduction factor, and ductility on these spectra. Taushanov [15] developed and presented relationships and corresponding graphs for the jerk response spectra. Moreover, in another study, Papandreou and Papagiannopoulos [17] examined the overall characteristics of jerk spectra using bilinear SDOF systems, focusing on hysteretic behavior, viscous damping ratio, and yield strength. An equation was also proposed to estimate the jerk demand of such inelastic systems. Yaseen et al. [19] explored the applicability of jerk as a ground motion intensity measure through nonlinear time-history analyses of representative reinforced concrete frame buildings under seismic excitations. Wakui et al. [20] introduced a method to predict plastic deformation in an SDOF system by employing jerk and snap. Snap refers to the second time derivative of acceleration. Additionally, Vukobratović and Ruggieri [21] conducted an extensive review of research focused on jerk in earthquake engineering. Despite the aforementioned research, no prior studies have examined the assessment of jerk demand under pulse-like ground motions. Moreover, comparable to earlier investigations focusing on multiple earthquake events, such as [22-27], future studies may aim to develop inelastic spectra that capture jerk response under these earthquake scenarios.

Near-fault ground motions with pulse-like characteristics can cause severe structural damage. In such earthquakes, when fault rupture propagates toward the site at a velocity close to the shear wave velocity of the soil, a substantial amount of seismic energy may be concentrated into a large pulse of motion, which is typically observable in the velocity time history [28-31], resulting in more severe structural damage compared to far-field earthquakes. A key parameter of near-fault pulse-like ground motions, the

* Corresponding author.
E-mail addresses: a.garakani@ujiroft.ac.ir (A. Garakaninezhad).

https://doi.org/10.22080/ceas.2025.30227.1049
ISSN: 3092-7749/© 2026 The Author(s). Published by University of Mazandaran.
This article is an open access article distributed under the terms and conditions of the Creative Commons Attribution (CC-BY) license (https://creativecommons.org/licenses/by/4.0/deed.en)
How to cite this article: Garakaninezhad, A., Amiri, S. Finite Developing Inelastic Jerk Spectra for Pulse-Like Earthquakes. Civil Engineering and Applied Solutions. 2026; 2(2): 85-97. doi:10.22080/ceas.2025.30227.1049.

pulse period (T_p), has a significant impact on the dynamic behavior of structures [32-35]. T_p corresponds to the dominant velocity pulse period extracted using the Baker wavelet-based algorithm [36]. Extensive research has focused on formulating inelastic spectra under pulse-like ground motions, especially with respect to the inelastic displacement ratio [33, 37, 38], residual displacement ratio [39, 40], and inelastic acceleration ratio [41]. Despite these efforts, jerk-based spectra for pulse-like ground motions remain largely unexplored.

Cited previous studies indicate that there is a potential connection between jerk and damage accumulation, fatigue-sensitive components, and seismic control device triggering. High jerk values correspond to rapid acceleration reversals, which can induce additional force spikes in acceleration-sensitive non-structural components and energy dissipation devices. This establishes a performance-based relevance for jerk spectra. Therefore, this study seeks to develop inelastic jerk response spectra using a constant-strength framework, considering the role of the vibration period normalized to the earthquake pulse period (T/T_p), strength reduction factor (R), hysteretic rule, and damping ratio (ξ). Additionally, an analytical equation is proposed to predict the jerk demand based on T/T_p and R for two different hysteretic models and various values of ξ.

2. Structure

In this study, constant-strength spectra are developed in terms of the jerk response under a set of pulse-like earthquakes. A wide range of elastic vibration period normalized by the pulse period (T/T_p), strength reduction factor, and viscous damping ratio is considered as described in Table 1.

Table 1. Structural parameters considered in numerical analyses.

Parameter	Range of parameters
Normalized elastic vibration period (T/T_p)	0.1–3.0 with an increment of 0.1
Strength reduction factor (R)	2.0-6.0 with an increment of 1.0
Viscous damping ratio (ξ)	0.05-0.2 with an increment of 0.05

Additionally, two hysteretic models are used: the linear elastic-perfectly plastic (PP) model and the deteriorating pinching (DP) model, as indicated in Fig. 1. The parameters considered for these models are illustrated in Table 2.

Table 2. Structural parameters.

Parameter	Symbol
K_e	Initial stiffness
u_y	Yield displacement
α	Postyield stiffness ratio
α_c	Degrading stiffness ratio
F_m	Maximum strength
u_m	Displacement value at the maximum strength
$\mu = u_m/u_y$	Displacement ductility ratio
β	Power to specify the degraded degree of the unloading stiffness based on μ
pinch$X$	Pinching factor for the displacement
pinch$Y$	Pinching factor for the strength
damage$_1$	Accumulated damage factor capturing the damage due to the ductility
damage$_2$	Accumulated damage factor capturing the damage due to the energy dissipation

It is noted that the postyield stiffness ratio, α, is assumed to be zero, and the superscripts + and − imply the tension and compression regions, respectively.

Moreover, the values of pinchX and pinchY are set as 0.5, representing moderate pinching effects [42, 43]. Furthermore, a moderate level of 0.05 is considered for damage1 and damage2 [42, 43], and the value of the degraded unloading stiffness factor (β) is zero, as indicated by the default value in [42]. The selected parameters represent moderate deterioration scenarios commonly used in OpenSees calibration examples.

The OpenSees software (Open System for Earthquake Engineering Simulation) [44] is employed to perform dynamic analyses. Additionally, the “Hysteretic material” model [45] which is available in OpenSees, is used to simulate the deteriorating pinching behavior of the SDOF systems.

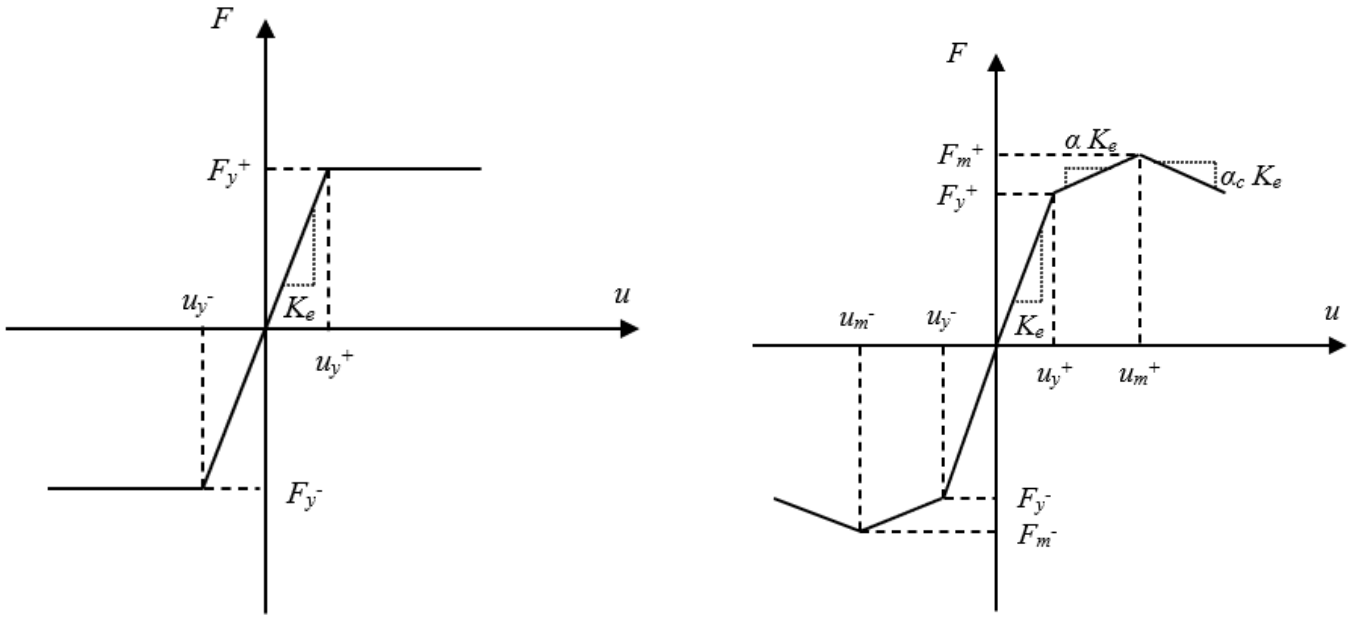

Fig. 1. Hysteretic models: (a) linear elastic-perfectly plastic (PP); and (b) deteriorating pinching (DP).

3. Ground motions

A dataset of pulse-like ground motion, including 91 records identified by Baker [36] is used in this study. These records have been assembled from the Pacific Earthquake Engineering Research (PEER) database [46]. Baker in a study [36] decomposed the original records, then extracted T_p and identified them as pulse-like or non-pulse-like earthquakes using the wavelet transform. Based on the research performed by Baker [36], ground motions could be classified as pulses if the following criteria would be met: (1) The residual ground motion is considerably less intense than the original ground motion, (2) The pulse arrives at the beginning of the time history by measuring the time point when 10% of the pulse energy is observed), (3) The original ground motion that its peak ground velocity (PGV) is higher than 30 cm/s. These criteria are determined by a pulse indicator, which is between 0 and 1. The seismic excitations consist of 23 pulse-like earthquakes, such that their moment magnitude (M_w) is varied from 5 to 7.6. The range of T_P of the earthquakes is from 0.4 s to 12.9 s. Table 3 illustrates the information about these pulse-like earthquakes.

4. Inelastic jerk spectra

4.1. Effect of the strength reduction factor on the inelastic jerk spectra

After conducting nonlinear time history analyses of the SDOF systems under the near-fault pulse-like ground motions, the jerk is derived by differentiating the relative acceleration response of the systems. Then, the mean jerk spectra for different R, ξ, and hysteretic models are presented in this section, such that the horizontal axis of the spectra is T/T_p. The effect of the strength reduction factor on the mean jerk spectra is illustrated in Figs. 2 and 3 for the PP and DP hysteretic rules, respectively. Fig. 2 shows that the impact of R on the jerk response is more pronounced for $T/T_p \leq 1.0$ s, such that decreasing R leads to an increase in the jerk demand. For instance, the mean jerk of the system with the PP hysteretic model, $T/T_p = 0.5$.

Table 3. Pulse-like ground motions.

No.	Event	Year	Station	T_p	PGV	M_w	Epi. distance	Pulse indicator
1	San Fernando	1971	Pacoima Dam (upper left abut)	1.6	116.5	6.6	11.9	0.97
2	Coyote Lake	1979	Gilroy Array #6	1.2	51.5	5.7	4.4	1.00
3	Imperial Valley-06	1979	Aeropuerto Mexicali	2.4	44.3	6.5	2.5	0.99
4	Imperial Valley-06	1979	Agrarias	2.3	54.4	6.5	2.6	1.00
5	Imperial Valley-06	1979	Brawley Airport	4.0	36.1	6.5	43.2	1.00
6	Imperial Valley-06	1979	EC County Center FF	4.5	54.5	6.5	29.1	1.00
7	Imperial Valley-06	1979	EC Meloland Overpass FF	3.3	115.0	6.5	19.4	1.00
8	Imperial Valley-06	1979	El Centro Array #10	4.5	46.9	6.5	26.3	1.00
9	Imperial Valley-06	1979	El Centro Array #11	7.4	41.1	6.5	29.4	0.92
10	Imperial Valley-06	1979	El Centro Array #3	5.2	41.1	6.5	28.7	1.00
11	Imperial Valley-06	1979	El Centro Array #4	4.6	77.9	6.5	27.1	1.00
12	Imperial Valley-06	1979	El Centro Array #5	4.0	91.5	6.5	27.8	1.00
13	Imperial Valley-06	1979	El Centro Array #6	3.8	111.9	6.5	27.5	1.00

14	Imperial Valley-06	1979	El Centro Array #7	4.2	108.8	6.5	27.6	1.00
15	Imperial Valley-06	1979	El Centro Array #8	5.4	48.6	6.5	28.1	1.00
16	Imperial Valley-06	1979	El Centro Differential Array	5.9	59.6	6.5	27.2	1.00
17	Imperial Valley-06	1979	Holtville Post Office	4.8	55.1	6.5	19.8	1.00
18	Mammoth Lakes-06	1980	Long Valley Dam (Upr L Abut)	1.1	33.1	5.9	14.0	1.00
19	Irpinia, Italy-01	1980	Sturno	3.1	41.5	6.9	30.4	0.94
20	Westmorland	1981	Parachute Test Site	3.6	35.8	5.9	20.5	0.89
21	Coalinga-05	1983	Oil City	0.7	41.2	5.8	4.6	0.92
22	Coalinga-05	1983	Transmitter Hill	0.9	46.1	5.8	6.0	0.96
23	Coalinga-07	1983	Coalinga-14th & Elm (Old CHP)	0.4	36.1	5.2	9.6	1.00
24	Morgan Hill	1984	Coyote Lake Dam (SW Abut)	1.0	62.3	6.2	24.6	0.99
25	Morgan Hill	1984	Gilroy Array #6	1.2	35.4	6.2	36.3	1.00
26	Taiwan SMART1(40)	1986	SMART1 C00	1.6	31.2	6.3	68.2	1.00
27	Taiwan SMART1(40)	1986	SMART1 M07	1.6	36.1	6.3	67.2	1.00
28	N. Palm Springs	1986	North Palm Springs	1.4	73.6	6.1	10.6	1.00
29	San Salvador	1986	Geotech Investig Center	0.9	62.3	5.8	7.9	0.99
30	Whittier Narrows-01	1987	Downey - Co Maint Bldg	0.8	30.4	6.0	16.0	1.00
31	Whittier Narrows-01	1987	LB - Orange Ave	1.0	32.9	6.0	20.7	1.00
32	Superstition Hills-02	1987	Parachute Test Site	2.3	106.8	6.5	16.0	1.00
33	Loma Prieta	1989	Alameda Naval Air Stn Hanger	2.0	32.2	6.9	90.8	1.00
34	Loma Prieta	1989	Gilroy Array #2	1.7	45.7	6.9	29.8	0.98
35	Loma Prieta	1989	Oakland - Outer Harbor Wharf	1.8	49.2	6.9	94.0	1.00
36	Loma Prieta	1989	Saratoga - Aloha Ave	4.5	55.6	6.9	27.2	0.86
37	Erzican, Turkey	1992	Erzincan	2.7	95.4	6.7	9.0	1.00
38	Cape Mendocino	1992	Petrolia	3.0	82.1	7.0	4.5	0.92
39	Landers	1992	Barstow	8.9	30.4	7.3	94.8	1.00
40	Landers	1992	Lucerne	5.1	140.3	7.3	44.0	1.00
41	Landers	1992	Yermo Fire Station	7.5	53.2	7.3	86.0	1.00
42	Northridge-01	1994	Jensen Filter Plant	3.5	67.4	6.7	13.0	1.00
43	Northridge-01	1994	Jensen Filter Plant Generator	3.5	67.4	6.7	13.0	1.00
44	Northridge-01	1994	LA - Wadsworth VA Hospital North	2.4	32.4	6.7	19.6	0.96
45	Northridge-01	1994	LA Dam	1.7	77.1	6.7	11.8	1.00
46	Northridge-01	1994	Newhall - W Pico Canyon Rd.	2.4	87.8	6.7	21.6	1.00
47	Northridge-01	1994	Pacoima Dam (downstr)	0.5	50.4	6.7	20.4	0.87
48	Northridge-01	1994	Pacoima Dam (upper left)	0.9	107.1	6.7	20.4	1.00
49	Northridge-01	1994	Rinaldi Receiving Sta	1.2	167.2	6.7	10.9	1.00
50	Northridge-01	1994	Sylmar - Converter Sta	3.5	130.3	6.7	13.1	0.92
51	Northridge-01	1994	Sylmar - Converter Sta East	3.5	116.6	6.7	13.6	1.00
52	Northridge-01	1994	Sylmar - Olive View Med FF	3.1	122.7	6.7	16.8	1.00
53	Kobe, Japan	1995	Takarazuka	1.4	72.6	6.9	38.6	0.87
54	Kobe, Japan	1995	Takatori	1.6	169.6	6.9	13.1	0.96
55	Kocaeli, Turkey	1999	Gebze	5.9	52.0	7.5	47.0	1.00
56	Chi-Chi, Taiwan	1999	CHY006	2.6	64.7	7.6	40.5	0.97
57	Chi-Chi, Taiwan	1999	CHY035	1.4	42.0	7.6	43.9	0.95
58	Chi-Chi, Taiwan	1999	CHY101	4.8	85.4	7.6	32.0	1.00
59	Chi-Chi, Taiwan	1999	TAP003	3.4	33.0	7.6	151.7	0.99
60	Chi-Chi, Taiwan	1999	TCU029	6.4	62.3	7.6	79.2	1.00
61	Chi-Chi, Taiwan	1999	TCU031	6.2	59.9	7.6	80.1	1.00
62	Chi-Chi, Taiwan	1999	TCU034	8.6	42.8	7.6	87.9	1.00
63	Chi-Chi, Taiwan	1999	TCU036	5.4	62.4	7.6	67.8	1.00
64	Chi-Chi, Taiwan	1999	TCU038	7.0	50.9	7.6	73.1	1.00

65	Chi-Chi, Taiwan	1999	TCU040	6.3	53.0	7.6	69.0	1.00
66	Chi-Chi, Taiwan	1999	TCU042	9.1	47.3	7.6	78.4	1.00
67	Chi-Chi, Taiwan	1999	TCU046	8.6	44.0	7.6	68.9	1.00
68	Chi-Chi, Taiwan	1999	TCU049	11.8	44.8	7.6	38.9	0.99
69	Chi-Chi, Taiwan	1999	TCU053	12.9	41.9	7.6	41.2	1.00
70	Chi-Chi, Taiwan	1999	TCU054	10.5	60.9	7.6	37.6	1.00
71	Chi-Chi, Taiwan	1999	TCU056	12.9	43.5	7.6	39.7	0.95
72	Chi-Chi, Taiwan	1999	TCU060	12.0	33.7	7.6	45.4	0.99
73	Chi-Chi, Taiwan	1999	TCU065	5.7	127.7	7.6	26.7	0.96
74	Chi-Chi, Taiwan	1999	TCU068	12.2	191.1	7.6	47.9	1.00
75	Chi-Chi, Taiwan	1999	TCU075	5.1	88.4	7.6	20.7	1.00
76	Chi-Chi, Taiwan	1999	TCU076	4.0	63.7	7.6	16.0	0.92
77	Chi-Chi, Taiwan	1999	TCU082	9.2	56.1	7.6	36.2	0.95
78	Chi-Chi, Taiwan	1999	TCU087	9.0	53.7	7.6	55.6	1.00
79	Chi-Chi, Taiwan	1999	TCU098	7.5	32.7	7.6	99.7	0.97
80	Chi-Chi, Taiwan	1999	TCU101	10.0	68.4	7.6	45.1	1.00
81	Chi-Chi, Taiwan	1999	TCU102	9.7	106.6	7.6	45.6	0.97
82	Chi-Chi, Taiwan	1999	TCU103	8.3	62.2	7.6	52.4	1.00
83	Chi-Chi, Taiwan	1999	TCU104	12.0	31.4	7.6	49.3	0.99
84	Chi-Chi, Taiwan	1999	TCU128	9.0	78.7	7.6	63.3	1.00
85	Chi-Chi, Taiwan	1999	TCU136	10.3	51.8	7.6	48.8	1.00
86	Northwest China-03	1997	Jiashi	1.3	37.0	6.1	19.1	1.00
87	Yountville	2000	Napa Fire Station #3	0.7	43.0	5.0	9.9	1.00
88	Chi-Chi, Taiwan-03	1999	CHY024	3.2	33.1	6.2	25.5	1.00
89	Chi-Chi, Taiwan-03	1999	CHY080	1.4	69.9	6.2	29.5	1.00
90	Chi-Chi, Taiwan-03	1999	TCU076	0.9	59.4	6.2	20.8	1.00
91	Chi-Chi, Taiwan-06	1999	CHY101	2.8	36.3	6.3	50.0	1.00

And $\xi = 0.05$ varies from 26.40 m/s^3 to 35.77 m/s^3, corresponding to an increase of roughly 35.5%, as R decreases from 6 to 2. Additionally, the structures with longer T/T_p values experience lower jerk response than those with shorter T/T_p values. Specifically, within the $2.0 \leq T/T_p \leq 3.0$ s range, the jerk demand stabilizes at an average value of 8.40 m/s^3 for all the considered R values. Moreover, similar trends are observed for the other values of ξ ($\xi = 0.1, 0.15, 0.2$); however, the effect of R on J diminishes in the region of $T/T_p \leq 1.0$ s with increasing ξ, as shown in Fig. 2(c)(e)(g). Based on Fig. 3, the effect of R on the mean jerk of the systems with the DP model and $T/T_p \leq 1.0$ is more significant than in the systems with the PP model. For example, in the system with the DP model, $T/T_p = 0.5$ and $\xi = 0.05$, the jerk changes from 21.18 m/s^3 to 34.48 m/s^3, an increase of approximately 62.80%, when R decreases from 6 to 2.

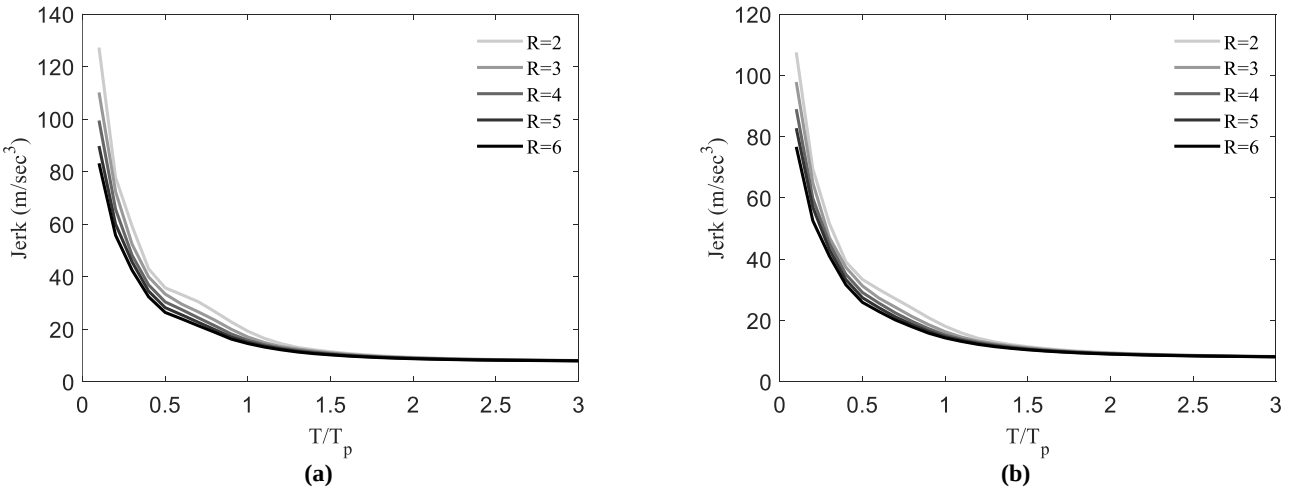

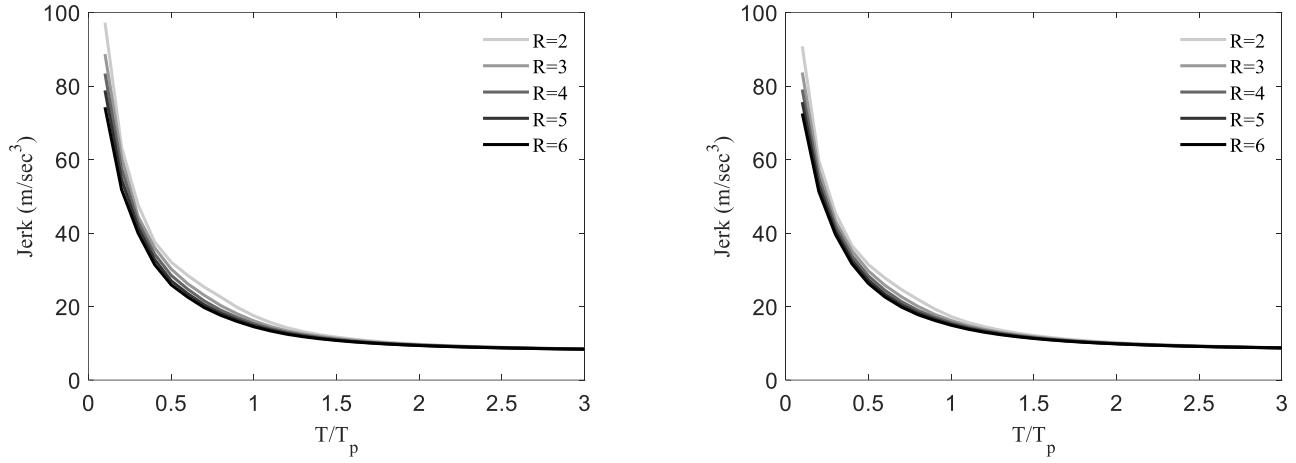

Fig. 2. Effect of the strength reduction factor on the mean jerk inelastic spectra for the PP hysteretic model with: (a): ξ = 0.05; (b): ξ = 0.10; (c): ξ = 0.15; (d): ξ = 0.20.

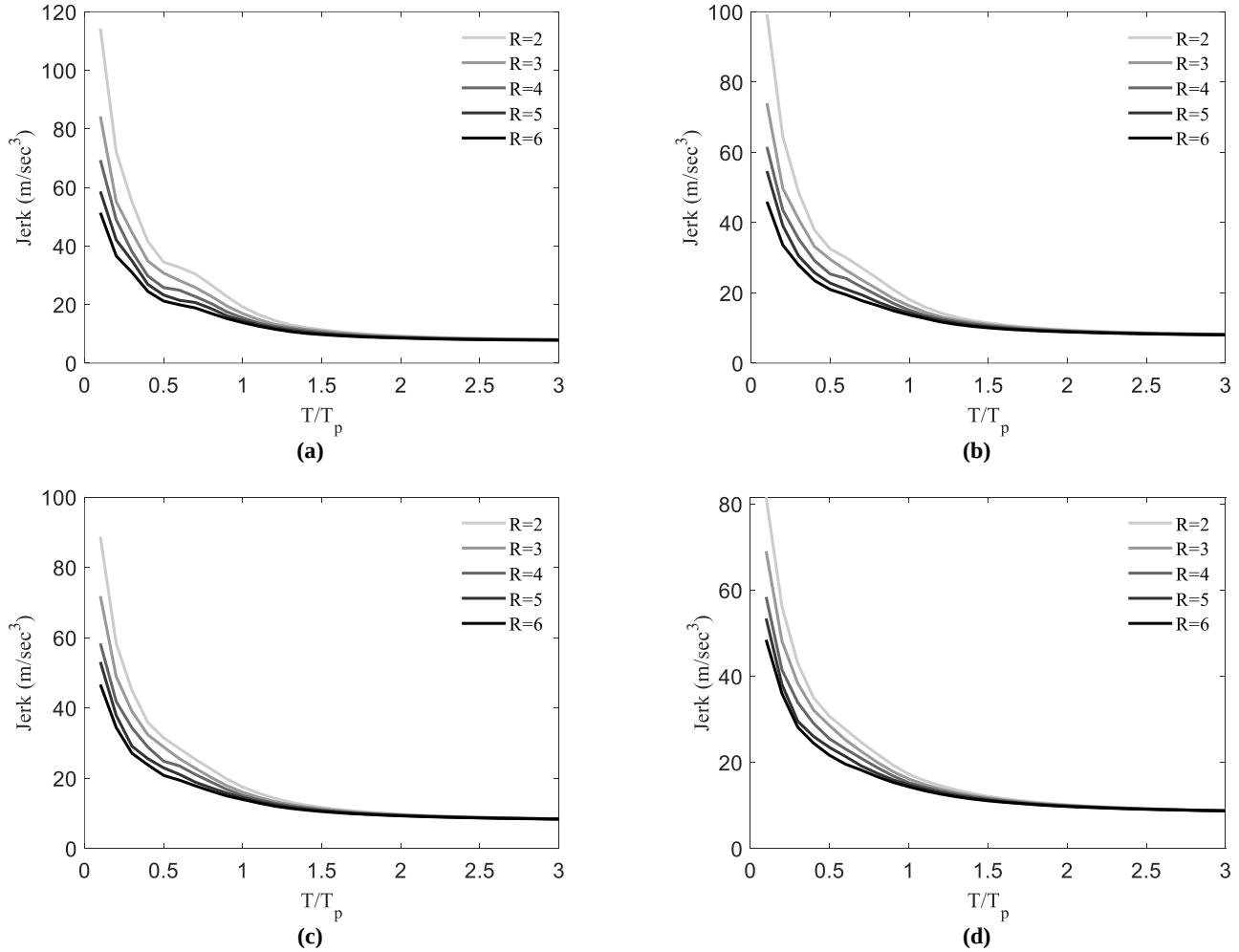

Fig. 3. Effect of the strength reduction factor on the mean jerk inelastic spectra for the DP hysteretic model with: (a): ξ = 0.05; (b): ξ = 0.10; (c): ξ = 0.15; (d): ξ = 0.20.

4.2. Effect of the viscous damping ratio on the inelastic jerk spectra

The effect of the viscous damping ratio on the mean jerk spectra is shown in Figs. 4 and 5 for the PP and DP behavior models, respectively. It is observed from Fig. 4 that this impact is slightly higher in the short normalized period region than in the long normalized period region. In other words, J values decline slightly if ξ increases. For instance, J varies from 35.77 m/s^3 to 31.40 m/s^3 for the SDOF systems with T/T_p = 0.5 and R = 2, when ξ changes from 0.05 to 0.2. Also, the effect of ξ on J becomes lower as R increases. On the other hand, the value of jerk remains stable in the long normalized period region. That is, if R = 2, and ξ = 0.05, J becomes constant by 9.13 m/s^3 on average in the period range $T/T_p \geq 1.5$. This grows slightly to 9.30 m/s^3, 9.54 m/s^3, 9.94 m/s^3 as ξ increases to 0.1, 0.15, and 0.2, respectively, for the same R.

Moreover, the sensitivity of J on ξ for the systems with short values of T/T_p decreases as R tends to increase, namely (R = 3, 4, 5, 6), however, the trend of the jerk response versus the damping ratio is similar as R = 2, as shown in Fig. 4(b)(c)(d)(e). Furthermore, similar trends can be concluded from Fig. 5 for the systems with the DP model, as discussed in Fig. 4; however, the value of the jerk parameter is lower for this type of behavior model.

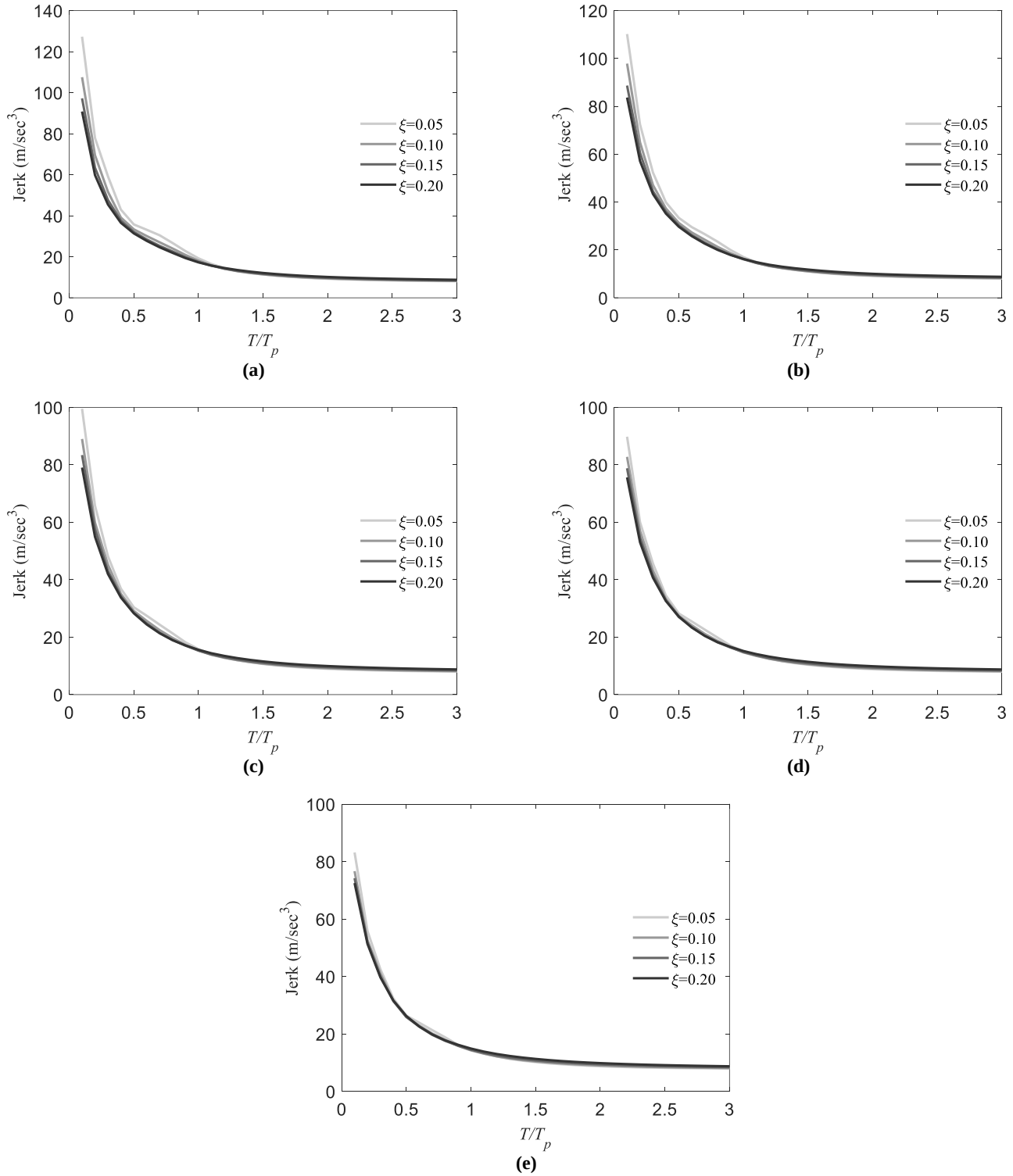

Fig. 4. Effect of the viscous damping ratio on the mean inelastic response spectra in terms of the jerk demand for the PP hysteretic rule and different strength reduction factors: (a) R = 2; (b) R = 3; (c) R = 4; (d) R = 5; and (e) R = 6.

4.3. Effect of the hysteretic model on the inelastic jerk spectra

Fig. 6 shows the sensitivity of the jerk response of the SDOF systems with R = 4 on the hysteretic models (PP and DP) for ξ = 0.05 and ξ = 0.10. As deduced from Fig. 6(a) that in the range of $T/T_p \leq$ 1.0 and ξ = 0.05, the jerk demand of the structures having the PP model is 23.94% on average higher than their equivalents having the DP model.

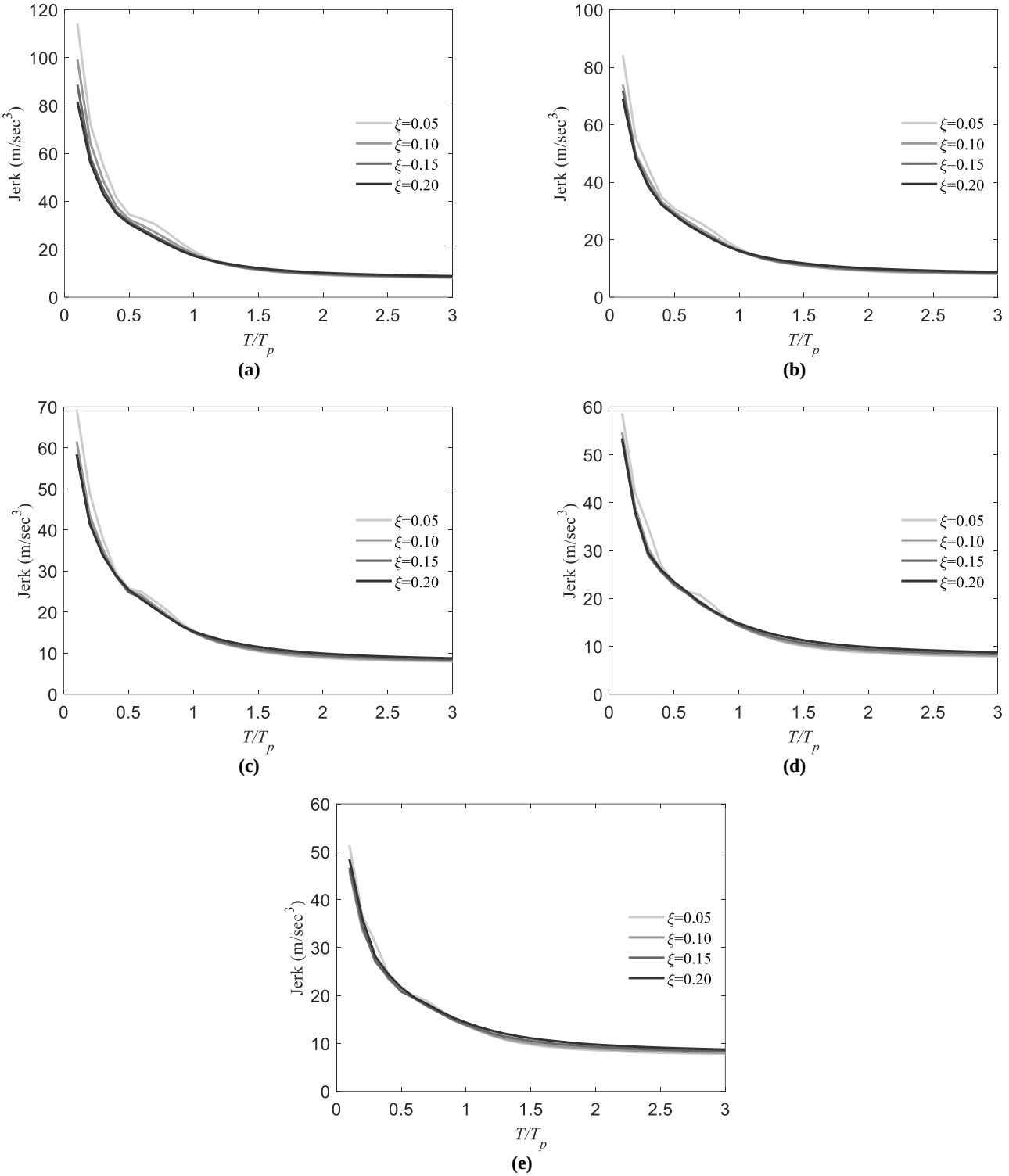

Fig. 5. Effect of the viscous damping ratio on the mean inelastic response spectra in terms of the jerk demand for the DP hysteretic rule and different strength reduction factors: (a) *R* = 2; (b) *R* = 3; (c) *R* = 4; (d) *R* = 5; and (e) *R* = 6.

This difference is negligible when $1.1 \leq T/T_p \leq 3.0$, such that this parameter remains constant in this range of T/T_p by 9.51 m/s^3 on average for both models. In addition, a comparative evaluation is depicted in Fig. 6(b) in the case of $\xi = 0.10$. It reveals that the systems with $T/T_p \leq 1.0$, ξ=0.10, and the PP model experience more jerk responses (22.84% on average) compared to those with the DP model. Furthermore, within the interval $1.1 \leq T/T_p \leq 3.0$, a stable level of the jerk parameter can be seen, whose average value is 9.68 m/s^3 for the two considered hysteretic models in the case of the DP model. This can arise from the fact that in long T/T_p ratios, structural response is governed by gradual displacement trends rather than sharp velocity shifts, which limits acceleration curvature and stabilizes jerk demand. It is noted that pinching and strength degradation reduce acceleration reversals and energy rebound, which directly suppresses jerk peaks, especially in the short T/T_p range.

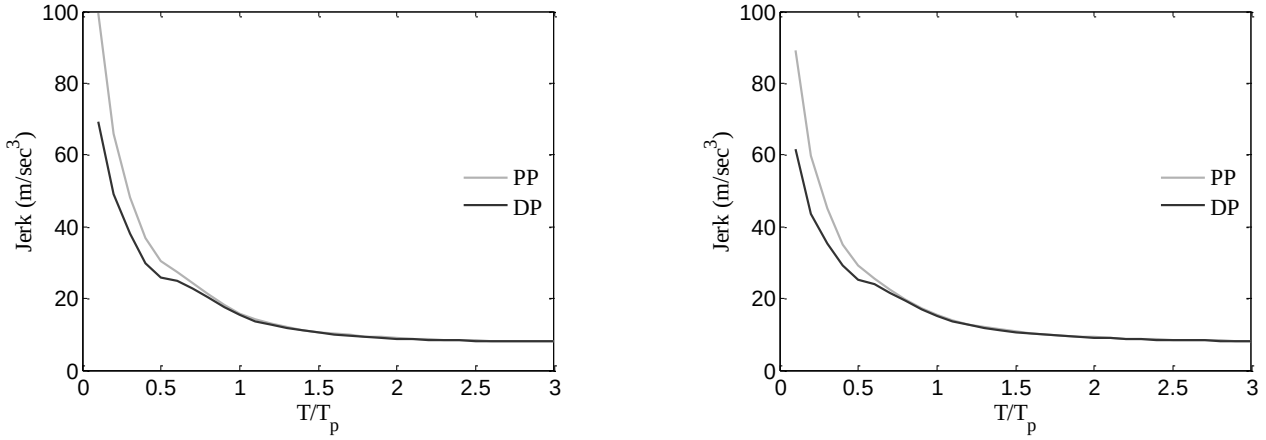

Fig. 6. Effect of the hysteretic model (PP and DP) on the mean inelastic response spectra in terms of the jerk demand for: (a) ξ = 0.05; (b) ξ = 0.1.

5. Prediction equation

In this section, an analytical equation is proposed to predict the mean jerk demand of the SDOF systems under the pulse-like earthquakes based on T/T_p and R for the two hysteretic models and the considered levels of ξ. Extensive nonlinear regression analyses are conducted employing the Least-Squares Fitting method based on the research results to find efficient models. Note that the equation can be extended to a class of steel or RC buildings for predicting the jerk response under pulse-like earthquakes. The mean values of the jerk demand (indicated by J) are predicted using Eq. 1. The unknown coefficient values (a1, a2, …, a8) for the PP and DP hysteretic models, as well as different levels of ξ considered in this study, are obtained from Table 4 and Table 5, respectively. The accuracy of the proposed equation is measured by the coefficient of determination, denoted as R^2. The R^2 values indicated in the tables reveal that the prediction equation is sufficiently accurate. Furthermore, Fig. 7 compares the mean values of jerk predicted by Eq. 1 for structures with the PP model and ξ = 0.05 with the actual values computed from nonlinear time history analyses. This comparison serves as an example of the additional verification and demonstrates the acceptable accuracy of the proposed equation. The presented equation can be employed to predict the jerk demand of structures based on their structural characteristics.

Eq. 1 is an empirical model fitted to the jerk responses obtained from 91 unscaled pulse-like ground motions. The predictor variables are the nondimensional period ratio T/T_p (with T_p the pulse period of each record) and the strength reduction factor R. Because the dataset includes records with a wide range of natural intensities and pulse characteristics, the effects of excitation amplitude are implicitly represented in the calibration through the resulting R values used in the regression. Therefore, Eq. 1 expresses the median relationship between absolute jerk demand, T/T_p, and R for the ensemble of records considered, rather than for any single motion. In practical use, the user applies Eq. 1 with the corresponding T_p of the selected record and the appropriate R value, provided these parameters lie within the calibration range of the 91 motions.

The relationship between jerk demand and structural damage can be interpreted through the strength reduction factor R, which reflects the ductility level of the system. As inelastic excursions increase (i.e., higher R), the system undergoes stiffness degradation and experiences a reduction in high-frequency response components. Consequently, the amplitude of the jerk response decreases with increasing R. This trend indicates that jerk can serve as a dynamic indicator of structural integrity, where large jerk spikes are associated with elastic or near-yield conditions, while reduced jerk amplitudes correspond to systems with pronounced inelastic behavior and energy dissipation.

$$J = a_1 + \frac{a_2}{T/T_p} + \frac{a_3}{R} + \frac{a_4}{\left(T/T_p\right)^2} + \frac{a_5}{R^2} + \frac{a_6}{(T/T_p)R} \quad (1)$$

Table 4. Values of unknown coefficients of Eq. 1 for the PP model.

ξ	a_1	a_2	a_3	a_4	a_5	a_6	R^2
0.05	-0.396	12.190	15.430	-0.611	-27.250	13.710	0.997
0.10	0.506	11.980	13.290	-0.589	-21.830	9.518	0.997
0.15	1.559	11.870	9.937	-0.572	-15.550	6.923	0.998
0.20	2.650	11.690	7.046	-0.562	-10.800	5.502	0.998

Table 5. Values of unknown coefficients of Eq. 1 for the DP model.

ξ	a_1	a_2	a_3	a_4	a_5	a_6	R^2
0.05	2.435	7.207	9.707	-0.588	-21.960	20.250	0.992
0.10	3.026	6.756	10.920	-0.542	-22.700	16.980	0.993
0.15	3.110	6.962	13.750	-0.510	-25.330	13.820	0.993
0.20	3.490	7.526	13.370	-0.510	-23.140	11.160	0.993

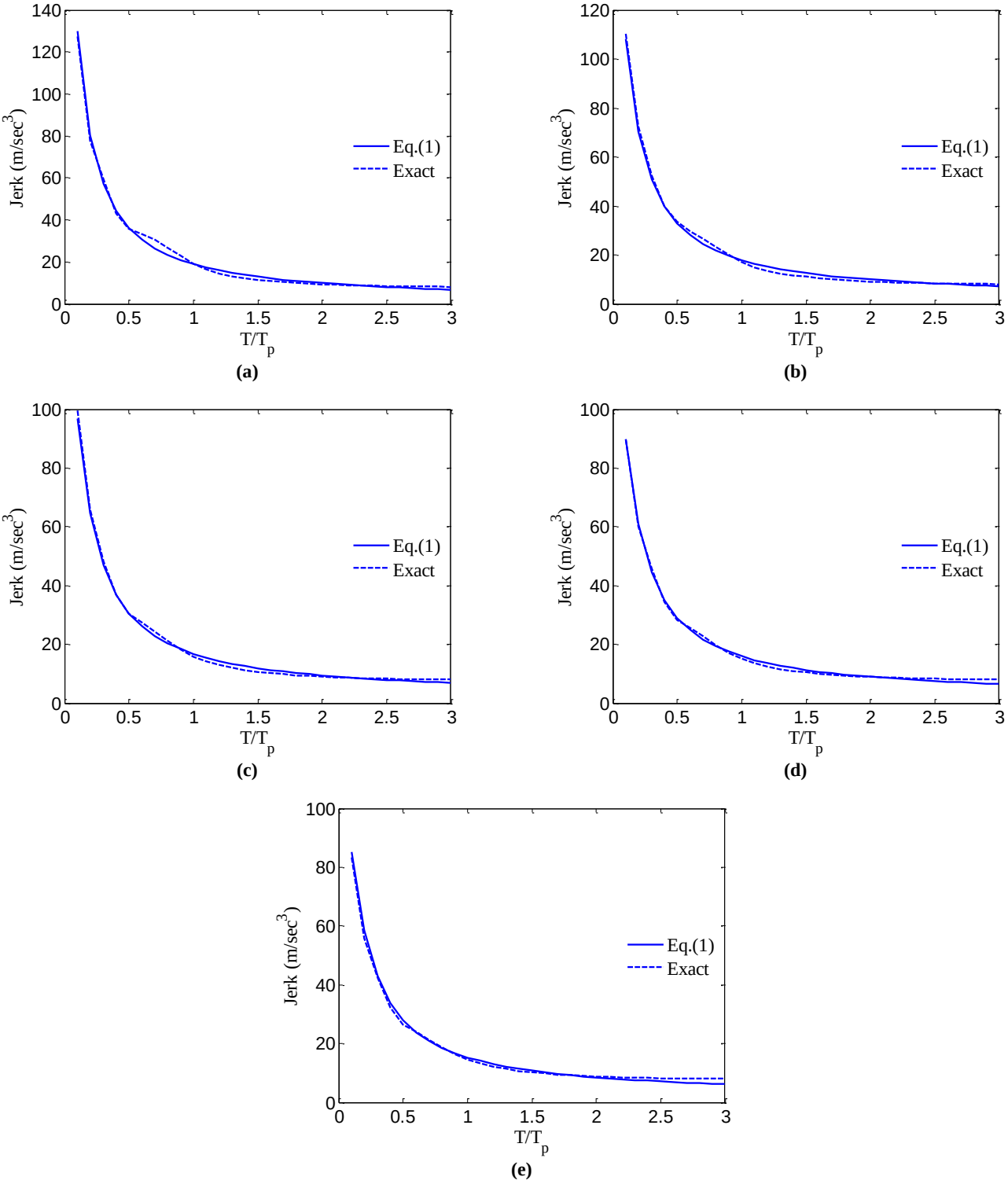

Fig. 7. Predicted values of jerk against actual ones for: (a) R = 2; (b) R = 3; (c) R = 4; (d) R = 5; and (e) R = 6.

6. Summary and conclusion

This study presents constant-strength spectra based on the jerk response of inelastic SDOF systems subjected to 91 pulse-like earthquakes. Different structural characteristics, including the strength reduction factor, hysteretic model, and viscous damping ratio, are considered. The key conclusions of this study are summarized as follows:

- The effect of R on the jerk demand of the structures with the PP model and $T/T_p \leq 1.0$ is relatively significant, such that this response increases as R decreases. For instance, the mean jerk of the SDOF system with $T/T_p = 0.5$ and $\xi = 0.05$ rises from 26.40 m/s^3 to 35.77 m/s^3 (an increase of about 35.5%) when R diminishes from 6 to 2. Moreover, in the range of $2.0 \leq T/T_p \leq 3.0$, the jerk response reaches a constant value of 8.40 m/s^3 on average for all the given R values.
- Similar trends can be observed for the DP model, such that for the same structure ($T/T_p = 0.5$ and $\xi = 0.05$), the mean jerk varies from 21.18 m/s^3 to 34.48 m/s^3 (an increase of roughly 62.80%), as R changes from 6 to 2.
- The effect of the viscous damping ratio on the jerk demand is slightly higher for the systems with short T/T_p values than for those with long values, such that J values decline slightly as ξ increases for the former structures. For example, as ξ changes from 0.05 to 0.2, the variation of J is from 35.77 m/s^3 to 31.40 m/s^3 for the SDOF systems with $T/T_p = 0.5$ and $R = 2$.
- In the long normalized period region ($T/T_p \geq 1.5$), with $R = 2$, and $\xi = 0.05$, the jerk parameter tends to stabilize at an average value of 9.13 m/s^3. This value rises marginally to 9.30 m/s^3, 9.54 m/s^3, and 9.94 m/s^3 as ξ increases to 0.1, 0.15, and 0.2, respectively, for the same R. Furthermore, the sensitivity of the jerk demand to ξ declines in the short normalized period region as R increases. However, the trend of J versus ξ is similar across all considered R values and for the DP model.
- For structures with $T/T_p \leq 1.0$ and $\xi = 0.05$, the jerk demand obtained using the PP model is, on average, 23.94% higher than that obtained using the DP model. This difference is negligible in the range of $1.1 \leq T/T_p \leq 3.0$, where the response is approximately constant at an average of 9.51 m/s^3 for both hysteretic models.
- A prediction equation is proposed to estimate the jerk demand of the structural systems as a function of the elastic vibration period normalized by the pulse period (T/T_p) and the strength reduction factor (R), considering different hysteretic models and viscous damping ratios.

Statements & Declarations

Author contributions

Alireza Garakaninezhad: Conceptualization, Methodology, Formal analysis, Investigation, Software, Validation, Visualization, Resources, Writing - Original Draft, Writing - Review & Editing.

Saeed Amiri: Conceptualization, Investigation, Resources, Writing - Review & Editing.

Funding

The authors received no financial support for the research, authorship, and/or publication of this article.

Data availability

The data presented in this study will be available on interested request from the corresponding author.

Declarations

The authors declare no conflict of interest.

References

[1] Hayati, H., Eager, D., Pendrill, A. M., Alberg, H. Jerk within the Context of Science and Engineering—A Systematic Review. Vibration, 2020; 3: 371-409. doi:10.3390/vibration3040025.

[2] Nemes, A., Mester, G. Energy Efficient Feasible Autonomous Multi-Rotor Unmanned Aerial Vehicles Trajectories. In: Proceedings of the 4th International Scientific Conference on Advances in Mechanical Engineering; 2016 Oct 15-16; Debrecen, Hungary. p. 369-376.

[3] Pendrill, A.-M. Rollercoaster loop shapes. Physics Education, 2005; 40: 517-521. doi:10.1088/0031-9120/40/6/001.

[4] Eager, D., Pendrill, A.-M., Reistad, N. Beyond velocity and acceleration: jerk, snap and higher derivatives. European Journal of Physics, 2016; 37: 065008. doi:10.1088/0143-0807/37/6/065008.

[5] Gierlak, P., Szybicki, D., Kurc, K., Burghardt, A., Wydrzyński, D., Sitek, R., Goczał, M. Design and dynamic testing of a roller coaster running wheel with a passive vibration damping system. Journal of Vibroengineering, 2018; 20: 1129–1143. doi:10.21595/jve.2017.18928.

[6] Sicat, S., Woodcock, K., Ferworn, A. Wearable technology for design and safety evaluation of rider acceleration exposure on aerial adventure attractions. In: Proceedings of the Annual Occupational Ergonomics and Safety Conference; 2018 Jun 7-8; Pittsburgh, Pennsylvania. p. 74-79.

[7] Vaisanen, A. Design of Roller Coasters (Master Thesis). Espoo (FI): Aalto University; 2018.

[8] Pendrill, A.-M., Eager, D. Velocity, acceleration, jerk, snap and vibration: forces in our bodies during a roller coaster ride. Physics Education, 2020; 55: 065012. doi:10.1088/1361-6552/aba732.

[9] Bae, I., Moon, J., Seo, J. Toward a Comfortable Driving Experience for a Self-Driving Shuttle Bus. Electronics, 2019; 8: 943. doi:10.3390/electronics8090943.

[10] Coats, T. W., Haupt, K. D., Murphy, H. P., Ganey, N. C., Riley, M. R. A Guide for Measuring, Analyzing, and Evaluating Accelerations Recorded During Seakeeping Trials of High-Speed Craft. Bethesda (MD): Naval Surface Warfare Center Carderock West Bethesda United States; 2016. Report No.: NSWCCD-80-TR-2016/003.

[11] Sosa, L., Ooms, J. A Comfort Analysis of an 86 m Yacht Fitted with Fin Stabilizers Vs. Magnus-Effect Rotors. In: 24th International HISWA Symposium on Yacht Design and Yacht Construction; 2016 Nov 14-15; Amsterdam, Netherlands. p. 1-13.

[12] Werkman, J. Determining and Predicting the Seakeeping Performance of Ships Based on Jerk in the Ship Motions (Master Thesis). Delft (NL): Delft University of Technology; 2019.

[13] Geoffrey Chase, J., Barroso, L. R., Hunt, S. Quadratic jerk regulation and the seismic control of civil structures. Earthquake Engineering & Structural Dynamics, 2003; 32: 2047-2062. doi:10.1002/eqe.314.

[14] He, Z., Xu, Y. Correlation between global damage and local damage of RC frame structures under strong earthquakes. Structural Control and Health Monitoring, 2017; 24: e1877. doi:10.1002/stc.1877.

[15] Taushanov, A. Jerk Response Spectrum. In: Proceedings of the International Jubilee Scientific Conference “75th Anniversary of UACEG”; 2017 Nov 1-3; Sofia, Bulgaria. p. 39-50.

[16] Tong, M., Wang, G.-Q., Lee, G. C. Time derivative of earthquake acceleration. Earthquake Engineering and Engineering Vibration, 2005; 4: 1-16. doi:10.1007/s11803-005-0019-6.

[17] Papandreou, I., Papagiannopoulos, G. On the jerk spectra of some inelastic systems subjected to seismic motions. Soil Dynamics and Earthquake Engineering, 2019; 126: 105807. doi:10.1016/j.soildyn.2019.105807.

[18] He, H., Li, R., Chen, K. Characteristics of jerk response spectra for elastic and inelastic systems. Shock and Vibration, 2015; 2015: doi:10.1155/2015/782748.

[19] Yaseen, A. A., Ahmed, M. S., Al-Kamaki, Y. S. S. The Possibility of Using Jerk Parameters as Seismic Intensity Measure. In: 3rd international conference on recent innovations in engineering (ICRIE); 2020 Sep 9-10; Duhok, Iraq. p. 254-277.

[20] Wakui, M., Iyama, J., Koyama, T. Estimation of plastic deformation of vibrational systems using the high-order time derivative of absolute acceleration. In: Proceedings of the 16th World Conference on Earthquake Engineering; 2017 Jan 9-13; Santiago, Chile. p. 3932.

[21] Vukobratović, V., Ruggieri, S. Jerk in earthquake engineering: State-of-the-art. Buildings, 2022; 12: 1123. doi:10.3390/buildings12081123.

[22] Amiri, S., Di Sarno, L., Garakaninezhad, A. On the aftershock polarity to assess residual displacement demands. Soil Dynamics and Earthquake Engineering, 2021; 150: 106932. doi:10.1016/j.soildyn.2021.106932.

[23] Amiri, S., Garakaninezhad, A., Bojórquez, E. Normalized residual displacement spectra for post-mainshock assessment of structures subjected to aftershocks. Earthquake Engineering and Engineering Vibration, 2021; 20: 403-421. doi:10.1007/s11803-021-2028-5.

[24] Amiri, S., Di Sarno, L., Garakaninezhad, A. Correlation between non-spectral and cumulative-based ground motion intensity measures and demands of structures under mainshock-aftershock seismic sequences considering the effects of incident angles. Structures, 2022; 46: 1209-1223. doi:10.1016/j.istruc.2022.10.076.

[25] Amiri, S., Koboevic, S. Inelastic spectra under mainshock-multiple aftershock sequences. In: 3rd European Conference on Earthquake Engineering & Seismology; 2022 Sep 4-9; Bucharest, Romania. p. 1-22.

[26] Garakaninezhad, A., Amiri, S., Noroozinejad Farsangi, E. Effects of Ground Motion Incident Angle on Inelastic Seismic Demands of Skewed Bridges Subjected to Mainshock–Aftershock Sequences. Practice Periodical on Structural Design and Construction, 2023; 28: 04023006. doi:10.1061/PPSCFX.SCENG-1218.

[27] Amiri, S., Koboevic, S. On the necessary number of aftershocks for seismic collapse risk assessment of buildings. In: 18th World Conference on Earthquake Engineering (WCEE2024); 2024 Jun 30-Jul 5; Milan, Italy. p. 1-9.

[28] Somerville, P. G., Smith, N. F., Graves, R. W., Abrahamson, N. A. Modification of Empirical Strong Ground Motion Attenuation Relations to Include the Amplitude and Duration Effects of Rupture Directivity. Seismological Research Letters, 1997; 68: 199-222. doi:10.1785/gssrl.68.1.199.

[29] Baker, J. W. Identification of near-fault velocity pulses and prediction of resulting response spectra. 1st ed. Reston (VA): 2008. doi:10.1061/40975(318)4.

[30] Rupakhety, R., Sigurdsson, S. U., Papageorgiou, A. S., Sigbjörnsson, R. Quantification of ground-motion parameters and response spectra in the near-fault region. Bulletin of Earthquake Engineering, 2011; 9: 893-930. doi:10.1007/s10518-011-9255-5.

[31] Ezzodin, A., Ghodrati Amiri, G., Raissi Dehkordi, M. A Random Vibration-Based Simulation Model for Nonlinear Seismic Assessment of Steel Structures Subjected to Fling-Step Ground Motion Records. Journal of Vibration Engineering & Technologies, 2022; 10: 2641-2655. doi:10.1007/s42417-022-00509-9.

[32] Bray, J. D., Rodriguez-Marek, A. Characterization of forward-directivity ground motions in the near-fault region. Soil Dynamics and Earthquake Engineering, 2004; 24: 815-828. doi:10.1016/j.soildyn.2004.05.001.

[33] Iervolino, I., Chioccarelli, E., Baltzopoulos, G. Inelastic displacement ratio of near-source pulse-like ground motions. Earthquake Engineering & Structural Dynamics, 2012; 41: 2351-2357. doi:10.1002/eqe.2167.

[34] Khoshnoudian, F., Ahmadi, E. Effects of pulse period of near-field ground motions on the seismic demands of soil–MDOF structure systems using mathematical pulse models. Earthquake Engineering & Structural Dynamics, 2013; 42: 1565-1582. doi:10.1002/eqe.2287.

[35] Khoshnoudian, F., Ahmadi, E. Effects of inertial soil–structure interaction on inelastic displacement ratios of SDOF oscillators subjected to pulse-like ground motions. Bulletin of Earthquake Engineering, 2015; 13: 1809-1833. doi:10.1007/s10518-014-9693-y.

[36] Baker, J. W. Quantitative Classification of Near-Fault Ground Motions Using Wavelet Analysis. Bulletin of the seismological society of America, 2007; 97: 1486-1501. doi:10.1785/0120060255.

[37] Zhai, C., Li, S., Xie, L., Sun, Y. Study on inelastic displacement ratio spectra for near-fault pulse-type ground motions. Earthquake Engineering and Engineering Vibration, 2007; 6: 351-355. doi:10.1007/s11803-007-0755-x.

[38] Dong, H., Han, Q., Du, X., Liu, J. Constant ductility inelastic displacement ratios for the design of self-centering structures with flag-shaped model subjected to pulse-type ground motions. Soil Dynamics and Earthquake Engineering, 2020; 133: 106143. doi:10.1016/j.soildyn.2020.106143.

[39] Ghanbari, B., Akhaveissy, A. H. Constant-damage residual ratios of SDOF systems subjected to pulse type ground motions. AUT Journal of Civil Engineering, 2020; 4: 145-154. doi:10.22060/ajce.2019.14984.5510.

[40] Dong, H., Han, Q., Qiu, C., Du, X., Liu, J. Residual displacement responses of structures subjected to near-fault pulse-like ground motions. Structure and Infrastructure Engineering, 2022; 18: 313-329. doi:10.1080/15732479.2020.1835997.

[41] Garakaninezhad, A., Amiri, S. Inelastic acceleration ratio of structures under pulse-like earthquake ground motions. Structures, 2022; 44: 1799-1810. doi:10.1016/j.istruc.2022.08.102.

[42] OpenSees Effects of Hysteretic-Material Parameters. 2006. Available online: https://opensees.berkeley.edu/OpenSees/manuals/usermanual/4052.htm (accessed on December 2025).

[43] Di Sarno, L., Amiri, S. Period elongation of deteriorating structures under mainshock-aftershock sequences. Engineering Structures, 2019; 196: 109341. doi:10.1016/j.engstruct.2019.109341.

[44] Mazzoni, S., McKenna, F., Scott, M. H., Fenves, G. L. OpenSees Command Language Manual. Pacific Earthquake Engineering Research (PEER) Center, 2006; 264: 137-158.

[45] Scott, M., Filippou, F. Hysteretic Material. 2016. Available online: https://opensees.berkeley.edu/wiki/index.php/Hysteretic_Material (accessed on December 2025).

[46] PEER ground motion database. Pacific Earthquake Engineering Research Center. 2010. Available online: https://ngawest2.berkeley.edu/ (accessed on December 2025).